uOttawa

L'Université canadienne
Canada's university

FACULTÉ DES ÉTUDES SUPÉRIEURES ET POSTOCTORALES

uOttawa

L'Université canadienne
Canada's university

FACULTY OF GRADUATE AND POSDOCTORAL STUDIES

Sean C.C. Bailey
AUTEUR DE LA THÈSE / AUTHOR OF THESIS

Ph.D. (Mechanical Engineering)
GRADE / DEGREE

Department of Mechanical Engineering
FACULTÉ, ÉCOLE, DÉPARTEMENT / FACULTY, SCHOOL, DEPARTMENT

The Interaction of a Wing-Tip Vortex and Free-Stream Turbulence

TITRE DE LA THÈSE / TITLE OF THESIS

Stavros Tavoularis
DIRECTEUR (DIRECTRICE) DE LA THÈSE / THESIS SUPERVISOR

CO-DIRECTEUR (CO-DIRECTRICE) DE LA THÈSE / THESIS CO-SUPERVISOR

EXAMINATEURS (EXAMINATRICES) DE LA THÈSE / THESIS EXAMINERS

B. Lee

M. Yaras

R. Milane

A. Smits

Gary W. Slater
Le Doyen de la Faculté des études supérieures et postdoctorales / Dean of the Faculty of Graduate and Postdoctoral Studies

The Interaction of a Wing-Tip Vortex and Free-Stream Turbulence

by

Sean C. C. Bailey

A thesis presented to the
Faculty of Graduate and Postdoctoral Studies
in partial fulfulment of the
requirement for the degree of

DOCTOR OF PHILOSOPHY
in
MECHANICAL ENGINEERING

Ottawa-Carleton Institute for Mechanical and Aerospace Engineering
Department of Mechanical Engineering
University of Ottawa
Ottawa, Ontario, Canada
December 2006

Your file Votre référence
ISBN: 978-0-494-25854-5
Our file Notre référence
ISBN: 978-0-494-25854-5

Abstract

The formation and development of a vortex generated by a wing with a NACA0012 airfoil section in the presence of grid-generated turbulence was studied at Reynolds numbers 29000 in a water tunnel and 240000 in a wind tunnel. Flow visualization indicated that the free-stream turbulence did not significantly affect the large-scale features of the vortex during its formation, however, it resulted in an increase in the turbulence within the vortex as well as an increase in the wandering motion of the vortex. Extensive single-point and two-point, three-component hot-wire anemometry.measurements were conducted for the no-grid case and four cases using two different grids. Time-averaged statistics were found to be significantly influenced by wandering of the vortex position. Quantitative analysis of vortex wandering showed a significant increase in its amplitude with increasing free-stream turbulence. The radial profile of the circumferential velocity with respect to the wandering vortex axis was reconstructed using two-point measurements. The rate of decay of the peak circumferential velocity was found to increase with increasing free-stream turbulence, but the radial location at which it occurred did not change significantly. Analysis of the velocity signals indicated that the turbulent eddies from the wing's wake and the grid turbulence tend to wrap around the vortex core.

For Tanya and my family.

Acknowledgments

I would like to thank Professor Tavoularis whose door was always open to discuss my research or whatever else was on my mind. His advice and guidance has always provided greater insight into my work and his support has always been wholehearted.

I would also like to thank NSERC, the OGSST program, including the Bank of Montreal and the Government of Ontario, the Faculty of Graduate and Postdoctoral Studies, as well as Professor Tavoularis for providing financial support for the duration of my doctoral studies.

I am grateful to Professor Petar Vukoslavčević, Professor Metin Yaras and Dr. Ben Lee for their assistance in the early stages of this work. In particular, Professor Petar Vukoslavčević was an immense help by not only building the four-sensor probes used in this study, but also in providing exceptional guidance about their repair and usage. Avi Aharoni is gratefully acknowledged for his assistance in solving the technical challenges with regards to the anemometers. I would also like to thank Professor Steen Sjolander who has allowed me the use of his anemometer for an extended period of time.

I would not have been able to perform my experiments without the constant assistance of the members of the Department of Mechanical Engineering machine shop: Brent Cotter, Leo Denner, Mike Burns, James MacDermid and John Perrins. These gentlemen were always quick to drop what they were doing and offer assistance when I needed it.

Finally, I would like to thank my fellow graduate students, Warren Dunn, Matthew Doyle, Tony Standbridge, Andrew Cameron and Dong Il Chang for their friendship. The time spent discussing our research or a myriad of other topics was always enjoyable.

Contents

Nomenclature

A	arbitrary random process; also arbitrary constant ; also area
A_{noz}	calibrator nozzle exit area
a	fluctuating component of arbitrary random process
a_i	arbitrary curve fit coefficient
a_{ij}	anisotropy tensor
B	arbitrary constant
B_i	arbitrary curve fit coefficient
b	wing semi-span
C	arbitrary constant
c	wing chord length
c_i	arbitrary curve fit coefficient
c_L	section lift coefficient
D	arbitrary constant
D_i	arbitrary curve fit coefficient; also arbitrary constant
E_a	anemometer output voltage
E_b	anemometer bridge output voltage

E_{noz}	calibrator thermistor output voltage
E_o	output voltage at zero input
E_{off}	offset voltage
E_{plen}	calibrator plenum pressure transducer voltage
E_{pitot}	Pitot-static tube pressure transducer output voltage
E_{wt}	wind tunnel temperature sensing circuit output voltage
E_{xx}	streamwise wavenumber spectrum
e	correlation coefficient
F_{ii}	frequency spectrum of U_i
f	frequency
f_1	arbitrary function used during probe calibration and data reduction
f_2	arbitrary function used during probe calibration and data reduction
f_3	arbitrary function used during probe calibration and data reduction
f_c	analogue filter cutoff frequency
f_p	peak frequency
f_w	average wandering frequency
G	gain
G_{yz}	cross-power spectrum of U_y and U_z
H_{noz}	height of nozzle exit referenced to plenum pressure tap
k	turbulent kinetic energy
L_x	longitudinal integral length scale
L_{x_o}	longitudinal integral length scale measured in grid turbulence

l_{mv}	length of one side of probe measurement volume
M	grid mesh size
m	arbitrary power law curve fit coefficient
$\dot{m}$	mass flow rate
$\dot{m}_u$	mass flow rate per unit span
n	arbitrary power law curve fit coefficient
n_i	unit vector normal to a plane ; or King's Law curve fit coefficient for wire i
P	pressure
P_{pitot}	Pitot-static tube pressure
P_{plen}	calibrator plenum pressure
P_v	probability density of vortex position
p	fluctuating component of pressure
Q_e	estimated velocity magnitude in probe-fixed coordinates
Q_{noz}	nozzle exit velocity magnitude
Q_p	velocity magnitude in probe-fixed coordinates
q	dimensionless swirl parameter
R_{xx}	autocorrelation of U_x
R_{yz}	cross-correlation of U_y and U_z
r	radial distance from vortex axis
r_{inv}	radial distance at which vortex is irrotational
r_p	radial distance of probe from vortex axis
$r_{\theta \max}$	radial distance of peak circumferential velocity

r_χ	radial distance from vortex axis in the vortex cross-plane
Re_c	Reynolds number based on chord
Re_λ	turbulence Reynolds number
S	distance between probes
S_{ij}	rate of strain tensor
s	magnitude of turbulent strain rate
s_i	distance vector
s_{ij}	fluctuating component of rate of strain tensor
s_o	magnitude of turbulent strain rate measured in grid turbulence
T_{noz}	calibrator exit air temperature
T_w	wire temperature
T_L	Lagrangian integral time scale
T_∞	wind tunnel free-stream temperature
t	time
U	velocity
U_{eff}	effective velocity
U_i	velocity vector
U_o	local free-stream velocity
U_p	peak streamwise velocity in core
U_r	velocity in the radial direction
U_x	velocity in x direction in vortex-fixed coordinates
U_{x_e}	estimated velocity in x_p direction in probe-fixed coordinates

U_{x_p} velocity in x_p direction in probe-fixed coordinates

U_y velocity in y direction in vortex-fixed coordinates

U_{yv} velocity in y direction induced by vortex

U_{y_e} estimated velocity in y_p direction in probe-fixed coordinates

U_{y_p} velocity in y_p direction in probe-fixed coordinates

U_z velocity in z direction in vortex-fixed coordinates

U_{zv} velocity in z direction induced by vortex

U_{z_e} estimated velocity in z_p direction in probe-fixed coordinates

U_{z_p} velocity in z_p direction in probe-fixed coordinates

U_θ velocity in the circumferential direction

$U_{\theta\,\max}$ peak circumferential velocity

$U_{\theta\chi}$ circumferential velocity in instantaneous cross-sectional plane of the vortex

U_∞ free-stream velocity

u_i fluctuating component of velocity vector

u_x fluctuating component of U_x

u_y fluctuating component of U_y

u_z fluctuating component of U_z

u'_{zo} standard deviation of U_z measured in grid turbulence

u_η Kolmogorov velocity scale

V volume

X streamwise distance from wing tip 1/4 chord location

X_w distance along chord from wing tip 1/4 chord location

x	streamwise direction in vortex-fixed coordinates
x_g	streamwise distance from grid
x_{go}	virtual origin in grid coordinates
x_i	direction vector
x_p	direction along probe axis
Y	spanwise distance from wing tip 1/4 chord location (positive outboard)
Y_w	spanwise distance from wing tip 1/4 chord location (perpendicular to chord)
y	distance from vortex axis in spanwise direction (positive outboard)
y_p	transverse direction in probe-fixed coordinates; also probe y position
y_v	instantaneous vortex y position
Z	distance in direction of lift from wing tip 1/4 chord location
Z_o	initial position of probe during boundary layer measurements
Z_w	distance perpendicular to wing chord from wing tip 1/4 chord location
z	distance from vortex axis in direction of lift
z_p	transverse direction in probe-fixed coordinates; also probe z position
z_v	instantaneous vortex z position

Greek Symbols

α	wing angle of attack
α_{eff}	four-wire probe effective wire angle
α_{mod}	angle about z_p between vortex cross-plane and measurement plane
α_w	four-wire probe wire angle

β_{mod}	angle about y_p between vortex cross-plane and measurement plane
Γ	circulation
Γ_o	total vortex circulation
γ_T	eddy diffusivity
δ_{ij}	Kronecker delta
ε	turbulent kinetic energy dissipation rate
ε_{ijk}	alternating tensor
ζ_{ij}	frequency distribution of anisotropy tensor
η	Kolmogorov microscale
θ	angular coordinate measured from positive y towards positive z
θ_{cal}	calibrator pitch angle
θ_{mod}	angle between y_p direction and y direction
κ_x	streamwise wavenumber
λ_x	longitudinal Taylor microscale
ν	kinematic viscosity
ξ	Gaussian random variable
ξ_i	local angle of wing surface to free stream
ρ	density
σ	wandering amplitude
σ_y	wandering amplitude in y direction
σ_z	wandering amplitude in z direction
τ	time displacement

τ_E	eddy turnover time
τ_o	time-displacement value at which autocorrelation is zero
τ_η	Kolmogorov time scale
ϕ_χ	vortex yaw angle
φ_{cal}	calibrator roll angle
ψ_χ	vortex pitch angle
Ω_i	vorticity vector
Ω_{ij}	rotation tensor
ω_i	fluctuating component of vorticity vector

Other Notation

$()^*$	denotes a Cartesian coordinate system in a rotated frame
$()'$	denotes standard deviation
$()_1$	denotes a value referring to probe 1
$()_2$	denotes a value referring to probe 2
$()_c$	denotes a value estimated from wandering correction
$()_m$	denotes a value estimated from curve fit of time-averaged profile
$()_x$	denotes a value in the x direction
$()_y$	denotes a value in the y direction
$()_z$	denotes a value in the z direction
$()_{\mathrm{act}}$	denotes an actual value
$()_{\mathrm{meas}}$	denotes a measured value

$()_{\mathrm{new}}$	denotes a new value for iteration
$()_{\mathrm{old}}$	denotes an old value for iteration
$()_{(99\%)}$	denotes value which is greater than 99% of remaining values
$\overline{()}$	denotes a time-average
$\widetilde{()}$	denotes an average value in a frame wandering with vortex
$\widehat{()}$	denotes an average of a bandpass filtered value
$\langle\rangle$	denotes an ensemble average

Acronyms

RDT	rapid distortion theory
DNS	direct numerical simulation
LES	large eddy simulation
PDF	probability density function
JPDF	joint probability density function
PVC	polyvinyl chloride
ASCII	american standard code for information interchange
PC	personal computer
rms	root-mean-square

List of Figures

List of Tables

Chapter 1

Introduction

1.1 Wing-tip vortices

The vortex is one of the most easily recognizable fluid mechanical entities. Throughout prehistory and history, the vortex has been a theme often repeated in artwork, legend, philosophy and cosmogony around the world. In the early 1600s, French philosopher and mathematician René Descartes employed vortices to explain the creation of the universe and the movement of bodies within it. Although his theory was later disproved, its conceptualization serves as an example to show the historical significance of the vortex.

There are innumerable examples of vortices in fluid mechanics, spanning a wide range of scales, ranging from hurricanes and tornadoes in atmospheric flows to microscopic vortices generated by self-propelled microorganisms (Lugt (1983)). Vortices play a significant role in a variety of engineering applications. An important application is the vortices that form at the tips of finite-span lifting surfaces, such as wings and propellers, which are used to generate lift and thrust.

As fluid flows past lifting surfaces, it typically accelerates over one side of the surface, while it decelerates over the other, thus generating a pressure difference across the surface. This pressure difference results in a force, which can be applied for lift or propulsion. As the fluid on the two sides of the surface is connected around the tip, the pressure difference must vanish at the tips, causing a spanwise pressure gradient, as illustrated in Figure 1.1. Figure 1.2 illustrates how the spanwise pressure gradient generates a spanwise component of velocity and a corresponding velocity gradient within a shear layer at the trailing edge of the lifting surface. The shear layer extends up to the wing tip, where high local shear causes it to roll up, as shown in Figure 1.3, and form a vortex. Commonly referred to as trailing vortices or wing-tip vortices, such vortices would occur inevitably at the edges of any lifting surface of finite span. Examples of wing-tip vortices can be found behind aircraft wings, helicopter rotors and propellers.

1.2 Turbulence

Turbulence is commonly understood to be a highly disorganized fluid motion, characterized by random velocity fluctuations in both time and space. Any laminar flow would become unstable and lead to turbulence if the inertial forces acting on it would increase sufficiently with respect to viscous forces. The ratio of inertial forces to viscous forces is commonly represented by the Reynolds number, Re, of the fluid flow. Although the exact definition of Re is dependent on the flow being studied, generally speaking, turbulence can be expected at high Reynolds numbers.

Due to the disorganized motion, turbulence results in a significant increase in the

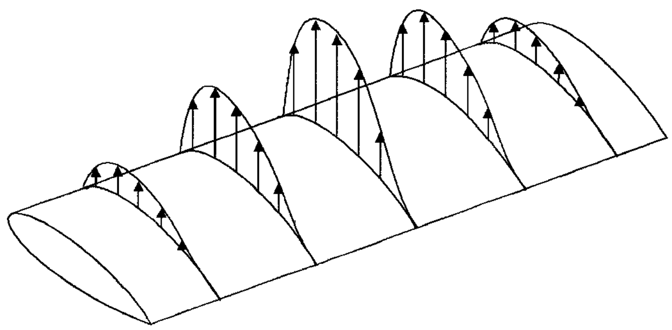

Figure 1.1: Sketch showing change in pressure difference across the span of a wing.

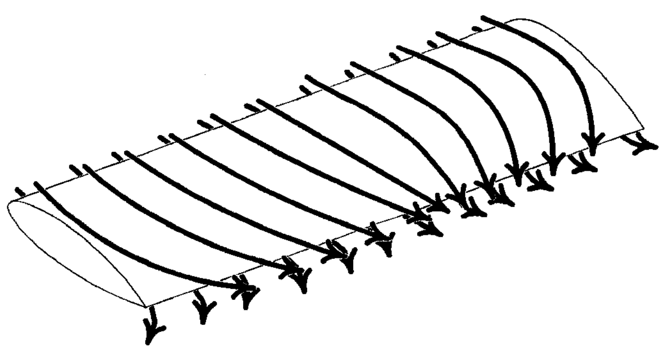

Figure 1.2: Sketch showing spanwise flow induced by changing pressure difference across span.

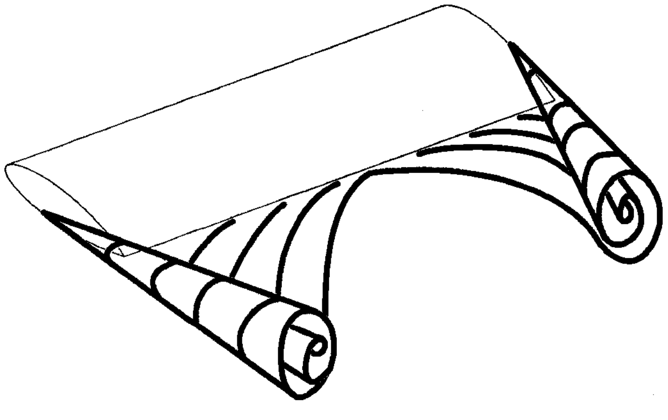

Figure 1.3: Sketch showing roll-up of shear layer into trailing vortices.

mixing and diffusion of mass, momentum and energy. Such mixing can be both beneficial and detrimental, as can be seen in the example of a boundary layer on an aircraft wing: increased mixing causes diffusion of lower momentum boundary fluid away from the wing, resulting in an increased velocity deficit at the wing trailing edge and hence increased skin friction drag; at the same time, turbulence also mixes the faster free stream fluid with the slower fluid near the wall, energizing the wing boundary layer and thereby delaying flow separation and stall.

A turbulent flow is classified as being homogeneous if its statistically averaged properties are independent of location. Isotropic is a turbulent flow whose statistical characteristics are independent of orientation. Although homogeneous and isotropic turbulence is rarely found in nature, this type of turbulence is commonly used as a paradigm to study and understand many turbulent phenomena. One of the simplest ways to generate such a flow in the laboratory is through the use of grids or other uniformly distributed flow obstructions in wind and water tunnels. The wakes of grid elements interact with each other, eventually breaking down and generating turbulence, which, when considered in a frame moving with the uniform mean flow speed, is nearly homogeneous and isotropic.

1.3 Motivation and objectives

The trailing vortices developed behind aircraft have long been known to create a hazard for other aircraft whose flight path might intersect them. Such an encounter results in the intersecting aircraft experiencing large rolling or pitching moments. This becomes a particularly dangerous situation when the aircraft is landing or taking off. Then, the aircraft is close to both stall speed and the ground, while, at the same time, a trailing vortex encounter is more likely to occur. The hazard caused by tip vortices is compounded by their strong stability and slow decay rate, corresponding to long periods of time for the flow disturbances to be reduced to safe levels.

Air traffic control regulations provide safe separation distances between aircraft grouped by weight. These procedures have been developed through experience and provide a safe environment for air travel. However, as the volume of civil aviation increases around the world, there is an increased need for a corresponding increase in the frequency of arrivals and departures at airports. There are two possible ways to increase this frequency: either by increasing the number of runways at an airport or by decreasing the spacing between aircraft arrivals or departures on the same runway. In the case of many airports, there is little or no space to increase airport size and noise abatement considerations prevent expansion. Even if expansion is possible, the trailing vortex hazard is not necessarily mitigated due to an increase in the number of aircraft sharing the airspace. Therefore, increasing the frequency of aircraft arrivals and departures is becoming a more necessary option. However, to do this safely, our understanding of tip vortices must be significantly increased.

Additionally, current procedures have been developed to respond to the needs of current aircraft. Development of heavier aircraft, such as the Airbus A380, or aircraft of different configurations, such as the blended wing concept (Liebeck (2004)), will require careful reassessment of safety requirements with regards to the vortex hazards that such aircraft could introduce.

One factor that is known to increase the rate of decay of tip vortices is the existence of atmospheric turbulence (Sarpkaya and Daly (1987)). Despite this knowledge, very few experimental studies have been conducted to increase the understanding of the mechanisms by which the rate of decay increases and the effect that increased turbulence levels have on vortex formation.

The study of an isolated vortex in a turbulent stream may also contribute towards understanding turbulence itself. The simultaneous existence of, and interactions among, coherent vortical structures has been observed in many studies of turbulence. These coherent structures take the form of small scale vortices and have been attributed to the production and dissipation of turbulence. Nevertheless, the interaction between the coherent structures and surrounding small scale turbulence is not well understood. Despite the importance of interaction of structures of different scales, there have been surprisingly few experimental studies which isolate a single vortex and study its interaction with the surrounding turbulent eddies (Bandyopadhyay et al. (1991), Heyes et al. (2004), Beninati and Marshall (2005)). The dearth of experimental studies results in an insufficient experimental database that can be used by turbulence modelers and computational fluid dynamicists (Marshall and Beninati (2000)). As a result, a focused and thorough study of the interaction of an isolated vortex and external turbulence will provide an extremely useful validation case for other researchers.

The specific objectives of this thesis can be summarized as follows:

- Determine what effect, if any, the free stream turbulence has on the mechanism of vortex formation at the wing
- Provide further insight into the phenomenon of vortex wandering

- Observe and document the effect of free stream turbulence on the fully formed vortex
- Document the distortion of the free-stream turbulence in the vicinity of the vortex
- Provide an extensive set of experimental data that can be used for the validation of turbulence models and computational methods.

Chapter 2

Analytical background

2.1 Vorticity and circulation

As described by Saffman (1995), the relative velocity of two fluid particles separated by an infinitesimal distance δx_i can be expressed as

$$\delta U_i = S_{ij}\delta x_j + \Omega_{ij}\delta x_j \ , \tag{2.1}$$

where S_{ij} is the rate of strain tensor, defined as

$$S_{ij} = \frac{1}{2}\left(\frac{\partial U_i}{\partial x_j} + \frac{\partial U_j}{\partial x_i}\right) \tag{2.2}$$

and Ω_{ij} is the rotation tensor, defined as

$$\Omega_{ij} = -\frac{1}{2}\varepsilon_{ijk}\Omega_k \ , \tag{2.3}$$

where the alternating tensor ε_{ijk} is defined as

$$\varepsilon_{ijk} = \begin{cases} 1 \text{ if the values of } i,j,k \text{ are an even permutation of 1,2,3 (i.e., 1,2,3)} \\ -1 \text{ if the values of } i,j,k \text{ are an odd permutation of 1,2,3 (i.e., 3,2,1)} \\ 0 \text{ if the values of } i,j,k \text{ are not a permutation of 1,2,3 (i.e., 1,1,3)} \end{cases} \cdot \tag{2.4}$$

and the vorticity vector Ω_k is defined as

$$\Omega_k = \varepsilon_{ijk}\frac{\partial U_j}{\partial x_i}. \tag{2.5}$$

The magnitude of the vorticity is equal to twice the angular velocity of the fluid particle; for inertial reference frames, it is independent of the frame of reference (Lugt (1983)).

In an analogy to the concept of a streamline, a "vorticity line" can be defined as a line tangential to the local vorticity vector at all its points. For an inviscid fluid where the fluid is barotropic (the density of the fluid depends on pressure alone) Saffman (1995) demonstrates that if a vorticity line and a material line coincide at some time instant, they will coincide at all times, in which case the vorticity line is said to move with the fluid. A "vorticity tube" is defined as a surface formed by the vorticity lines passing through a closed curve in space. An isolated vorticity tube surrounded by irrotational fluid is commonly referred to as a "vortex tube" or simply vortex.

The strength of a vortex is defined as the circulation around a curve surrounding it, namely

$$\Gamma = \oint U_i ds_i = \int\int \Omega_i n_i dA \ , \tag{2.6}$$

where ds_i is an element of a closed curve in space enclosing the area A with unit normal n_i. Therefore, the strength of the vortex is equal to the flux of vorticity through the closed path, s_i. Some texts (i.e. Bertin and Smith (1989)) define circulation as being negative when defined as in Equation 2.6, whereas others (i.e. Saffman (1995)) define it as above. Within this report, circulation is defined as in Equation 2.6, which results in positive vortex circulation in the coordinate system used in this study.

2.2 Incompressible viscous flow

For the proposed research, the fluid can be approximated as Newtonian, either having constant density or being incompressible and barotropic and under negligible body forces. Under these conditions, conservation of mass and momentum can be expressed as

$$\frac{\partial U_i}{\partial x_i} = 0 \tag{2.7}$$

and

$$\frac{\partial U_i}{\partial t} + U_j \frac{\partial U_i}{\partial x_j} = -\frac{1}{\rho}\frac{\partial P}{\partial x_i} + \nu \frac{\partial^2 U_i}{\partial x_j x_j}\ , \tag{2.8}$$

where ρ and ν are, respectively, the density and kinematic viscosity of the fluid.

Cylindrical coordinates are commonly used in vortex studies. Equations 2.7 and 2.8 can be written in cylindrical coordinates using $x = x_1$ as the direction tangential to the vortex axis, $\theta = \arctan(-x_2/x_3)$ as the azimuthal direction and $r = ({x_2}^2 + {x_3}^2)^{\frac{1}{2}}$ as the radial direction. The corresponding velocity components are U_x, U_θ and U_r. In cylindrical coordinates, and under the assumptions that the vortex is axi-symmetric and its axis is straight, the continuity and momentum equations can be written as (Lugt (1983))

$$\frac{\partial U_r}{\partial r} + \frac{U_r}{r} + \frac{\partial U_x}{\partial x} = 0 \tag{2.9}$$

and

$$\frac{\partial U_r}{\partial t} + U_r \frac{\partial U_r}{\partial r} + U_x \frac{\partial U_r}{\partial x} - \frac{U_\theta^2}{r} = -\frac{1}{\rho}\frac{\partial P}{\partial r} + \nu\left(\frac{\partial^2 U_r}{\partial r^2} + \frac{\partial}{\partial r}\left(\frac{U_r}{r}\right) + \frac{\partial^2 U_r}{\partial x^2}\right)\ , \tag{2.10}$$

$$\frac{\partial U_\theta}{\partial t} + U_r \frac{\partial U_\theta}{\partial r} + U_x \frac{\partial U_\theta}{\partial x} - \frac{U_\theta U_r}{r} = \nu \left(\frac{\partial^2 U_\theta}{\partial r^2} + \frac{\partial}{\partial r} \left(\frac{U_\theta}{r} \right) + \frac{\partial^2 U_\theta}{\partial x^2} \right) , \tag{2.11}$$

$$\frac{\partial U_x}{\partial t} + U_r \frac{\partial U_x}{\partial r} + U_x \frac{\partial U_x}{\partial x} = -\frac{1}{\rho} \frac{\partial P}{\partial z} + \nu \left(\frac{\partial^2 U_x}{\partial r^2} + \frac{\partial}{\partial r} \left(\frac{U_x}{r} \right) + \frac{\partial^2 U_x}{\partial x^2} \right) . \tag{2.12}$$

The assumptions of axi-symmetry and straightness are valid approximations for fully formed, steady vortices. However, Devenport et al. (1996) show that the vortex trajectory is curved near the wing tip. Even so, at its maximum curvature closest to the wing, the vortex trajectory deviates from the streamwise direction by typically 2°, so that the assumption of a straight trajectory appears to be appropriate, at least over relatively short sections and for vortices which are not drastically distorted by vortex wandering (described in Section 3.3).

By taking the curl of Equation 2.8, an equation for vorticity transport can be found as

$$\frac{\partial \Omega_i}{\partial t} + U_j \frac{\partial \Omega_i}{\partial x_j} - \Omega_j \frac{\partial U_i}{\partial x_j} = \nu \frac{\partial^2 \Omega_i}{\partial x_j x_j} , \tag{2.13}$$

with

$$\frac{\partial \Omega_i}{\partial x_i} = 0 \tag{2.14}$$

found from Equation 2.7. These equations have the useful property that they do not explicitly contain pressure, which is very difficult to measure at a single point.

2.3 Model vortices

A vortex is commonly understood to be a swirling or rotational fluid flow. Although the velocity field of a vortex is sometimes described as having closed streamlines, this description is not always valid, such as in the case of a vortex advecting in a moving fluid. In fact, an exact mathematical definition of a vortex is actually quite elusive, in no small part due to the multitude of flows in which they exist.

The simplest analytical treatment of a straight vortex of infinite length is that of the irrotational (or potential) vortex, which induces a velocity field with a circumferential velocity given by

$$U_\theta = \frac{\Gamma_o}{2\pi r}\ , \tag{2.15}$$

where Γ_o is the strength of the vortex, equal to the circulation around it. This field has zero vorticity everywhere except at the vortex centre, where the vorticity is approximated by a Dirac delta function: $\Omega(r) = \Gamma_o \delta(r)$ (Saffman (1995)). Irrotational vortices are often used in potential flow analysis to generate circulation.

One undesirable mathematical property of the irrotational vortex is that the velocity tends to infinity on its axis. Another vortex model, called the Rankine vortex, is free of this singularity. A Rankine vortex consists of both a "free", irrotational part

$$U_\theta = \frac{\Gamma_o}{2\pi r} \quad \text{when } r > r_c \tag{2.16a}$$

and a "forced", rotational part

$$U_\theta = \frac{\Gamma_o}{2\pi r_{\theta\,\max}^2} r \quad \text{when } r \leq r_{\theta\,\max}\ . \tag{2.16b}$$

The Rankine vortex introduces the concept of a vortex "core" for $r \leq r_{\theta\,\max}$ in which the velocity profile is linear. All vorticity in the Rankine vortex is concentrated in the core and is uniformly distributed.

Through the solution of the Navier-Stokes equation, an additional vortex model can be devised. By assuming an axi-symmetric, laminar flow, the vorticity transport equation, Equation 2.13, can be simplified to

$$\frac{\partial \Omega_x}{\partial t} = \nu \frac{\partial^2 \Omega_x}{\partial x_j x_j}$$

for which an exact solution can be found, following (Saffman (1995)), as

$$\Omega_x = \frac{\Gamma_o}{4\pi \nu t} e^{-r^2/4\nu t} , \tag{2.17a}$$

which indicates a Gaussian distribution of vorticity. The radial profile of circumferential velocity is

$$U_\theta = \frac{\Gamma_o}{2\pi r} \left(1 - e^{-r^2/4\nu t}\right) . \tag{2.17b}$$

This model is called the Lamb-Oseen vortex and may be used to model viscous vortex diffusion, assuming that the vortex was a potential one at $t = 0$. Saffman (1995) also shows that the peak circumferential velocity and the radius at which it occurs can be found as

$$\begin{aligned} U_{\theta\,\max} &= \frac{0.716\Gamma_o}{2\pi r_{\theta\,\max}} , \\ r_{\theta\,\max} &= 2.24\sqrt{\nu t} . \end{aligned} \tag{2.18}$$

This value for $r_{\theta\,\max}$ can then be used to create a form of Equation 2.17b in which the time dependency is contained entirely within $r_{\theta\,\max}$ and $U_{\theta\,\max}$ so that

$$U_\theta = \frac{U_{\theta\,\max}}{0.716} \frac{r_{\theta\,\max}}{r} \left(1 - e^{-1.2526(r/r_{\theta\,\max})^2}\right) . \tag{2.19}$$

This form of Equation 2.17b is useful for representing the velocity field of a vortex using known or assumed values of $r_{\theta\,\max}$ and $U_{\theta\,\max}$. The potential, Rankine and Lamb-Oseen vortices are compared in Figure 2.1, and the evolution of the Lamb-Oseen vortex in time is illustrated in Figure 2.2. Comparing the Lamb-Oseen model to the other models, one can see that, near the centre of the vortex ($r/r_{\theta\,\max} < 0.7$ in Figure 2.2), the Lamb-Oseen model can be observed to have a core region of nearly uniform velocity gradient, similar to the Rankine vortex, whereas, far from the centre of the vortex ($r/r_{\theta\,\max} > 2$ in Figure 2.2), the velocity profile of the Lamb-Oseen model approaches that of the irrotational potential vortex. These three vortex models provide the basis for numerous other models (Gerz et al. (2002)) and are commonly used to further our understanding of vortex behaviour through analytical studies or as boundary conditions for numerical studies.

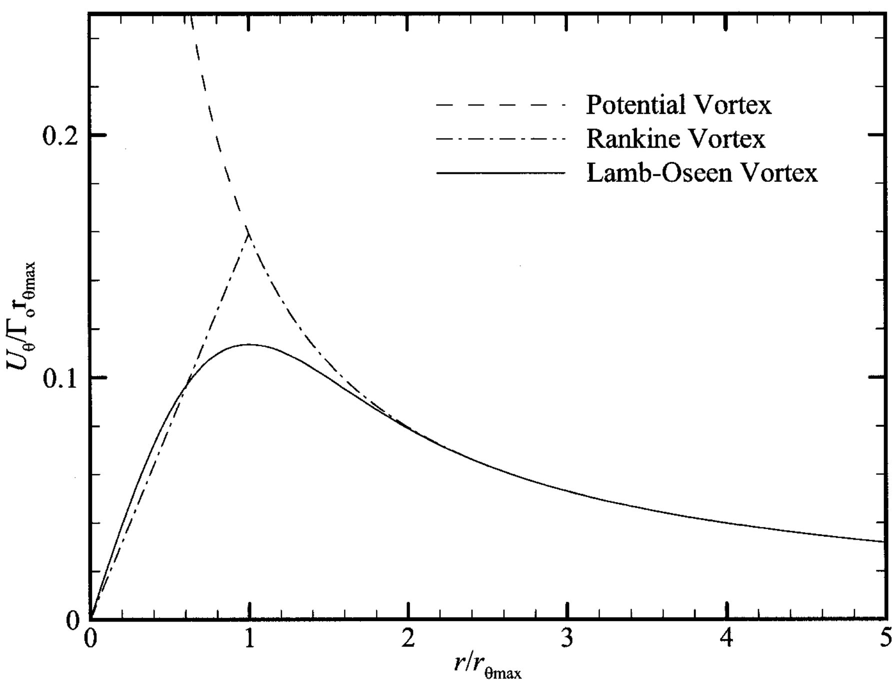

Figure 2.1: Comparison of potential, Rankine and Lamb-Oseen vortex models.

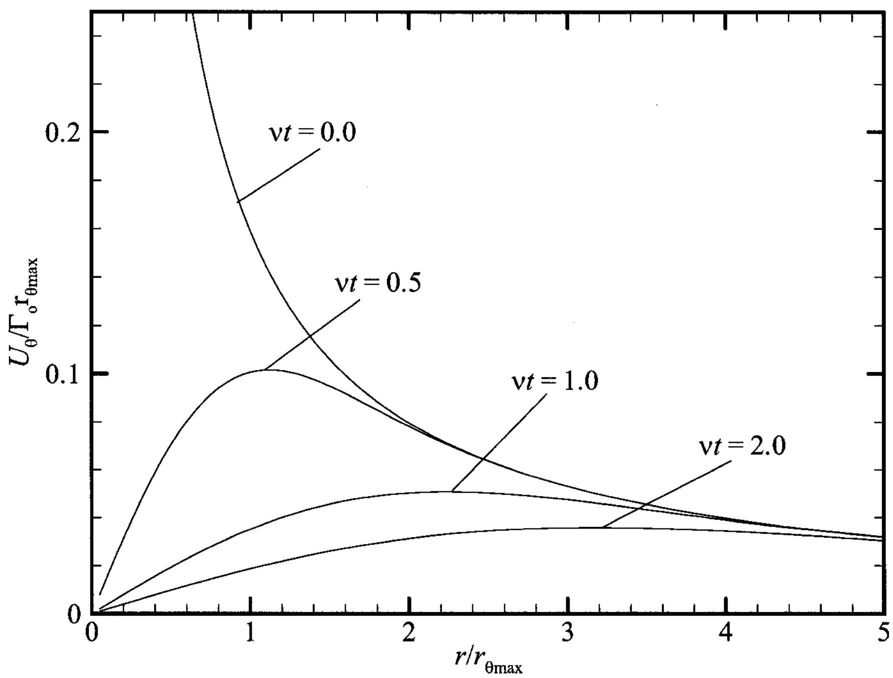

Figure 2.2: Lamb-Oseen model of viscous vortex decay.

2.4 Inviscid vortex flows

Helmholtz vortex laws

Lugt (1983) describes the derivation of two of the Helmholtz vortex laws, which are based on the inviscid form of Equation 2.13 ($\nu = 0$) and the assumption that the fluid is barotropic. The first law states that the strength of a vortex tube is unchanged with time. This law can be found by integrating Equation 2.14 over a volume and applying Gauss' theorem, giving

$$\int \frac{\partial \Omega_i}{\partial x_i} dV = \oint \Omega_i n_i dA = 0 \ , \tag{2.20}$$

which shows that the net flux of vorticity out of any closed surface is zero. When the closed surface is a vorticity tube, this law demonstrates that the vorticity tube must be either a closed loop or end in a boundary.

The second Helmholtz vortex law states that a fluid element without vorticity cannot obtain vorticity at a later time. This follows from the inviscid form of Equation 2.13

$$\frac{D\Omega_i}{Dt} = \left(\frac{d\Omega_i}{dt}\right)_\sigma = \Omega_j \frac{\partial U_i}{\partial x_j} \ , \tag{2.21}$$

where $\frac{D}{Dt}$ is the material derivative and $\left(\frac{d}{dt}\right)_\sigma$ indicates a Lagrangian time derivative. Thus, if Ω_j is initially zero, there is no mechanism to provide a positive rate of change of vorticity to the fluid element. Therefore, a necessary component for the production of vorticity is the effect of viscosity. It should also be noted that both the magnitude and orientation of an element's vorticity can change due to vortex stretching. Saffman (1995) observes that Equation 2.21 can also appear in the form

$$\frac{D\Omega_i}{Dt} = \left(\frac{d\Omega_i}{dt}\right)_\sigma = S_{ij}\Omega_j \ , \tag{2.22}$$

which shows that the rate of change of the vorticity of a fluid element is related to the local rate of strain tensor and not due to the local rotation tensor. Saffman (1995) also describes a third Helmholtz vortex law, again assuming that the fluid is inviscid and barotropic, which states that the fluid particles on the vorticity line at any time will remain on the vorticity line for all subsequent times, indicating that the vorticity line moves with the fluid.

Kelvin's theorem

Kelvin's theorem states that, in inviscid flow, the circulation along a closed curve travelling with the fluid remains constant in time

$$\frac{D}{Dt}\Gamma = \left(\frac{d}{dt}\Gamma\right)_\sigma = 0 \; . \tag{2.23}$$

Its proof (Lugt (1983)) is based on the inviscid form of the momentum Equation 2.8 (Euler's equation)

$$\frac{DU_i}{Dt} = -\frac{1}{\rho}\frac{\partial P}{\partial x_i} \; , \tag{2.24}$$

combined with the expression

$$\left(\frac{d}{dt}\Gamma\right)_\sigma = \frac{D}{Dt}\Gamma = \frac{D}{Dt}\oint U_i ds_i = \oint \frac{DU_i}{Dt} ds_i + \oint U_i dU_i \tag{2.25}$$

and assuming that the fluid is barotropic.

2.5 Homogenous and Isotropic Turbulence

Tennekes and Lumley (1972) show that using Reynolds decomposition

$$A = \langle A \rangle + a \; , \tag{2.26}$$

where the random process A is considered to be the sum of the mean $\langle A\rangle$ and the fluctuations a, the momentum equation for the mean velocity can be written as

$$\frac{\partial\langle U_i\rangle}{\partial t}+\langle U_j\rangle\frac{\partial\langle U_i\rangle}{\partial x_j}=-\frac{1}{\rho}\frac{\partial\langle P\rangle}{\partial x_i}+\nu\frac{\partial^2\langle U_i\rangle}{\partial x_j\partial x_j}-\frac{\partial\langle u_iu_j\rangle}{\partial x_j}\ . \tag{2.27}$$

The final term on the right hand side represents the contribution of the Reynolds stress tensor $-\rho\langle u_iu_j\rangle$ to momentum transport. Following a similar procedure, a balance equation for the Reynolds stress tensor can be found as

$$\begin{aligned}\frac{\partial\langle u_iu_m\rangle}{\partial t}+\langle U_j\rangle\frac{\partial\langle u_iu_m\rangle}{\partial x_j}&=-\langle u_ju_m\rangle\frac{\partial\langle U_i\rangle}{\partial x_j}-\langle u_iu_j\rangle\frac{\partial\langle U_m\rangle}{\partial x_j}-\frac{\partial\langle u_iu_ju_m\rangle}{\partial x_j}\\&-\frac{1}{\rho}\left(\left\langle u_m\frac{\partial p}{\partial x_i}\right\rangle+\left\langle u_i\frac{\partial p}{\partial x_m}\right\rangle\right)+\nu\left(\left\langle u_m\frac{\partial^2u_i}{\partial x_j\partial x_j}\right\rangle+\left\langle u_i\frac{\partial^2u_m}{\partial x_j\partial x_j}\right\rangle\right)\ .\end{aligned} \tag{2.28}$$

Further understanding of this equation can be found by introducing the turbulent kinetic energy

$$k=\frac{1}{2}\langle u_iu_i\rangle \tag{2.29}$$

and setting $i=m$ in all terms of Equation 2.28, which leads to the form

$$\begin{aligned}\frac{\partial k}{\partial t}+\langle U_j\rangle\frac{\partial k}{\partial x_j}&=-\langle u_iu_j\rangle\frac{\partial\langle U_i\rangle}{\partial x_j}-\frac{1}{\rho}\frac{\partial\langle u_jp\rangle}{\partial x_j}-\frac{1}{2}\frac{\partial\langle u_ju_iu_i\rangle}{\partial x_j}+\nu\frac{\partial^2k}{\partial x_j\partial x_j}\\&+\nu\frac{\partial^2\langle u_iu_j\rangle}{\partial x_i\partial x_j}-\frac{1}{2}\nu\left\langle\left(\frac{\partial u_i}{\partial x_j}+\frac{\partial u_j}{\partial x_i}\right)\left(\frac{\partial u_i}{\partial x_j}+\frac{\partial u_j}{\partial x_i}\right)\right\rangle\ .\end{aligned} \tag{2.30}$$

The physical significances of the terms on the right hand side in Equation 2.30 are described by Tennekes and Lumley (1972) as follows:

- $-\langle u_iu_j\rangle\frac{\partial\langle U_i\rangle}{\partial x_j}$ represents the rate of production of k
- $-\frac{1}{\rho}\frac{\partial\langle u_jp\rangle}{\partial x_j}$ represents the rate of work by pressure fluctuation gradients
- $-\frac{1}{2}\frac{\partial\langle u_ju_iu_i\rangle}{\partial x_j}$ represents the turbulent diffusion of k

- $\nu\frac{\partial^2\langle u_i u_j\rangle}{\partial x_i \partial x_j}$ and $\nu\frac{\partial^2 k}{\partial x_j \partial x_j}$ represent viscous diffusion of k

- $\frac{1}{2}\nu\left\langle\left(\frac{\partial u_i}{\partial x_j}+\frac{\partial u_j}{\partial x_i}\right)\left(\frac{\partial u_i}{\partial x_j}+\frac{\partial u_j}{\partial x_i}\right)\right\rangle$ represents the rate of dissipation, ε, of k

For homogeneous and isotropic turbulence, Equation 2.30 reduces to

$$\frac{dk}{dt} = -\varepsilon\ , \tag{2.31}$$

indicating that there is no production of turbulence and therefore the turbulent kinetic energy will decay with time.

An analogy for Equation 2.27 can be found for vorticity by performing Reynolds decomposition

$$\Omega_i = \langle\Omega_i\rangle + \omega_i \tag{2.32}$$

and substituting into Equation 2.13 to get

$$\frac{\partial\langle\Omega_i\rangle}{\partial t} + \langle U_j\rangle\frac{\partial\langle\Omega_i\rangle}{\partial x_j} = \langle\Omega_j\rangle\frac{\partial\langle U_i\rangle}{\partial x_j} + \nu\frac{\partial^2\langle\Omega_i\rangle}{\partial x_j x_j} - \frac{\partial\langle u_j\omega_i\rangle}{\partial x_j} + \frac{\partial\langle u_i\omega_j\rangle}{\partial x_j}\ . \tag{2.33}$$

Similarly, an analogy can be found for Equation 2.30 by introducing the concept of turbulent enstrophy, $\langle\omega_i\omega_i\rangle$, as a measure of intensity of fluctuations in rotation

$$\begin{aligned}\frac{\partial\frac{1}{2}\langle\omega_i\omega_i\rangle}{\partial t} + \langle U_j\rangle\frac{\partial\frac{1}{2}\langle\omega_i\omega_i\rangle}{\partial x_j} &= -\langle u_i\omega_j\rangle\frac{\partial\langle\Omega_i\rangle}{\partial x_j} - \frac{1}{2}\frac{\partial\langle u_j\omega_i\omega_i\rangle}{\partial x_j} \\ &+ \langle\omega_i\omega_j s_{ij}\rangle + \langle\omega_i\omega_j\rangle\langle S_{ij}\rangle + \langle\Omega_j\rangle\langle\omega_i s_{ij}\rangle + \nu\frac{\partial^2\langle\omega_i\omega_i\rangle}{\partial x_j\partial x_j} - \nu\left\langle\frac{\partial\omega_i}{\partial x_j}\frac{\partial\omega_i}{\partial x_j}\right\rangle\ ,\end{aligned} \tag{2.34}$$

where s_{ij} is the fluctuation component of the rate of strain tensor, S_{ij}. The significances of the terms on the right hand side of Equation 2.34 are described by Tennekes and Lumley (1972) as:

- $-\langle u_i\omega_j\rangle\frac{\partial\langle\Omega_i\rangle}{\partial x_j}$ represents the production by the mean vorticity gradient

- $\frac{1}{2}\frac{\partial\langle u_j\omega_i\omega_i\rangle}{\partial x_j}$ represents the turbulent transport of the turbulent enstrophy

- $\langle\omega_i\omega_j s_{ij}\rangle$ represents production by stretching due to turbulent strain

- $\langle\omega_i\omega_j\rangle\langle S_{ij}\rangle$ represents production by stretching due to the mean strain

- $\langle\Omega_j\rangle\langle\omega_i s_{ij}\rangle$ represents production by stretching coupled with the mean vorticity

- $\nu\frac{\partial^2\langle\omega_i\omega_i\rangle}{\partial x_j\partial x_j}$ represents molecular diffusion of turbulent enstrophy

- $\nu\left\langle\frac{\partial\omega_i}{\partial x_j}\frac{\partial\omega_i}{\partial x_j}\right\rangle$ represents viscous dissipation of turbulent enstrophy

Chapter 3

Literature review

The variety of engineering flows in which trailing vortices are significant is reflected in the volume of research, both experimental and theoretical, that has been directed towards them. Among the important research topics that have been associated with the trailing vortex problem are the following:

- The formation of the vortex and vortex roll-up
- The velocity profiles of a fully formed vortex and the existence of axial velocity surplus or deficit in the core of the vortex
- The phenomenon of vortex wandering
- Turbulence and instability in the vortex
- The interaction between a vortex and turbulence

These topics of import form subsections within the current literature review.

3.1 Vortex formation and roll-up

The process of vortex formation over the wing is highly dependent on the geometry and flow conditions, which include Reynolds number, aspect ratio, planform shape, wing loading, lift distribution, tip shape and wing boundary layer turbulence. Considering the large number of influencing parameters, Donaldson and Bilanin (1975) observed that there is no one vortex description which can be applied to all cases. Pressure variation along the span of a finite wing induces a spanwise component of velocity over the surface of the wing. At the tip, fluid from the pressure surface rolls up towards the suction surface, forming a discrete vortex that is convected downstream, as illustrated in Figure 1.3. At the trailing edge of the wing, the spanwise flow generates a spanwise shear layer, which is also convected downstream. At the same time, the boundary layers on the two surfaces merge into a wake, which has streamwise momentum deficit and coexists with the shear layer.

The formation process of a wing-tip vortex depends largely on the wing geometry. Planform shape affects the distribution of pressure on the wing, and thus the spanwise flow. Boundary layers on the wing contain turbulence and vorticity, which are encased in the vortex during roll-up (Spalart (1998)). Depending on the shape of the wing-tip, roll-up of the main vortex may include the merging of multiple smaller vortices forming from local shear layers separating from sharp edges (Katz and Galdo (1989), Birch et al. (2003)). Conversely, Green (1995) noted that, for rounded tips, the flow separates from the pressure surface and reattaches on the suction surface by the mid-chord location. For sharp edged (i.e., square) tips, multiple vortices have been observed through flow visualization (Katz and Galdo (1989)), surface pressure measurements (McInerny et al. (1990)), and more recently by particle image velocimetry measurements (Birch et al. (2003)). Two large vortices were found to form at the suction-tip and pressure tip interfaces with tertiary vortices forming depending on the angle of attack and airfoil shape. Within one chord length of the wing, these multiple vortices merged into a single tip vortex. Finally, additional co-rotating vortices, generated by part-span flaps and other discontinuities, could merge with the main vortex at some downstream distance from the tip (Jacquin et al. (2001)).

Downstream of the wing, the shear layer and the wing wake roll up in a spiral around the vortex (Figure 1.3). This roll-up process continues until the shear layer vorticity has been fully integrated into the vortex through turbulent and molecular diffusion (Saffman (1995)). Phillips (1981) considered the vortex to be undergoing roll-up as long as the wake spiral is distinct from the vortex core, with such a condition persisting several wingspans downstream of the wing. However, other researchers, such as Shekarriz et al. (1993), considered the roll-up process to be complete when the vortex reaches its maximum circulation and found this to be the case at the trailing edge of the wing. Alternatively, roll-up may be considered to be complete when the vortex core becomes axi-symmetric. Under this definition, Ramaprian and Zheng (1997) found the roll-up process to be complete within two chord lengths downstream of the wing. Using three-component laser-Doppler velocimetry measurements and a fine measurement grid, Ramaprian and Zheng (1997) were able to determine the mean vorticity vector and found that the vorticity in the wing wake rapidly aligns itself azimuthally as the wake spirals around the vortex. This effect is different from the hypothesis that the trailing vortex sheet is aligned with the streamwise flow as it wraps itself around the core, a concept commonly used in lifting line methods.

After leaving the wing, the vortex tends to shift towards the wing root, as the wing wake rolls around the vortex. Devenport et al. (1996) found that the vortex initially traveled toward the root with a trajectory proportional to the square root of the streamwise distance and asymptotically approached a location that was further inboard than predicted by the lifting line theory of Donaldson et al. (1974). A single, isolated vortex in a wind tunnel will tend to have a different trajectory relative to the wing than that of a vortex pair in the atmosphere, due to several effects. Most importantly, each vortex of the pair will induce motion on the other, resulting in a downward (opposite to the direction of lift) trajectory of the pair. Spalart (1998) discussed that the velocity of the trajectory is not uniform, resulting in deformation of the vortex sheet trailing the wing. Additional effects on the trajectory of a single vortex in a wind tunnel, which are not present in the atmosphere, are caused by the tunnel walls which tend to straighten the trajectory.

3.2 Velocity field and circulation of a fully formed vortex

Several chord lengths downstream of the wing, the velocity profile of a wing-tip vortex becomes nearly axi-symmetric. Within a region near the axis of the vortex, the fluid is in approximately solid body rotation with a radial profile of circumferential velocity that is nearly linear (Figure 2.1). This region is often referred to as the viscous core of the vortex; it is sometimes identified as the region within the radial range $r < r_{\theta\,\max}$, where $r_{\theta\,\max}$ is the radius at which the maximum circumferential velocity occurs. Outside the viscous core, the circumferential velocity profile resembles that of a potential vortex. Spalart (1998) identified the minimum radius beyond which the velocity profile is approximately potential as r_{inv}

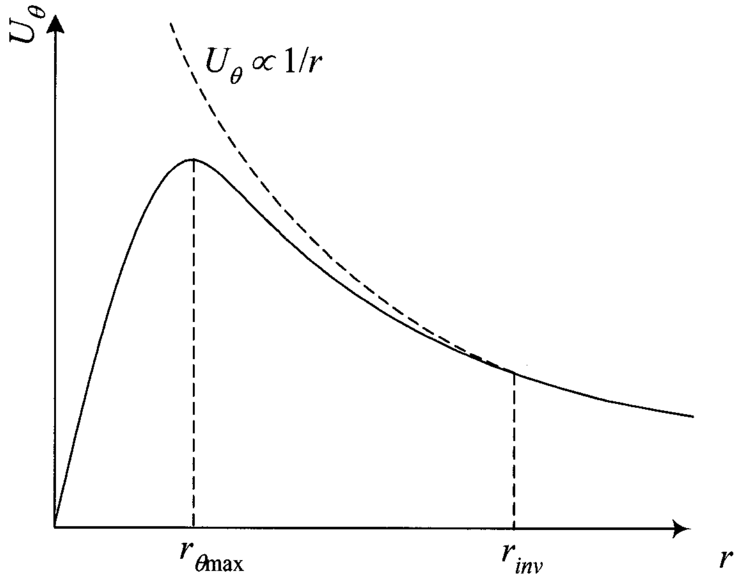

Figure 3.1: Sketch of a typical radial profile of the circumferential velocity of a wing-tip vortex, defining $r_{\theta\,\max}$ and r_{inv}

and observed that the region $r < r_{inv}$ provides a more significant contribution towards rolling moments on aircraft than the region $r < r_{\theta\,\max}$, although $r_{\theta\,\max}$ has received more attention in the literature than r_{inv}. A sketch of a typical circumferential velocity profile of a wing-tip vortex is shown in Figure 3.1 identifying locations $r_{\theta\,\max}$ and r_{inv}. For a Lamb-Oseen vortex, $r_{inv} \approx 2r_{\theta\,\max}$ (Figure 2.1).

Phillips (1981) analyzed the formation of the velocity profile from the spiralling shear layer shed from the wing and observed that the vortex becomes approximately self-similar with three distinct regions, as illustrated in Figure 3.2. Inside the vortex, where viscosity has merged the spiral shear layer into a continuous profile, the vortex can be divided into three regions: Region I, which is approximately in solid body rotation and which is dominated by viscous effects; Region II, in which the viscous effects are weaker,

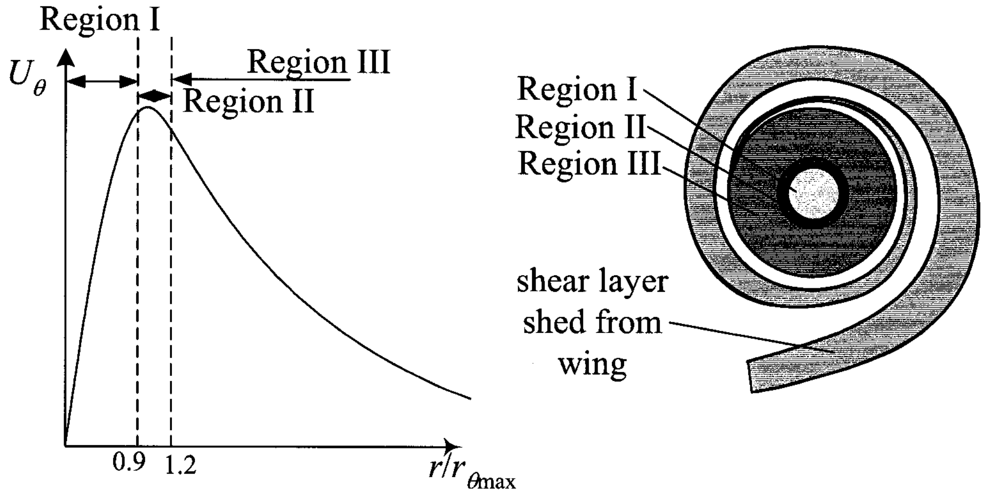

Figure 3.2: Illustration of Regions I, II and III in the vortex (adapted from Phillips (1981))

the velocity peaks, and in which the circulation grows approximately logarithmically with radial distance (Hoffman and Joubert (1963)); and Region III, in which viscous diffusion and turbulent diffusion have merged the spiralling shear layer, resulting in a circumferential velocity profile dependent on the characteristics of the shear layer. Phillips (1981) found that experimental data were approximately self-self similar in Regions I and II; however for Region III, the initial conditions strongly affected the spiral shear layer and the experimental results did not follow any self-similarity. Outside the three regions, the velocity profile was characterized by discontinuities caused by the un-merged spirals which were highly dependent on the initial conditions at the wing.

Devenport et al. (1996) found that their experimentally measured spiral of axial velocity deficit shed by the wing, referred to as the spiral wake, was self-similar at distances greater than 5 chord lengths from the wing. They normalized the shape of the wake spiral by the distance between the centreline of the two-dimensional portion of the wing wake and the centre of the vortex core. Their results also indicated that the velocity profiles were self-similar when normalized by velocity and length scales determined from the two-dimensional portion of the wing wake, reflecting the significance of the wing wake on the vortex characteristics.

Within the vortex, in the initial stages of vortex formation, the pressure in the vortex core gradually decreases along the vortex axis as the circumferential velocity increases, generating a favourable axial pressure gradient which accelerates the core fluid in the streamwise direction, possibly resulting in a "jet-like" core having an axial velocity surplus (Devenport et al. (1996)). The analysis of Batchelor (1964) showed that the axial velocity can be either jet-like or wake-like, depending on the balance between circulation and dissipation of momentum due to losses. Further downstream, viscous actions decelerate the flow, tending to convert the core to "wake-like", having a velocity deficit relative to the free-stream. Both wake-like and jet-like axial flows have been reported. For example, Dacles-Mariani et al. (1995) reported a jet-like core at the trailing edge of their wing with a maximum streamwise velocity 1.77 times the free stream velocity, whereas Ramaprian and Zheng (1997) reported a wake-like core with a minimum 0.68.times the free stream velocity. Anderson and Lawton (2003) used various tip geometries and angles of attack to generate both types of axial flow. They found that, at higher angles of attack and with rounded wing tips, jet-like flow was produced; however, at lower angles of attack and with square wing tips, wake-like flow was produced. They suggested that the smaller core produced by the rounded tips results in a higher vorticity density, contributing to jet-like flow. Increased losses caused by the formation of multiple vortices for a square wing tip resulted in a slightly larger vortex core and a wake-like flow.

3.3 Vortex wandering

A significant complication for every experimental study is the random transverse motion of the vortex about its average path, referred to as vortex wandering or meandering. These motions could introduce a large error on the measurement of single-point statistics taken with a fixed probe near the axis of the vortex. Due to the large radial variation of the velocity in the core, even a small sideways displacement of the vortex would result in a large change in velocity at the measurement point, which would significantly affect time-averages.

This phenomenon has been observed in experimental studies for many years, but no consensus concerning its cause has yet been reached. By analyzing the spectra of vortex core position determined from smoke flow visualization, Corsiglia et al. (1973) and Baker et al. (1974) have concluded that the motion is caused by wind tunnel turbulence. In contrast, Green (1995) attributed the wandering to the ejection of packets of vorticity from the core and suggested that point measurement techniques are not useful at distances greater than one chord length from the wing. More recently, Gursul and Xie (1999) proposed that the wandering was a result of interactions with secondary vortices (formed from the shear layer during flow separation from the wing), which induce motion in the primary vortex through Biot-Savart induction. Rokhsaz et al. (2000) also proposed that Biot-Savart induction is involved in the vortex wandering process, but suggested that the vortex induces its own motion when its trajectory is mildly perturbed. Other mechanisms which have been proposed include interaction with tunnel walls and the interaction of multiple vortices which occur during vortex formation.

Using single component hot-wire anemometry to study the trailing vortex generated from the tip of a flat plate set at an angle of attack to the flow, Rokhsaz et al. (2000) found that the growth rate of the wandering amplitude depends on the vortex strength and that the amplitude grows with downstream distance. An increase in amplitude was also found by Devenport et al. (1996) in their three-component hot-wire measurements downstream of a NACA0012 semi-span wing; however they report an inverse relationship between circulation and wandering amplitude and suggest that this supports the source of vortex wandering as being due to wind-tunnel unsteadiness. Additionally, Devenport et al. (1996) used an analytical approach to determine the magnitude of vortex wandering and to correct the effects of it on their point measurements. They found that there was a significant effect of wandering only on the point statistics measured within the vortex core, that the wandering occurred in a broad-band, low frequency range. Devenport et al. (1996) also note that the wandering amplitude decreased with increasing vortex strength, indicating that wandering was caused by some source external to the vortex, such as wind tunnel unsteadiness.

A recent study by Heyes et al. (2004) used particle image velocimetry to study a trailing vortex from a NACA0012 semi-span wing. They found excellent agreement between their results and the analytical correction of Devenport et al. (1996), observing that the probability density function of vortex position was approximately Gaussian in appearance, that measured velocity fluctuations within the core of the vortex were due entirely to vortex wandering, and that the wandering decreases with increasing vortex strength. Heyes et al. (2004) noted that the latter observation contradicts the model for vortex wandering proposed by Rokhsaz et al. (2000), which suggested that Biot-Savart interaction between different streamwise segments of the vortex was the cause of vortex wandering.

In a detailed study using two-point measurements in the wake of a model aircraft, Jacquin et al. (2001), examined vortex wandering and proposed that wind tunnel unsteadiness is not a likely source of wandering. Instead, they proposed that vortex wandering is caused by a combination of excitation of the vortex by free-stream turbulence, interactive instabilities between the trailing vortex and other vortices in the flow, and vibration of the vortex generator. Jacquin et al. (2001) also noted that the frequency range of vortex wandering from the aircraft model appeared to be broadband, in agreement with observations made by Devenport et al. (1996). They also noted that the wandering perturbations convected downstream at the free-stream velocity.

Beninati and Marshall (2005), using a vortex generator specifically designed to minimize vortex wandering from wind tunnel unsteadiness and model vibration, focused on the effects of free-stream turbulence on the vortex. Using spectral filtering of three-component hot-wire measurements, they examined the frequency content of the fluctuating velocity in the vortex core. Beninati and Marshall (2005) noted that the turbulence induced bending waves in the vortex, which had wavelengths comparable to the wavelengths of azimuthally aligned turbulent structures observed in the numerical simulations of Marshall and Beninati (2005). Beninati and Marshall (2005) concluded that it is these structures that induce bending waves into the vortex. In a fixed measurement plane, these bending waves would be interpreted as vortex wandering. In a related numerical study, Takahashi et al. (2005) noted that the amplitude of the bending waves increased with the amplitude of the free-stream turbulence.

3.4 Turbulence and instability within the vortex

One important question when considering decay of a vortex is the strength of diffusion of vorticity due to turbulence in the vortex core. Spalart (1998) pointed out that there are several types of turbulence which could become entrained into the vortex: turbulent boundary layers on the wing, turbulence in separated wakes, turbulence produced by the vortex circumferential velocity gradients, turbulence produced by the streamwise velocity gradient, and free-stream turbulence. He also observed that these sources of turbulence have scales differing from each other by orders of magnitude and noted that turbulent eddies of vastly different scales would not likely interact with each other. Squire (1965) produced one of the earliest attempts to model the effect of turbulence on the vortex. By assuming an eddy viscosity proportional to the vortex circulation, he found simple solutions for the diffusion of an isolated line vortex and the diffusion of a vortex in downwash.

The vortex core has received the most attention with regards to the effect of turbulence. Using measurements within the vortex core during formation, Chow et al. (1994) found that the turbulence is poorly represented using an isotropic eddy viscosity model. Additionally, they found that the turbulence within the core rapidly relaminarizes. Bradshaw (1969) attributed the relaminarization to the high level of streamline curvature within the vortex core, which acts in a stabilizing way, analogous to stable density stratification, to impede radial motions and thus enhance turbulence decay. Cotel and Breidenthal (1999) modeled this process and found that the stability of the core flow is strong enough to prevent even the smallest external perturbations from penetrating the core. The vortex core is also stable to axi-symmetric instabilities as long as it satisfies the Rayleigh criterion (Saffman (1995)), which indicates stability if

$$\frac{d\Gamma^2}{dr} > 0 \; . \tag{3.1}$$

In general, velocity profiles of vortices far from the effects of solid boundaries and other vortices would satisfy this criterion. Experimental evidence of a laminar core is provided by the studies of Devenport et al. (1996) and Heyes et al. (2004), both of which observed little or no measured velocity fluctuations within the vortex core.

Axial velocity gradients introduce a possible mechanism of turbulence production within the core (Singh and Uberoi (1976)). The influence of axial velocity gradients on the vortex are frequently studied using the stability analysis of a model vortex, called the q-vortex, (Batchelor (1964)). Fabre and Jacquin (2004) simplify Batchelor's vortex such that

$$U_x \propto e^{-r^2} \; , \tag{3.2a}$$

$$U_\theta \propto q/r\left(1 - e^{-r^2}\right) \; , \tag{3.2b}$$

Where q is a dimensionless swirl parameter which is proportional to the ratio of peak tangential velocity to the maximum velocity excess or deficit. This vortex is essentially the superposition of a Gaussian jet or wake and a Lamb-Oseen vortex.

Jacquin et al. (2003) provides a review of aircraft wake vortices and describes three forms of instability that have been identified using the q-vortex as a model. The first form are inviscid instabilities which tend to arise when $q < 1.5$. These instabilities have been shown to result in the production of small-scale turbulence, which, however, decays quickly due to the stabilizing influence of the vortex rotation. The second form are viscous instabilities. These instabilities occur for roughly the same range of swirl parameter as the inviscid instabilities; however their amplitude is much lower and therefore less likely to be as important as the inviscid instabilities. The third form of instability is a viscous instability which occurs at large Reynolds numbers and at higher swirl numbers than the inviscid instability, which is further investigated by Fabre and Jacquin (2004). These instabilities were found to affect only a very narrow region near the vortex axis.

Ragab and Sreedhar (1995) numerically simulated the effects of axial velocity gradient using a q-vortex model. When the vortex was perturbed in an unstable helical instability mode, they observed large-scale helical vortex sheets forming in the core which broke up into filaments and were ejected from the core. Small scale turbulence was also produced but relaminarized. High amplitude, random perturbations of the core did not affect the vortex velocity profile.

These q-vortex studies observed, as described by Marshall and Beninati (2000), that turbulence generated by axial velocity gradients tends to reduce this gradient through turbulent diffusion, thus weakening further production of turbulence. This process also tends to increase the swirl parameter, which further weakens turbulence production. In summary, the production of turbulence by an axial velocity gradient is a self-destructing mechanism.

Although production of turbulence within the vortex core appears to be unsustainable, Bandyopadhyay et al. (1991) determined using flow visualization that activity within the core is far from being passive. They report that the core frequently exchanges fluid with the surroundings, partially relaminarizing it before ejecting it again. Bandyopadhyay et al. (1991) also determined that the Rossby number (proportional to the ratio of the axial velocity deficit and the maximum circumferential velocity) is a more significant controlling parameter in core turbulence than the vortex Reynolds number (proportional to the ratio of circulation and viscosity).

When the vortex is immersed in an external strain field, such as created when two vortices are in close proximity, bending waves can be excited along the vortex (Saffman (1995)). For trailing vortex pairs, these waves can be long-wave (Crow (1970)) or short-wave (Tsai and Widnall (1976)) cooperative instabilities. In addition to the bending waves, Pradeep and Hussain (2001) found that an external strain field could also excite axi-symmetric instabilities within the vortex.

3.5 Interaction between a vortex and free-stream turbulence

When a vortex is immersed in free-stream turbulence, it is expected that the vortex and the turbulence would interact with each other, so that the characteristics of both would be altered. Using particle image velocimetry and two different turbulence producing grids, Heyes et al. (2004) measured the influence of free-stream turbulence on a wing-tip vortex downstream of a NACA0012 wing using particle image velocimetry. They observed little change in the location of peak circumferential velocity, but a measurable effect on the peak circumferential velocity. At each streamwise measurement plane, the peak circumferential velocity was found to be reduced with increased free-stream turbulence; however the amount of decrease was similar at all streamwise locations implying that the rate of decrease in peak circumferential velocity was unchanged with the additional turbulence. Heyes et al. (2004) concluded that the influence of free-stream turbulence must therefore occur during vortex formation.

Using flow visualization and cross-wire measurements, Bandyopadhyay et al. (1991) examined the effect of different free-stream turbulence levels on a vortex generated using two oppositely loaded airfoils joined at a central hub. They observed intermittent exchange of core fluid with the turbulent free-stream, with the fluid drawn into the vortex core re-laminarizing. Three characteristic wavelengths were identified and were associated with the relaminarization process.

Several numerical studies of the interaction of a vortex and a turbulent free stream have been performed, revealing unique insight into the three-dimensional nature of the interaction. Melander and Hussain (1993) used direct numerical simulation (DNS) to study the interaction between a vortex and small-scale isotropic velocity fluctuations. They observed that small-scale non-coherent turbulence was organized by the vortex as the strain imposed by the vortex stretched the eddies, increasing the magnitude of the azimuthal component of vorticity. By azimuthally arranging the vorticity within the free-stream eddies, pairing of eddies with similar sense of rotation occurred, resulting in the development and growth of organized secondary structures arranged in spirals around the vortex.

The appearance of these structures are illustrated in Figure 3.3. Coherent structures of both positive and negative azimuthal vorticity were observed and the alignment of each secondary structure spiral was found to depend on the sign of azimuthal vorticity

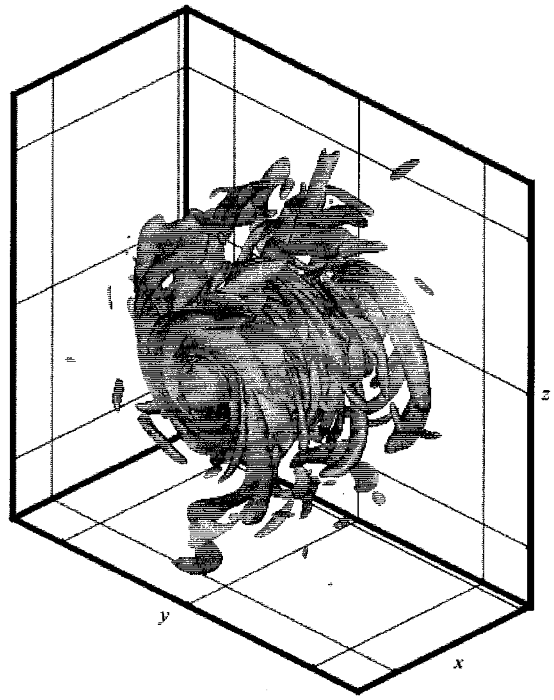

Figure 3.3: Iso-vorticity surfaces from Marshall and Beninati (2005) showing secondary structures wrapping around the vortex. (Permission granted according to http://www.cambridge.org/uk/information/rights/permission.htm)

within the structure. Melander and Hussain (1993) also investigated the influence of free-stream fluctuation levels. They found that for low fluctuation levels the structures would form, but decay with the free-stream turbulence, leaving the vortex nearly unaltered. For high free-stream turbulence levels, the vortex was found to be destroyed by the free-stream turbulent eddies. At moderate levels, turbulence was sustained in the secondary structures and the vortex coexisted with these structures. At sufficiently high free-stream turbulence levels, bending waves were induced in the vortex, which corrupted the axi-symmetry of the secondary structures due to the reorientation of the vortex vorticity.

Sreedhar and Ragab (1994) also observed the development of azimuthally aligned secondary structures in the large eddy simulation (LES) of a vortex that was unstable according to the Rayleigh criterion (Equation 3.1) immersed in an initially random perturbation field. They found that the secondary structures interacted with the vortex core, resulting in its destruction.

Using rapid distortion theory (RDT) of initially homogenous isotropic turbulence interacting with a vortex, Miyazaki and Hunt (2000) found that the secondary structures evolved rapidly, within two turns of the vortex.

In a study using LES to investigate the decay mechanisms of aircraft wakes in homogenous and isotropic turbulence, Holzäpfel et al. (2003) also observed the formation of secondary vortical structures and attributed the vortex decay to the existence of these structures. They proposed that rotational energy is transferred to the secondary structures from the vortex during the stretching and formation of the secondary structures, noting that once the secondary structures were fully formed vortex decay became minimal. For a case with free-stream turbulence of root-mean-square velocity fluctuations of 24% the peak circumferential velocity of the vortex, Holzäpfel et al. (2003) found that the vortex broke down before the secondary structures could form

Extending the work of Melander and Hussain (1993), Takahashi et al. (2005) used DNS to investigate the interaction between a Lamb-Oseen vortex and temporally evolved homogeneous and isotropic turbulence. These authors also observed the formation of secondary structures and the excitation of various bending modes in the vortex. They found that the secondary structures were spaced irregularly in the axial direction, formed at a radius of approximately twice the core radius and had a length of the same order as the core radius. Like Holzäpfel et al. (2003), Takahashi et al. (2005) found that the vortex vorticity decreased faster in the presence of free-stream turbulence and observed enhanced energy dissipation in the vicinity of the secondary structures.

Marshall and Beninati (2000) suggested that secondary structures can also result in additional turbulence being generated within the vortex core by bending and deforming the vortex. This turbulence is consequently stripped from the core by the counter rotation of the structures and reorganized into additional secondary structures. The net result is a self-preserving mechanism for the structures. The flow visualization of Sarpkaya and Daly (1987) demonstrated that bursting of the vortex is a primary form of vortex decay in cases with large free-stream turbulence, which Marshall and Beninati (2000) cite as evidence of the stripping of core fluid by the secondary structures.

This vorticity stripping mechanism is investigated by Marshall (1997) using an idealized model consisting of counter-rotating vortex rings surrounding a columnar vortex. The vorticity stripped from the columnar vortex was found to be dissipated by the vortex rings. Direct numerical simulations performed by Marshall and Beninati (2005) of a vortex immersed in temporally evolved turbulence found little evidence of stripping of core fluid into the free stream, except for immediately before the break-up of the vortex in very high free-stream turbulence conditions.

Chapter 4

Experimental facilities, instrumentation and measurement procedures

4.1 Overview

This study utilized a variety of experimental techniques to study the interaction of a wing-tip vortex and free-stream turbulence. Qualitative studies were performed of the vortex formation utilizing dye injection flow visualization in a water tunnel and oil film flow visualization and single-sensor hot-wire anemometry in a wind tunnel. Quantitative studies were also performed in a wind tunnel with measurements of wing surface pressure and local flow velocity measurements utilizing multi-sensor hot-wire probes.

This chapter first describes the experimental apparatus, separated into water tunnel and wind tunnel experiments then the experimental procedure, followed by the analysis and data reduction procedure. Finally, the experimental errors and uncertainty are discussed.

4.2 Experimental apparatus

4.2.1 Water tunnel experiments

Water tunnel

The water tunnel used in these experiments was the University of Ottawa's closed loop facility. The test section had glass sides and bottom with a free surface at the top and dimensions of approximately 0.5 m wide $\times$ 0.75 m high $\times$ 4 m long. Flow was driven by a 0.3 m diameter axial flow pump capable of providing flow rates between $0.003\,\mathrm{m^3/s}$ to $0.1875\,\mathrm{m^3/s}$. At the inlet to the test section was a slot which could be used to insert flow altering devices such as turbulence and shear generators. Details about this facility have been presented by Dunn (1997).

Wing

The wing used in the water tunnel studies was a square-tipped, rectangular planform, NACA0012 airfoil with a chord, $c = 0.1778\,\mathrm{m}$ and a semi-span $b = 0.2286\,\mathrm{m}$. The wing was fabricated by rapid prototyping using a ZCorp Z400 three-dimensional printer, which was capable of generating solid models using a plaster powder and binder. The surface of the model was sanded smooth and was water-proofed using several coats of epoxy resin. The wing was inserted in the flow through the free surface of the water tunnel and

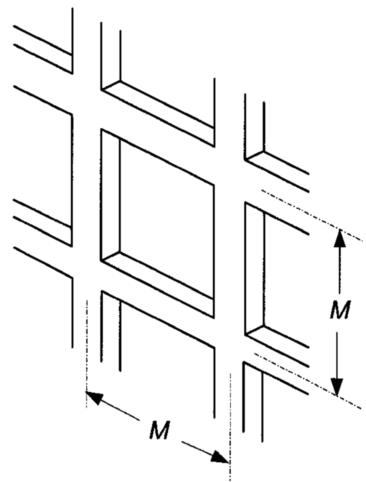

Figure 4.1: Sketch illustrating definition of turbulence grid mesh size, M.

was mounted on a carriage riding on rails, which allowed the position and angle of attack of the wing to be changed. A boundary layer trip wire of 1 mm diameter was mounted on the suction surface, $0.1c$ from the leading edge of the wing to induce transition to turbulence in the boundary layer.

Turbulence grids

Two different turbulence-generating grids were used in the study. Both were perforated plates, with square openings punched out from 3.175 mm-thick aluminum plates and had identical solidities, defined as the ratio of closed area to open area, equal to 0.44. The first grid, which will be hereafter referred to as the small grid, had a mesh size, M (defined in Figure 4.1) of 25.4 mm. The second grid, referred to hereafter as the large grid, had $M = 50.8$ mm.

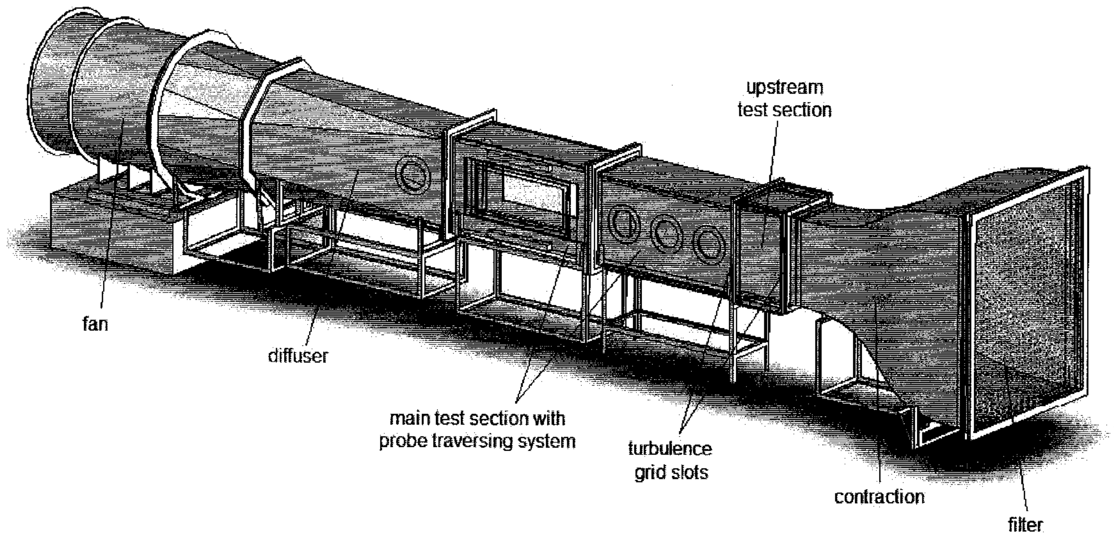

Figure 4.2: Sketch of the open-circuit wind tunnel facility at the University of Ottawa.

4.2.2 Wind tunnel experiments

Wind tunnel

The wind tunnel used for this study was the University of Ottawa's open-circuit suction-type wind tunnel, shown schematically in Figure 4.2. Its main components are described in the following subsections. Felt gaskets, designed to minimize wall vibrations, were inserted at the joints between adjacent components.

Filter: The inlet of the tunnel was protected by a filter to prevent the ingestion of dust and dirt that would reduce flow quality and could damage the measurement probes. The filter consisted of AAF International 150-908-112 filter sheets, sandwiched in place between two wire meshes consisting of 0.05 m× 0.08 m rectangular grids to provide rigidity. Additional rigidity was also provided to the filter by a layer of nylon window screen which was also held in place by the meshes.

Contraction: The wind tunnel contraction was made from welded aluminum and had inlet dimensions of 2.6 m high $\times$ 1.8 m wide and outlet dimensions of 0.90 m high $\times$ 0.61 m wide resulting in a for a 7.6:1 contraction over a length of 2.7 m.

Upstream section: The upstream section was designed and installed by the author. Originally intended to allow the installation of shear generators, this section could also be fitted with test models and instrumentation. This section had a sealed outer shell made from a steel frame and Plexiglas walls, with one of its side walls easily removable to allow insertion of different devices. A simple rectangular duct, 0.90 m high $\times$ 0.61 m wide $\times$ 0.61 m long (inner dimensions) and made from wood reinforced with aluminum, was inserted in the upstream section for this study. Threaded screws positioned on all four sides of the outer frame allowed accurate alignment of the walls of this duct with the contraction and the main test section.

This section was added part way through the study. Comparison of measurement cases with and without upstream section in place verified that the vortex was unaffected by the addition of the section. Within the remainder of the report, unless otherwise noted, values are reported with the upstream section in place.

Turbulence grid slots: The wind tunnel was equipped with two slots to allow the insertion of turbulence generating grids. The upstream slot was located between the contraction and the upstream section, and the downstream slot was located between the upstream section and the main test section. When grids were not in place, the empty spaces in the slots were filled with pieces of rubber cut to size.

Main test section: The main test section was constructed of wood reinforced by aluminum and was 3.66 m long with a rectangular cross section 0.90 m high and 0.61 m wide. The test section floor and ceiling were covered with a smooth PVC sheet to minimize boundary layer growth and flow disturbances. Two stainless steel rails, 0.016 m in diameter, were mounted near the two corners on the floor of the test section, running the length of the section; they were used to guide the traversing system carriage. Access to the test section was provided by five removable circular windows, 0.28 m in diameter, and a 1.17 m$\times$ 0.51 m rectangular access window. One of the circular windows was instrumented with a Pitot-static tube and a hot-wire probe for measuring the wind tunnel velocity and a temperature sensor was also mounted in the tunnel to allow monitoring of the flow temperature. The instrumentation is described in detail in Section 4.3.3. A 0.64 m $\times$ 0.28 m access hole was located in the tunnel floor 0.86 m downstream of the contraction to allow insertion of the wing (see description in the following).

Traversing system: The main test section was equipped with an automated two-axis traversing system. The system consisted of an orthogonal combination of two Velmex Uni-Slide MA/4000 low-profile linear positioning devices which were streamlined by rounding their upstream sides and fairing their downstream edges. The vertical travel of the traverse was 0.80 m and its horizontal travel was 0.47 m. A Slo-Syn M06 1-LS-57S stepper motor drove each axis with a positioning accuracy of 0.005 mm/step. The stepper motors were driven by a Velmex NF90 programmable motor controller, which was programmed by a PC

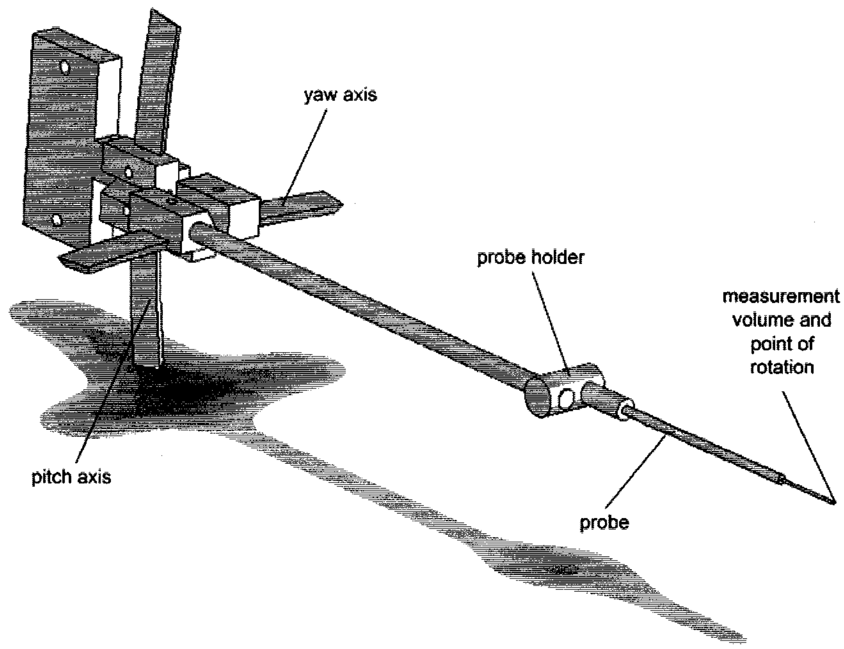

Figure 4.3: Sketch showing the angular positioning device and probe holder.

computer via an RS-232-C COM port.

Anticipating a possible need to re-orient the four-wire probe to reduce errors due to high relative flow angles, the author designed the two-axis angular positioning device shown in Figure 4.3. This device was mounted on the motorized linear traverse and allowed angular positioning of both pitch and yaw axis within the range $\pm 10°$ with an accuracy of approximately $0.5°$. Rotation was about a point 0.360 m upstream of the traverse, corresponding to the location of the measurement volume of four-wire probe number one mounted on the probe holder at the end of a 0.203 m long shaft. This device was in place, but kept at an orientation of $0°$, for all measurements in this study.

For two-probe measurements performed late in the study, a specialized probe

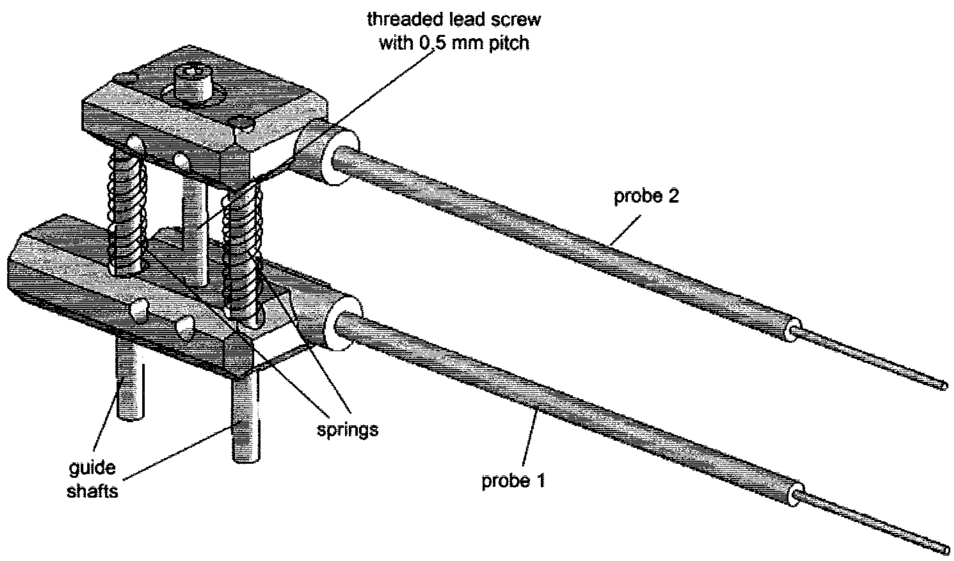

Figure 4.4: Sketch showing dual probe holder.

holder was designed by the author to be mounted at the end of the device shown in Figure 4.3. This device, shown in Figure 4.4 was designed to allow accurate separation of probe number two from probe number one. Springs were incorporated in the device to minimize lead screw backlash by providing positive force on the threads. Utilizing a lead screw with a 0.5 mm pitch, the manually operated traverse had a positioning accuracy of approximately 0.05 mm. The probe holder was designed to allow a minimum probe separation of 7.1 mm, which was the lowest possible value permitted by the probe body thicknesses. The maximum probe spacing, set by the length of the lead screw, was 27.6 mm.

Diffuser: The test section expanded, at its downstream end, into a 3.33 m long wooden diffuser with an expansion ratio of 2.74:1. The diffuser also provided a smooth transition from the wind-tunnel's rectangular test section to the circular fan housing.

Fan: Flow was drawn through the tunnel by a nine bladed, 1.37 m diameter, axial flow fan manufactured by Canadian Blower and Forge Co. Ltd. as a 54 C9 Type-S Adjustax. The angle of the fan blades were set at 23°, optimized for a rotational velocity of 1170 rpm. Immediately downstream of the fan was a row of stator blades, which reduced the angular momentum of the flow.

The fan was driven by a 746 W (30 hp), 30 Hz electric motor through a belt. Although the motor operated at a constant rotational velocity of 30 Hz, the rotational velocity supplied to the belt could be controlled from 0 to 104 Hz (0 to 1000rpm) using a Regutron II magnetic drive.

Wind tunnel flow properties: The wind tunnel was capable of producing flow velocities up to about 30 m/s with the core of the tunnel at approximately uniform velocity within 1% of the centreline velocity. Boundary layer 99% thicknesses are estimated from the measurements of Pilette (2000) as being 8% of the tunnel height, 0.9 m downstream of the contraction (these measurements were performed before the addition of the upstream test section and the wall boundary layers can be expected to be thicker in the current results). Free-stream velocity fluctuations measured at a tunnel speed of 20 m/s were found to be nearly uniform across the test section at an rms level of about 0.2% of the free-stream velocity , 0.61 m downstream of the contraction. These velocity fluctuations increased approximately linearly with streamwise distance to reach about 0.3% at the end of the test section.

For reference, frequency spectra, $F_{xx}(f)$, measured in the empty tunnel along the wind-tunnel centreline are presented in Figure 4.5. The spectra can be integrated to show

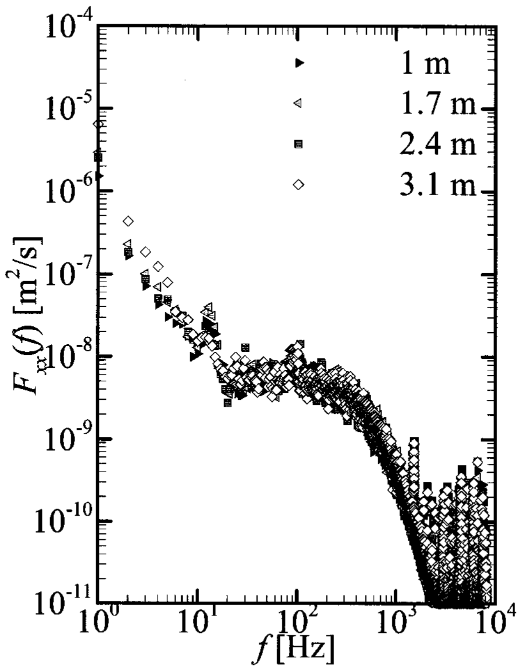

Figure 4.5: Frequency spectra of the flow velocity in the empty wind-tunnel, measured 1 m, 1.7 m, 2.4 m and 3.1 m downstream of the contraction.

that 50% of energy of the velocity fluctuations was contained within the range $f < 10$ Hz and 45% of this energy was in the range $10\,\mathrm{Hz} < f < 1\,\mathrm{kHz}$. Also evident in Figure 4.5 is that velocity fluctuations with frequencies higher than 2 kHz had a negligible amount of energy and the spectra were contaminated by the electronic noise of the hot-wire anemometer .

Wing

In the wind tunnel studies, the tip vortex was generated by a NACA0012 profile wing, machined from an aluminium block. The wing had a rectangular planform with a semi-span $b = 0.5207$ m and a chord $c = 0.1778$ m. The wing tip was plane with sharp edges. The wing was mounted 38.1 mm above the tunnel floor. Its root was attached to a circular end plate with a diameter 0.318 m and sharpened edges to minimize the interaction with the wind tunnel boundary layer. The wing angle of attack could be changed using a rotary table mounted beneath the wind tunnel with the axis of rotation passing through the wing's aerodynamic centre (1/4 chord point). The wing was mounted through the floor of the wind tunnel such that its 1/4 chord point was along the centreline of the wind tunnel, 1.37 m downstream from the contraction. A boundary layer trip wire of diameter 0.58 mm was attached at the 10% chord location on the suction surface to reduce sensitivity to initial conditions for the different cases considered.

The wing was instrumented with pressure taps on the surface of the cylinder at 5 spanwise stations located $0.68b$, $0.83b$, $0.93b$, $0.95b$ and $0.96b$ from the wing root. Each spanwise station consisted of 18 taps, 0.36 mm in diameter at the wing surface, with their chordwise locations indicated in Figure 4.6. Each tap was connected to pressure tubing outside the tunnel through 0.81 mm diameter copper tubing imbedded in slots machined on the surface of the wing and filled with adhesive to provide a smooth finish.

Turbulence grids

Two different turbulence generating grids were used in this study. Both grids were of identical solidity (equal to 0.44) and mesh size, M, to the grids described above for the water tunnel studies. The small grid had a mesh size, M (defined in Figure 4.1)of 25.4 mm whereas the large grid had $M = 50.8$ mm.

Probe calibrator

Directional calibration of the four-wire probes was performed in a calibration apparatus designed by the author. The calibrator is motorized such that the pitch angle θ_{cal}

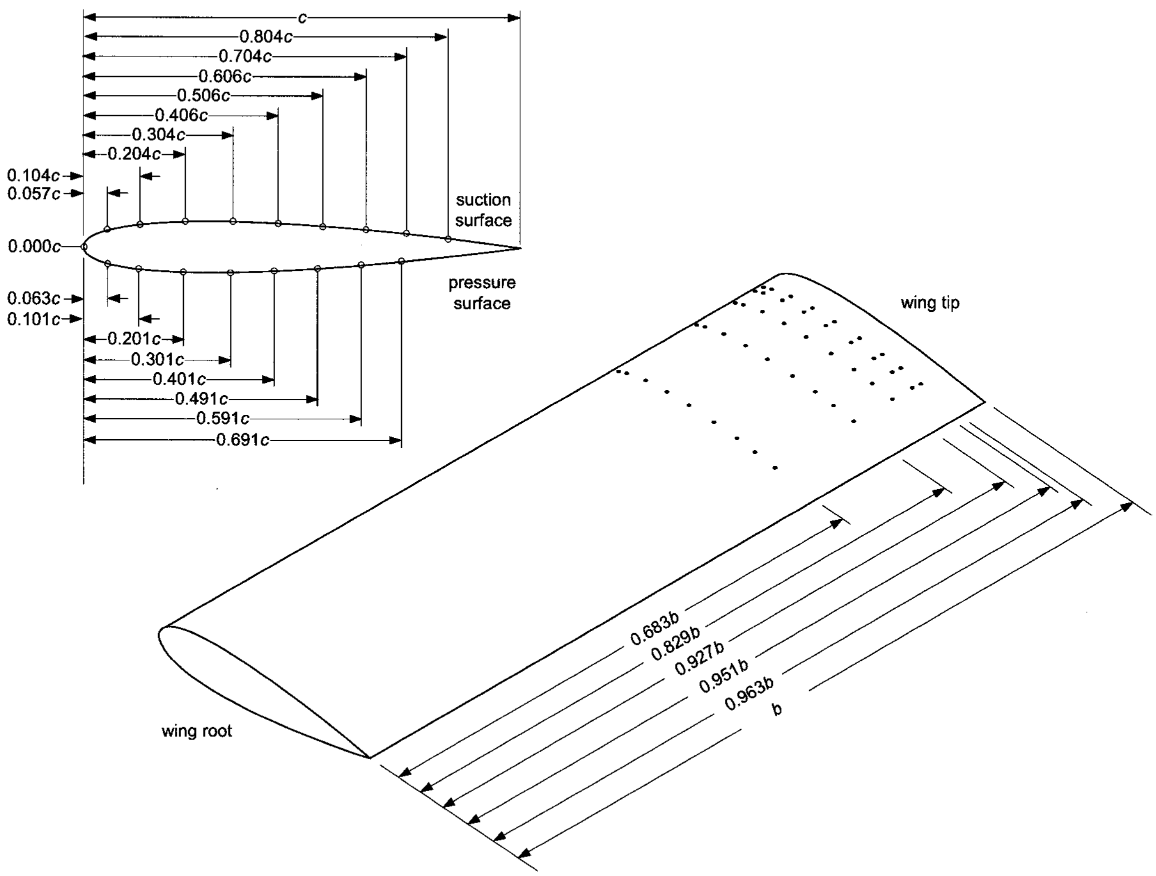

Figure 4.6: Sketch of the wing illustrating pressure tap locations.

and roll angle φ_{cal} between the axis of the probe and the axis of the nozzle could be adjusted in the ranges $-60° \leq \theta_{cal} \leq +60°$ and $0 \leq \varphi_{cal} \leq 360°$. Both axes of rotation intersected 2.5 mm downstream from the centre of the nozzle exit plane and the position of the probe with respect to the intersection of the axis could be confirmed using sight holes located in the device.

The calibration apparatus is shown in Figure 4.7 with various components described below identified on the drawing.

Nozzle: Controlled airflow was provided using an available nozzle unit (Dantec 55DH5), equipped with four different nozzles having exit areas A_{noz} (corrected for boundary layer displacement thicknesses) $= 120, 60, 24$ and $12\,\text{mm}^2$, respectively. Various flow velocity ranges up to Mach 1 could be generated depending on the nozzle being used. For the current study, only the $120\,\text{mm}^2$ nozzle was required, giving a maximum exit velocity of approximately 35 m/s. A 689 kPa (100psi) compressed air line was used as an air source. It was connected to the nozzle inlet through a pressure regulator/valve combination. Nozzle exit velocity was controlled using the same valve. The flow could be heated using a resistance heater mounted upstream of the nozzle inlet, although this capability was only used when calibrating temperature probes.

Rotary tables: Angular position was adjusted using two rotary tables (Velmex B5990TS) driven by stepper motors (Vexta PK245-01AA), which were controlled by a motor controller (Velmex NF90) through two adapter cables provided by the manufacturer. Positioning resolution with these rotary tables was nominally 0.01°, however, the positioning uncertainty

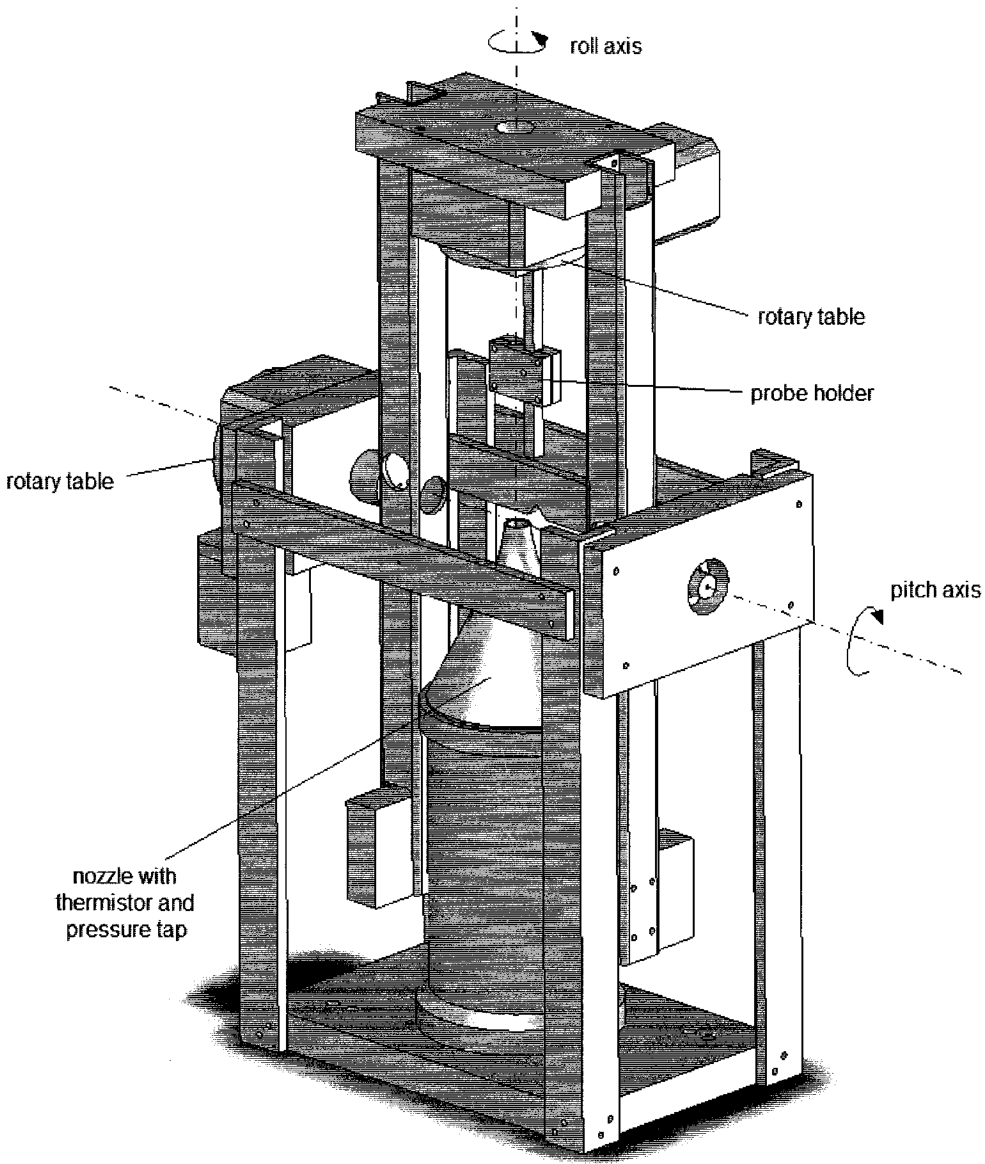

Figure 4.7: Sketch of the directional calibrator

was 0.05° because of backlash within the rotary tables.

Probe holder: The probe was clamped in place using a probe holder that could be adjusted vertically using a rail with a square cross-section. Different probe holders were manufactured to accommodate the different dimensions of the two four-wire probes used in this study.

Temperature measurement: Nozzle exit temperature was monitored using a glass probe thermistor (Sensor Scientific SP43A, $10\,\mathrm{k\Omega}$) with a $5\,\mathrm{s}$ time constant located near the nozzle wall at the exit plane of the nozzle. A custom circuit shown in Figure 4.8 was designed by the author to drive the thermistor and provide output amplification. The voltage output of the thermistor circuit was calibrated at different flow temperatures against a second pre-calibrated thermistor. The circuit response could be represented by the equation $T_{noz} = 7.6031E_{noz} + 2.9332$, where T_{noz} is the air temperature in °C and E_{noz} is the thermistor circuit output voltage in Volts. Due to the self heating of the thermistor, this equation became inaccurate for flow velocities lower than approximately $5\,\mathrm{m/s}$. Also, due to thermal boundary layers in the nozzle, this calibration was invalid when the flow was heated.

Velocity measurement: The nozzle output velocity Q_{noz} (in m/ s) was determined from the measured gauge pressure P_{plen} (in Pa) in the nozzle plenum chamber as

$$Q_{noz} = \frac{1}{1 - A_{noz}/2800}\left(\frac{2P_{plen}}{\rho} - 2gH_{noz}\right)^{0.5}$$

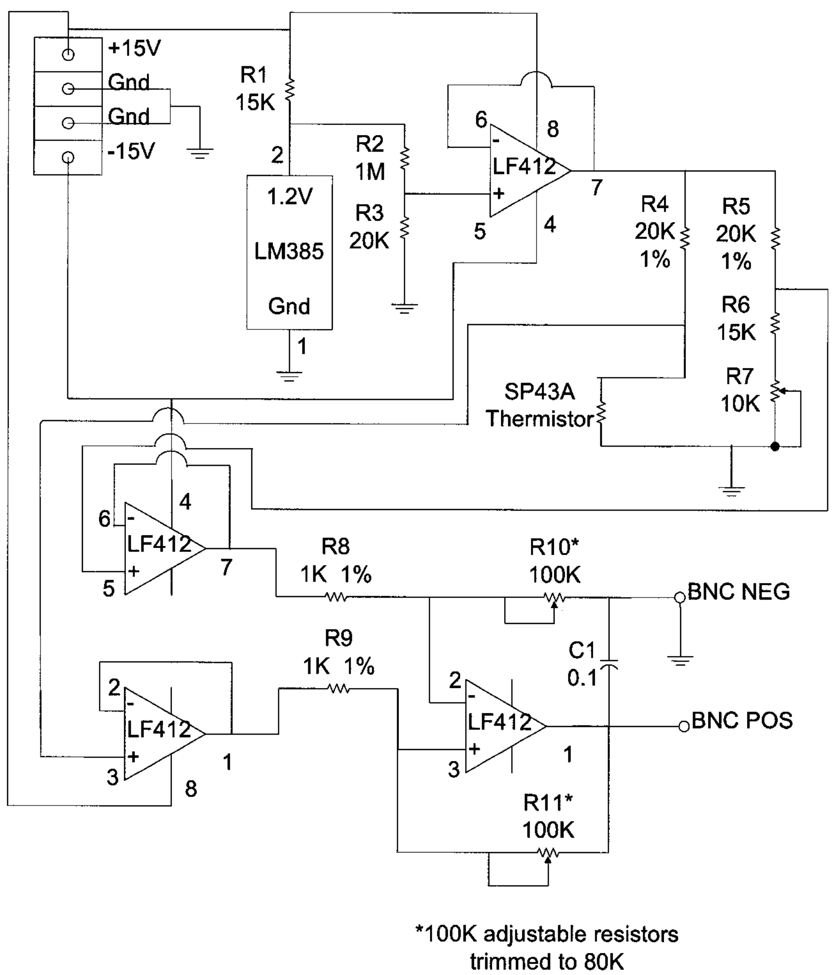

Figure 4.8: Circuit used to convert calibrator thermistor resistance to voltage output.

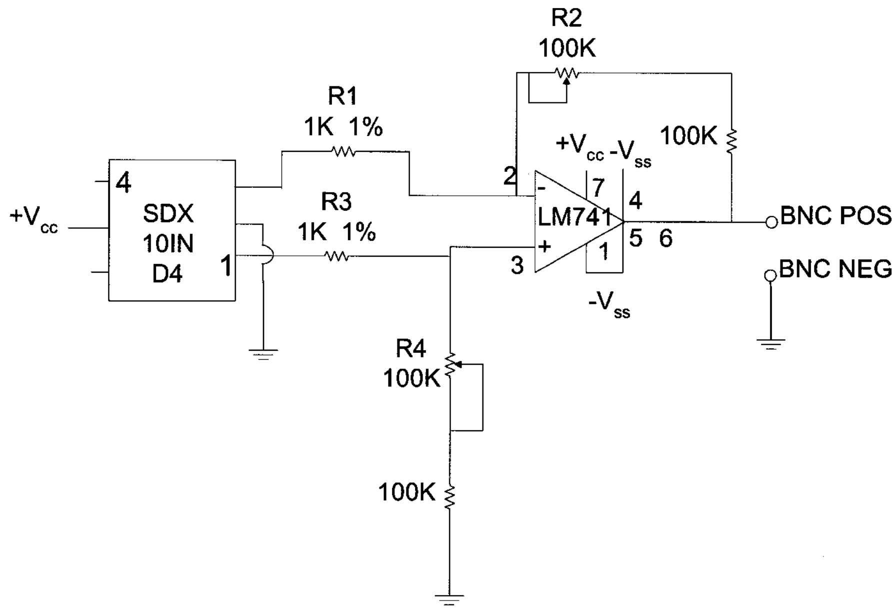

Figure 4.9: Circuit used to amplify pressure transducer output.

where A_{noz} was the nozzle exit area (in mm^2), ρ (in $\mathrm{kg/m}^3$) was the air density determined from the ideal gas law and $H_{noz} = 0.085\,\mathrm{m}$ was the height difference between the nozzle exit and the plenum pressure tap.

The plenum gauge pressure was measured with a pressure transducer (Sensym ICT SDX010IND4), which had a maximum reading of 2.5 kPa and was equipped with temperature compensation. A circuit, shown in Figure 4.9, was used to power the transducer and provide output amplification. The circuit response, calibrated against a water manometer, could be described by the equation $P_{plen} = 2305.10\,(E_{plen} - E_o)$, where E_{plen} was the circuit voltage output and E_o was the output voltage measured at zero pressure difference, determined at the beginning of each calibration run.

Welder

The sensors of hot-wire probes are extremely fragile and occasionally break or burn during probe handling or during a measurement. Hot-wire probe repairs were conducted by the author using a welding apparatus designed by the author and shown in Figure 4.10. The entire apparatus was located on a slate table to minimize vibrations due to outside influences. A typical repair required the wire to be initially held in place with the wire holder. Using a stereoscopic microscope with magnification between 21× to 135× (XTS model SB2U with 20× eyepieces and 1.5× objective lens), the probe was then positioned so that the prong surface was in the correct position followed by positioning of an electrode manufactured from silver wire sanded down to a fine tip. Accurate positioning of the probe and electrode was provided by two commercial translation stages (Thor Labs XYZ 6.35 mm), which were capable of 6.35 mm of travel and moved 250 μm per rotation of the lead screw. These translation stages were mounted on custom made dovetail slides to allow initial positioning of the probe and electrode over a larger adjustment range. Angular positioning was also made using the rotary accessory of the nozzle unit, converted for use in the welder. Once the wire was pressed to the prong surface by the electrode, the quality of the contact between the electrode, wire and probe prong was verified using the continuity check feature of a multi-meter connected in parallel with the electrode and probe. If the connection through the wire between the electrode and prong was poor (intermittent signal from the continuity check), damage to the prong could occur. Once good contact had been determined, welding energy was discharged through the electrode from a welding generator (Dantec 55A12), capable of discharging up to 300 mJ of electric energy in 100, 200 or 400 μs.

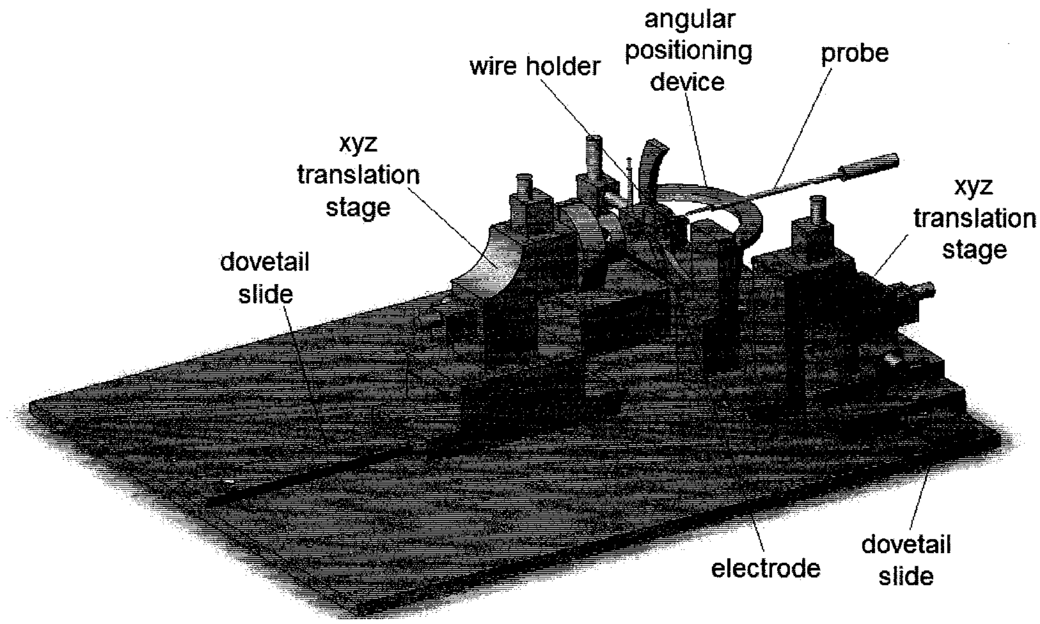

Figure 4.10: Sketch of hot-wire probe welding apparatus.

The discharge of energy through the wire would partially melt the wire, fixing it to the probe prong. It was found that setting the welder to discharge 100 mJ in 100 μs worked well for welding the single-sensor probe, while discharging 50 mJ in 200 μs proved to be the best welding settings for the four-sensor probes used in this study.

4.3 Instrumentation

This section describes the instrumentation used for the experiments and contains the following subsections corresponding to each type of experiment.

- dye injection flow visualization
- oil film flow visualization

- wing surface pressure measurements
- hot-wire anemometry.

4.3.1 Dye injection flow visualization

Dye injection system

The dye injection system in the water tunnel studies consisted of containers of different colored dye which were pressurized using a regulated compressed air line. Two different dyes were used in this study, Congo red and gentian violet. The air pressure drove the dye through tubing to dye injectors, which injected dye into the water tunnel at the desired location. Dye injectors used in this study had orifice with diameters at most equal to 1 mm. Dyes were injected into the test section isokinetically by carefully adjusting the air pressure in the dye collectors. Additional information about the dye injection system has been presented by Dunn (1997).

Video camera

Flow visualization images were recorded at a rate of 30 frames/s using a digital video camera (Sony DCR-VX1000) mounted on a tripod. Selected frames were then captured from the video using a PC running VideoMach software connected to the camera through a FireWire card.

4.3.2 Oil film flow visualization

Oil film flow visualizations were performed in the wind tunnel using a mixture of light machining oil and graphite powder. The mixture ratio was adjusted using direct experimentation to provide a balance between graphite deposit on the wing and free flowing fluid. Images of each run were captured using a Nikon FE2 35 mm camera equipped with a Nikkor 50 mm lens and ISO 300 film.

4.3.3 Wind tunnel instrumentation

The wind tunnel was instrumented to allow monitoring of the free-stream velocity and temperature. To monitor the velocity, one of the circular windows in the wind tunnel was equipped with a Pitot-static tube and a single-sensor hot-wire. This window, whose centre was positioned 0.44 m above the wind tunnel floor, could be inserted at two different wall openings. The first position, with the window centre 0.95 m downstream of the contraction, was used to monitor the free-stream velocity during an experiment run. The second position, with the window centre 1.49 m downstream from the contraction, was used for in-situ velocity calibration of the hot-wire probes. The Pitot-static tube had an outer diameter of 4.76 mm and was positioned such that its tip was 95 mm away from the wind tunnel side wall and 1.49 m downstream of the contraction. The Pitot-static tube pressure difference was converted to a voltage difference using a pressure transducer (Sensym ICT SDX01D4) with a maximum reading of 6895 Pa. The transducer was driven and amplified using the circuit shown in Figure 4.11 and the output voltage was calibrated at the National Research Council facilities. Its response (in Pa) was found to be $P_{pitot} = 2305.10\,(E_{pitot} - E_o)$, where

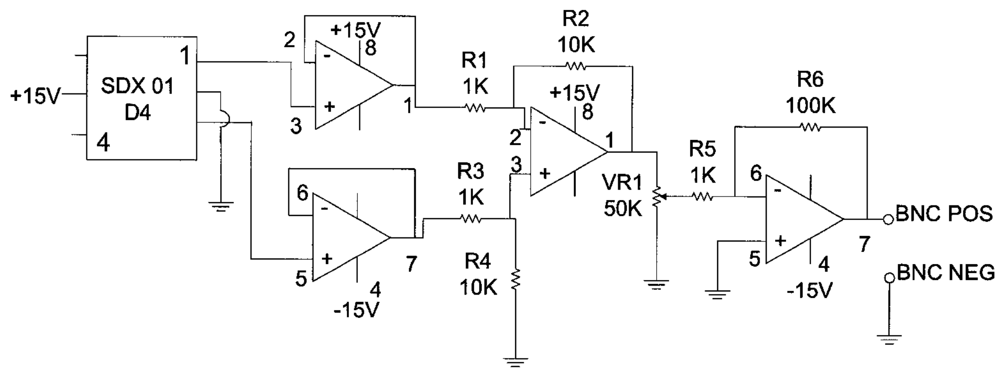

Figure 4.11: Wind tunnel pressure transducer circuit.

E_{pitot} was the circuit output (in Volt) and E_o was the output measured at zero pressure difference, determined at the beginning of each measurement series.

A single-sensor hot-wire probe was added to the instrumented window after it was discovered that a bias error was introduced in the Pitot-static tube response by the free-stream turbulence. It was a single wire probe (Dantec 55P11) with a 1.25 mm long, 5 μm diameter Platinum-Rhodium sensing wire. It was positioned such that the sensing wire was vertically oriented, 89 mm away from the wind tunnel side wall and at the same downstream position as the Pitot-static tube tip.

Wind tunnel temperature was monitored using a glass probe thermistor (Sensor Scientific SP43A 10 kΩ) with a 5 s time constant. The thermistor was positioned 0.44 m from the wind tunnel floor, 50.8 mm away from the wind tunnel side wall opposite to the instrumented window, and 0.95 m downstream of the contraction. A custom-made circuit, shown in Figure 4.12 was designed by the author to power the thermistor and provide output amplification. The voltage output of the thermistor circuit was then calibrated

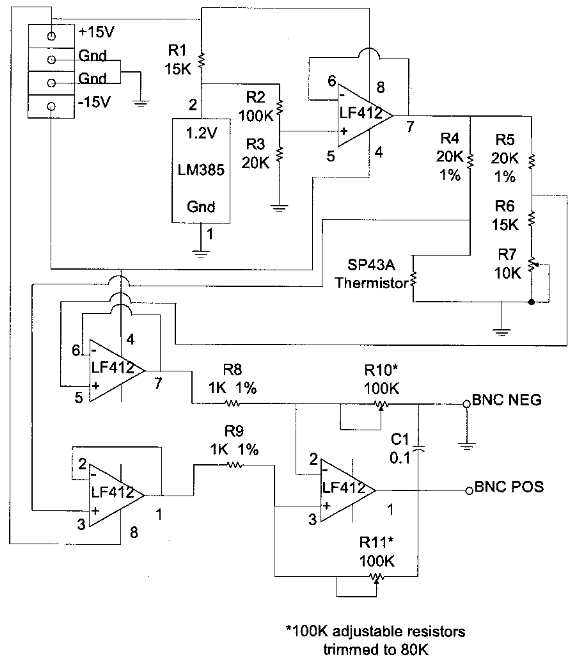

Figure 4.12: Thermistor circuit used to measure the flow temperature in the wind tunnel..

against a mercury thermometer. The circuit response could be described by the expression $T_\infty = 13.2746E_{wt} + 1.6825E_{wt} + 0.7649E_{wt}^2$ where T_∞ was the air temperature in °C and E_{wt} was the circuit output voltage in Volt. Due to self-heating, this calibration curve was inaccurate for flow velocities lower than approximately 5 m/ s.

4.3.4 Wing surface pressure measurements

Pressure measurements were performed using the pressure transducer described in the calibrator instrumentation section connected to the wing pressure taps using PVC medical tubing with 0.46 mm ID. The wind tunnel velocity was monitored using the wind tunnel Pitot-static tube. Voltage time series were recorded using the data acquisition system (UEI PD2 MFS-8-300/16 PowerDAQ) described in more detail below.

4.3.5 Hot-wire anemometry

The principal measurement technique used in this study was constant temperature hot-wire anemometry. Operating principles of constant temperature hot-wire anemometry are fully described by Tavoularis (2005) and will be described here only briefly. A typical hot-wire probe consists of a very small sensing wire. This sensing wire is heated using an anemometer circuit which contains a feedback component that adjusts the current through the sensing wire to maintain a constant temperature. When the sensing wire is immersed in a flowing fluid, it is cooled through convection. Monitoring the voltage required to maintain a constant temperature in the sensing wire provides a measure of the convective cooling and hence the local velocity of the fluid flow. Calibration of the probe against a known fluid flow allows conversion of the measured voltage to velocity. Although single sensor hot-wire probes are sensitive to flow direction changes, using arrangements of multiple sensors on a single probe, all three velocity components can be determined.

Three different types of hot-wire experiments were performed. Single-sensor hot-wire measurements were used to provide a qualitative description of the vortex formation. Single-point four-wire probe measurements of the vortex were performed downstream of the wing to obtain quantitative information about the vortex velocity. Finally, two-point measurements were performed with two four-wire probes to determine the velocity profile of the vortex in a frame of reference moving with the vortex. Each experiment used slightly different instrumentation, which is schematically shown in Figures 4.13, 4.14 and 4.15 for the single sensor, single four-wire probe and two four-wire probe measurements, respectively. The instrumentation is described in more detail below.

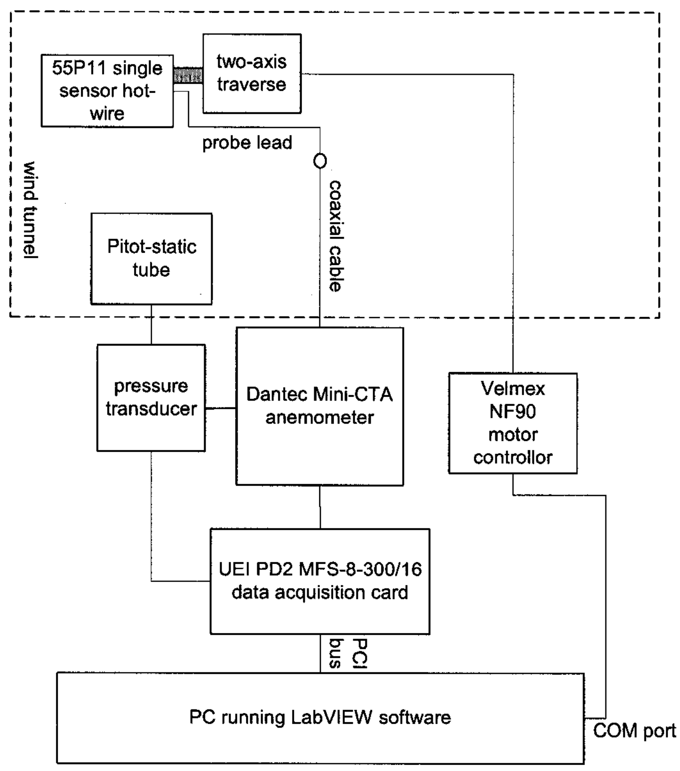

Figure 4.13: Diagram illustrating the connections of the instrumentation used for the single-sensor hot-wire probe measurements.

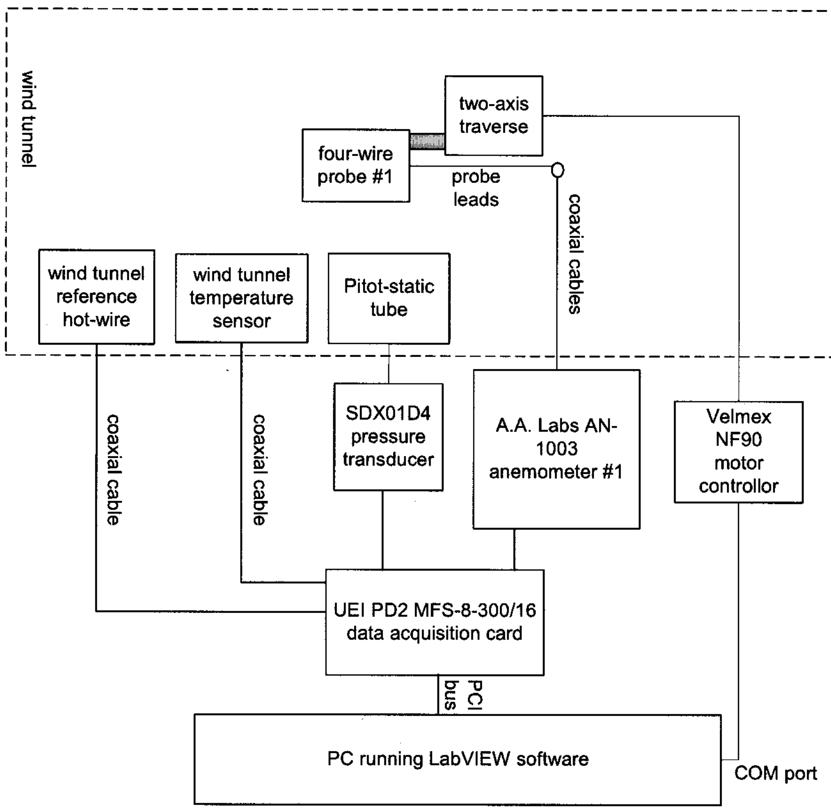

Figure 4.14: Diagram illustrating the connections of the instrumentation used for the four-sensor hot-wire probe measurements.

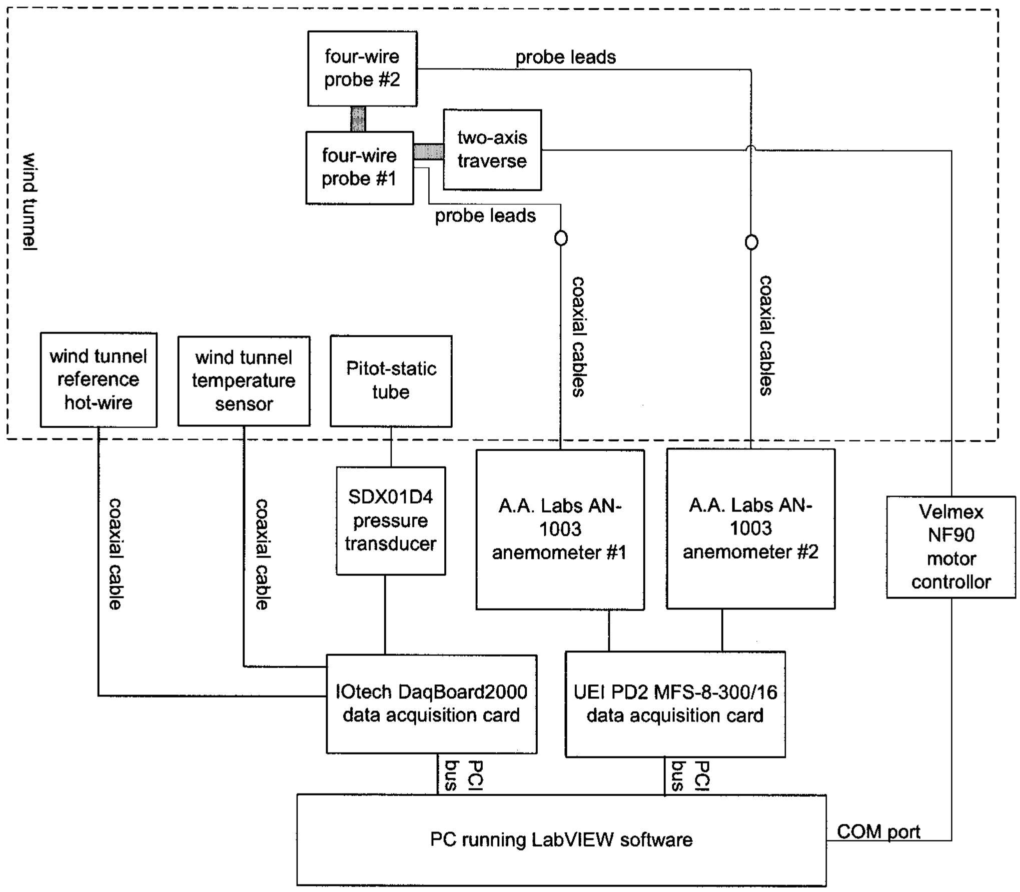

Figure 4.15: Diagram illustrating the connections of the instrumentation used for the dual four-sensor hot-wire probe measurements.

Probes

Three different hot-wire probes were used over the course of this investigation to measure velocity at locations arranged in yz planes. An additional hot-wire probe was used to monitor the wind tunnel free-stream velocity; this probe is described in Section 4.3.3.

Single-sensor hot-wire The single-sensor hot-wire probe used in this study was a Dantec 55P11 probe. This probe was equipped with a single Platinum-coated Tungsten wire, oriented perpendicular to the probe axis. Sensor dimensions were $5\,\mu$m in diameter and 1.5 mm in length. Prong resistance of the probe was $0.6\,\Omega$ and the sensing wire had a typical cold resistance of $3.3\,\Omega$.

Four-sensor hot-wire probe 1 The main measurement probe used in this investigation was a four-sensor hot-wire probe. This probe was a custom-built Kovasnay-type probe with dimensions as well as prong and sensor numbering illustrated in Figure 4.16. For Kovasnay-type probes, the sensor wires are arranged into two orthogonal X-wire arrays with each sensor inclined by an angle of approximately 45° to the oncoming flow. The wire angles for this particular probe, indicated by α_w in Figure 4.16, were approximately 46° for all sensors. Sensors were arranged to provide a measurement volume of $0.21\,\text{mm}^3$. Sensor wires were made from $2.5\,\mu$m Platinum-10%Rhodium wire welded onto the probe prongs and had a length of approximately 0.66 mm.

Effective wire angles, α_{eff}, which reflect the probe's response characteristics and not the physical wire angle, were determined by probe calibration (described in Section 4.4.2). These angles varied depending on the individual sensor characteristics, however

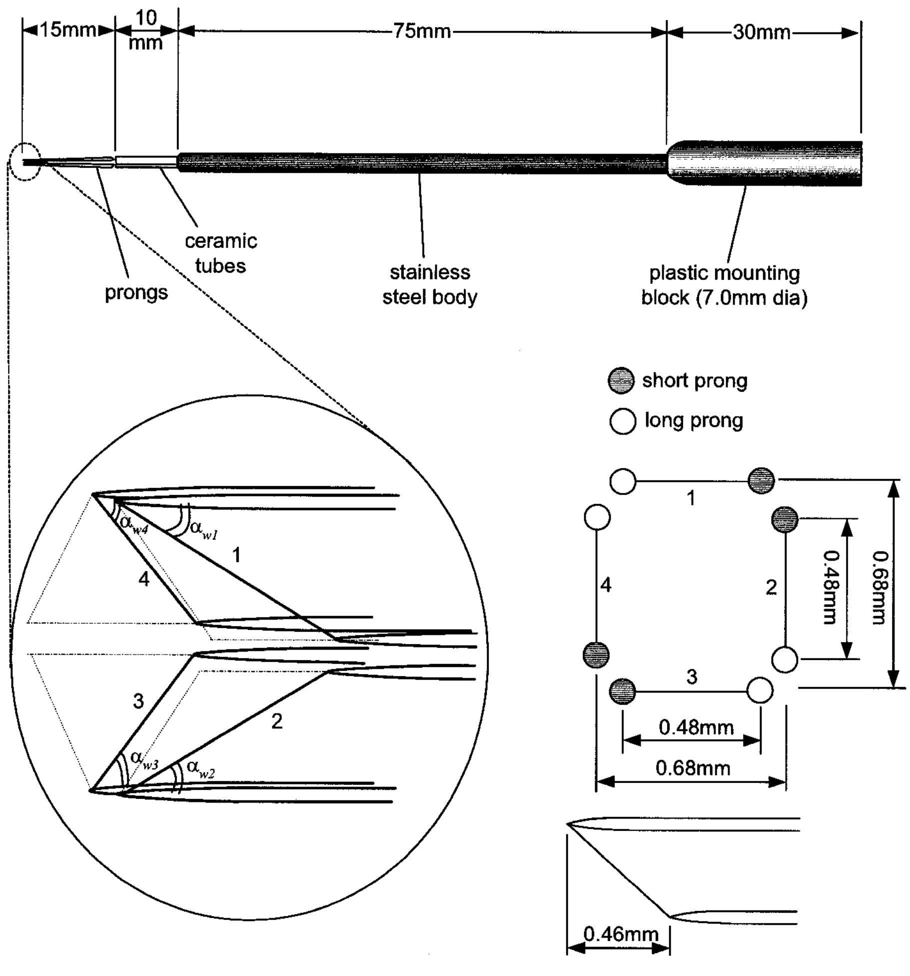

Figure 4.16: Sketch of four-sensor probe 1 (not to scale).

they were found to be near 50° for all sensors. Lead resistance for each sensor was 7.8 Ω and the cold resistance was found to be in the range of 32 to 35 Ω, with the actual values varying from sensor to sensor following each probe repair.

Four-sensor hot-wire probe 2 The second four-sensor hot-wire probe used was only employed in the two-point measurements. Although not very different from probe 1 in design, it had some differences from it and, for this reason, its dimensions and sensor labelling are given separately in Figure 4.17. Exact physical dimensions of the prong arrangement are not known for this probe, however the dimensions shown are believed to be accurate. The slightly different prong arrangement resulted in a smaller sensing volume of approximately 0.11mm^3, however, sensors 1 and 3 had wire angles of approximately 31° and sensors 2 and 4 had wire angles of approximately 46°. Sensor wires were Platinum-10%Rhodium, welded onto the probe prongs, having a diameter of 2.5 μm and approximate length between 0.5 and 0.7 mm, depending on the sensor. Effective wire angles, α_{eff} were found to be approximately 40° for sensors 1 and 3 and approximately 50° for sensors 2 and 4. As will be discussed in Section 4.4.2, this sensor arrangement caused a reduced measurement acceptance range in certain flow angles. The lead resistances of different sensors varied between approximately 16 and 18 Ω and the cold resistances were found to be near 14 Ω for sensors 1 and 3 and close to 20 Ω for sensors 2 and 4, with the actual values varying from sensor to sensor and after each probe repair.

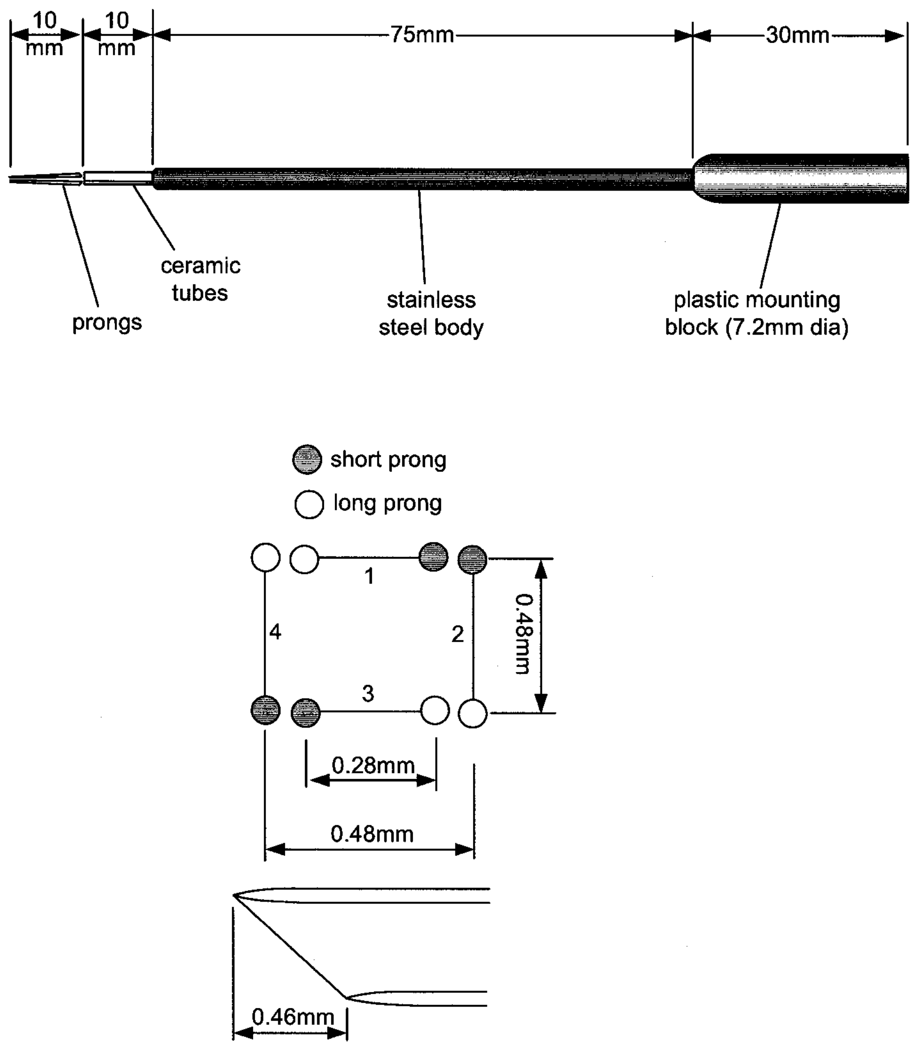

Figure 4.17: Sketch of four-sensor probe 2 (not to scale).

Probe leads

The single-sensor probe was positioned in a Dantec 55H20 probe holder. This holder is equipped with a bnc connector and a coaxial cable with a length of 1m and a resistance of $0.1\,\Omega$. Custom-built leads, 1 m in length and with a resistance of approximately $0.1\,\Omega$, were used to connect the connectors that were attached to the two four-wire probes and the bnc connectors on the coaxial cables that were connected to the anemometer circuits.

Coaxial cables

Early in the study, it was determined that the existing coaxial cables were a source of electronic noise and anemometer drift. As a result, new cables were manufactured using high quality components. Manufactured using Belden 8262 RG 58(c/u) $50\,\Omega$ coaxial cable, these cables were 5 m in length and had Amphenol M23329/3-01/3-03 $50\,\Omega$ bnc connectors on each end. Resistance of these cables was approximately $0.3\,\Omega$.

Anemometers

Three different anemometer systems were used over the course of this study. A Dantec Mini-CTA anemometer was used for single sensor hot-wire measurements, whereas A.A. Labs AN-1003 anemometers were used for the multi-sensor hot-wire measurements.

Dantec Mini-CTA anemometer The Dantec 54T30 Mini-CTA anemometer was a compact, single channel anemometer with a frequency response of 10 kHz and a 1:20 bridge ratio. The anemometer was capable of operating sensors with a maximum operating resistance of $20\,\Omega$. Output signal gain, offset and filter cutoff frequency could be adjusted using variable resistors mounted on the anemometer board. The type of filter employed by this anemometer could not be determined.

A.A. Labs AN-1003 #1 The principal anemometer used in this study was an AA Labs AN-1003 anemometer with six channels, all with optional high frequency compensation circuitry. This anemometer was capable of operating at both 1:1 and 1:10 bridge ratios with maximum operating resistances of $99.9\,\Omega$ and $9.99\,\Omega$, respectively. Due to limitations in the anemometer power supply, at 1:1 bridge ratios, only five channels could be operated. The frequency response of the anemometer depended on the probes used, with an upper cutoff frequency of up to 250 kHz achievable through adjustment of circuit capacitance and inductance. The anemometer had output signal conditioning, in the form of adjustable output gain and offset as well as an analogue filter of selectable cutoff frequency consisting of two double-pole low-pass filters.

It was discovered early in the study, that the four-wire probes described above caused the feedback circuit of the anemometer to oscillate due to their high impedance. These oscillations could be harmful for the probe or anemometer and would contaminate the data. After contacting A.A. Labs, it was determined that, by changing capacitor C31 on the anemometer circuit, the frequency response of the circuit could be altered to restore circuit stability. Through trial and error, it was found that by replacing the existing 2.2 nF capacitor with an 820 pF capacitor, the circuit oscillations were eliminated and a high frequency response was maintained.

A.A. Labs AN-1003 #2 For experiments utilizing two four-wire probes, a second anemometer was required because the number of channels available in the first unit was insufficient. A second AN-1003 anemometer was used, on loan from Carleton University, to operate the second probe. The capabilities of this anemometer were virtually identical to those of anemometer #1, however, anemometer #2 had 10 channels, only two of which had the optional high frequency compensation circuitry.

The circuit oscillation problem that occurred with anemometer #1 was also evident with the second anemometer with four-sensor probe #2. To avoid altering the circuitry of the borrowed anemometer, it was found through direct experimentation and consultation with A.A. Labs that increasing the length of the cables to the probe through the addition of a short length of unshielded wire sufficiently increased the circuit damping to eliminate the oscillations. It was determined that a balance between oscillation reduction and frequency response could be obtained using 0.5 m long sections of wire on sensors 1 and 3 and 0.9 m long sections of wire for sensors 2 and 4.

Data acquisition

Two data acquisition cards were used over the course of this study, both of which were installed on the PCI bus of a PC computer. For single-probe measurements, a UEI PD2 MFS-8-300/16 PowerDAQ acquisition card was used. For experiments using two four-wire probes, a second acquisition system was required to provide enough analogue input channels. An IOtech DaqBoard/2000 data acquisition system was used to provide the additional channels.

UEI data acquisition system A UEI PD2 MFS-8-300/16 PowerDAQ acquisition card was used for the majority of measurements performed in this study. This card could perform pseudo-simultaneous sampling of up to eight analogue input channels. It was capable of performing analogue-to-digital conversion with a resolution of 16bits at up to 300 kHz for a single channel or 37.5 kHz for all eight channels. Input voltage ranges were user selectable as either 0-5 V, 0-10 V, ± 5 V or ± 10 V. For this study, the majority of measurements were performed using a 0-5 V input range to maximize the resolution of the analogue-to-digital conversion. The system had rms noise levels of 1-2 bits determined by measuring the rms voltage fluctuations across a shorted input.

IOtech data acquisition system An IOtech DaqBoard/2000 acquisition system was used in the dual probe measurements to monitor the wind tunnel instrumentation. This system was capable of performing analogue to digital conversions with 16bit resolution for up to sixteen channels. Sampling rates of up to 200 kHz were possible for a single channel or 12.5 kHz for all sixteen channels. Input voltage ranges were fixed at ± 10 V. Although it was possible for this card to operate with simultaneous sample-and-hold through a DBK17 add-on card, this feature was disabled due to complications getting the simultaneous sample-and-hold to operate in LabVIEW. Because only reference signals from the wind tunnel thermistor, Pitot-static tube and reference hot-wire were sampled with this card, simultaneous measurements of the three channels were deemed unnecessary.

PC running LabVIEW software

The control centre of the experiment was a PC computer. Both data acquisition systems were installed on this computer and communication with the traverse motor controller was performed using the serial port. Each experiment was controlled using LabVIEW software running G-code programs written by the author. The software automated and coordinated each experiment in the following sequence.

1. Moving the probe(s) to the desired measurement location (read from an ASCII text file).
2. Performing a 1 s measurement of the input voltage from the wind tunnel instrumentation and determining the wind tunnel temperature and velocity from the average.
3. Recording the wind tunnel temperature and velocity in ASCII format for later use.
4. Measuring the voltage output from the anemometers at specified sampling rates and times through the data acquisition card.
5. Recording the data to a hard disk in binary format for later processing.
6. Repeating the process until all data had been acquired at all desired measurement locations.

Software with similar capabilities were also written to control velocity and directional calibration.

4.4 Data reduction technique

Although four-sensor hot-wire probes are theoretically capable of measuring the three-dimensional velocity vector for flow angles within an acceptance cone of 40° from the probe axis (Vukoslavcevic et al. (2004)), the actual acceptance cone is dependent on the individual probe's configuration. The computation of flow velocity from the four sensor voltages can be achieved with the use of an iterative analytical solution of an over-defined system of equations or, alternatively, with the use of a look-up table, constructed by extensive calibration. The technique used in this study was the look-up table technique of Wittmer et al. (1998), which will be summarized here. Other techniques available include those of Döbbeling et al. (1990) and Maciel and Gleyzes (2000).

The technique of Wittmer et al. (1998) was selected for several reasons. Early in the study, a comparison of the techniques of Wittmer et al., Maciel and Gleyzes, and Döbbeling et al. was performed. Although the technique of Döbbeling et al had a theoretically larger acceptance cone (approximately 45°) than that of Wittmer et al. (approximately 30°), the processing time of the former technique was prohibitive, requiring almost 50 times longer to process a single measurement position. The times to process the signals using the Wittmer et al. and Maciel and Gleyzes techniques were comparable, however, the technique of Wittmer et al. resulted in a slightly larger acceptance cone. In addition, the technique of Wittmer et al. had been successfully used by Devenport et al. (1996) to study a similar vortex to the one used in the current study. A comparison of different four-wire data reduction techniques by Lavoie and Pollard (2003) also demonstrated that the Wittmer et al. technique provided accurate results in flows with low and moderate turbulence intensity.

The data reduction technique of Wittmer et al. requires two separate calibrations for the probe, a velocity calibration which changes over time as the sensors age and accumulate dirt, and a directional calibration, which tends to be unaffected by time.

4.4.1 Velocity calibration

Velocity calibrations established the relationships between the bridge output from each anemometer E_{b_i}, where the index i indicates the individual sensor, and the effective cooling velocity U_{eff_i} measured by the corresponding sensor. The effective cooling velocity is commonly defined as the equivalent flow velocity parallel to the probe axis that would produce the same sensor cooling as the actual flow velocity.

Velocity calibrations were performed in the wind tunnel before and after each measurement run. To perform the velocity calibration, the four-sensor probe was positioned with its measurement volume within 10 mm of the tip of the Pitot-static tube. The anemometer output voltage E_{ai}, the velocity measured by the Pitot-static tube and the wind tunnel temperature were recorded over thirty second intervals at nine different free-stream velocities. The bridge output E_{b_i} was determined from E_{a_i} for each sensor as $E_{b_i} = E_{a_i}/G_i - E_{offi}$, where G_i is the channel conditioning gain and E_{offi} is the offset. The relationship between E_{b_i} and U_{eff_i} was then determined using the modified King's law (Tavoularis (2005)),

$$\frac{E_{b_i}^2}{T_{w_i} - T_\infty} = A_i + B_i U_{eff_i}^{n_i}, \tag{4.1}$$

where A_i and B_i and n_i are calibration constants, T_{w_i} is the sensor temperature and T_∞ is the free-stream temperature. Least squares curve fitting was performed using the MATLAB function *lsqcurvefit*. A representative set of calibration results for all four sensors is shown

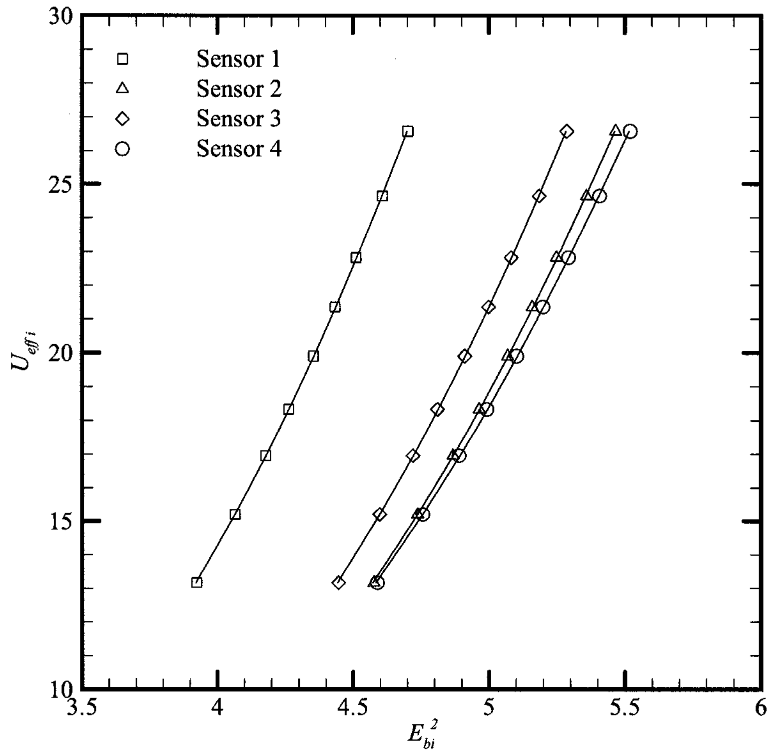

Figure 4.18: Example of velocity calibration results for the four sensors of probe 1. Solid lines indicate King's Law curve fit.

in Figure 4.18.

4.4.2 Directional calibration

The second calibration required by the Wittmer et al. (1998) technique was the directional calibration. This calibration established the relationship between the effective velocities measured by the four sensors and the three velocity components and is most dependent on the physical characteristics of the probe. Directional calibrations were performed after each sensor repair using the directional calibrator described previously.

Directional calibrations were performed in the following multi-step sequence:

1. velocity calibration
2. pitch alignment
3. velocity calibration
4. roll alignment
5. velocity calibration
6. determination of effective sensor angle
7. velocity calibration
8. final directional calibration

Velocity calibrations

Velocity calibrations were performed before each stage of the directional calibration process to ensure that the velocity response of the probe was as accurate as possible. These velocity calibrations were similar to those carried out in the wind tunnel with the only difference that the nozzle plenum pressure was used to determine the flow velocity. The response was represented by the modified King's Law as described previously.

Pitch alignment

The first main step of the directional calibration was to align the probe axis and the nozzle velocity direction. This process involved pitching the probe over a range from $-2.5°$ to $+2.5°$ at $0.1°$ increments and, for each pitch angle, performing measurements over a range of roll angles from $-180°$ to $+180°$ at $10°$ intervals. Once these measurements were complete, the standard deviations of the effective velocities measured for each pitch angle and all roll angles considered were compared to each other and the pitch angle with the smallest standard deviation was assumed to correspond to probe-flow alignment. The pitch axis motor was then zeroed at that position.

Roll alignment

Alignment of the roll axis was then performed. First the probe was pitched by 43° to the nozzle axis, then measurements were performed over roll angles from $-180°$ to $+180°$ at 1° increments. The effective velocities were then examined to identify the angles at which each sensor produced a minimum effective velocity (at this velocity, the sensor was assumed to be in the wake of the longest of the two supporting prongs). The roll axis motor was then zeroed such that the minimum effective velocities for the four sensors occurred as nearly as possible to roll angles of $-180°$, $-90°$, 0° and 90°.

Determination of effective sensor angles

Next, the effective sensor angle α_{eff} was determined for each sensor. This angle is defined by Bradshaw (1975) and is used to simplify the analytical treatment of the response of the sensors to different flow directions. For each sensor, the probe was first rolled and pitched such that the selected sensor was approximately normal to the nozzle flow direction and the pitch axis. Measurements were then performed for a pitch angle range of $\pm 5°$ from the estimated normal orientation at 0.1° increments. The effective wire angle was then estimated from the pitch angle at which the effective velocity measured by the sensor was maximized.

Final directional calibration

Once the probe was aligned with the nozzle flow, the directional calibration could be performed. This calibration involved performing measurements at 721 combinations of pitch and yaw angles over a range from $-180°$ to $+180°$ in roll and a range from $-45°$ to $+45°$ in pitch.

In the technique of Wittmer et al., the four-wire probe is treated as two perpendicular cross-wire probes, allowing one to estimate the three components of velocity U_{x_p}, U_{y_p}, and U_{z_p} as U_{x_e}, U_{y_e}, and U_{z_e}, respectively. The subscripted p is used to denote a Cartesian coordinate system whose origin is at the probe's measurement volume with the U_{x_p} component of velocity along the axis of the probe. The orientation of U_{y_p} and U_{z_p} was determined by orientation of the probe during calibration and was typically selected such that U_{y_p} was parallel to wires 1 and 3 and U_{z_p} was parallel to wires 2 and 4.

The purpose of the directional calibration was to determine the approximate analytical functions $f_1\left(U_{y_e}/Q_e, U_{z_e}/Q_e\right)$, $f_2\left(U_{y_e}/Q_e, U_{z_e}/Q_e\right)$ and $f_3\left(U_{y_e}/Q_e, U_{z_e}/Q_e\right)$, where $Q_e^2 = U_{x_e}^2 + U_{y_e}^2 + U_{z_e}^2$. In essence, these functions define the corrections required to determine the actual velocity components from the estimates U_{x_e}, U_{y_e}, and U_{z_e}.

The functions $f_1\left(U_{y_e}/Q_e, U_{z_e}/Q_e\right)$, $f_2\left(U_{y_e}/Q_e, U_{z_e}/Q_e\right)$ and $f_3\left(U_{y_e}/Q_e, U_{z_e}/Q_e\right)$ were determined as follows. At each calibration position, the estimated velocity components were found using

$$U_{z_e} = \frac{C_4\sqrt{C_2}U^*_{eff_2} - C_2\sqrt{C_4}U^*_{eff_4}}{C_4D_2 - C_2D_4} \tag{4.2}$$

$$U_{y_e} = \frac{C_3\sqrt{C_1}U^*_{eff_1} - C_1\sqrt{C_3}U^*_{eff_3}}{C_3D_1 - C_1D_3} \tag{4.3}$$

$$U_{x_e} = \frac{1}{2}\left(\frac{U^*_{eff_4}}{\sqrt{C_4}} - \frac{D_1}{C_1}U_{y_e} + \frac{U^*_{eff_3}}{\sqrt{C_3}} - \frac{D_3}{C_3}\left(-U_{z_e}\right)\right), \tag{4.4}$$

where

$$C_i = \sin^2(\alpha_{eff_i}) \quad i = 1..4$$

$$\begin{aligned} D_i &= \sin(\alpha_{eff_i})\cos(\alpha_{eff_i}) \quad i = 1..2 \\ D_i &= -\sin(\alpha_{eff_i})\cos(\alpha_{eff_i}) \quad i = 3..4. \end{aligned}$$

These equations were derived by treating the four-wire probe as two cross-wire probes. Note that Wittmer et al. rotate the effective velocities to the sensor normal through $U^*_{eff_i} = U_{eff_i}\sin\alpha_{eff_i}$.

At each calibration position, the actual velocity components were determined from the nozzle velocity Q_{noz} and the calibrator pitch angle θ_{cal}, and roll angle φ_{cal} as

$$U_{x_p} = Q_{noz}\cos(\theta_{cal}) \tag{4.5}$$

$$U_{y_p} = Q_{noz}\sin(\varphi_{cal})\sin(\theta_{cal}) \tag{4.6}$$

$$U_{z_p} = Q_{noz}\sin(\theta_{cal})\cos(\varphi_{cal}). \tag{4.7}$$

The values of the three functions $f_1(U_{y_e}/Q_e, U_{z_e}/Q_e)$, $f_2(U_{y_e}/Q_e, U_{z_e}/Q_e)$ and $f_3(U_{y_e}/Q_e, U_{z_e}/Q_e)$ at each calibration angle were then determined using

$$f_1(U_{y_e}/Q_e, U_{z_e}/Q_e) = \frac{U_{y_p} - U_{y_e}}{Q_e} \tag{4.8}$$

$$f_2(U_{y_e}/Q_e, U_{z_e}/Q_e) = \frac{U_{z_p} - U_{z_e}}{Q_e} \tag{4.9}$$

$$f_3(U_{y_e}/Q_e, U_{z_e}/Q_e) = \frac{Q_p - Q_e}{Q_e}, \tag{4.10}$$

where $Q_p^2 = U_{x_p}^2 + U_{y_p}^2 + U_{z_p}^2$.

At large flow angles, f_1, f_2 and f_3 were not single valued, and hence these points had to be eliminated from the calibration data. The flow angles at which these functions

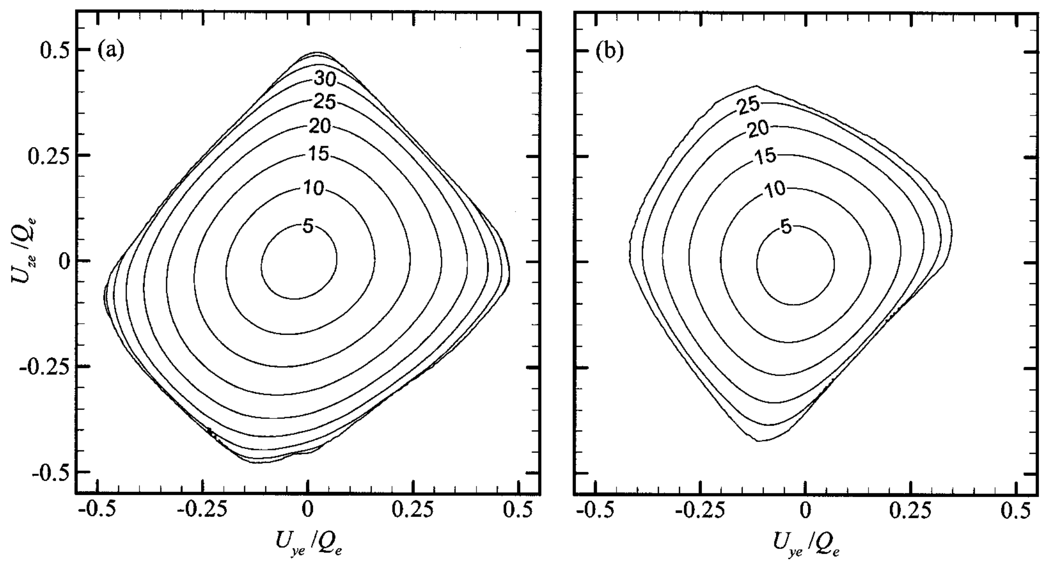

Figure 4.19: Probe acceptance range for (a) probe 1 and (b) probe 2. Contours indicate angle of flow velocity vector and probe axis in degrees.

become multi-valued form the limit of the acceptance range for this technique. Following Wittmer et al., these points can be identified by a change in the sign of the Jacobian

$$\begin{vmatrix} \frac{\partial(U_{ye}/Q_e)}{\partial(U_y/Q_p)} & \frac{\partial(U_{ye}/Q_e)}{\partial(U_z/Q_p)} \\ \frac{\partial(U_{ze}/Q_e)}{\partial(U_y/Q_p)} & \frac{\partial(U_{ze}/Q_e)}{\partial(U_z/Q_p)} \end{vmatrix},$$

although in practice it was found that a threshold near zero (typically -0.02) provided better results, most likely due to the discretization of derivatives used to find the Jacobian.

The acceptance ranges for probes 1 and 2 are plotted in Figure 4.19. As can be observed in Figure 4.19 probe 1 has an acceptance range of flow angles of at least 30°, depending on the angle of the flow with respect to the probe. Due to its different prong arrangement, probe 2 has the much more limited acceptance range of at least 22°, depending on the angle of the flow with respect to the flow.

Typical results for f_1, f_2 and f_3 are plotted in Figure 4.20 for probe 1 and Figure

4.21 for probe 2.

The method of Döbbeling et al. (1990) was also used in this study to replace data points which fell outside the range of the Wittmer et al. technique. This method finds the flow angle by comparing the values of $U_{eff_i}/\left(U_{eff_1}^2 + U_{eff_2}^2 + U_{eff_3}^2 + U_{eff_4}^2\right)$ for each of the wires with those found during calibration as a function of flow pitch and yaw. By determining the flow angle with the smallest error between the two values, the velocity vector magnitude, pitch angle and yaw angle are determined.

4.4.3 Data reduction procedure

Four-sensor voltage time series acquired from the anemometer were reduced to three-component velocity time series using the velocity calibration and the functions f_1, f_2 and f_3 using the following procedure:

1. the effective velocity U_{eff_i} was determined for each sensor from the anemometer voltages using King's Law, Equation 4.1
2. U_{eff_i} was transformed to $U_{eff_i}^*$ using $U_{eff_i}^* = U_{eff_i} \sin \alpha_{eff_i}$
3. U_{x_e}, U_{y_e}, and U_{z_e} were determined from the effective velocities using Equations 4.2-4.4
4. the value of the functions f_1, f_2 and f_3 at $(U_{y_e}/Q_e, U_{z_e}/Q_e)$ were determined using a third order polynomial interpolation scheme
5. U_{x_p}, U_{y_p}, and U_{z_p} were then found using Equations 4.8-4.10 (the subscripted p indicates the the Cartesian velocity components where the orientation of the axes is dependent on the orientation of the probe during calibration).

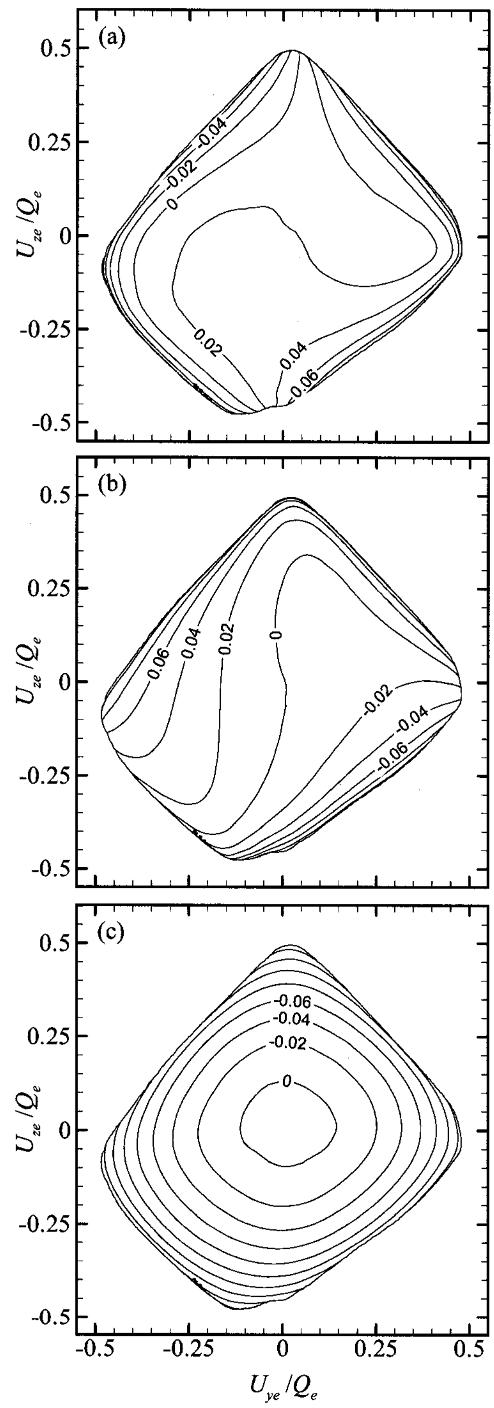

Figure 4.20: Example of probe 1 correction functions (a) f_1, (b) f_2 and (c) f_3 determined by directional calibration.

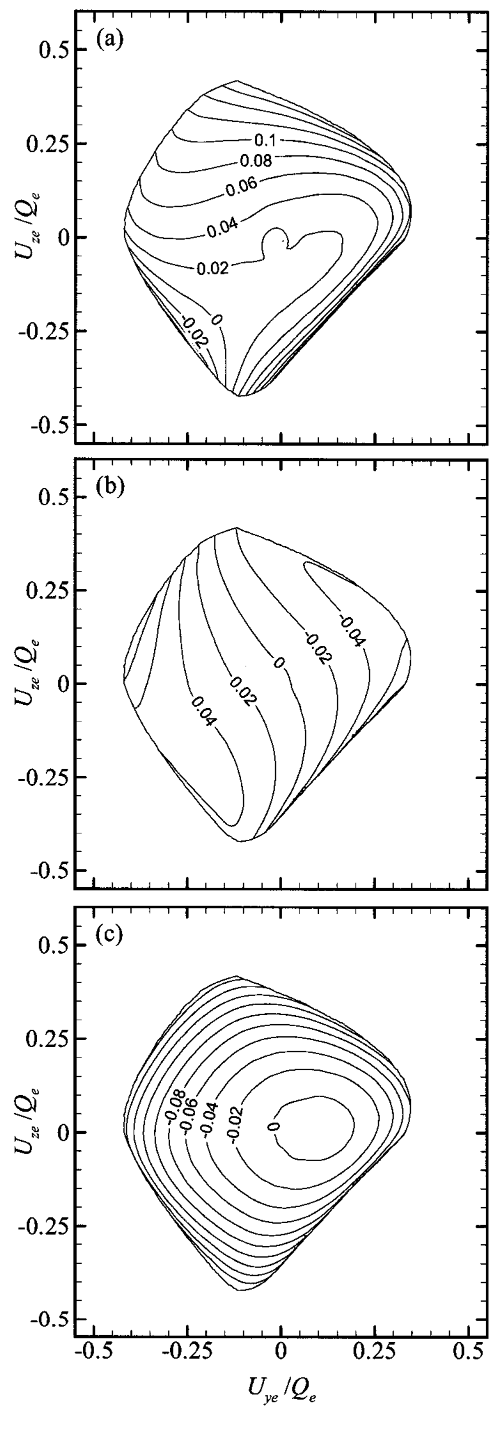

Figure 4.21: Example of probe 2 correction functions (a) f_1, (b) f_2 and (c) f_3 determined by directional calibration.

Data values that resulted in $(U_{y_e}/Q_e, U_{z_e}/Q_e)$ combinations outside the acceptance range were replaced using the technique of Döbbeling et al. This step was performed to minimize statistical biasing caused by the acceptance range. Typically, less than 0.5% of the data fell outside the acceptance range and hence the effects of these values on statistical properties were insignificant

Once the U_{x_p}, U_{y_p}, and U_{z_p} time series had been determined, the coordinate system was rotated such that the x-axis of the velocity vector was aligned with the time-averaged vortex axis (the laboratory coordinate system is defined in Figure 5.1). The coordinate system rotation was performed by first rotating the system by an angle β_{mod} about z_p, followed by by rotation by an angle α_{mod} about the (rotated) y_p and a final rotation about the x-axis by θ_{mod}. This rotation resulted in the following expressions (Etkin and Reid (1996))

$$U_x = U_{x_p}\cos\alpha_{\text{mod}}\cos\beta_{\text{mod}} + U_{y_p}\cos\alpha_{\text{mod}}\sin\beta_{\text{mod}} - U_{z_p}\sin\alpha_{\text{mod}}$$

$$\begin{aligned} U_y &= U_{x_p}(\sin\theta_{\text{mod}}\sin\alpha_{\text{mod}}\cos\beta_{\text{mod}} - \cos\theta_{\text{mod}}\sin\beta_{\text{mod}}) + \\ &\quad U_{y_p}(\sin\theta_{\text{mod}}\sin\alpha_{\text{mod}}\sin\beta_{\text{mod}} + \cos\theta_{\text{mod}}\cos\beta_{\text{mod}}) + U_{z_p}\sin\theta_{\text{mod}}\cos\alpha_{\text{mod}} \end{aligned} \tag{4.11}$$

$$\begin{aligned} U_z &= U_{x_p}(\cos\theta_{\text{mod}}\sin\alpha_{\text{mod}}\cos\beta_{\text{mod}} + \sin\theta_{\text{mod}}\sin\beta_{\text{mod}}) + \\ &\quad U_{y_p}(\cos\theta_{\text{mod}}\sin\alpha_{\text{mod}}\sin\beta_{\text{mod}} - \sin\theta_{\text{mod}}\cos\beta_{\text{mod}}) + U_{z_p}\cos\theta_{\text{mod}}\cos\alpha_{\text{mod}} \end{aligned}$$

where U_{x_p}, U_{y_p} and U_{z_p} are the velocity components measured by the probe before rotation (whose orientation is determined by the orientation of the probe during calibration and the orientation of the probe in the wind-tunnel during measurement). The angles α_{mod}, β_{mod} and θ_{mod} were determined by inspection of the isocontours of the time-averaged velocity magnitude $(\overline{U}_{y_p}^2 + \overline{U}_{z_p}^2)^{\frac{1}{2}}$ on the measuring plane. The angles α_{mod}, β_{mod} and θ_{mod} were then adjusted to yield isotachs that were as circular as possible, with θ_{mod} determined such that $U_y \approx 0$ and $U_z \approx 0$ in the vertical and horizontal directions respectively, thus correcting for slight misalignment of the probe axis with respect to the vortex axis. Typical values of axis rotations were $|\alpha_{\mathrm{mod}}|, |\beta_{\mathrm{mod}}| < 5^\circ$ and $|\theta_{\mathrm{mod}}| < 10^\circ$, thus the measurement plane vertical directions and horizontal directions were virtually identical to the y and z directions of the rotated plane.

After coordinate system rotation, the results were normalized by the local free-stream velocity U_o on the corresponding measuring plane, which was higher by up to 5% than the undisturbed free-stream velocity U_∞ because of blockage by the wing and its wake.

4.5 Measurement uncertainty

Quantifying the uncertainty in curve-fitting of calibration data and in converting measured cooling velocities to Cartesian velocity components is not a trivial task. Following Wittmer et al. (1998), uncertainties in the data reduction technique were estimated by comparing the Cartesian velocity components measured by the probe to those calculated from the calibration jet velocity and probe orientation. The error determined using this technique for a sample calibration is presented as a contour map in Figure 4.22. As can be seen in this figure, the maximum uncertainties were approximately $\Delta\overline{U}_x/U_\infty \approx 0.3\%$, $\Delta\overline{U}_y/U_\infty \approx 0.5\%$ and $\Delta\overline{U}_z/U_\infty \approx 0.4\%$. Figure 4.22 also illustrates the effect of the probe orientation on the error and demonstrates that the largest error occurred at large flow angles.

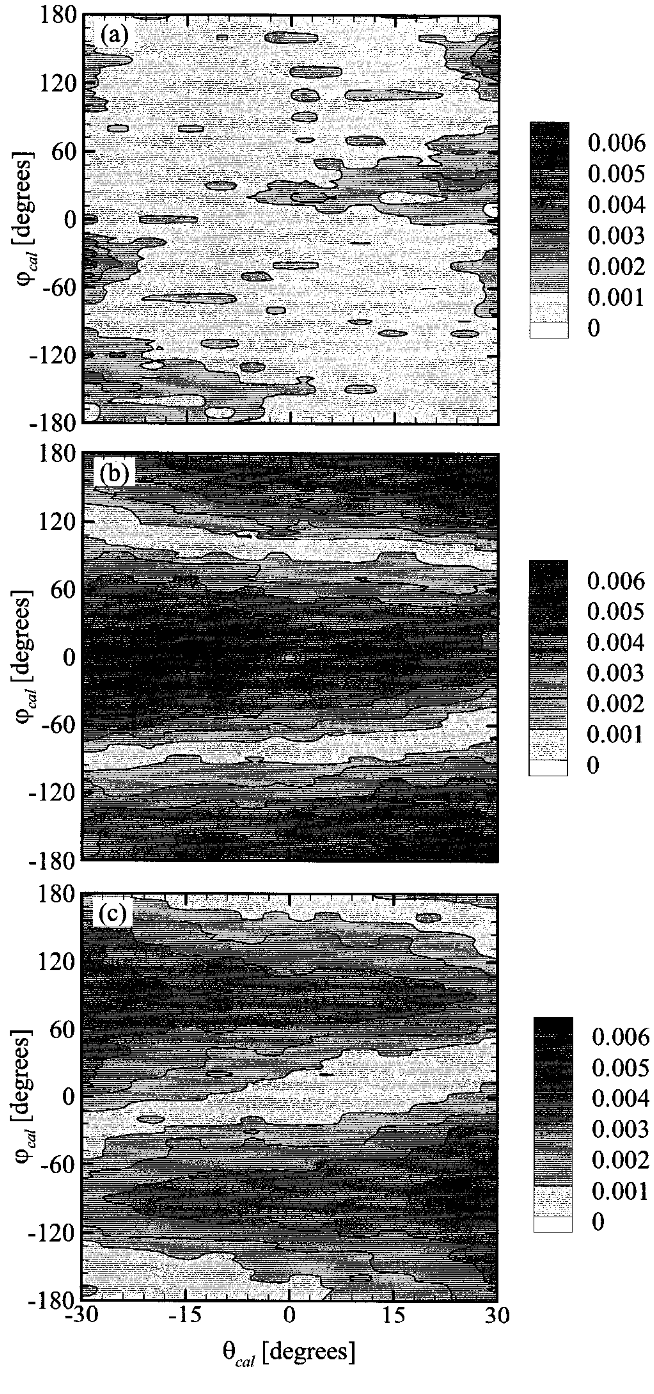

Figure 4.22: Contour maps illustrating the difference between the calibrator nozzle velocity and the velocity output from the data reduction procedure. Isocontours show (a) $\Delta\overline{U}_x/U_\infty$, (b) $\Delta\overline{U}_y/U_\infty$ and (c) $\Delta\overline{U}_z/U_\infty$.

The streamwise position uncertainty was $\Delta X/c \approx 3\%$. The uncertainty in relative spatial position within a measurement plane due to the finite size of the probe was $\Delta Y/c \approx \Delta Z/c \approx 0.3\%$. The uncertainty in absolute spatial position (referenced to the wing), caused by reinsertions of the probe in the wind tunnel, was $\Delta Y_w/c \approx \Delta Z_w/c \approx \Delta Y/c \approx \Delta Z/c \approx 1\%$ (see the Nomenclature for symbol definitions). Uncertainty in probe separation S due to the pitch of the lead screw on the probe holder was $\Delta S \approx \pm 0.05\,\mathrm{mm}$.

4.5.1 Spatial resolution of four-sensor probe

The finite measurement volume of the four-sensor probe could result in errors when measuring small-scale turbulent fluctuations. Using values of the integral, Taylor and Kolmogorov length scales (L_x, λ_x and η, respectively) calculated in Section 5.2, one can estimate the ratios of these scales and the transverse length l_{mv} of one side of the measurement volume as $30 < L_x/l_{mv} < 70$, $6 < \lambda_x/l_{mv} < 14$ and $0.2 < \eta/l_{mv} < 0.5$.

A comparison of the measurement volume dimensions to the integral length scale indicates that the spatial resolution of the probe is more than sufficient for the measurement of the large-scale motions. Bruun (1995) provides an estimate of the difference between the actual streamwise normal stress $\overline{u^2_{x\mathrm{act}}}$ and the value $\overline{u^2_{x\mathrm{meas}}}$ measured by a sensor with length l_{mv} normal to the streamwise direction normal stress as

$$\overline{u^2_{x\mathrm{act}}} = \overline{u^2_{x\mathrm{meas}}} \left(1 - \frac{l^2_{mv}}{12\lambda^2_x}\right)^{-1} \tag{4.12}$$

For $6 < \lambda_x/l_{mv} < 14$, this expression predicts that the Reynolds stress value would be overestimated by between 0.3% and 2%. Concerning the temporal resolution of hot-wire sensors, Bruun (Figure 2.28, Bruun (1995)) notes that, for a single sensor normal to the flow with a length in the range, $0.2 < \eta/l_{mv} < 0.5$ the spectral response of the probe would be attenuated by more than 10% only for frequencies higher than 40 kHz, which is higher that the sampling rates used in this study.

The previous estimates apply to single-sensor probes normal to the flow, whereas the present multi-sensor probe design would require much more complicated error estimate procedures. Bruun notes that the spectral attenuation for cross-wire probes is nearly identical to that of the single-sensor probe. Lekakis (1996) observed that, for cross-wire probes, large spacing between sensors can result in over-estimation of the transverse velocity component and an underestimation of the streamwise velocity component and recommend a ratio of η/l_{mv} within the range 0.33 to 0.5. Moreover, Wyngaard (1969) analyzed the vorticity output from a Kovasznay probe (which is different from the Kovasznay-type probe used in the present study) and found that, to limit the attenuation of the vorticity spectra to 90%, one should have $\eta/l_{mv} > 0.45$ (Wyngaard (1969) uses the length of the sensing wire for this ratio, which here has been approximated as $\sqrt{2}l_{mv}$). Wallace and Foss (1995) note that the model spectrum used in Wyngaard's analysis did not accurately represent an actual turbulent spectrum and recommended that η/l_{mv} should not be less than 0.25 to 0.5 for accurate measurement of vorticity. This range has also been cited by Lekakis (1996) for accurate measurement of velocity gradients.

It therefore appears that the range $0.2 < \eta/l_{mv} < 0.5$ used in the present study is close to the ranges identified for accurate measurement of turbulent flows. Although there could be some residual error introduced in the cases with small η, it has not been possible to quantify it or devise a correction method.

4.6 Probe interference

A concern when using hot-wire probes is the possibility of flow distortion. Using flow visualization, Devenport et al. (1996) found that a four-wire probe with dimensions nearly identical to those used in this study did not cause measurable disturbances within the vortex core. The presently measured intensity of the streamwise velocity fluctuations in the vortex core (Figure 4.23a) was much lower than that in Devenport et al.' s study at the same streamwise position and wing angle of attack but at different Re_c and aspect ratio (Figure 4.23c); this implies that probe-induced disturbances would be negligible in the present case as well. The issue of possible probe disturbances was also addressed early in this study, when measurements were taken with a larger four-wire probe, having a measurement volume with dimensions $2.8\,\mathrm{mm}\times 2.8\,\mathrm{mm}\times 1.4\,\mathrm{mm}$. Representative results with this probe, presented in Figure 4.23b, show significantly stronger velocity fluctuations at the centre of the vortex than those measured with the smaller probe. It is believed that the stronger velocity fluctuations with the larger probe are due to disturbances caused by the introduction of the larger probe into the flow. As will be shown later in this report, the velocity fluctuations at the centre of the vortex in Figure 4.23a can be attributed to vortex wandering and are therefore unlikely to be caused by probe disturbances.

Probe interference was of even greater concern for the two-probe measurements. To determine whether or not addition of a second probe would have an adverse effect on the measurements with the first probe, measurements of the vortex without turbulence were performed in a yz plane 1.6 m from the wing trailing edge, both with and without the second probe in place. No significant difference was observed when comparing the statistics

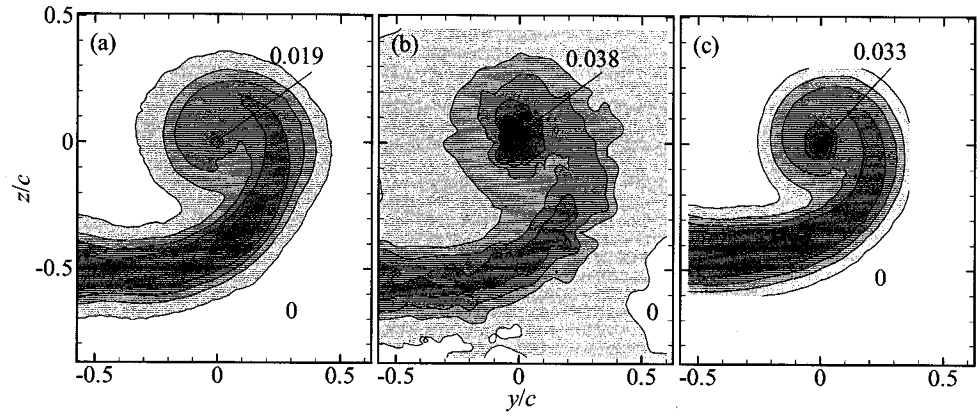

Figure 4.23: Isocontours of the standard deviation of the streamwise velocity u'_x/U_∞, $10c$ from wing leading edge (a) measured by a four-wire probe with sensing dimensions 0.68 mm × 0.68 mm× 0.46 mm (b) measured by a four-wire probe with sensing dimensions 2.8 mm × 2.8 mm× 1.4 mm (c) results of Devenport et al. (1996). Contour lines are spaced 0.004 apart.

measured by probe 1 with and without probe 2 present.

Changing the separation of the two probes appeared to have a measurable effect. When examining the results from measurements with probe 1 fixed in space and probe 2 at varying separations, some variation in the average flow angle was observed in probe 1. This variation was typically less than 3° and is not believed to have a significant effect on the results. It is unclear as to whether this flow angle variation was caused by changing disturbance of the flow around the probe holder or was caused by minor changes in the orientation of probe 1 occurring during the process of changing the probe separation.

4.7 Probe vibrations

During experiments performed with the two-probe holder shown in Figure 4.4, it was discovered that the probes were vibrating at a frequency of 30 Hz, excited by the fan motor. This vibration was only observed when the two-probe holder was used and it is attributed to the mass at the probe end of the probe holder. Moreover, the vibration was only observed in velocity signals when the wind-tunnel motor was running decoupled from the fan (i.e., the fan was not turning) and at free-stream velocities lower than approximately $2\,\mathrm{m/s}$, for which the velocity signal was very weak. In power spectra calculated for measurement cases without grid turbulence, this vibration appeared as a spike in the spectra at $30\,\mathrm{Hz}$.

Chapter 5

Experimental results

5.1 Experimental conditions

A sketch of the experimental setup is shown in Figure 5.1. It illustrates the coordinate systems used, nomenclature and some of the important dimensions used in the experiments. A wing-based, fixed Cartesian coordinate system X, Y, Z was defined such that its origin coincided with the quarter-chord point of the wing at the tip. Then, the downstream location of each measurement plane was specified by X. Moreover, a Cartesian/cylindrical coordinate system was defined on each measurement plane such that the orientations of the three Cartesian axes, x, y, z remained the same for all planes but the origin of the coordinate system was adjusted to coincide with the local time-averaged centre of the vortex. The Cartesian axes in these planes were rotated slightly so that the x axis was coincident with the axis of the vortex (see Section 4.4.3). When two probes were used in the experiments, the probe separation, S, was parallel to the Y-axis with both measurement volumes located at the same X.

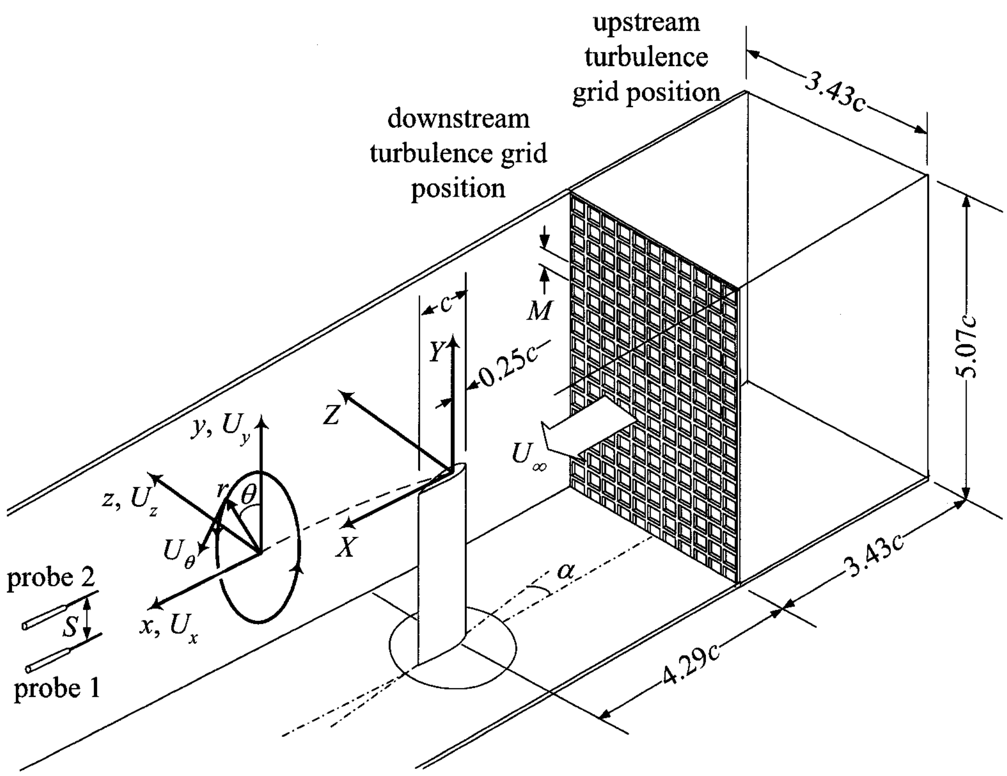

Figure 5.1: Sketch of the experimental arrangement illustrating the coordinate system.

The two turbulence grids (small grid, $M = 25.4\,\mathrm{mm}$, and large grid, $M = 50.8\,\mathrm{mm}$) could be inserted in slots at two different streamwise positions. The majority of the measurements were performed with the grid located at $X = -0.76\,\mathrm{m}$. Measurements performed with the turbulence grid in this position will be simply referred to as either *large-grid* or *small-grid* test cases, depending on which grid was being used. In addition, some experiments were performed with the turbulence grid at $X = -1.37\,\mathrm{m}$. Experiments with the grid in this position will be identified as either *small-grid-upstream* or *large-grid-upstream,* test cases depending on which grid was used. An additional reference case was also studied with no turbulence grid in place. This case will be identified as the *no-grid* case.

A large number of measurements were performed over an almost five-year period. Experimental conditions were adjusted over time to meet different requirements and based on cumulative experience. For this reason, the experimental conditions are described separately for each set of experiments, as follows.

5.1.1 Oil film flow visualization

In a preliminary stage of the wind-tunnel investigation, oil film flow visualization was used to investigate qualitatively the vortex formation process at a wing angle of attack $\alpha = 8^\circ$ and a free-stream velocity $U_\infty = 20\,\mathrm{m/s}$, corresponding to $\mathrm{Re}_c = U_\infty c/\nu = 2.4\times 10^5$. Two cases were investigated, the no-grid case and the large-grid case.

5.1.2 Single-sensor hot-wire measurements

To provide further qualitative information and to help interpret the oil film flow visualization, single-sensor hot-wire measurements were performed in the wind tunnel at an angle of attack $\alpha = 8°$ and a free-stream velocity $U_\infty = 20\,\mathrm{m/s}$, corresponding to $\mathrm{Re}_c = 2.4 \times 10^5$. Two cases were investigated, the no-grid case and the large-grid case. Measurements were performed on transverse planes with $X/c = 0.0$, 0.25, 0.40, 0.55, 0.65 and 0.75.

Additional measurements were performed at the same free-stream conditions to examine the wing boundary layer and to identify any possible flow separation. For the boundary layer measurements, single-sensor hot-wire measurements were performed in traverses parallel to the Z-axis from less than 1 mm from the wing surface into the free-stream. These boundary layer measurements were performed at streamwise locations at $X/c = 0.55$ for three spanwise stations, $Y/b = -0.25$, -0.50 and -0.75.

For all single-sensor hot-wire measurements, the sensing wire of the single-sensor probe was aligned such that it was parallel with the span of the wing (i.e., parallel to the Y axis). The anemometer was operated at an overheat ratio of 1.8. The frequency response of the probe was 10 kHz and the signal was low-pass filtered at a 3-dB cutoff frequency of 5 kHz. The analogue output of the anemometer was digitized at a rate of 10 kHz. A time history of 15 s duration was recorded at each measurement location.

5.1.3 Dye injection flow visualization

To further investigate qualitative, three-dimensional aspects of the vortex formation, dye injection flow visualization was performed in the water tunnel at $\alpha = 5°$ and $U_\infty = 0.16\,\mathrm{m/s}$, corresponding to $\mathrm{Re}_c = 2.9 \times 10^4$. Three different free-stream conditions were studied: the no-grid, small-grid and large-grid cases. In view of differences in wing aspect ratio and Reynolds number between the water tunnel and wind tunnel experiments, the water tunnel results were used only for qualitative purposes, to assist in understanding of the vortex formation process.

5.1.4 Wing surface pressure measurements

To provide quantitative information about the wing loading at each of the free-stream conditions, surface pressure measurements were performed in the wind tunnel at $\alpha = 5°$ and $U_\infty = 20\,\mathrm{m/s}$, corresponding to $\mathrm{Re}_c = 2.4 \times 10^5$. The effective angle of attack, estimated using the general downwash blockage correction of Rae and Pope (1984), was $5.6°$. These measurements were performed for the no-grid, small-grid and large-grid cases. For each case, the pressure transducer signal was sampled at a rate of 400 Hz over 30 s. A separate measurement was performed for each pressure tap.

5.1.5 Four-sensor hot-wire measurements

To investigate the streamwise development of the vortex and spiral wake, four-sensor hot-wire measurements were performed to measure the velocity vector on transverse measuring planes with $X/c = 0.75$, 1.75, 3.75, 5.75, 7.75 and 9.75, for the no-grid, small-grid, small-grid-upstream, large-grid and large-grid-upstream cases. In all cases, $\alpha = 5°$ and $U_\infty = 20\,\mathrm{m/s}$, corresponding to $\mathrm{Re}_c = 2.4 \times 10^5$. The effective angle of attack was estimated to be $5.6°$. All sensors were operated at an overheat ratio of 1.4 and an output signal gain of 3. The probe frequency response of the senors was determined to be uniform up to at least 40 kHz and the analogue signals were low-pass filtered at a 3dB cutoff frequency of 8.2 kHz. The analogue outputs of the anemometer were digitized simultaneously at a rate of 20 kHz with 15 s long records acquired at each measurement location.

Additional measurements were performed to further investigate the vortex core. These measurements were performed with a high density of measurement points near the time-averaged vortex centre. Conditions were identical to those described previously, with the exceptions that measurements were only performed at $X/c = 9.75$ for the no-grid, small-grid and large-grid cases and sample record lengths were increased to 60 s.

5.1.6 Dual four-sensor hot-wire measurements

To provide information about the instantaneous spatial properties of the vortex, measurements were performed using two four-wire probes simultaneously, providing two-point, three-component velocity data. Measurements were performed in the wind tunnel at $\alpha = 5°$ and $U_\infty = 20\,\mathrm{m/s}$, corresponding to $\mathrm{Re}_c = 2.4 \times 10^5$. measurements were recorded for streamwise measurement planes with $X/c = 3.75$, 5.75, 7.75 and 9.75 for the no-grid, small-grid, and large-grid cases. The effective angle of attack was estimated to be 5.6°. The anemometers were operated at an overheat ratio of 1.4 and an output signal gain of 6. The probe frequency responses were determined to be at least 40 kHz and the analogue signals were low-pass filtered at 14.0 kHz.

Each measurement was performed in two phases. In the first phase, the two probes were separated in the y-direction by $S = 7.1\,\mathrm{mm}$ and measurements were performed on each measurement plane with higher density near the time-averaged vortex centre. The analogue outputs of the eight anemometers were digitized simultaneously at a rate of 30 kHz with 15 s long records acquired at each measurement location. Following these measurements, probe 1 was positioned at the time averaged vortex centre and probe 2 was traversed away from probe 1 and measurements were performed in the range $7.1\,\mathrm{mm} \leq S \leq 27.6\,\mathrm{mm}$ at

0.5 mm increments. The analogue outputs of the anemometers were digitized at a rate of 30 kHz with 180 s long records acquired at each measurement location.

5.2 Grid turbulence characteristics

To characterize the free-stream conditions generated by each grid, three-component velocity measurements of the grid turbulence were performed with four-sensor probe 1 at $\mathrm{Re}_c = 2.4 \times 10^5$ with the wing removed from the wind tunnel. Velocity measurements were taken along the centreline of the wind tunnel at streamwise locations between $X/c = -2.25$ and $X/c = 12.75$ at intervals of $1c$ for the small-grid-upstream, small-grid, large-grid-upstream and large-grid cases.

Previous researchers have observed that the turbulent kinetic energy

$$k = \frac{1}{2}\left(\overline{u_x^2} + \overline{u_y^2} + \overline{u_z^2}\right) \tag{5.1}$$

of grid turbulence decays as a power law according to

$$\frac{k}{U_o^2} = A\left(\frac{x_g - x_{go}}{M}\right)^{-n} \tag{5.2}$$

where A and n are constants, x_g is the streamwise distance from the grid and x_{go} is a "virtual origin" of the turbulence (Pope (2000)). Figure 5.2 shows the turbulent kinetic energy measured for each of the grid cases plotted as a function of $x_g - x_{go}$ normalized by M and using $x_{go}/M = 3$. With this x_{go} value, the turbulence kinetic energy for all cases was found to be described well by Equation 5.2, using $n = 1.32$ and $A = 0.153$. This value for n is within the range of previous experimental values $1.15 < n < 1.45$ cited by Pope (2000). Thus, the grid turbulence in the current measurements appears to

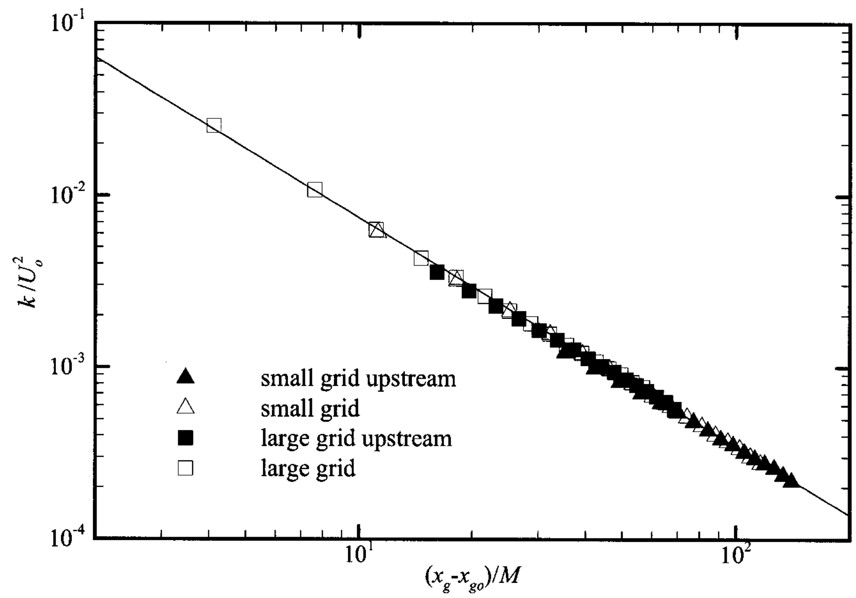

Figure 5.2: Streamwise development of turbulent kinetic energy measured downstream of the present grids with the wing removed from the wind tunnel. Solid line indicates power law fit using Equation 5.2.

be consistent with previous grid turbulence measurements, which represent approximately isotropic turbulence.

The streamwise decay of the normal Reynolds stresses $\overline{u_x^2}/U_o^2$, $\overline{u_y^2}/U_o^2$ and $\overline{u_z^2}/U_o^2$ is presented in Figure 5.3a-c, respectively, as a function of $(x_g - x_{go})/M$. The stresses were found to collapse for the four different cases with the decay well represented by a power law, shown in Figure 5.3 as a solid line. Each normal stress was found to decay $\propto (x_g - x_{go})^{-n}$ with $n = 1.33$ for $\overline{u_x^2}/U_o^2$, $n = 1.31$ for $\overline{u_y^2}/U_o^2$ and $n = 1.35$ for $\overline{u_z^2}/U_o^2$. The observed small differences among the decay exponents of the three normal Reynolds stresses could be systematic in grid turbulence, as similar differences have been observed by Warhaft and Lumley (1978); they could be, at least partially, attributed to the effective contraction along the wind-tunnel test section caused by boundary layer growth and to the differences in the boundary layers along the horizontal and vertical walls because of the differences between the height and the width of the wind tunnel test section.

The streamwise decay of the normal Reynolds stresses in Cartesian coordinates is illustrated in Figures 5.4a-d. Comparison of the different cases indicates that the magnitude of normal stresses in the region of interest ($X/c > 1.75$) was lowest for the small-grid-upstream case and increased, in sequence, for the small-grid case, large-grid-upstream case and large-grid case. For all cases, the streamwise normal stress $\overline{u_x^2}/U_o^2$ was found to be approximately 20% higher than both transverse Reynolds stresses $\overline{u_y^2}/U_o^2$ and $\overline{u_z^2}/U_o^2$. This is a well known result for grid turbulence. Comte-Bellot and Corrsin (1966) used a second test section contraction downstream of the grid to improve the degree of isotropy of the turbulence. In the current results, $\overline{u_y^2}/U_o^2$ was found to be slightly larger than $\overline{u_z^2}/U_o^2$. At $X/c = 12.75$, $\overline{u_y^2}/U_o^2$ was approximately 10% larger than $\overline{u_z^2}/U_o^2$. As discussed above, this anisotropy could be explained by the geometry of the wind tunnel due to the differences in the width and height of the test section.

The anisotropy of the grid turbulence was investigated further by examining the components of the anisotropy tensor (Pope (2000))

$$a_{ij} = \frac{\overline{u_i u_j}}{\overline{u_k u_k}} - \frac{1}{3}\delta_{ij} \; , \tag{5.3}$$

where δ_{ij} is the Kronecker delta and the indices take values 1, 2 and 3, which correspond to the axes x, y and z. By definition, all components of this tensor would be zero in perfectly isotropic turbulence, whereas the sum a_{ii} of the three diagonal components should vanish under all circumstances.

The diagonal components of a_{ij} are shown in Figure 5.5a-c. Values of a_{xx} are

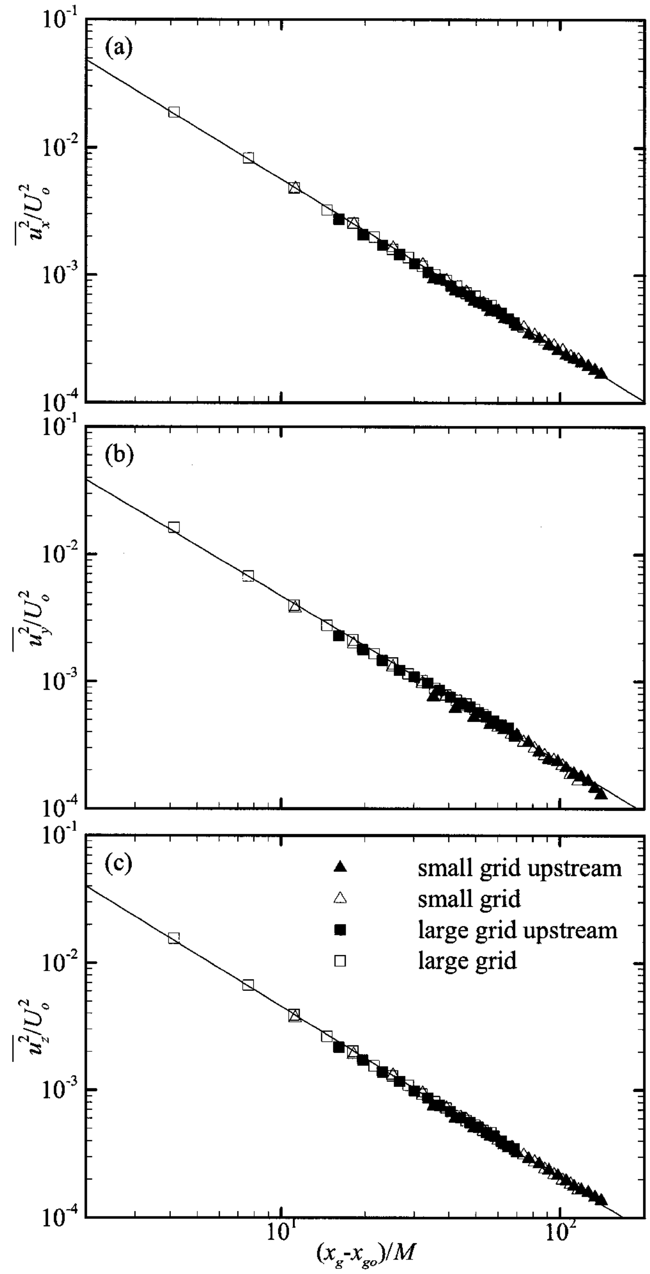

Figure 5.3: Streamwise development of measured Reynolds normal stresses (a) $\overline{u_x^2}$,(b) $\overline{u_y^2}$ and (c) $\overline{u_z^2}$ measured as a function of $(x_g - x_{go})/M$.

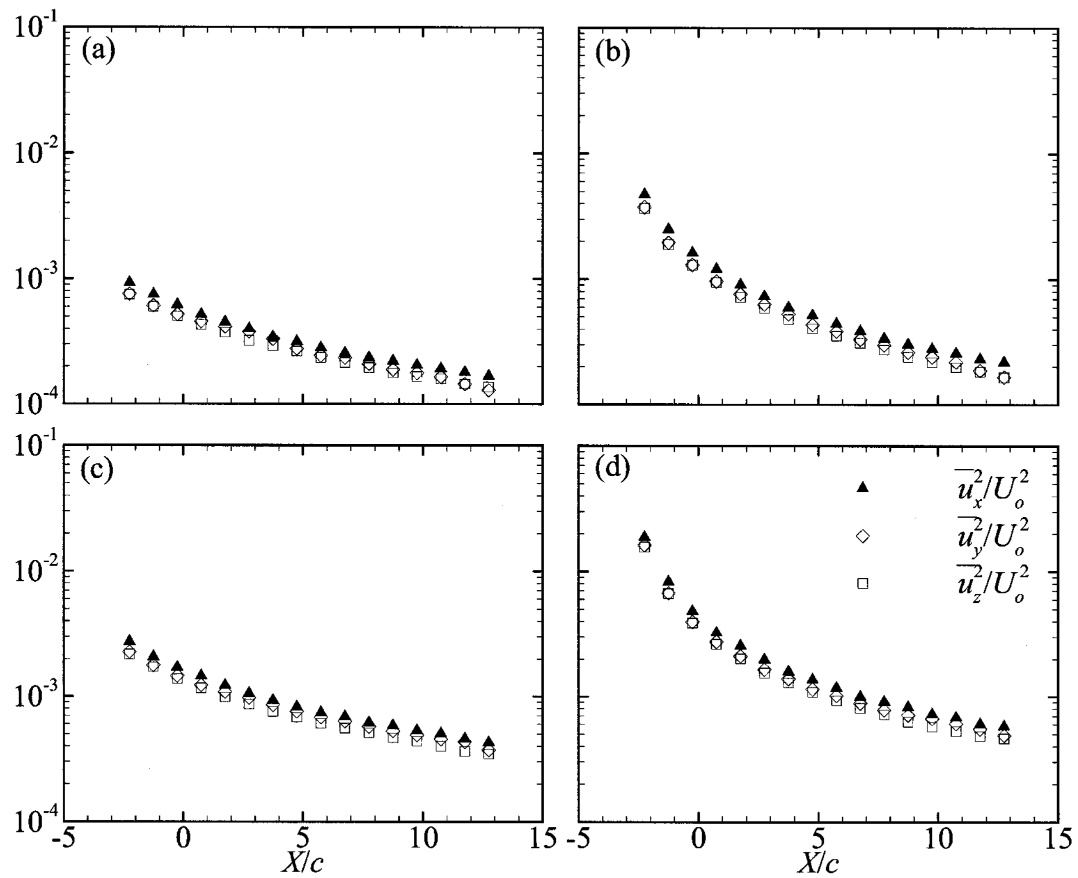

Figure 5.4: Streamwise development of measured Reynolds normal stresses $\overline{u_x^2}$, $\overline{u_y^2}$ and $\overline{u_z^2}$ measured for (a) small-grid-upstream, (b) small-grid, (c) large-grid-upstream and (d) large-grid cases.

shown in Figure 5.5a and are near 0.05 for all cases, reiterating the observations from Figure 5.4 that $\overline{u_x^2}$ has a higher contribution to k than $\overline{u_y^2}$ and $\overline{u_z^2}$. Figure 5.5c, showing the streamwise variation of a_{zz}, indicates that $\overline{u_z^2}$ makes a somewhat lesser contribution to k than $\overline{u_y^2}$, which, as discussed above, is most likely due to differences in the height and width of the wind-tunnel test section. One observation that can be made from Figure 5.5a-c is that the values of a_{xx}, a_{yy} and a_{zz} are comparable for all grid cases over the entire range of X/c measured. This consistency confirms the self-similarity of the turbulence structures in all cases considered.

The anisotropy tensor can also be used to quantify the deviation of the Reynolds shear stresses from the isotropic value of zero. The components of the anisotropy tensor corresponding to $\overline{u_x u_y}$, $\overline{u_x u_z}$ and $\overline{u_y u_z}$ (a_{xy}, a_{xz} and a_{yz}) are shown in Figure 5.6a-c, respectively. These figures show that all cross-anisotropies were relatively small. The largest one in magnitude was a_{yz} (Figure 5.6c), which took values near 0.02, and appeared to increase slightly with streamwise distance. The non-zero value of a_{yz} suggests the existence of a weak correlation between u_y and u_z, which is possibly connected to the inequality of $\overline{u_y^2}$ and $\overline{u_z^2}$.

The magnitude of the turbulent length scales within the free-stream could play an important role in the interaction between the turbulence and the vortex. Three scales in particular were measured for each of the grid turbulence cases: a) the longitudinal integral length scale, which characterizes the size of the larger turbulent eddies, b) the longitudinal Taylor microscale, which has been associated with the spacing between regions with intense dissipation activity (Tennekes (1968)), although other researchers find that this scale

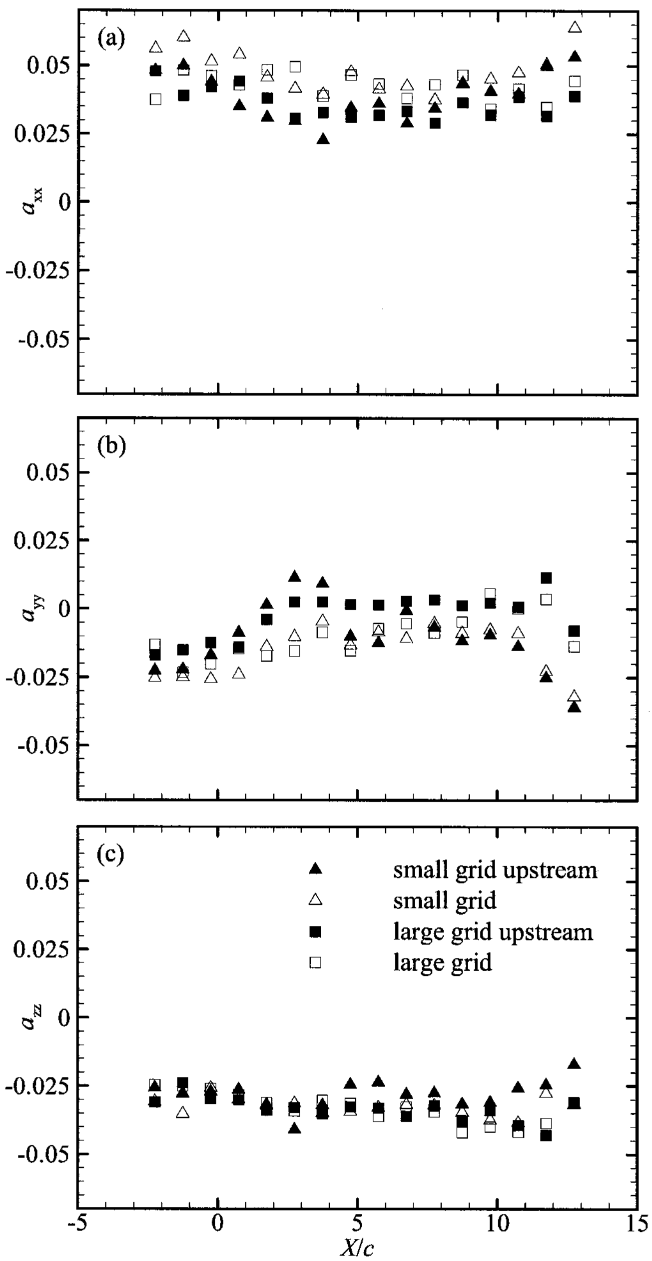

Figure 5.5: Diagonal components of the anisotropy tensor (a) a_{xx}, (b) a_{yy} and (c) a_{zz} as a function of streamwise distance, measured in the grid turbulence with the wing removed from the wind-tunnel.

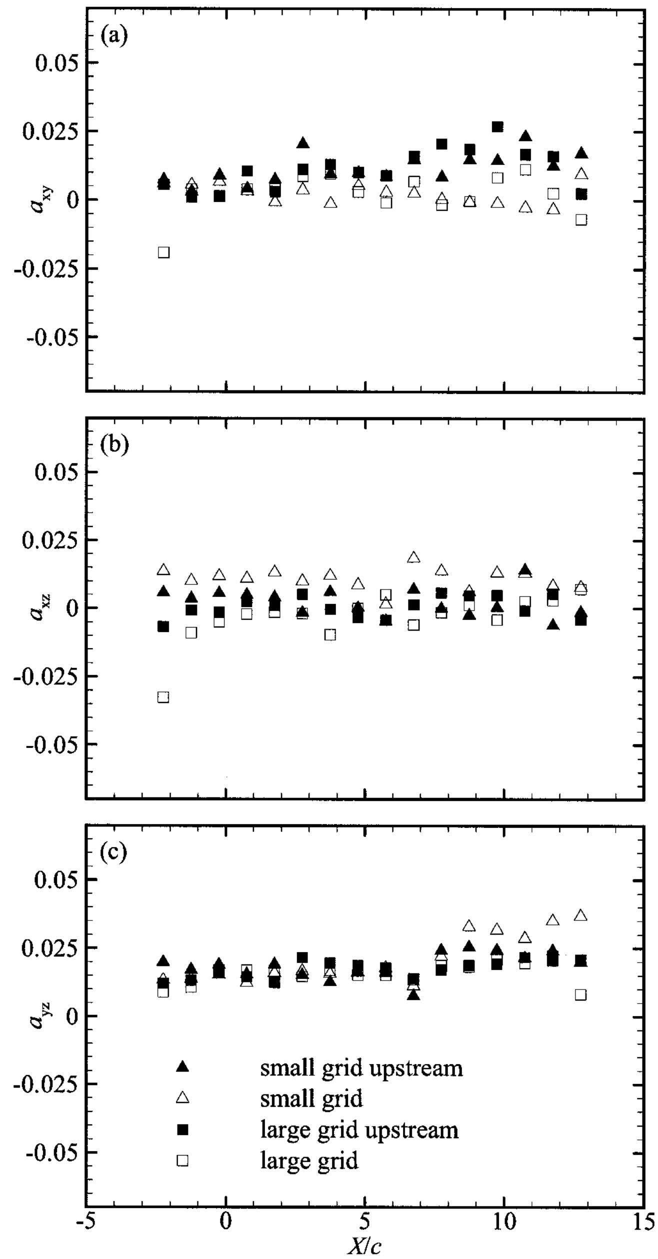

Figure 5.6: Streamwise development of anisotropy tensor components (a) a_{xy}, (b) a_{xz} and (c) a_{yz} measured in each of the grid turbulence cases without the wing in the wind tunnel.

has no clear physical significance (Pope (2000)) and c) the Kolmogorov microscale, which characterizes the smallest (dissipative) scales of turbulence.

The longitudinal integral length scale was determined as

$$L_x = \frac{\overline{U}_x}{u'_x u'_x} \int_0^{\tau_o} R_{xx}(\tau)\, \mathrm{d}\tau \tag{5.4}$$

where $u'_x = \overline{u_x^2}^{0.5}$ and $R_{xx}(\tau)$ is the temporal autocorrelation of the streamwise velocity component

$$R_{xx}(\tau) = \frac{1}{T} \int_0^{T} u_x(t)\, u_x(t-\tau)\, \mathrm{d}t, \tag{5.5}$$

T is the length of the time history and τ_o is the value of τ where the autocorrelation crosses zero for the first time (R_{xx} was calculated using the MATLAB function *xcorr*). The measured integral length scales are plotted in Figure 5.7 for all four grid cases normalized by M as a function of $(x_g - x_{go})/M$, where x_{go} is identical to the value used in Figure 5.2. This figure shows good collapse of the data for the cases with the same value of M, however when scaled in the manner shown in Figure 5.7, there is a clear difference between the results for the two small-grid cases and those of the two large-grid cases. This result suggests that the size of the integral length scale is not solely dependent on the grid mesh size but also depends on the turbulence Reynolds number (see below).

In all cases, the integral length scale increases with streamwise distance. Power law curve fits of the results (not shown in Figure 5.7 for clarity) indicate that L_x grows with streamwise distance at a rate $\propto (x_g - x_{go})^n$ where $n = 0.3$, 0.2, 0.2 and 0.3 for the small-grid-upstream, small-grid, large-grid-upstream and large-grid cases respectively. Comparatively, Tennekes and Lumley (1972) and Comte-Bellot and Corrsin (1971) note that L_x/M grows $\propto (x/M)^{0.5}$ and Sreenivasan et al. (1980) found that $L_x/M \propto (x/M)^{0.4}$.

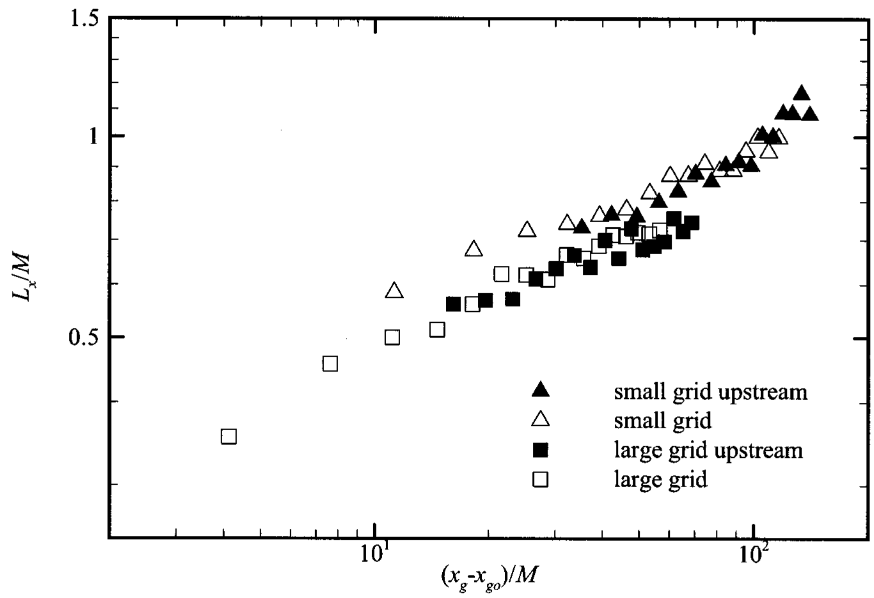

Figure 5.7: Streamwise development of L_x/M as a function of $(x_g - x_{go})$ normalized by M for each of the grid turbulence cases without the wing in the wind tunnel.

It is unclear why the growth rate of L_x is smaller in the current results. It is also worth noting that fitting the power law using x/M rather than $(x_g - x_{go})/M$ resulted in nearly identical values of n (0.34, 0.24, 0.22 and 0.31 when scaling by x/M instead of 0.33, 0.22, 0.20 and 0.26 when scaling by $(x_g - x_{go})/M$).

When plotted as a function of X/c, as in Figure 5.8, a slight increase in L_x is evident when the turbulence grid is in the upstream position. Due to data scatter, the increase in length scale is difficult to quantify.

The longitudinal Taylor microscale was determined with the use of Taylor's frozen flow approximation as

$$\lambda_x = \sqrt{2}\overline{U}_x \left(\frac{\overline{u_x^2}}{\overline{\left(\frac{\partial u_x}{\partial t}\right)^2}} \right)^{1/2} \tag{5.6}$$

where the instantaneous temporal derivative of the streamwise velocity was estimated from

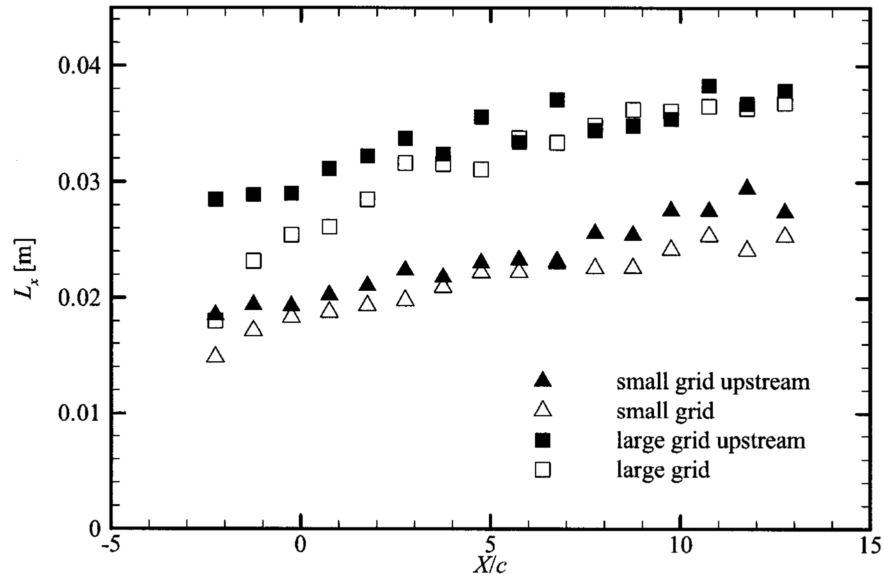

Figure 5.8: Streamwise development of L_x measured in each of the grid turbulence cases without the wing in the wind tunnel.

the velocity time series by using a third order backward finite difference scheme.

The longitudinal Taylor microscale, normalized by M is plotted against $(x_g - x_{go})/M$ in Figure 5.9. As with the integral length scale (Figure 5.7), the values do not collapse for the two different grids. As streamwise distance increases, λ_x increases following a power law as indicated by the curve fit shown in Figure 5.9. At small distance from the grid, $(x_g - x_{go})/M < 40$, the growth was not well represented by the power law fit, possibly indicating slower development of the self-similarity of the turbulence length scales when compared to the self-similarity of the velocity scales. For $(x_g - x_{go})/M > 40$, λ_x increases $\propto (x_g - x_{go})^{0.6}$ which is close to the growth rate measured by Sreenivasan et al. (1980) who found the Taylor microscale to grow $\propto (x_g - x_{go})^{0.5}$. The longitudinal Taylor microscale is plotted in Figure 5.10 as a function of X/c.

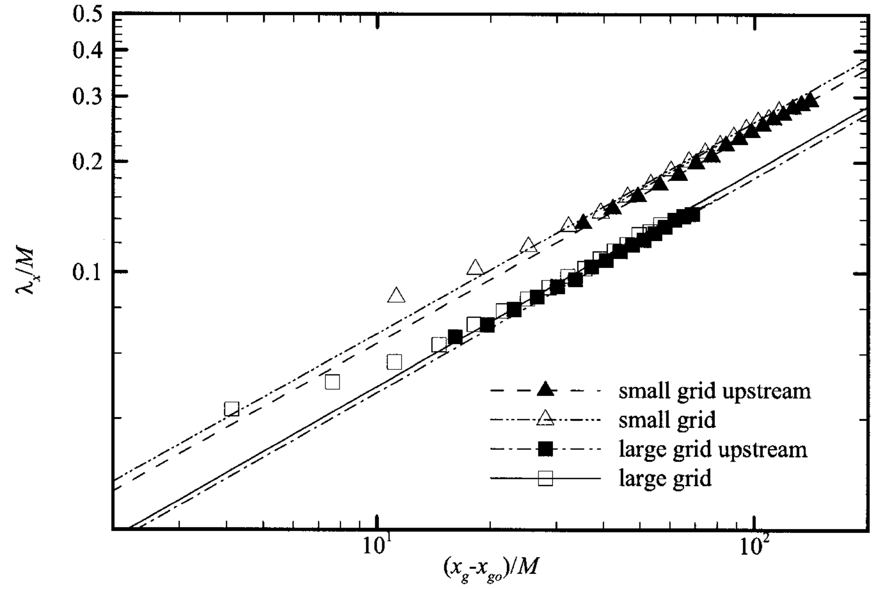

Figure 5.9: Development of λ_x measured for each of the grid turbulence cases as a function of $(x_g - x_{go})$ normalized by M. Solid line indicates power law curve fit of data.

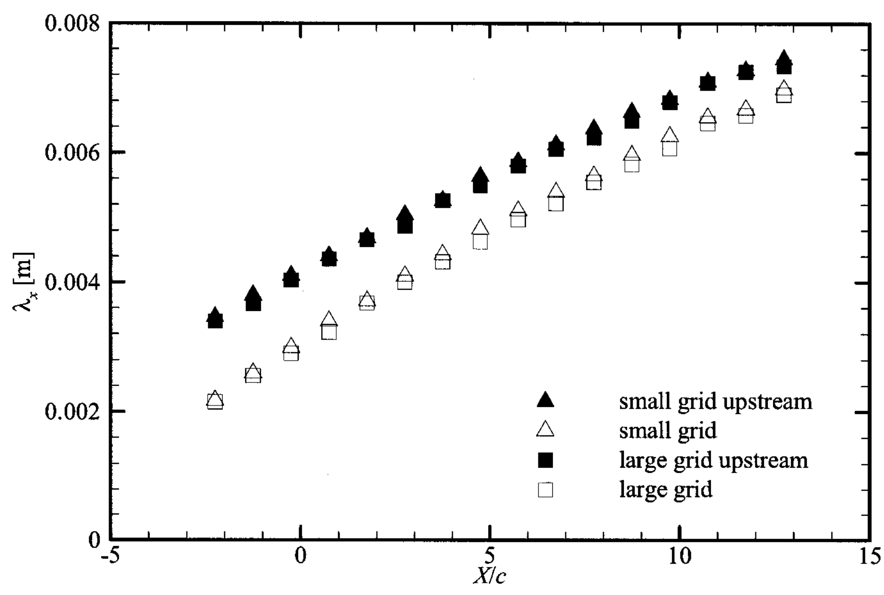

Figure 5.10: Streamwise development of λ_x measured for each of the grid turbulence cases without the wing in the wind tunnel.

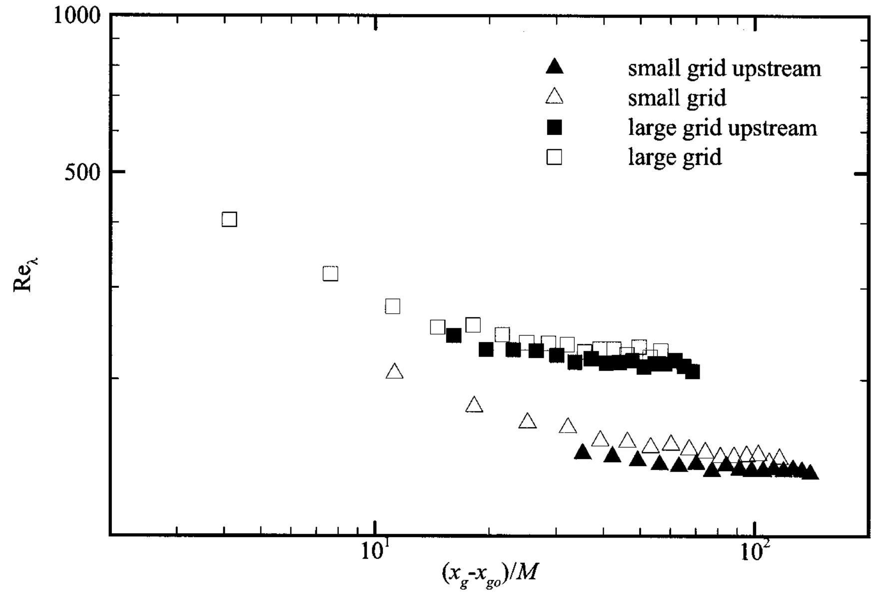

Figure 5.11: Streamwise development of Re_λ as a function of $(x_g - x_{go})/M$

The Taylor microscale is commonly used to define the turbulence Reynolds number

$$\mathrm{Re}_\lambda = \frac{u'_x \lambda_x}{\nu} , \tag{5.7}$$

where ν is the kinematic viscosity. The streamwise evolutions of the turbulence Reynolds number are shown in Figure 5.11 for all four grid cases as functions of $(x_g - x_{go})/M$. For the range $(x_g - x_{go})/M > 10$, $\mathrm{Re}_\lambda \approx 150$ for the small-grid-upstream and small-grid cases and $\mathrm{Re}_\lambda \approx 250$ for the large-grid-upstream and large-grid cases.

The kinetic energy dissipation rate in the grid turbulence was estimated using Taylor's frozen flow approximation and assuming local isotropy of the turbulence, as

$$\varepsilon = \frac{15\nu}{U_x^2}\overline{\left(\frac{\partial u_x}{\partial t}\right)^2} , \tag{5.8}$$

where Taylor's frozen flow hypothesis states that, for $\overline{u_x^2}^{0.5}/\overline{U}_x \ll 1$, $\frac{\partial}{\partial x} \approx -\frac{1}{\overline{U}_x}\frac{\partial}{\partial t}$ (Pope (2000)). The kinetic energy dissipation rate has been plotted in Figure 5.12 as a function

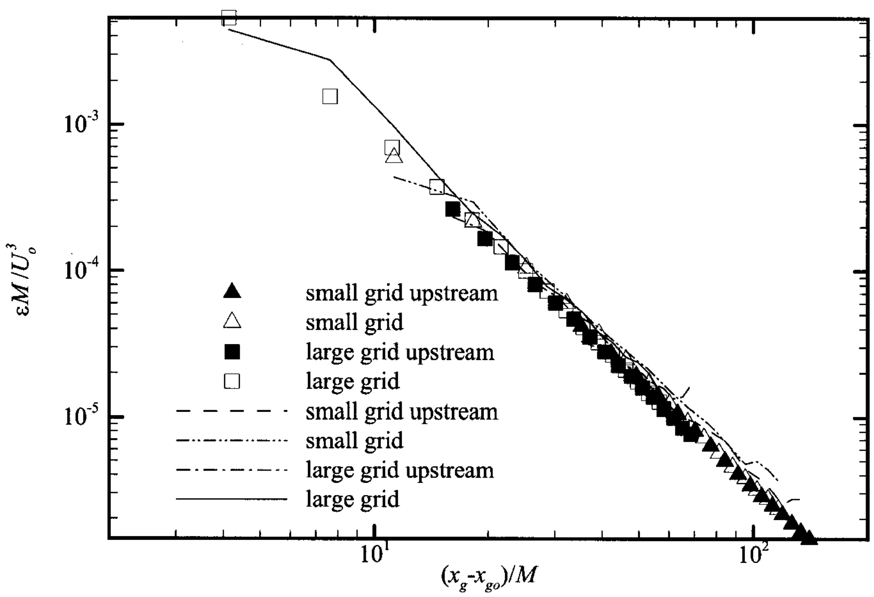

Figure 5.12: ε normalized using M and U_o as a function of $(x_g - x_{go})/M$ measured for all grid turbulence cases. Symbols, calculated using Equation 5.8. Lines, calculated using measured dk/dt.

of streamwise distance for all cases. It was found to decay rapidly for all cases, consistently with homogeneous isotropic turbulence theory. Values of ε calculated using the streamwise velocity gradient (Equation 5.8) in time, which are plotted as symbols in Figure 5.12, were found to be in good agreement with those calculated using dk/dt calculated from the Reynolds normal stresses, plotted as lines in Figure 5.12. Dissipation calculated using Equation 5.8 decays $\propto (x - x_o)^{-2.40}$ which, when compared to the fitted values of Equation 5.2 ($n = -1.32$), indicates a slight discrepancy between the two methods of calculation, possibly due to small errors introduced by fitting the data. Values of ε calculated using Equation 5.8 are plotted against X/c in Figure 5.13.

Using the previously determined values of dissipation rate, the Kolmogorov mi-

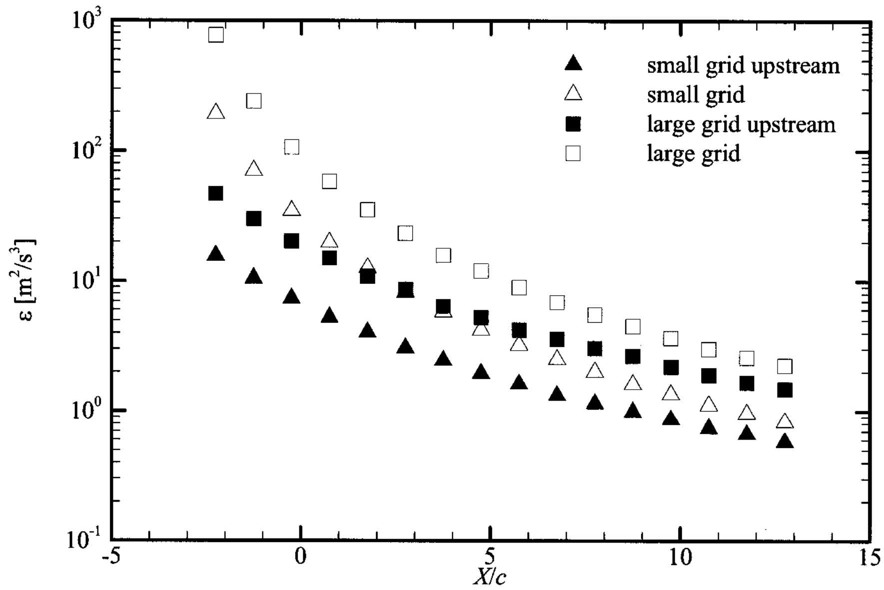

Figure 5.13: Streamwise development of ε measured in each of the grid turbulence cases without the wing in the wind tunnel.

croscale η, velocity scale u_η, and time scale τ_η were determined as (Pope (2000))

$$\eta \equiv \left(\frac{\nu^3}{\varepsilon}\right)^{1/4} \tag{5.9}$$

$$u_\eta \equiv (\nu\varepsilon)^{1/4} \tag{5.10}$$

$$\tau_\eta \equiv \left(\frac{\nu}{\varepsilon}\right)^{1/2} . \tag{5.11}$$

Difficulty in accurately determining dk/dt from the limited resolution of streamwise measurement points resulted in increased scatter in ε, hence the values of ε calculated using Equation 5.8 were used for calculation of the Kolmogorov scales.

The Kolmogorov scales have been plotted, normalized by U_o and M, as functions of $(x_g - x_{go})/M$ in Figure 5.14. Consistent with isotropic turbulence theory, η and τ_η were observed to increase with streamwise distance while u_η was observed to decrease as the turbulence decays and the kinetic energy of the smallest scales decreased. The Kolmogorov length scales, shown in Figure 5.14a, were found to be approximately 100 times smaller than the integral length scales for the small-grid and small-grid-upstream cases, whereas values of η determined for the higher Re_λ large-grid and large-grid upstream cases were approximately 300 times smaller than the integral length scales. Similar decreases with increased Re_λ were also observed for u_η and τ_η (Figures 5.14b and c, respectively).

The Kolmogorov scales have been plotted as functions of X/c in Figure 5.15. The Kolmogorov length scales were found to be approximately two orders of magnitude smaller than the integral length scales with the smallest scales observed for the large-grid case. Comparing the estimated Kolmogorov length scale to the prong spacing of the measurement probe, it can be observed that the prong spacing was approximately 2 to 5 times the Kolmogorov scale. The Kolmogorov velocity scale was found to be two orders of magnitude smaller than the free-stream velocity and the Kolmogorov time scale was found to be of the same order as the $1/f_c$, where f_c is the cutoff frequency of the analogue low-pass filter used during measurement.

The spectral distribution of turbulent kinetic energy in grid turbulence is commonly described by the wavenumber spectrum of U_x

$$E_{xx} = \frac{\overline{U}_x}{2\pi} F_{xx} \tag{5.12}$$

where

$$F_{xx}(f) = 4 \int_0^\infty R_{xx}(\tau) \cos(2\pi f \tau) \, \mathrm{d}\tau \tag{5.13}$$

is the frequency spectrum (calculated using the MATLAB function *pwelch*) and the wavenumber spectrum is plotted against the streamwise wavenumber $\kappa_x = 2\pi f / U_x$ (where f is frequency). The wavelength $1/\kappa_x$ is a measure of eddy size (Pope (2000)). Wavenumber

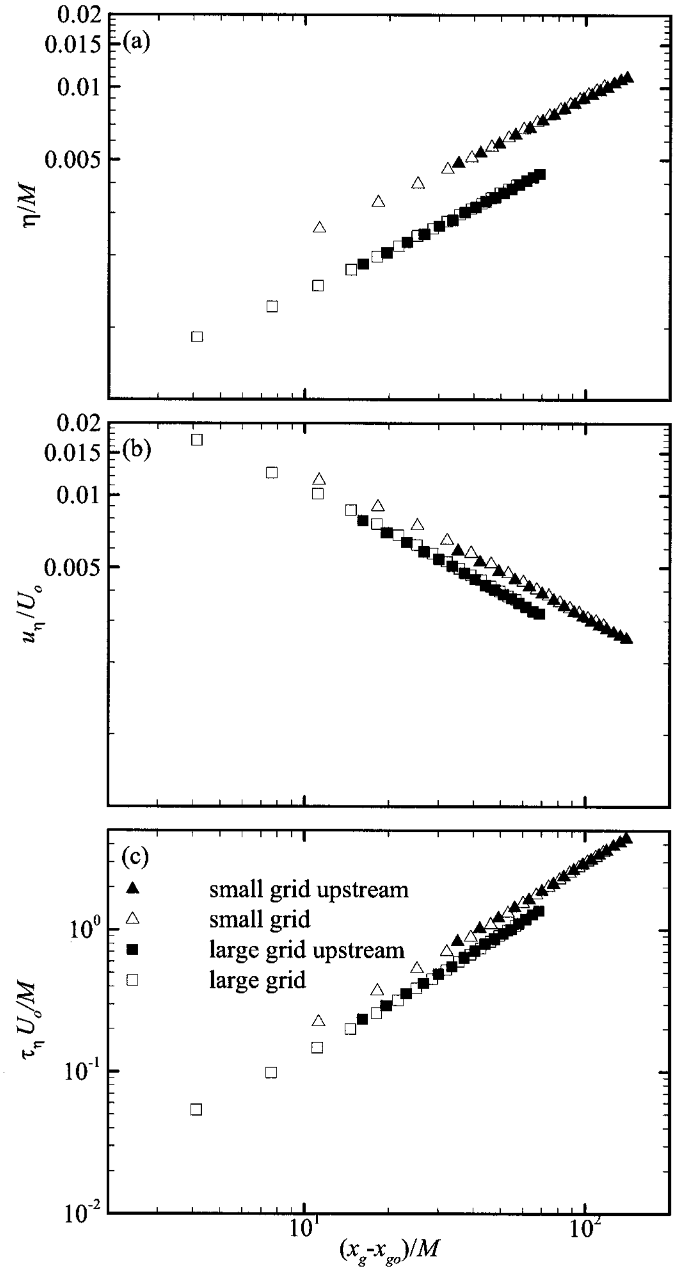

Figure 5.14: Streamwise development of (a) η, (b) u_η and (c) τ_η normalized by U_o and M and plotted against $(x_g - x_{go})/M$ as measured for each of the grid turbulence cases without the wing in the wind tunnel.

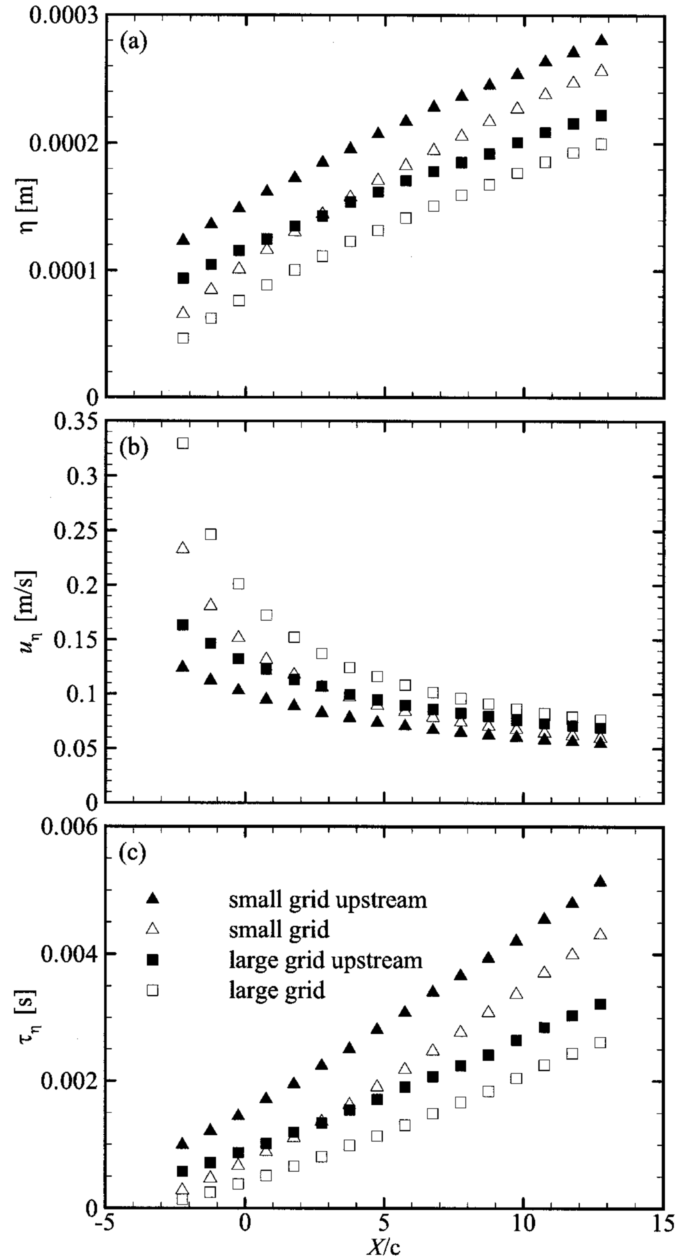

Figure 5.15: Streamwise development of (a) η, (b) u_η and (c) τ_η measured for each of the grid turbulence cases without the wing in the wind tunnel.

spectra $E_{xx}(\kappa_x)$ are shown in Figure 5.16 scaled by the Kolmogorov scales. In this figure, each successive streamwise location starting with $X/c = 1.75$ was shifted down by a decade to increase the visibility of the figure. According to Kolmogorov's hypothesis of universality of the fine structure of turbulence at large Reynolds numbers, spectra scaled in this manner should collapse at high wavenumbers. The present measurements seem to comply with this hypothesis.

At sufficiently high Reynolds number, three distinct wavenumber ranges can be identified in the one-dimensional energy spectra of isotropic turbulence (Pope (2000)):

- the energy containing range, characterized by relatively flat spectra; this is observed at relatively low wavenumbers
- the inertial subrange, characterized by a slope of $-5/3$ in logarithmic axes; this is observed at intermediate wavenumbers
- the viscous subrange, characterized by an increasing rate of decrease of $E_{xx}(\kappa_x)$ with increasing κ_x; this is observed at high wavenumbers

Physically, the energy containing range is described as the range of wavenumbers containing large-scale energetic eddies, the inertial subrange is a range of eddies associated with energy transfer from larger to smaller motions without any considerable loss of kinetic energy and the viscous subrange is associated with the dissipation of the kinetic energy at small scales due to viscosity. These three ranges are apparent in Figure 5.16 for all measurement locations, and they correspond to $\kappa_x\eta \lesssim 10^{-3}$, $10^{-3} \lesssim \kappa_x\eta \lesssim 10^{-1}$ and $\kappa_x\eta \gtrsim 10^{-1}$, respectively. A line of $-5/3$ slope has been drawn in Figure 5.16 to help

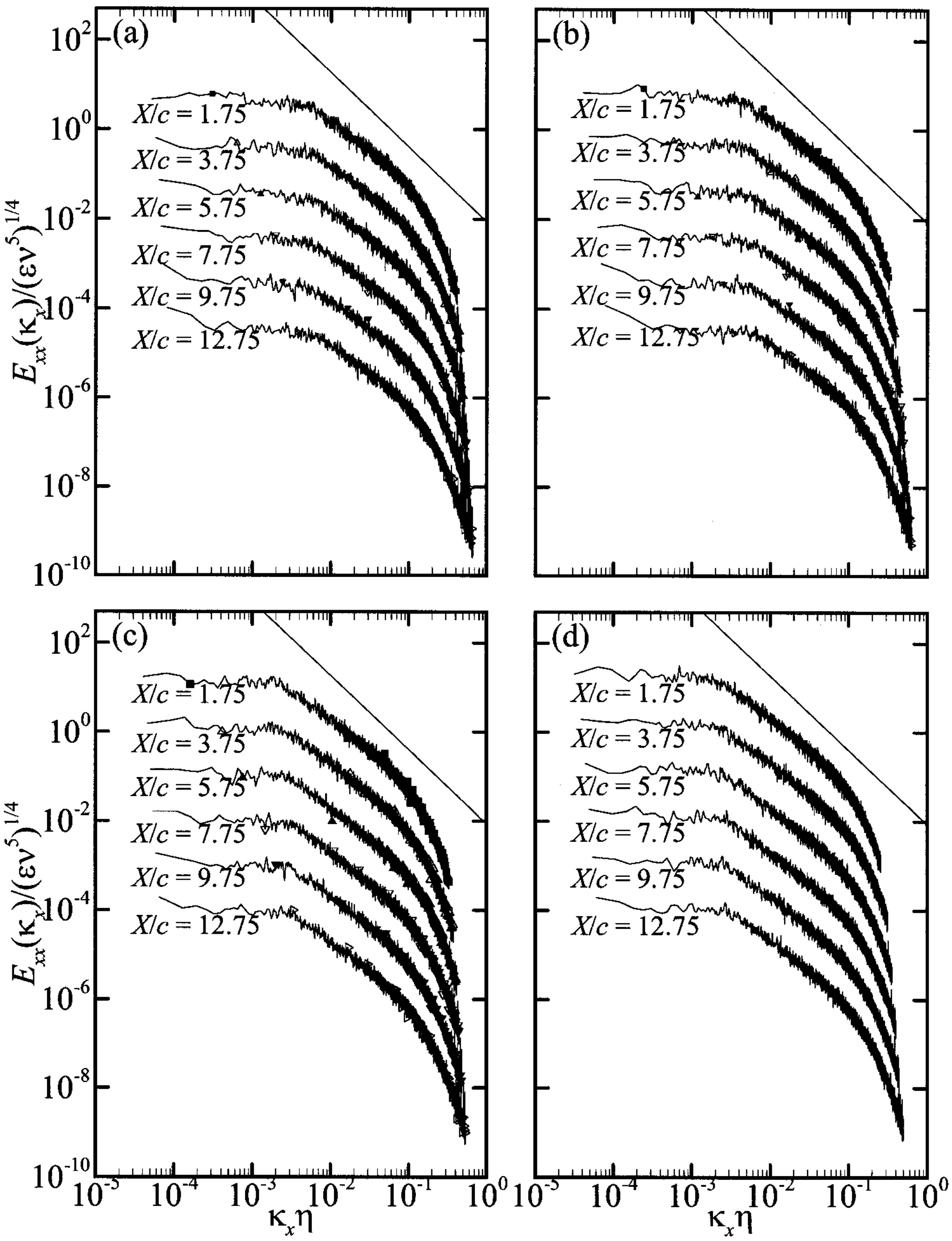

Figure 5.16: Power spectra as a function of wavenumber normalized by Kolmogorov scales for (a) small-grid-upstream, (b) small-grid, (c) large-grid-upstream and (d) large-grid cases. Each streamwise position downstream of $X/c = 1.75$ shifted down by one decade for clarity. Solid line indicates a -5/3 slope.

identify the inertial subrange. The slope of this range appears to be less than $-5/3$ for all results, which suggests that the turbulence Reynolds number Re_λ of the current experiments ($150 < \mathrm{Re}_\lambda < 250$, see Figure 5.11) is not sufficiently large for the $-5/3$ scaling to apply (Ferchichi and Tavoularis (2000)). The slope in the current experiments was found to be about -1.5, which is consistent with the value cited by Pope (2000) for $\mathrm{Re}_\lambda \approx 200$.

For comparison with data presented later in this chapter, the frequency spectra $F_{xx}(f)$, which show the energy distribution of the fluctuations as a function of frequency (inverse time scale), are presented in Figure 5.17a-d for the small-grid-upstream, small-grid, large-grid-upstream and large-grid cases, respectively. The spectra in Figure 5.17 clearly show the decay in energy with streamwise distance observed in Figure 5.2.

5.3 Single-sensor hot-wire measurements

To characterize the vortex formation process and identify possible effects of free-stream turbulence, single-sensor hot-wire measurements were performed at the wing tip and over the suction surface at $\alpha = 8°$ and $\mathrm{Re}_c = 2.4 \times 10^5$ for both the no-grid and large-grid cases. Single-sensor hot-wires with a sensor axis normal to the probe axis measure an effective cooling velocity U_{eff}, defined as the equivalent flow velocity parallel to the probe axis that would produce the same sensor cooling as the actual flow velocity.

To examine the wing boundary layer and to identify any possible flow separation, single-sensor hot-wire measurements were performed in traverses in the Z direction starting at a distance, Z_o and extending into the free-stream. The exact value of Z_o was not determined, as the measurements were conducted by first moving the probe as near to the

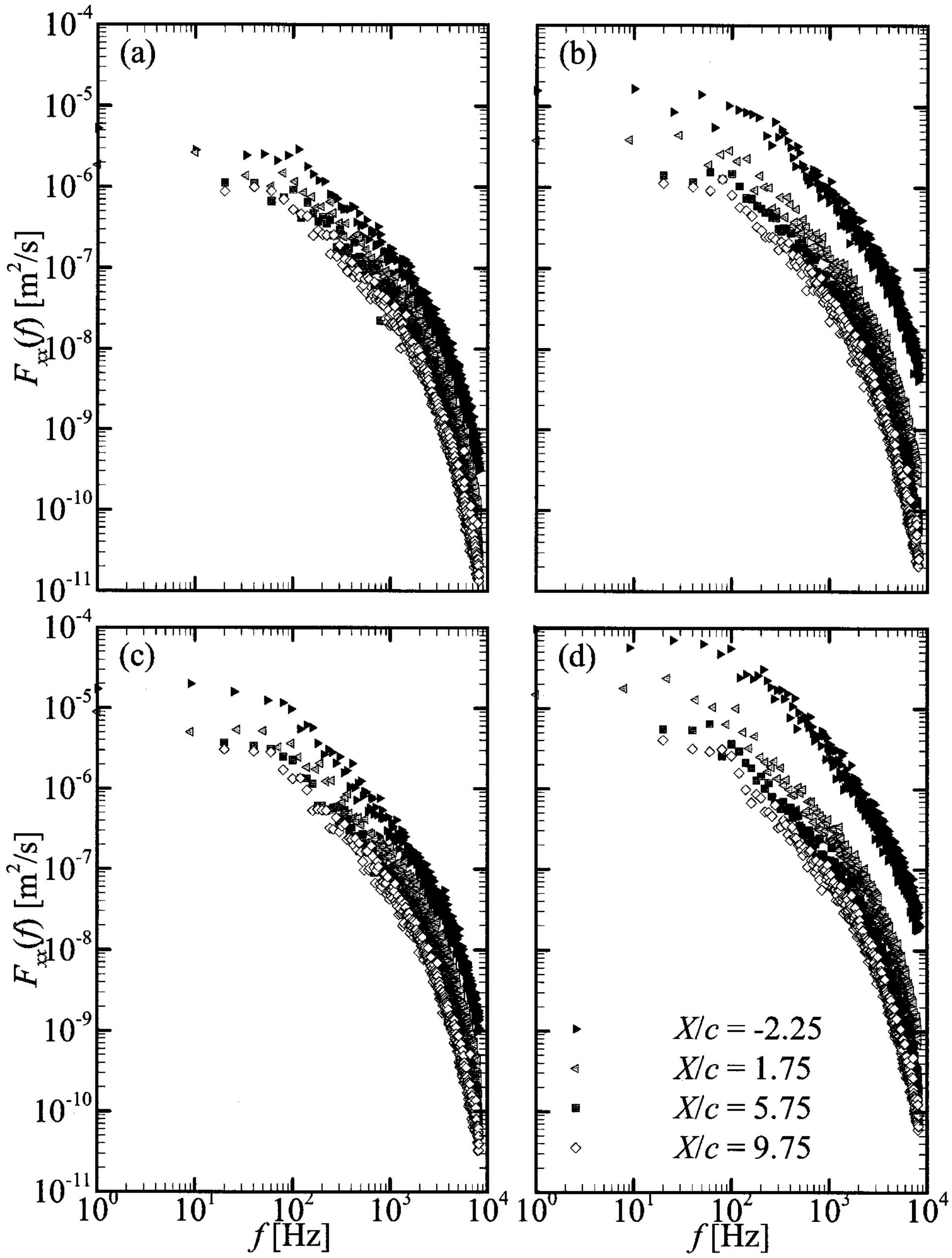

Figure 5.17: Frequency spectra of (a) small-grid-upstream, (b) small-grid, (c) large-grid-upstream and (d) large-grid cases calculated at $X/c = -2.25$, $X/c = 1.75$, $X/c = 5.75$ and $X/c = 9.75$ without the wing in place.

wing as possible without contacting the wing with the probe, then traversing away from the wing. It is believed, however, that Z_o was less than 1 mm from the wing surface.

These boundary layer measurements were performed at $X/c = 0.55$ and at three spanwise stations, $Y/b = -0.75$, -0.50 and -0.25. At the spanwise measurement locations selected, the flow was expected to be sufficiently distant from the wing-tip vortex to be approximately parallel to the measurement probe axis so that $U_{eff} \approx U_x$ and $u'_{eff} \approx u'_x$ (primes here denote standard deviations). Time averaged profiles of U_{eff}/U_∞ for the no-grid and large-grid cases are shown in Figure 5.18a and b, respectively, whereas profiles of u'_{eff}/U_∞ for the no-grid and large-grid cases are shown in Figure 5.18c and d, respectively. In this figure, the X, Y, Z coordinate system has been rotated about the Y axis by α to X_w, Y_w, Z_w so that X_w was aligned with the wing chord line.

In both cases, the boundary layer appeared to remain attached, however, in the large-grid case, it was approximately 30% thicker and had peak rms fluctuation levels 30% larger than the corresponding values in the no-grid case. The location of peak measured u'_{eff}/U_∞ was at the measurement location nearest to the surface of the wing for the no-grid case and at approximately 30% of the boundary layer thickness for the large-grid case.

The flow in the vicinity of the wing-tip is expected to be strongly three-dimensional, and the single-sensor probe should be unable to resolve the velocity magnitude and direction. Nevertheless, by comparing single-sensor measurements downstream of the wing to three-component velocity measurements, it has been found that the shapes of isocontours of the rms effective cooling velocity $\overline{u^2_{eff}}/U_\infty$ measured at $X/c = 4.75$ with the single sensor probe matched fairly well the isocontours of $\overline{u^2_x}$ measured by Devenport et al. (1996) with a four-

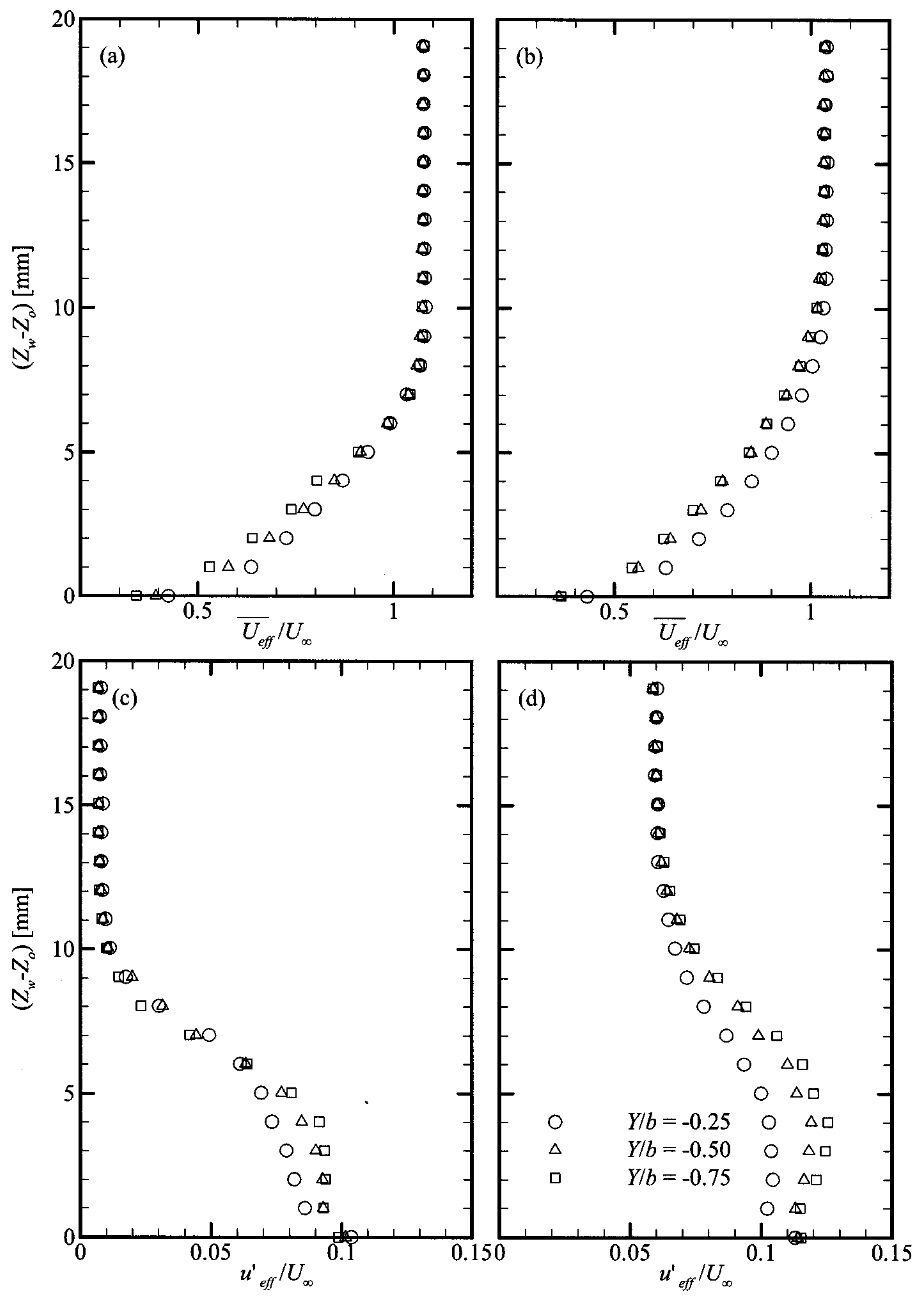

Figure 5.18: Profiles of $\overline{U}_{eff}/U_\infty$ measured in the wing boundary layers for (a) the no-grid case and (b) the large-grid case. Also shown are the corresponding profiles of u'_{eff}/U_∞ for (c) the no-grid and (d) large-grid cases.

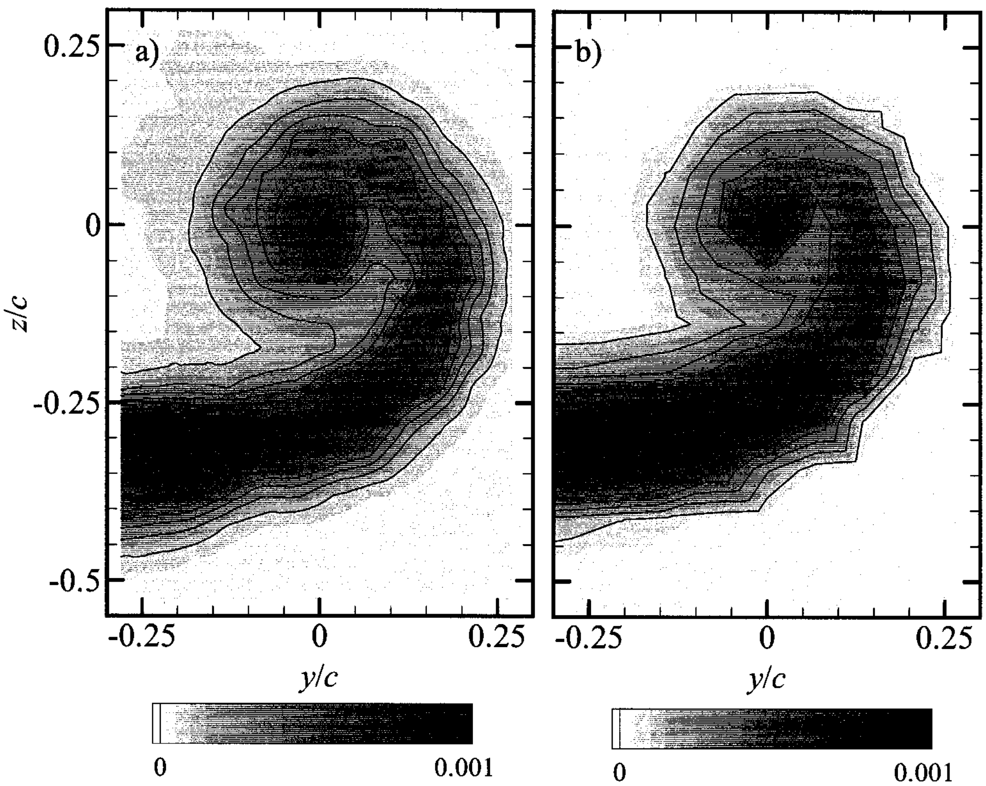

Figure 5.19: Contours of (a) $\overline{u_{eff}^2}$ measured with single-sensor probe and (b) $\overline{u_x^2}$ measured by Devenport et al. (1996) at $X/c = 4.75$. Contour spacing 5×10^{-5}.

sensor probe, as shown in Figure 5.19. Therefore, it is believed that the distribution of turbulent activity over the measurement plane can be determined, at least qualitatively, by examining u'_{eff}/U_∞.

Isocontours of u'_{eff}/U_∞ are presented in Figure 5.20a and b for the no-grid and large-grid cases, respectively. Both sets of contours presented maxima of u'_{eff}/U_∞ at approximately the same locations. At $X/c = 0.0$, two local maxima ("peaks") were evident, one at the wing tip, labelled A in the figure, and another towards the suction surface near the tip, labelled B in the same figure. A smaller peak, labelled C in Figure 5.20 was also evident, appearing in the furthest downstream planes near the very tip of the wing.

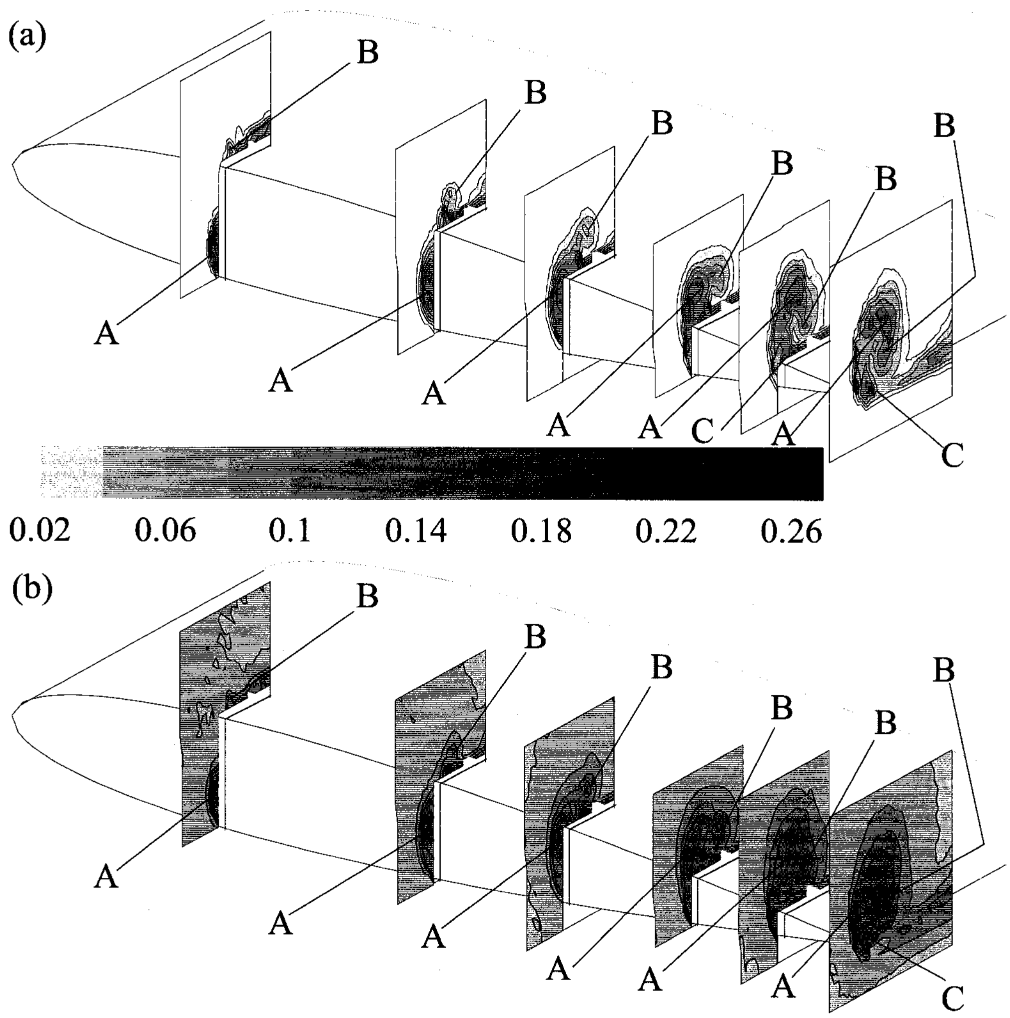

Figure 5.20: Contours of u'_{eff}/U_∞ measured at X/c = 0.0, 0.25, 0.40, 0.55, 0.65 and 0.75 for (a) no grid case and (b) large grid case.

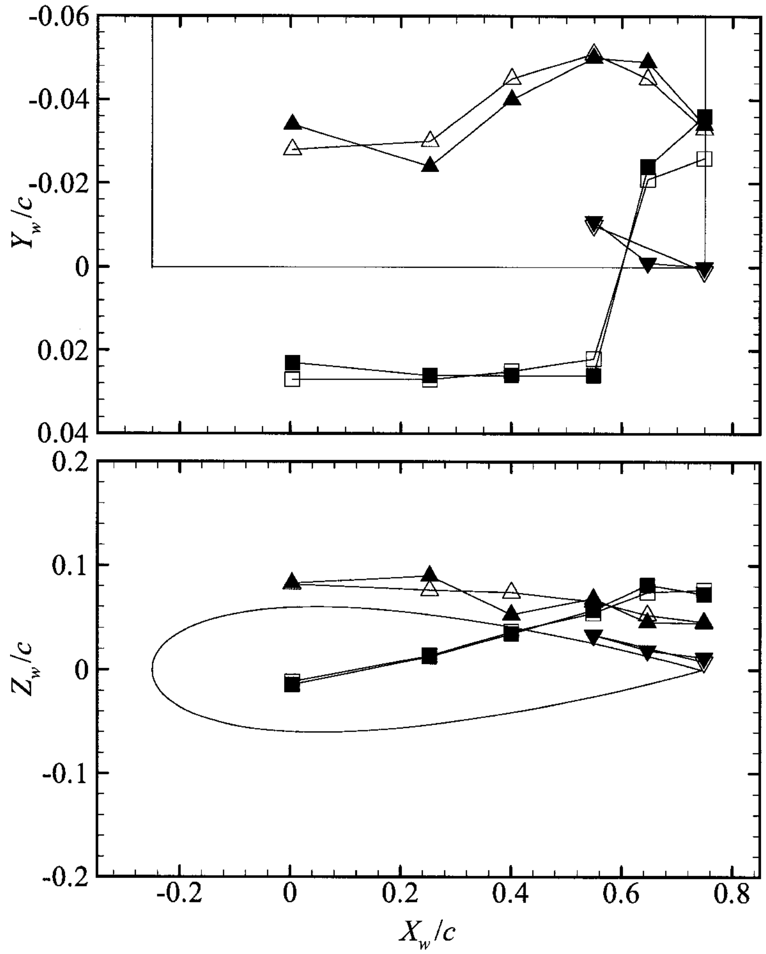

Figure 5.21: Peak u'_{eff}/U_∞ locations for the no-grid (solid symbols) and large-grid (hollow symbols) cases in wing-aligned coordinates. Peak A is indicated by squares, peak B is indicated by upright triangles and peak C is indicated by inverted triangles.

The locations of the local peak values of u'_{eff}/U_∞ are indicated in Figure 5.21 for both the no-grid and large-grid cases. In this figure, the X, Y, Z coordinate system has been rotated about the Y axis by α to X_w, Y_w, Z_w so that X_w was aligned with the wing chord line. This figure clearly shows the similarities in peak location between the no-grid and large-grid cases.

In downstream measurement planes, the location of peak A moved towards the suction surface, rolling over the tip's edge somewhere between $X/c = 0.4$ and 0.55. Peak B, remained close to the suction surface in downstream planes, moving away from the tip until peak A rolled over to the suction surface, at which point is started to move towards the tip again. Peak A was wider than peak B in all planes and contained higher values of u'_{eff}/U_∞. At $X/c = 0.75$, the two peaks A and B appeared to have merged together. Peak C remained close to the suction surface of the wing at the very tip until shed from the trailing edge.

Although the locations of the characteristic peaks were unaltered by free-stream turbulence, larger u'_{eff}/U_∞ values were recorded for the large grid case and the contours of u'_{eff}/U_∞ were wider, appearing more diffuse. If the vortex position were steady, this observation would indicate that free-stream turbulence increased the turbulence inside the vortex during formation. However, in view of the steep local velocity gradients which could result in large measured values of u'_{eff}/U_∞ under even small-scale wandering, one needs additional evidence before making such statement with any degree of confidence.

5.4 Oil film surface flow visualization

Oil film surface flow visualizations were performed on the suction surface of the wing near the tip at $\alpha = 8°$ and $\mathrm{Re}_c = 2.4 \times 10^5$ for the no-grid and large-grid cases. Similar visualizations of the pressure surface revealed nothing of interest and limitations in accessibility prevented photography of the tip surface; hence, photographs were only taken of the suction surface flow visualizations. A representative image for the no-grid case is shown in Figure 5.22a, with virtually identical patterns observed for the large-grid case,

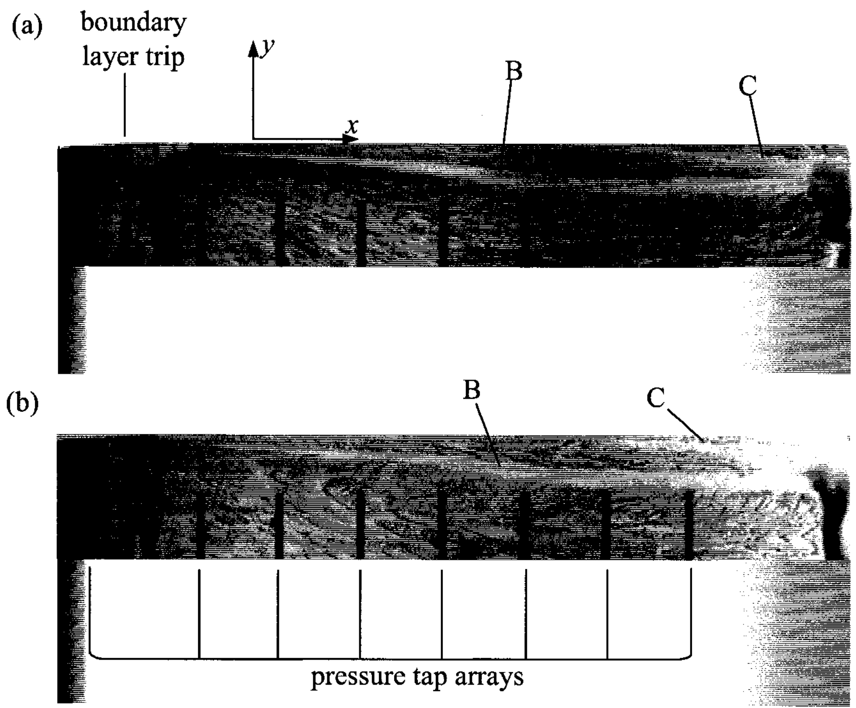

Figure 5.22: Representative oil film flow visualization images for (a) no-grid and (b) large-grid cases showing the oil-free regions corresponding to the signatures of vortices B and C on the wing surface. Also indicated on the figure are the locations of the boundary layer trip, pressure tap rows and coordinate system origin.

shown in Figure 5.22b. Two characteristic lines, labelled B and C are evident as oil-free regions in Figure 5.22a-b, indicating high local wall shear stress. The position of lines B and C observed in the oil film images correspond to the location of the peak u'_{eff}/U_∞ values observed in the single wire measurements (Figure 5.21).

5.5 Dye injection flow visualization

To characterize the time dependent aspects of the vortex formation process, flow visualization by dye injection was performed in the water tunnel at $\mathrm{Re}_c = 2.9 \times 10^4$ and $\alpha = 5°$ for the no-grid, small-grid and large-grid cases. Despite differences in Reynolds number,

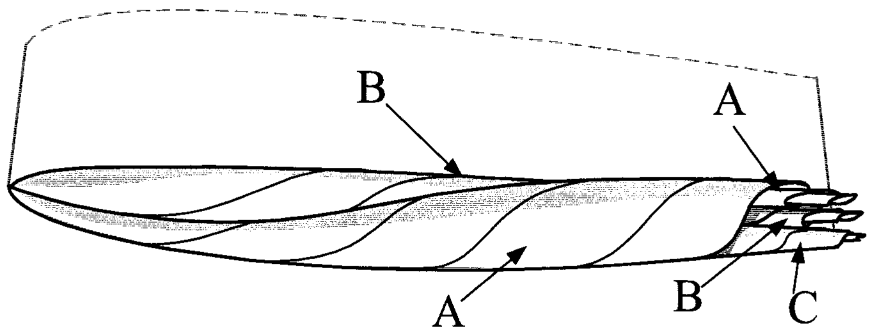

Figure 5.23: Sketch of multiple vortices observed during vortex formation.

aspect ratio and angle of attack between these experiments and the wind tunnel studies, comparisons between patterns observed in the dye injection images and those inferred from single wire measurements showed strong qualitative similarities. The dye injection flow visualization revealed that, in the initial formation phase, one could identify three distinct co-rotating vortices, illustrated in Figure 5.23, which correspond to the characteristic peaks A, B and C in the contours of u'_{eff}/U_∞ shown in Figure 5.20. Vortex A developed along the wing tip, as fluid from the pressure surface flowed around the tip edge. Vortex B developed along the suction surface, as fluid from the tip surface rolled up around the other edge of the tip. Finally, vortex C formed at the very tip of the trailing edge, as slow-moving fluid on the pressure surface rolled towards the suction surface near the tip of the trailing edge. Other experimental studies using flow visualization, velocity and pressure measurements (Katz and Galdo (1989), Birch et al. (2003), McInerny et al. (1990)) have also identified the formation of multiple vortices, the number and arrangement of which varied with wing-tip geometry.

Based on observations of the rotation rate of the injected dye, vortices A and B appeared to be comparable in strength, however vortex A was initially more turbulent, as evident from an increased rate of dye diffusion and increased fluctuation levels measured by the single-sensor probe. At approximately $X/c = 0.5$, vortex A rolled over to the suction surface and began to interact with vortex B. The interaction of the two vortices was turbulent and could not be observed in detail due to strong dye diffusion in both vortices.

All three vortices were noticeable in the three cases at different free-stream turbulence levels, as shown in representative dye injection images in Figure 5.24 and Figure 5.25. When the grids were placed upstream of the wing, dye injection showed that the formations and trajectories of both vortices A and B were unaffected. However, vortex B appeared to be distorted by interactions with free-stream eddies. Moreover, free-stream turbulence seemed to increase the turbulence within both vortices, as implied by increased rates of dye diffusion. The influence of free-stream turbulence on vortex C can be observed by comparing the images shown in Figure 5.25a for the no-grid case and Figure 5.25b for the small-grid case. In the presence of free-stream turbulence, vortex C was clearly more turbulent, as evidenced by more rapid dye diffusion.

5.6 Wing surface pressure

Measurements of wing surface pressure were performed to characterize the lift distribution across the span of the wing. The static pressure difference, ΔP, between the wing surface and the free-stream (as measured by the Pitot-static tube) was measured at each of the wing pressure taps for the no-grid, small-grid and large-grid cases at $\alpha = 5°$ and $\mathrm{Re}_c = 2.4 \times 10^5$. The time-averaged pressure difference was then integrated at each

(a)

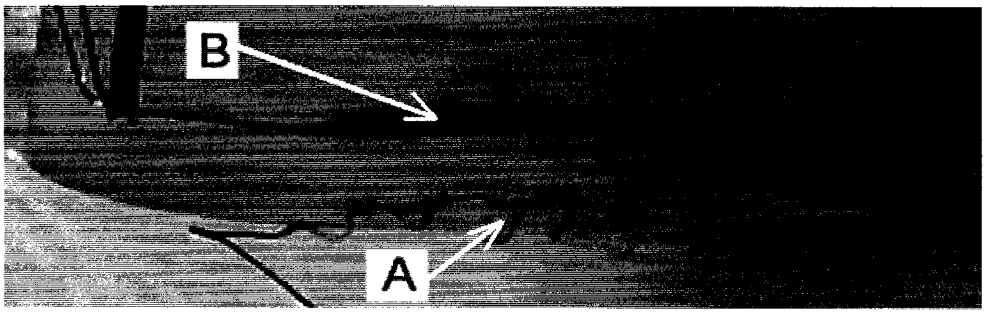

(b)

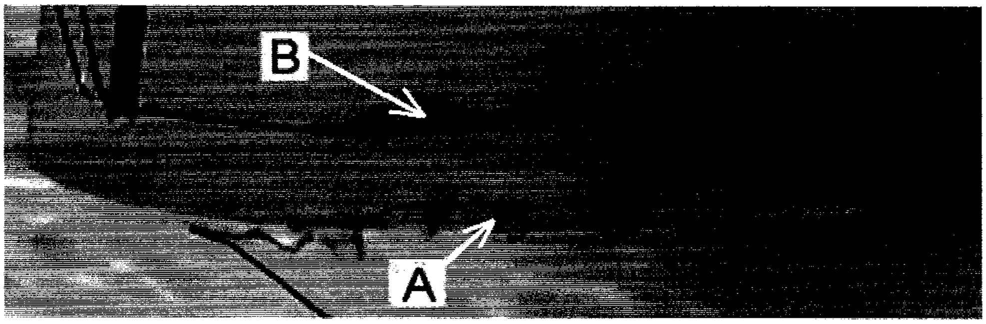

Figure 5.24: Dye injection images showing vortices A and B for the (a) no-grid and (b) small-grid cases.

(a)

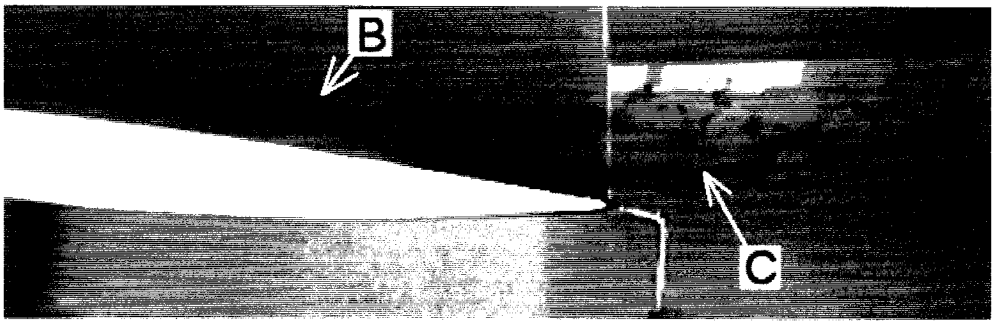

(b)

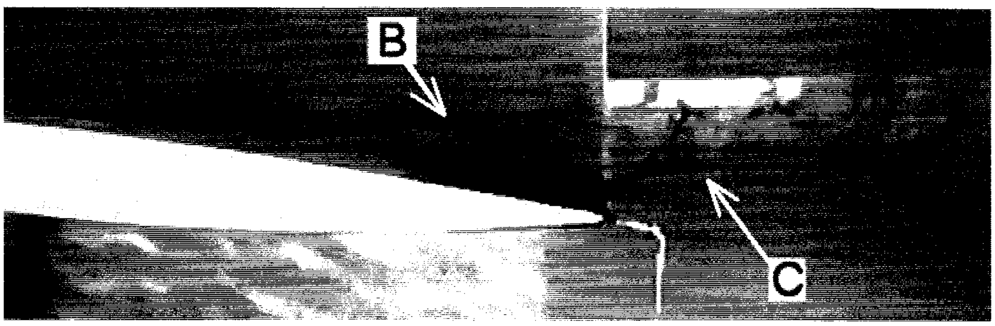

Figure 5.25: Dye injection patterns showing vortices B and C for the (a) no-grid and (b) small-grid cases.

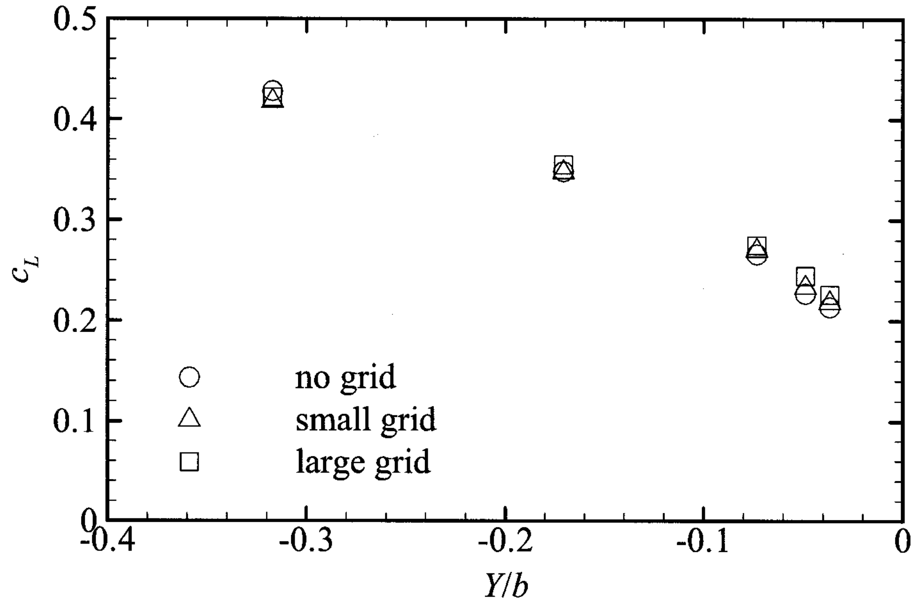

Figure 5.26: Variation of section lift coefficients calculated from surface pressure measurements.

spanwise location to determine the local section lift coefficient as

$$c_L = \frac{A}{\frac{1}{2}\rho U_\infty^2 c} \sum_{i=1}^{N} (\Delta P_i) \cos \xi_i \Delta x_i \ , \tag{5.14}$$

where ΔP_i is the pressure difference measured by the transducer at pressure tap i and is assumed constant over a length Δx_i which is adjusted to account for the spacing of the pressure taps. The angle ξ_i is the angle of the length Δx_i to the free-stream and the constant A is equal to -1 for pressure taps on the suction surface and $+1$ for pressure taps on the pressure surface. The resulting section lift coefficient at each spanwise location is plotted in Figure 5.26 for the no-grid, small-grid and large-grid cases. Nearly identical lift distributions were measured for the three cases.

5.7 Location of time-averaged vortex axis

The average location of the intersection of the vortex axis with each measuring plane was identified as the centre of a family of concentric circles fitted to isocontours of the magnitude of the time averaged velocity $(\overline{U}_y^2 + \overline{U}_z^2)^{0.5}$ on the measuring plane. The locus of the centre of the time average, which may be called the average vortex axis or average vortex trajectory, is illustrated in Figure 5.27. It can be seen that, for all three free-stream turbulence levels examined, the vortex moved inboard and upward from the tip of the wing. Also apparent from Figure 5.27 is that the vortex trajectory was not significantly affected by the introduction of free-stream turbulence.

5.8 Time-averaged streamwise velocity

The variations of the dimensionless mean streamwise velocity over the measurement plane are presented as contours of $\overline{U}_x/U_o$ for each of the five free-stream conditions in Figure 5.28 for the no-grid case, Figure 5.29 for the small-grid-upstream case, Figure 5.30 for the small-grid case, Figure 5.31 for the large-grid-upstream case and in Figure 5.32 for the large-grid case. The results have been normalized by the local free-stream velocity U_o on the corresponding measuring plane, which was higher by up to 5% than the undisturbed free-stream velocity U_∞ because of blockage by the wing and its wake. Measurements at the streamwise stations $X/c = 1.75$, 3.75, 5.75, 7.75 and 9.75 indicate the trends of streamwise development for the different cases.

In all five figures, the wing wake can be identified as a thin region having a velocity deficit. At $X/c = 1.75$, the isovelocity contours within the wake contain long, relatively

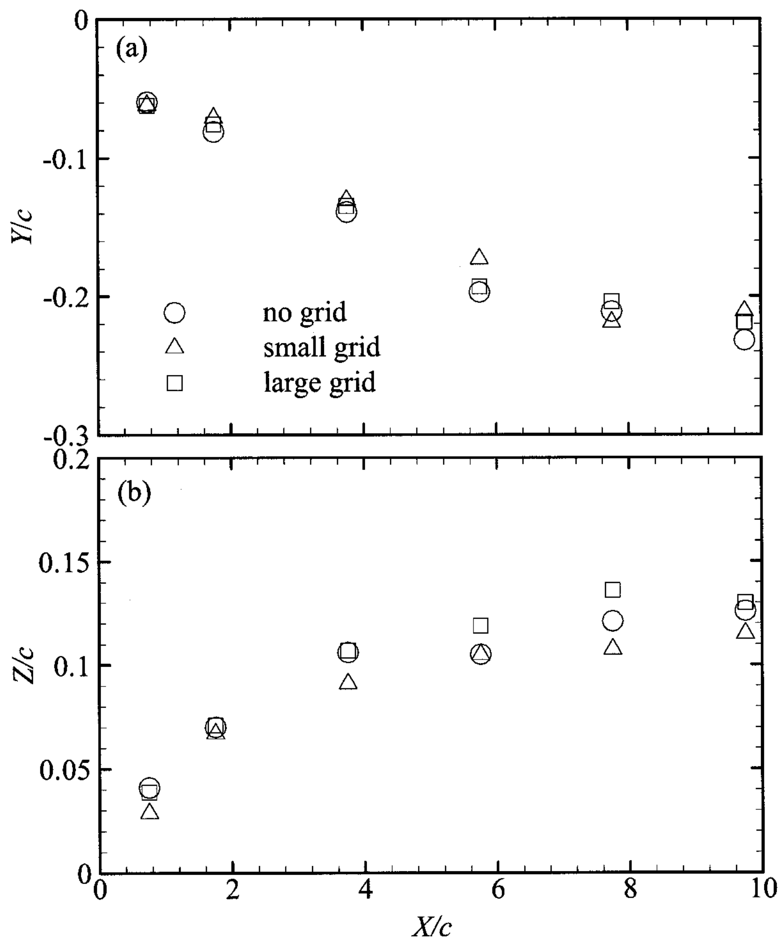

Figure 5.27: Distances of vortex axis from a streamwise line passing through the wing's aerodynamic center in (a) the spanwise direction and (b) the direction of lift.

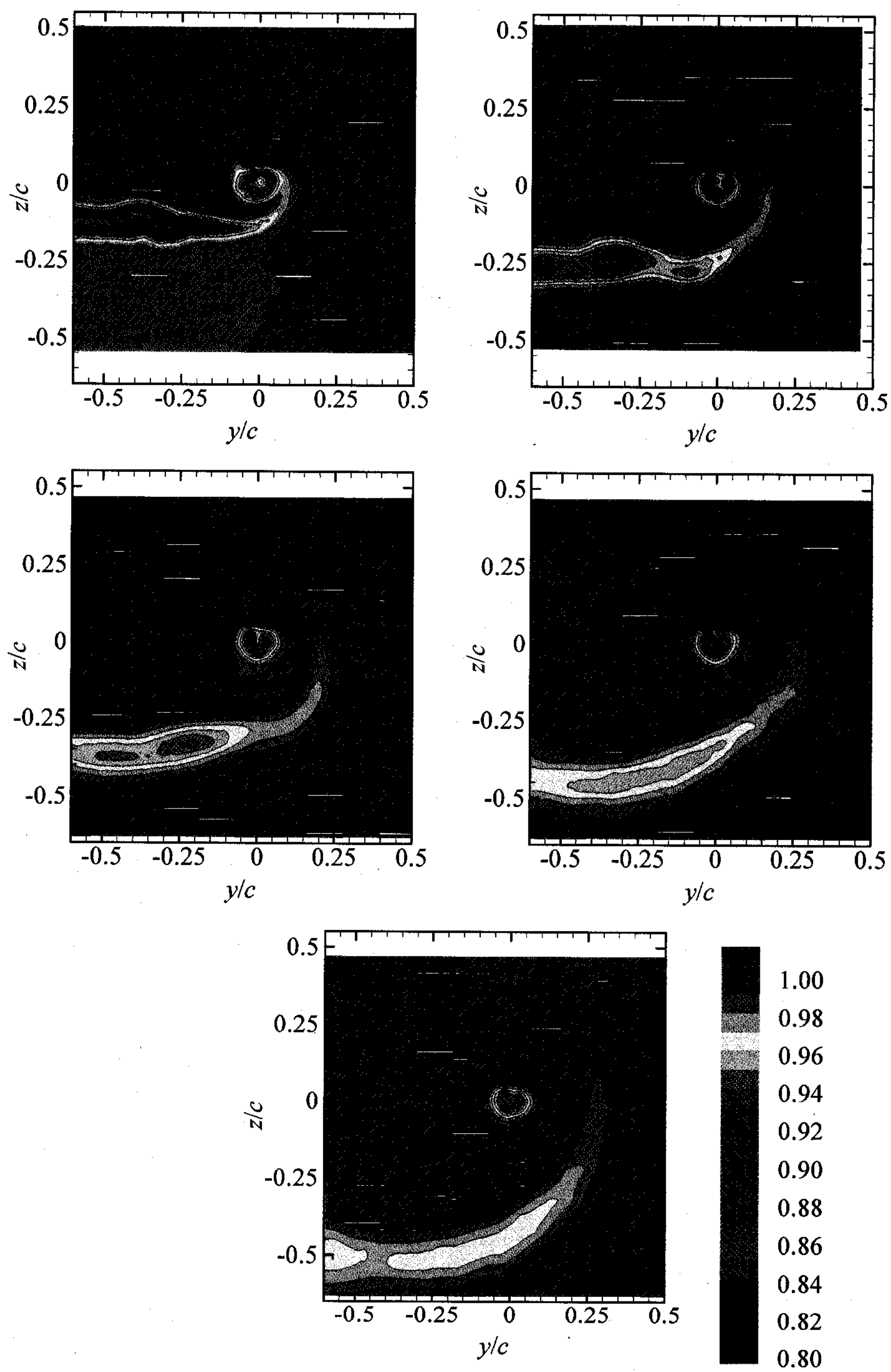

Figure 5.28: Contours of $\overline{U}_x/U_o$ for each streamwise plane measured for the no-grid case. Contour lines are spaced 0.01 apart, execept for $X/c = 1.75$ where they are spaced 0.02 apart to increase clarity. Contour colouring identical for all measurement planes.

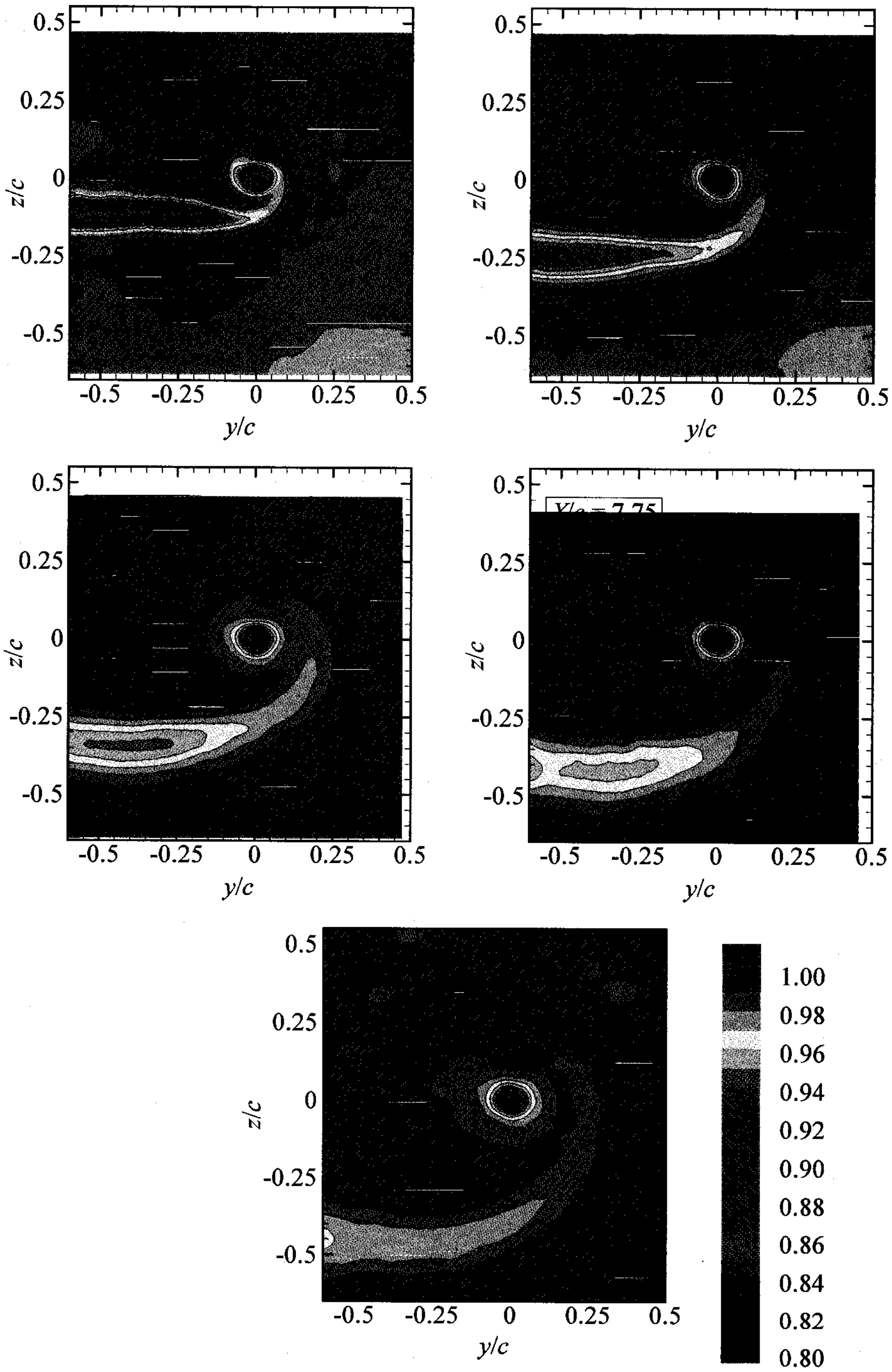

Figure 5.29: Contours of $\overline{U}_x/U_o$ for each streamwise plane measured for the small-grid-upstream case. Contour lines are spaced 0.01 apart, execept for $X/c = 1.75$ where they are spaced 0.02 apart to increase clarity. Contour colouring identical for all measurement planes.

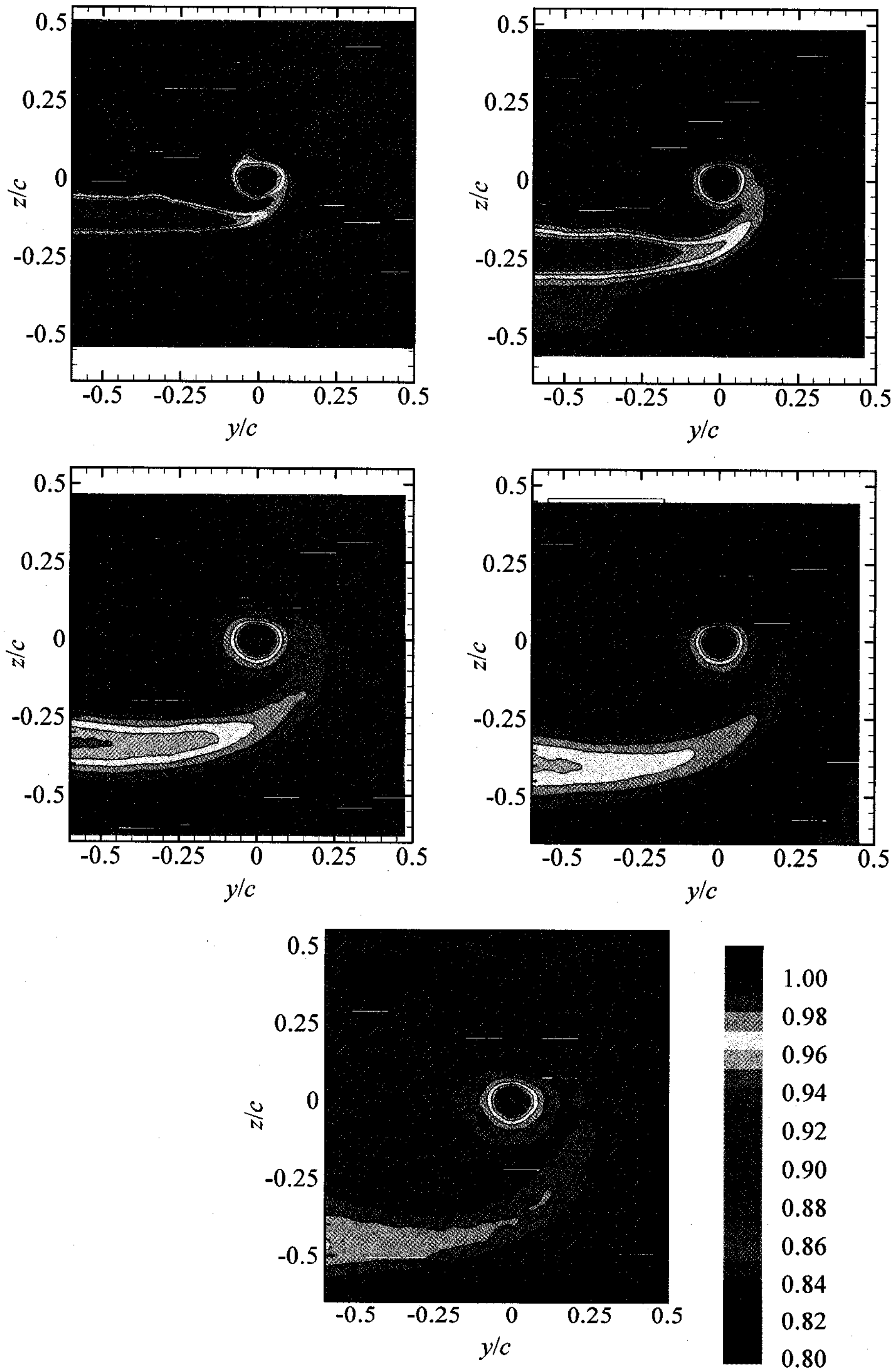

Figure 5.30: Contours of $\overline{U}_x/U_o$ for each streamwise plane measured for the small-grid case. Contour lines are spaced 0.01 apart, execept for $X/c = 1.75$ where they are spaced 0.02 apart to increase clarity. Contour colouring identical for all measurement planes.

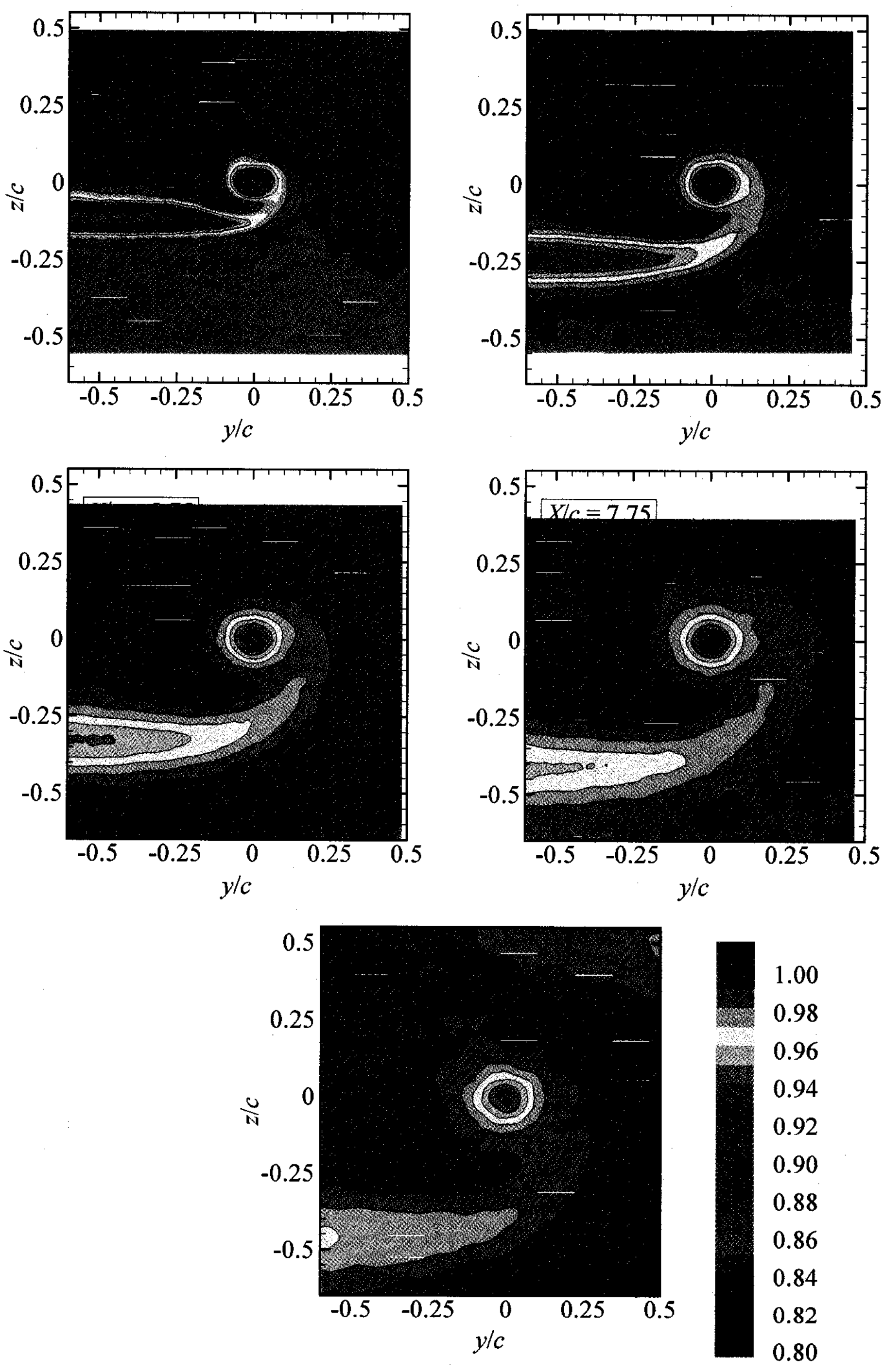

Figure 5.31: Contours of $\overline{U}_x/U_o$ for each streamwise plane measured for the large-grid-upstream case. Contour lines are spaced 0.01 apart, execept for $X/c = 1.75$ where they are spaced 0.02 apart to increase clarity. Contour colouring identical for all measurement planes.

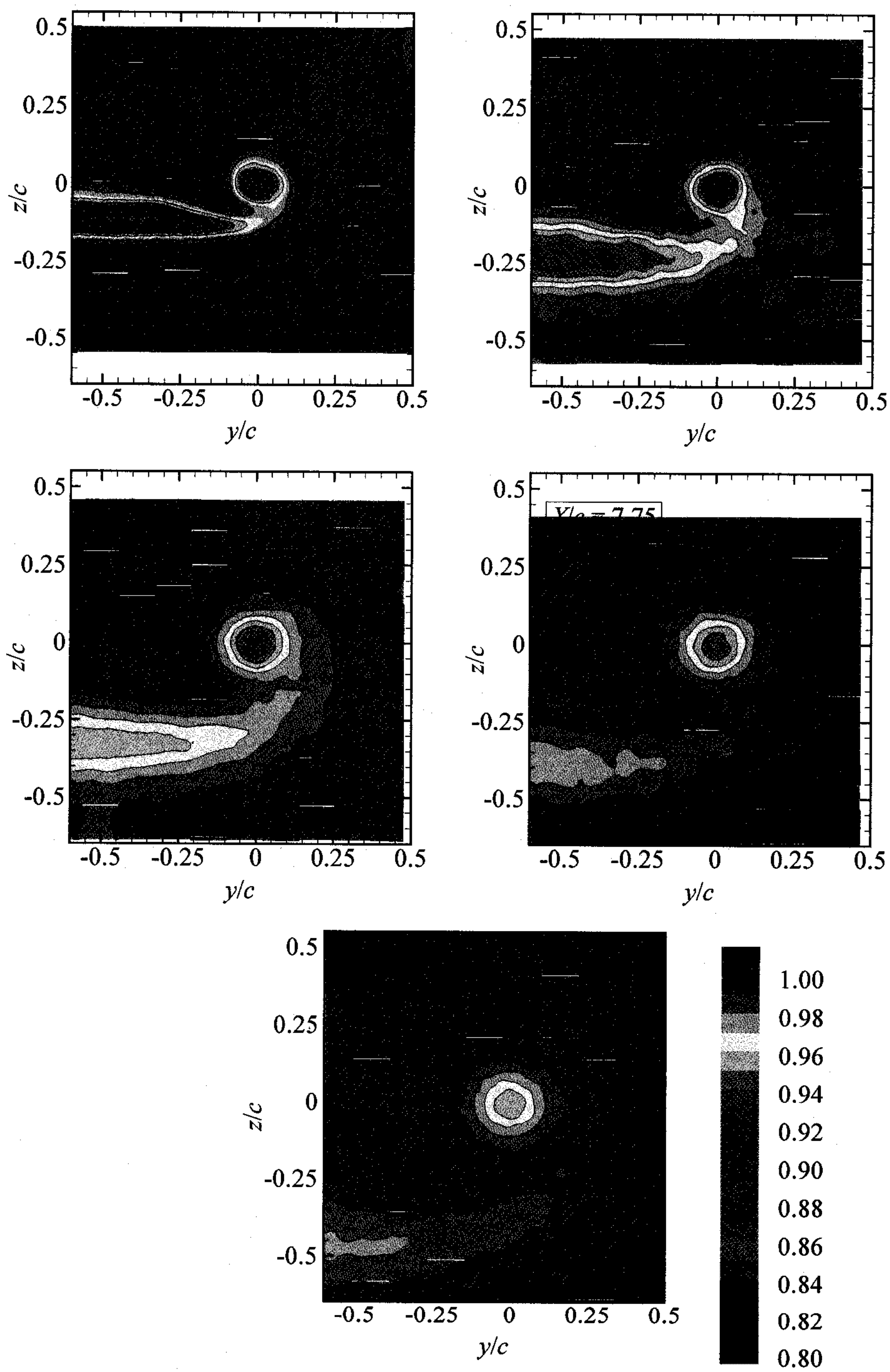

Figure 5.32: Contours of $\overline{U}_x/U_o$ for each streamwise plane measured for the large-grid case. Contour lines are spaced 0.01 apart, execept for $X/c = 1.75$ where they are spaced 0.02 apart to increase clarity. Contour colouring identical for all measurement planes.

straight sections, but contour curvature increases with increasing downstream distance, as the wake spirals around the vortex due to the velocity field induced by the latter. A nearly axi-symmetric region of velocity deficit surrounding the time-averaged vortex axis, is evident in all figures.

For a closer examination of the axial velocity variation near the time-averaged vortex axis, the radial variations of the dimensionless mean streamwise velocity $\overline{U}_x/U_o$ for each of the five free-stream conditions are shown in Figures 5.33-5.37. For clarity, measurements within the spiral wake are indicated by solid squares, so that they can be distinguished from measurements in the free stream.

The measurements in the no-grid case at $X/c = 1.75$ (Figure 5.33) show a local maximum at the time-averaged vortex centre, roughly equal to the local free-stream velocity, surrounded by an annular region with a velocity deficit. As the vortex develops downstream, both the central maximum and the annular deficit decrease and the axial velocity profile approaches a wake-like form. The local maximum at the time-averaged vortex centre is also evident in the small-grid-upstream case at $X/c = 1.75$ (Figure 5.34). However, the maximum is lower and decreases more rapidly than that observed for the no-grid case.

The measured profiles of $\overline{U}_x/U_o$ are presented for the small-grid case in Figure 5.35, the large-grid-upstream case in Figure 5.36 and the large-grid case in Figure 5.37. In all these cases the velocity distributions appear wake-like. The three profiles were clearly asymmetric near the vortex axis at $X/c = 1.75$, but their asymmetry decreased with increasing downstream distance. Whereas the profiles in the small-grid case show very little change in magnitude and radial scale as the downstream distance increases, those in the

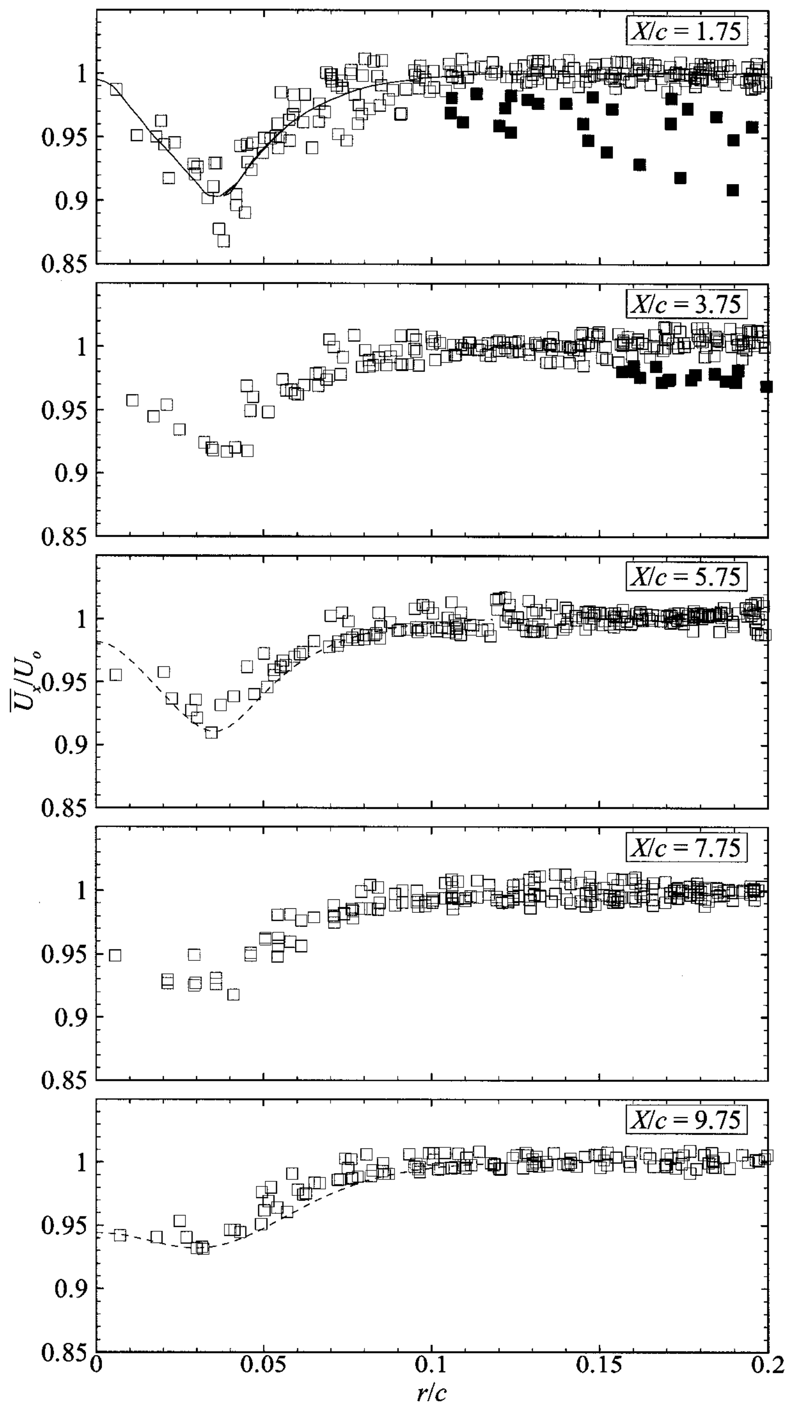

Figure 5.33: Radial variation of the measured normalized mean axial velocity for the no-grid case. Solid symbols indicate measurements in the spiral wake, while open symbols indicate measurements outside the spiral wake. The solid line in (a) has been fitted to the measurements, whereas the dashed lines in (b) and (c) indicate the result of subjecting the profile fitted in (a) to random lateral motions with rms amplitudes equal to $0.017c$ for (b) and $0.028c$ for (c).

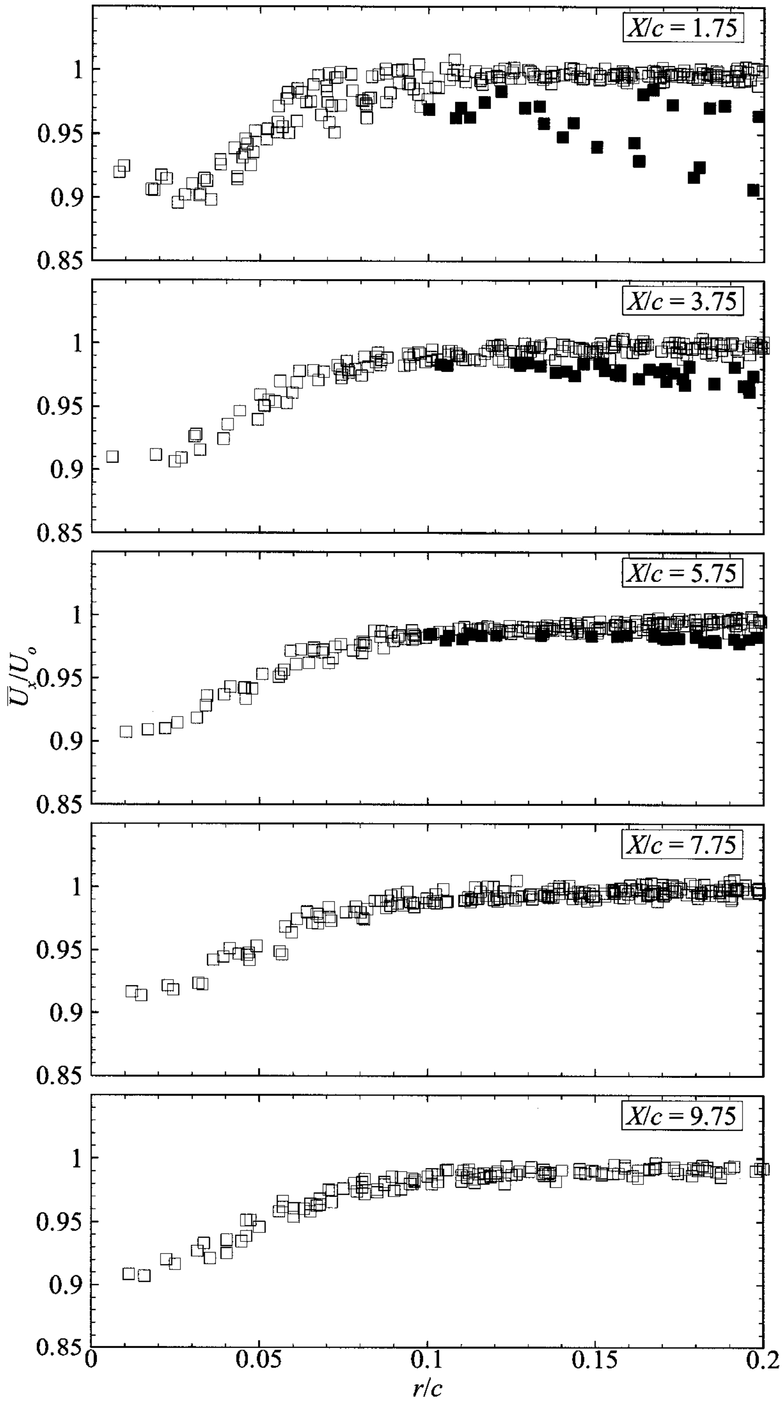

Figure 5.34: Radial variation of the mean streamwise velocity normalized by local free-stream velocity $\overline{U}_x/U_o$ for the small-grid-upstream case. Solid squares indicate data points located in the spiral wake.

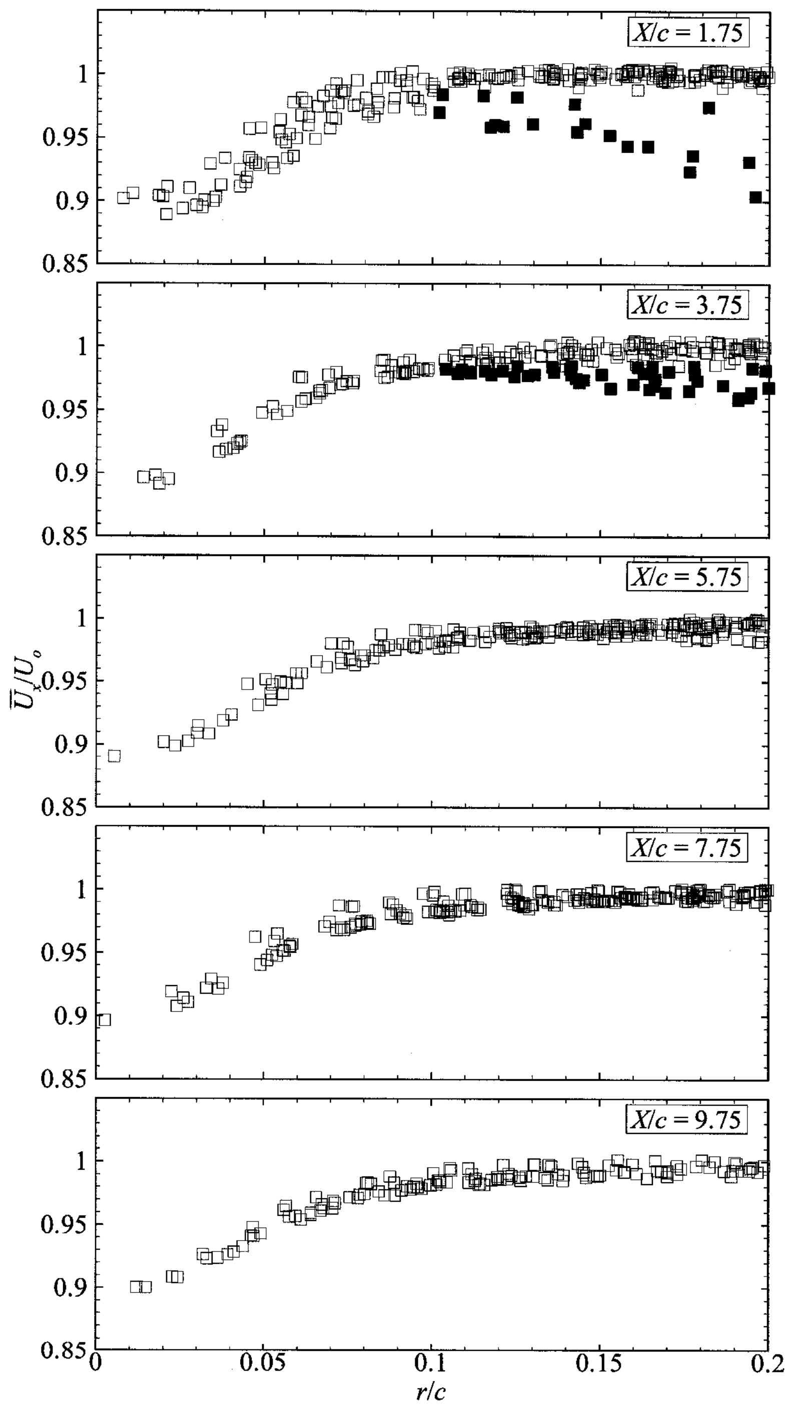

Figure 5.35: Radial variation of the mean streamwise velocity normalized by local free-stream velocity $\overline{U}_x/U_o$ for the small-grid case. Solid squares indicate data points located in the spiral wake.

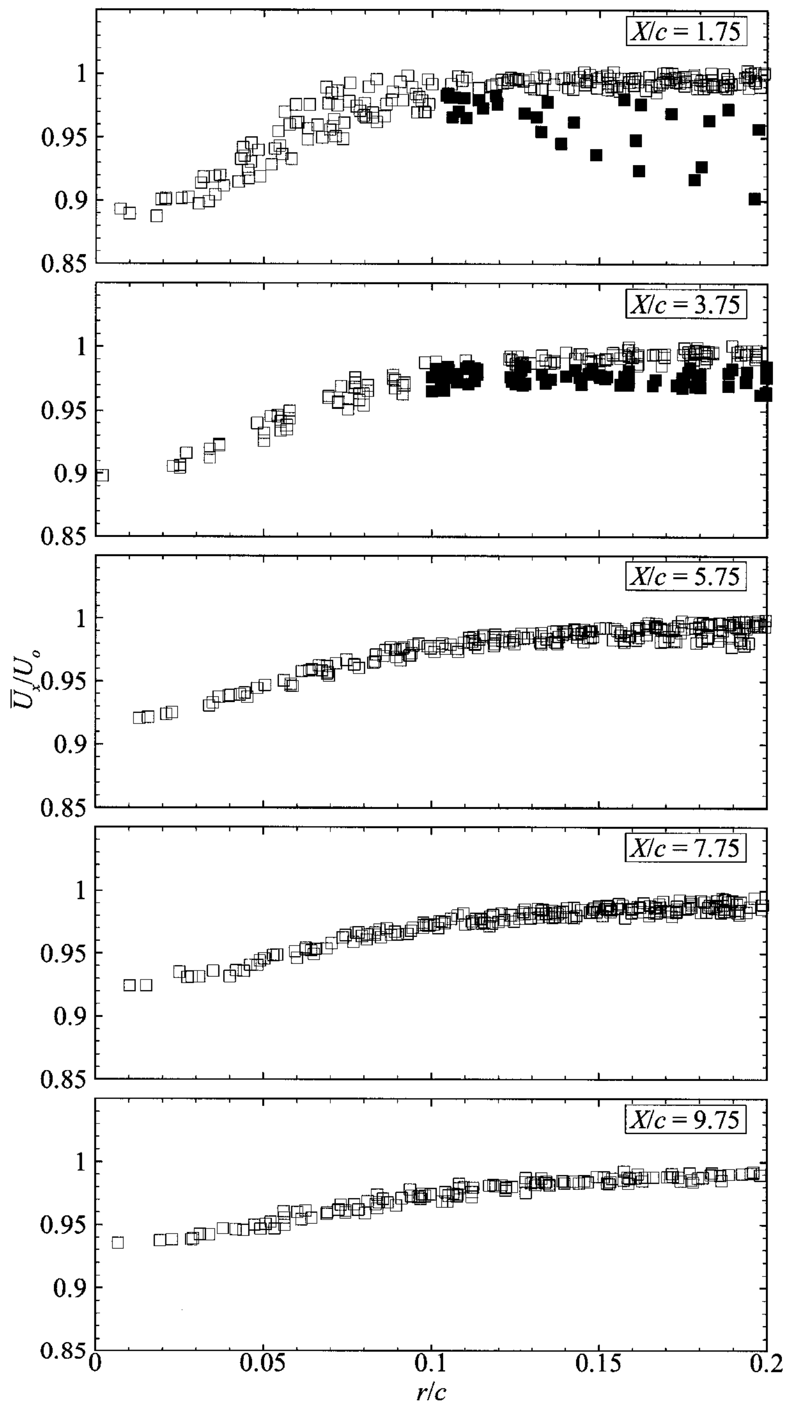

Figure 5.36: Radial variation of the mean streamwise velocity normalized by local free-stream velocity $\overline{U}_x/U_o$ for the large-grid-upstream case. Solid squares indicate data points located in the spiral wake.

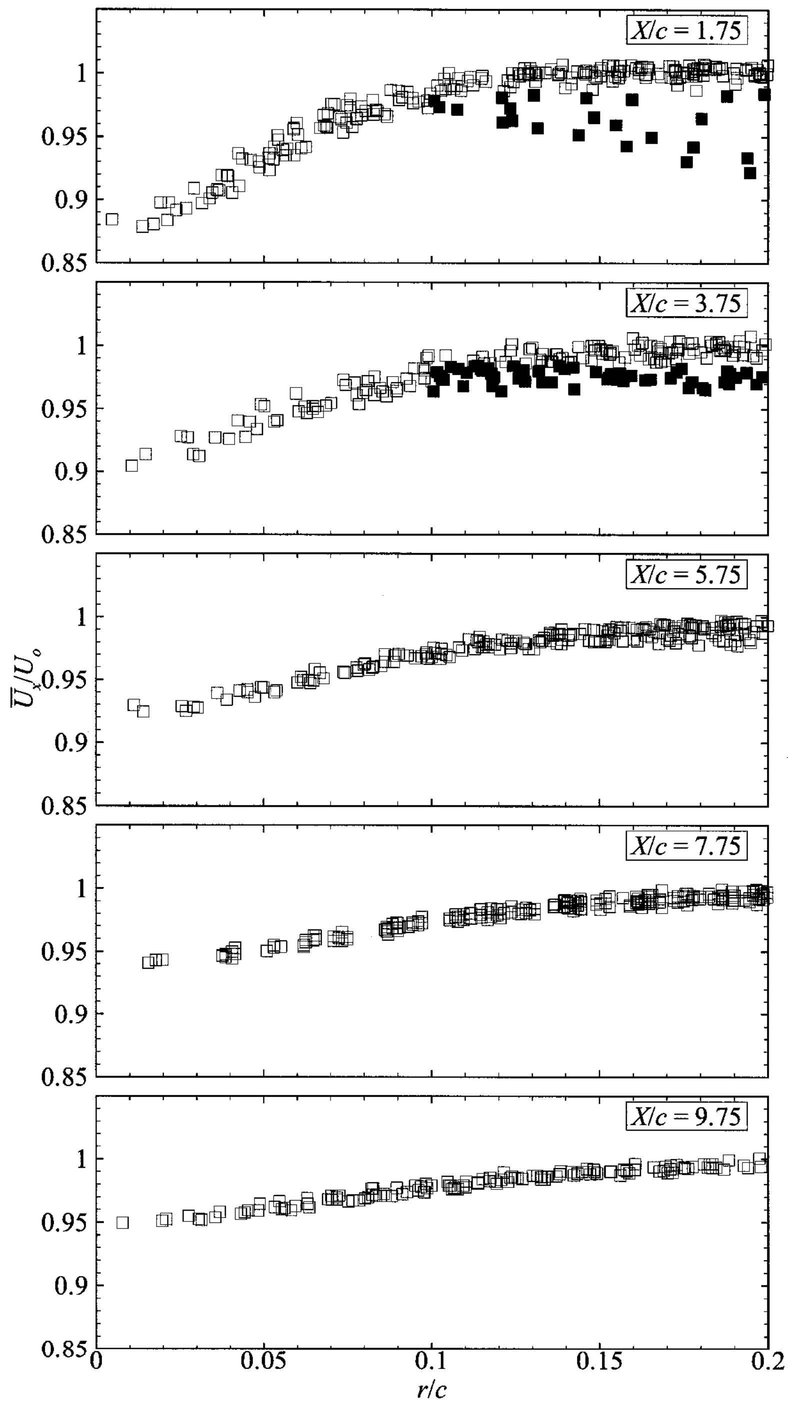

Figure 5.37: Radial variation of the mean streamwise velocity normalized by local free-stream velocity $\overline{U}_x/U_o$ for the large-grid case. Solid squares indicate data points located in the spiral wake.

large-grid-upstream and large-grid cases show a decreasing deficit and an increasing radial scale.

5.9 Time-averaged circumferential velocity

In the present study, the mean circumferential velocity is defined as

$$\overline{U}_\theta = \overline{U}_z \cos\theta - \overline{U}_y \sin\theta \ , \tag{5.15}$$

where the angle θ is the circumferential coordinate of the probe in a Cartesian coordinate system having the local time-averaged vortex centre as origin (Figure 5.27). Distributions of $\overline{U}_\theta/U_o$ in the measurement planes are presented as contours for each of the three free-stream conditions in Figure 5.38 for the no-grid case, Figure 5.39 for the small-grid-upstream case, Figure 5.40 for the small-grid case, Figure 5.41 for the large-grid-upstream case and Figure 5.42 for the large-grid case. The locus of minimum $\overline{U}_x/U_o$ in the spiral wake has been indicated in each plot by a dashed line.

Near the vortex axis, $\overline{U}_\theta/U_o$ appears to be nearly axi-symmetric, however, as r/c increases, the asymmetry in circumferential velocity becomes more pronounced. Near the wing, at X/c = 1.75, the outer isotachs resemble a mirrored letter C in shape, whereas, further downstream, the contours evolve to include an arm of increased circumferential velocity in the spiral wake region. This asymmetry is most likely caused by effects of the spanwise velocity induced over the pressure and suction surfaces of the wing, the residual of which is visible at X/c = 1.75. Downstream of the wing, this induced velocity evolves through viscous effects into a shear layer, which appears as the arm of increased $\overline{U}_\theta/U_o$ at X/c = 3.75 to 9.75. The shear layer largely coincides with the spiral wake, and both follow

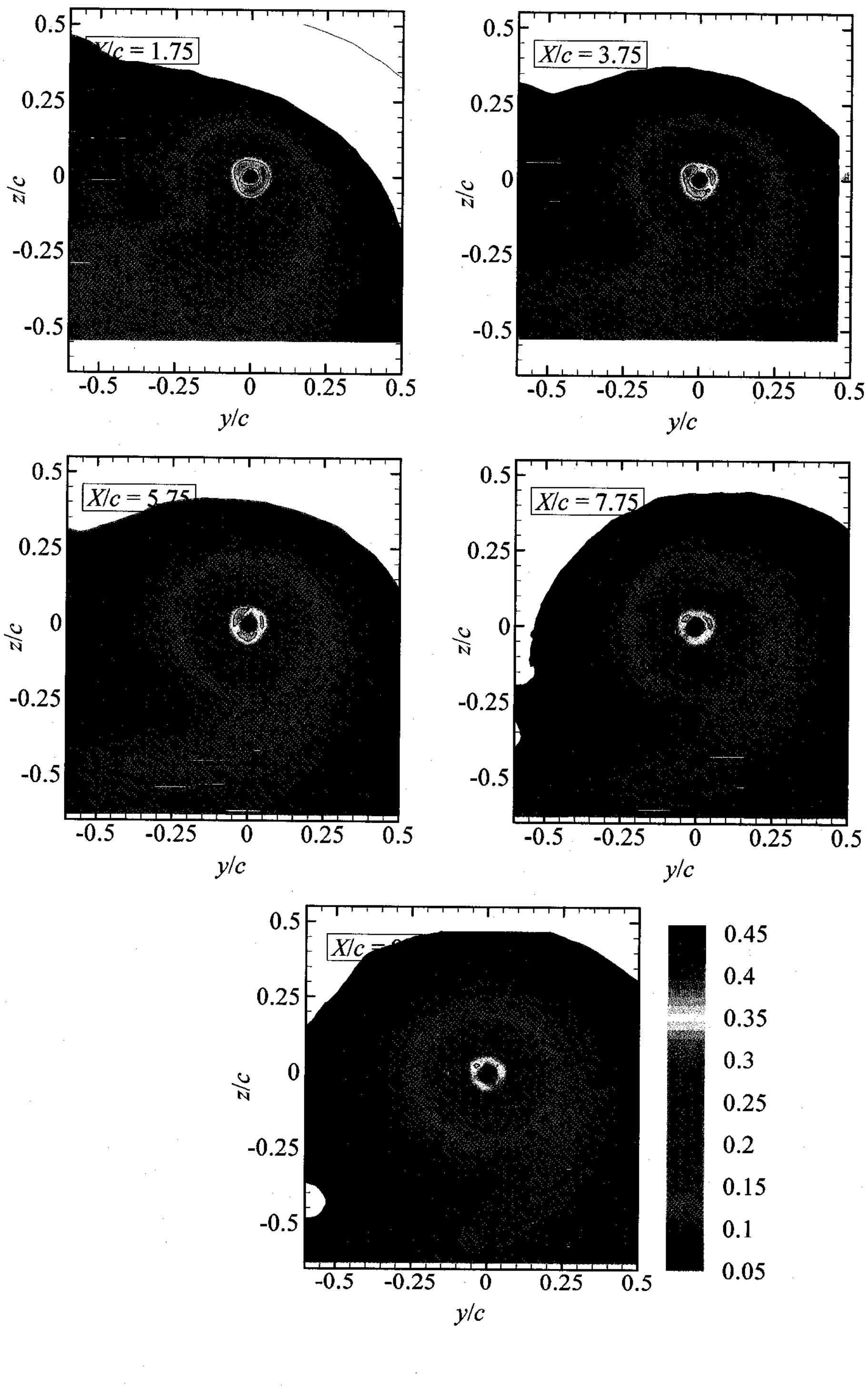

Figure 5.38: Contours of $\overline{U}_\theta/U_o$ for each streamwise plane measured for the no-grid case. Contour lines are spaced 0.05 apart and the contour colouring below 0.05 not shown. Dashed line indicates the locus of the local minima of $\overline{U}_x/U_o$ in the spiral wake.

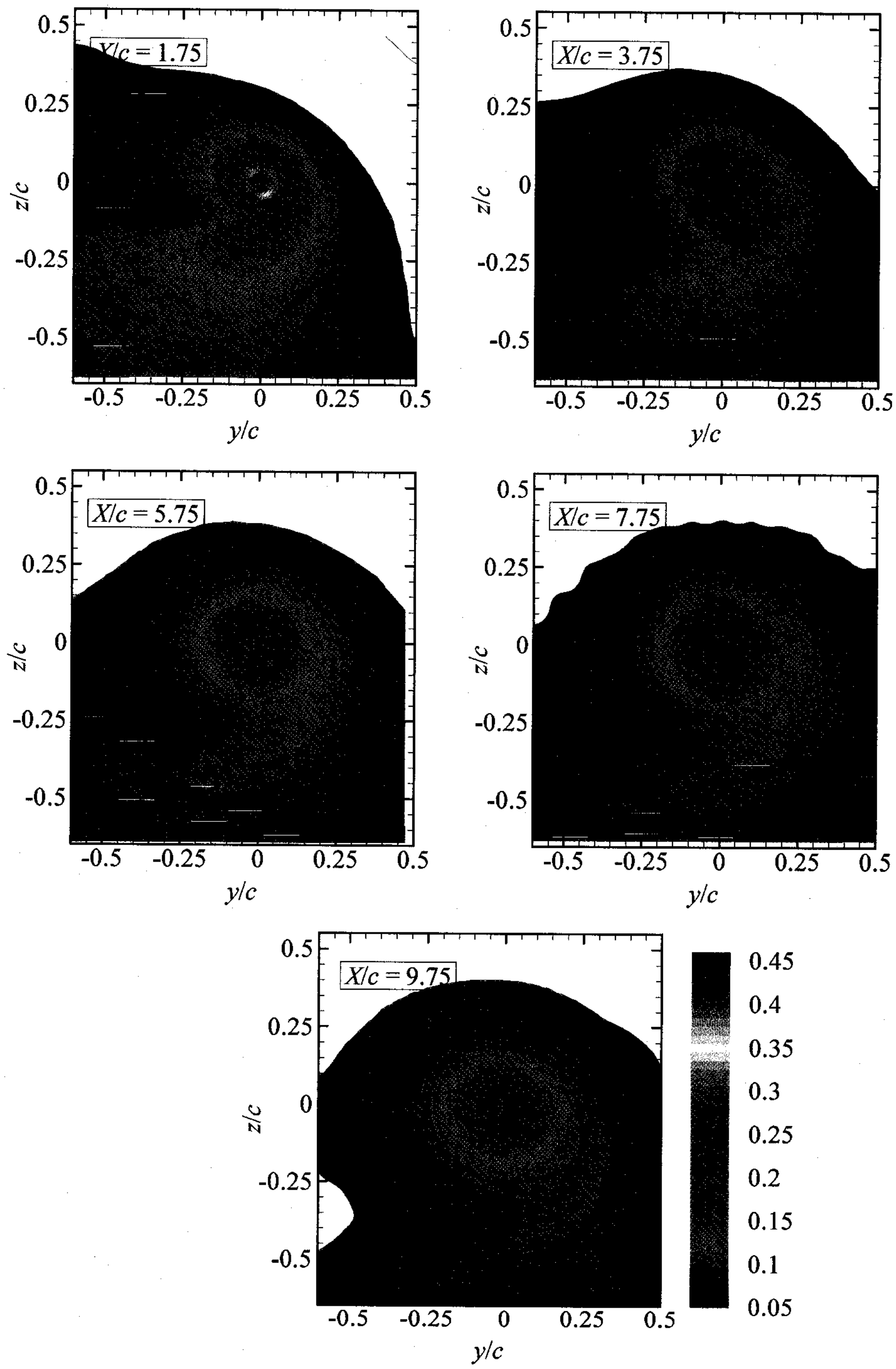

Figure 5.39: Contours of $\overline{U}_\theta/U_o$ for each streamwise plane measured for the small-grid-upstream case. Contour lines are spaced 0.05 apart and the contour colouring below 0.05 not shown. Dashed line indicates the locus of the local minima of $\overline{U}_x/U_o$ in the spiral wake.

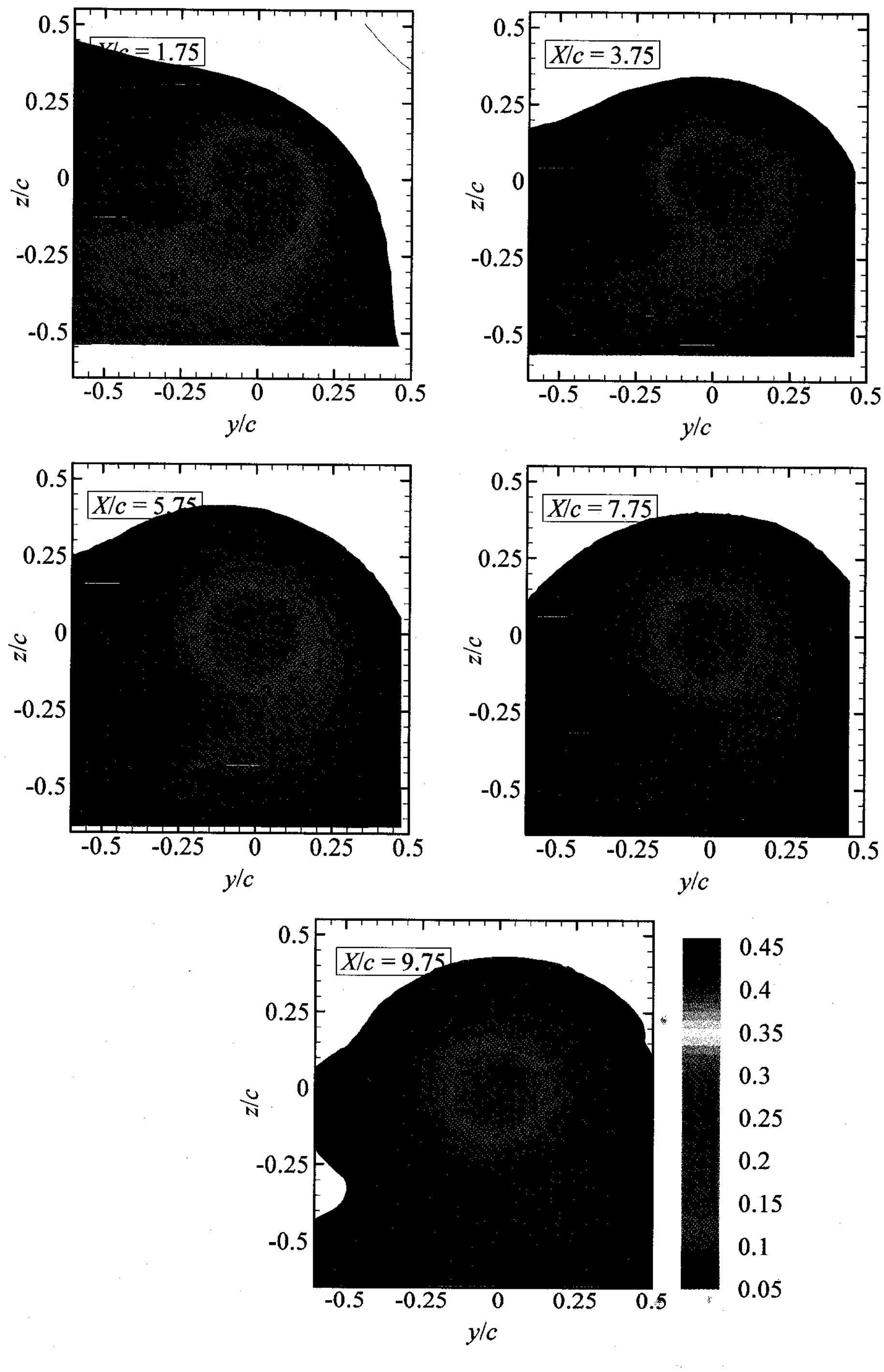

Figure 5.40: Contours of $\overline{U}_\theta/U_o$ for each streamwise plane measured for the small-grid case. Contour lines are spaced 0.05 apart and the contour colouring below 0.05 not shown. Dashed line indicates the locus of the local minima of $\overline{U}_x/U_o$ in the spiral wake.

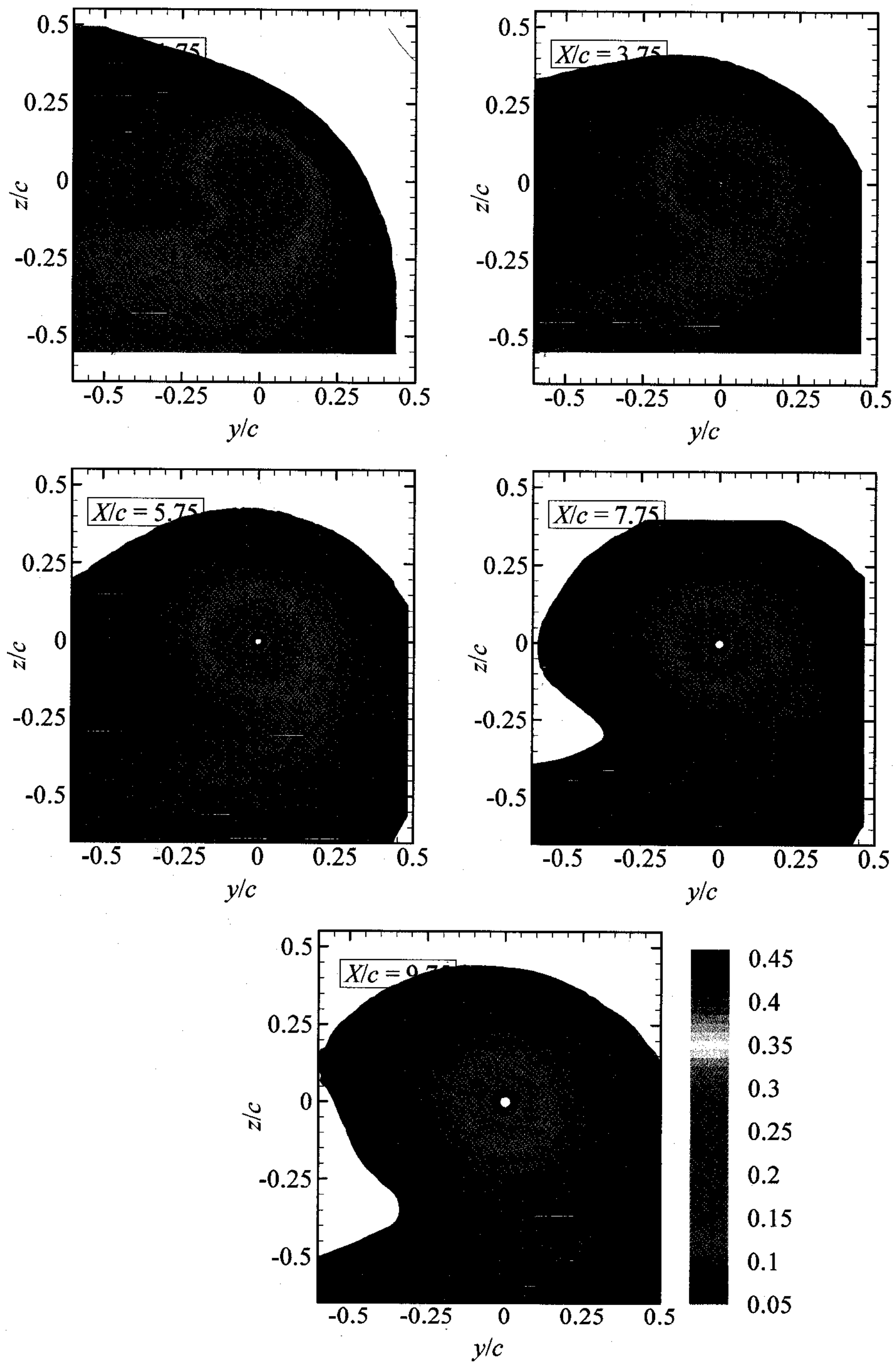

Figure 5.41: Contours of $\overline{U}_\theta/U_o$ for each streamwise plane measured for the large-grid-upstream case. Contour lines are spaced 0.05 apart and the contour colouring below 0.05 not shown. Dashed line indicates the locus of the local minima of $\overline{U}_x/U_o$ in the spiral wake.

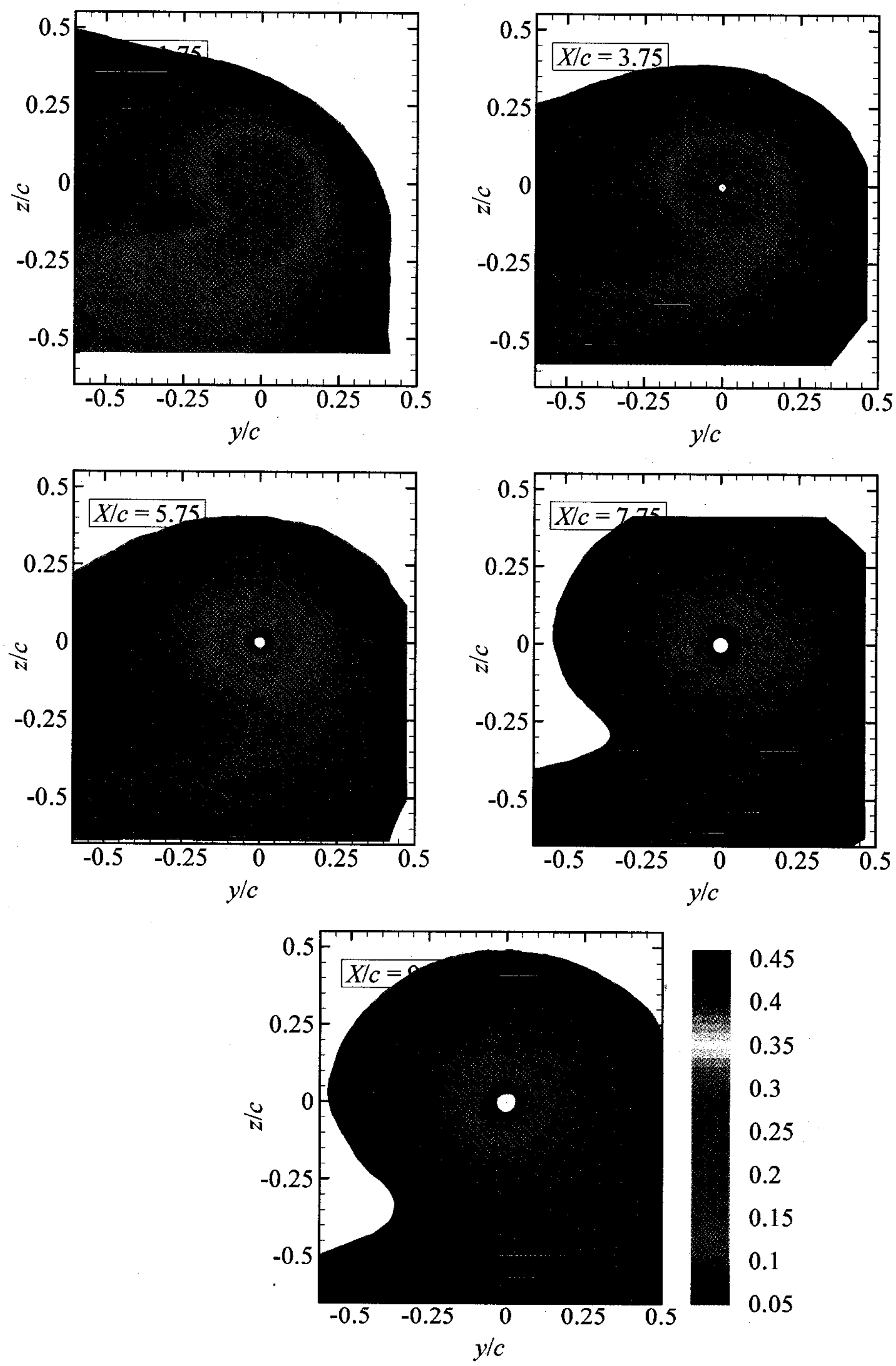

Figure 5.42: Contours of $\overline{U}_\theta/U_o$ for each streamwise plane measured for the large-grid case. Contour lines are spaced 0.05 apart and the contour colouring below 0.05 not shown. Dashed line indicates the locus of the local minima of $\overline{U}_x/U_o$ in the spiral wake.

the same trajectory, as illustrated by the dashed lines in Figures 5.38-5.42.

The axi-symmetric region of $\overline{U}_\theta/U_o$ near the vortex axis is illustrated by the radial profiles of $\overline{U}_\theta/U_o$, shown in Figures 5.43-5.47, respectively, for each of the five free-stream conditions. The increasing scatter in $\overline{U}_\theta/U_o$ as r/c increases beyond about 0.075 is attributed to the shear layer observed in Figures 5.38-5.42. This scatter diminishes with streamwise distance, which indicates a decrease in the mean shear, as the shear layer becomes integrated into the vortex. To clarify the contribution of measurements in the spiral wake to the overall scatter, such measurements have been indicated by solid symbols in Figures 5.43-5.47. All profiles have a distinct peak with a value $\overline{U}_{\theta\,\max}/U_o$, located at a radial distance $\overline{r}_{\theta\,\max}/c$. Both the peak values and the peak locations have been identified in the figures. Other than a decreasing amount of scatter in the data, the no-grid circumferential velocity profile showed little change with streamwise distance (Figure 5.43). In contrast, the peak in the small-grid and small-grid-upstream profiles decreased measurably and moved to clearly larger radial positions (Figures 5.44-5.45). The same trends were demonstrated in a much more dramatic way by the large-grid-upstream and large-grid profiles (Figures 5.46-5.47). For comparative purposes, the region encircled within the radius of the peak in the mean circumferential velocity will be referred to as the apparent vortex core. The term apparent is used to reflect the influence of vortex wandering on point statistics, which can obscure the actual $\overline{U}_{\theta\,\max}$ and $\overline{r}_{\theta\,\max}$ of the vortex core by creating the illusion of an apparent diffusion in the results. Correspondingly, the peak amplitude and radial position will be referred to as the apparent core peak velocity and the apparent core radius, respectively.

The changes of the apparent core parameters $\overline{U}_{\theta\,\max}/U_o$ and $\overline{r}_{\theta\,\max}/c$ with stream-

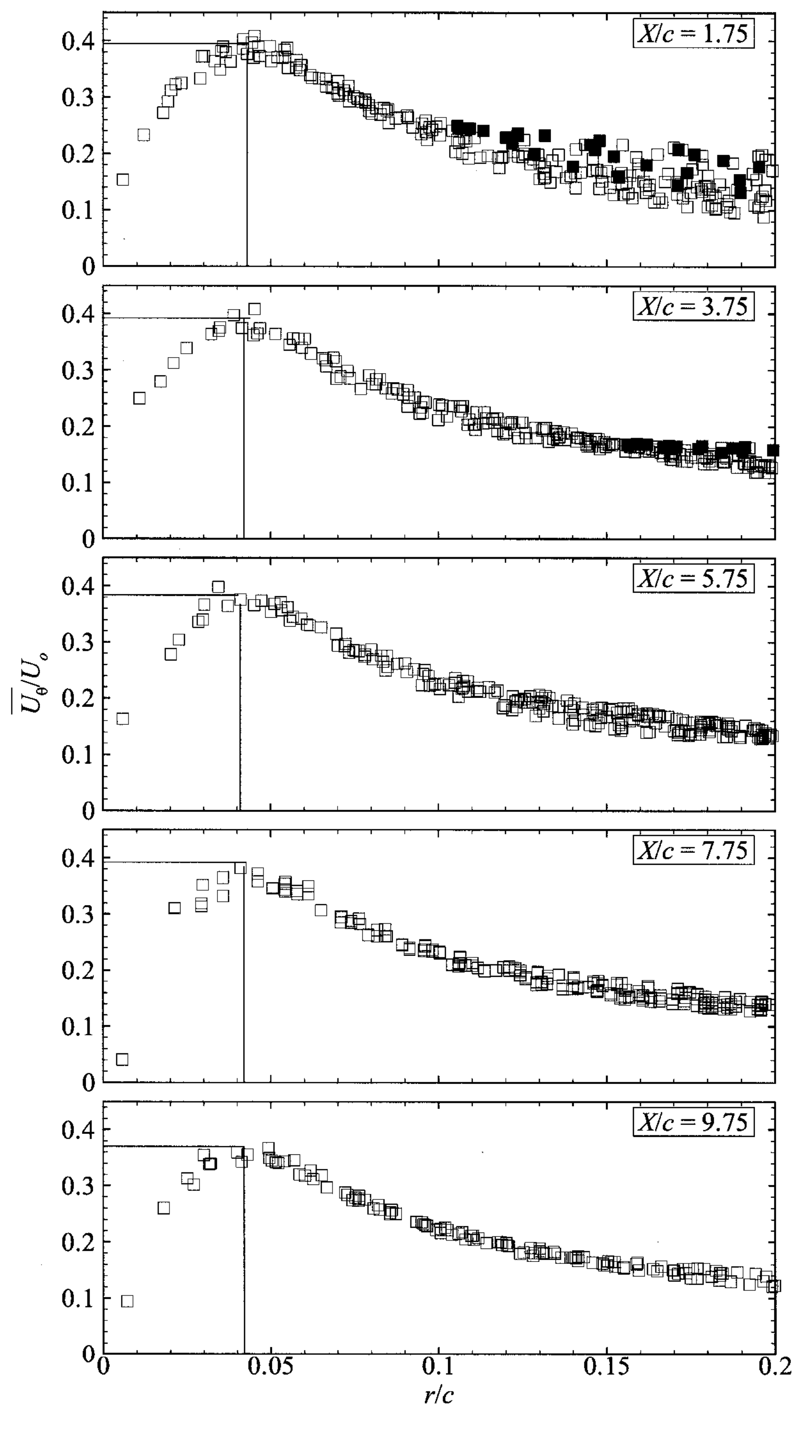

Figure 5.43: Radial variation of the mean circumferential velocity normalized by local free-stream velocity $\overline{U}_\theta/U_o$ for the no-grid case. Solid squares indicate data points located in the spiral wake.

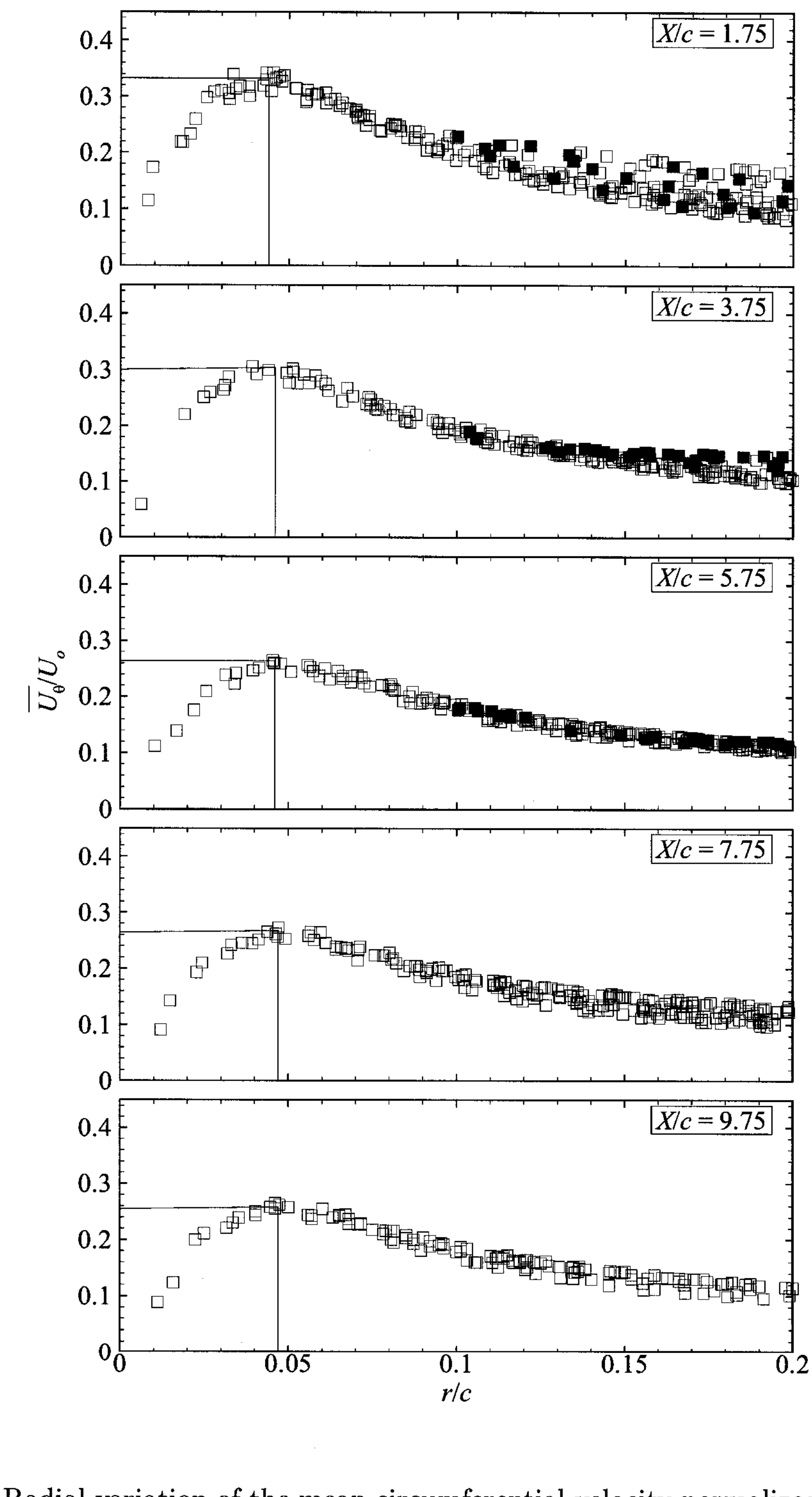

Figure 5.44: Radial variation of the mean circumferential velocity normalized by local free-stream velocity $\overline{U}_\theta/U_o$ for the small-grid-upstream case. Solid squares indicate data points located in the spiral wake.

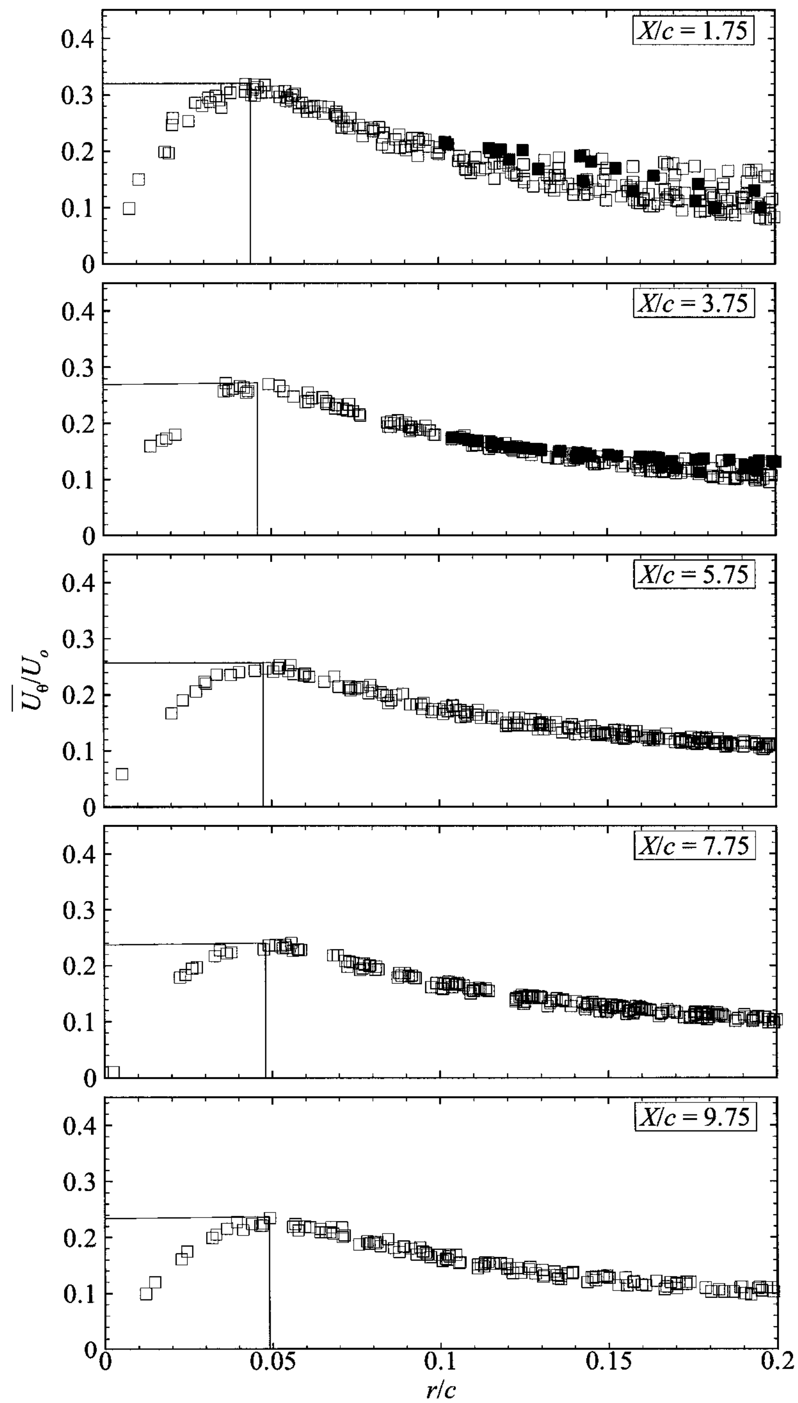

Figure 5.45: Radial variation of the mean circumferential velocity normalized by local free-stream velocity $\overline{U}_\theta/U_o$ for the small-grid case. Solid squares indicate data points located in the spiral wake.

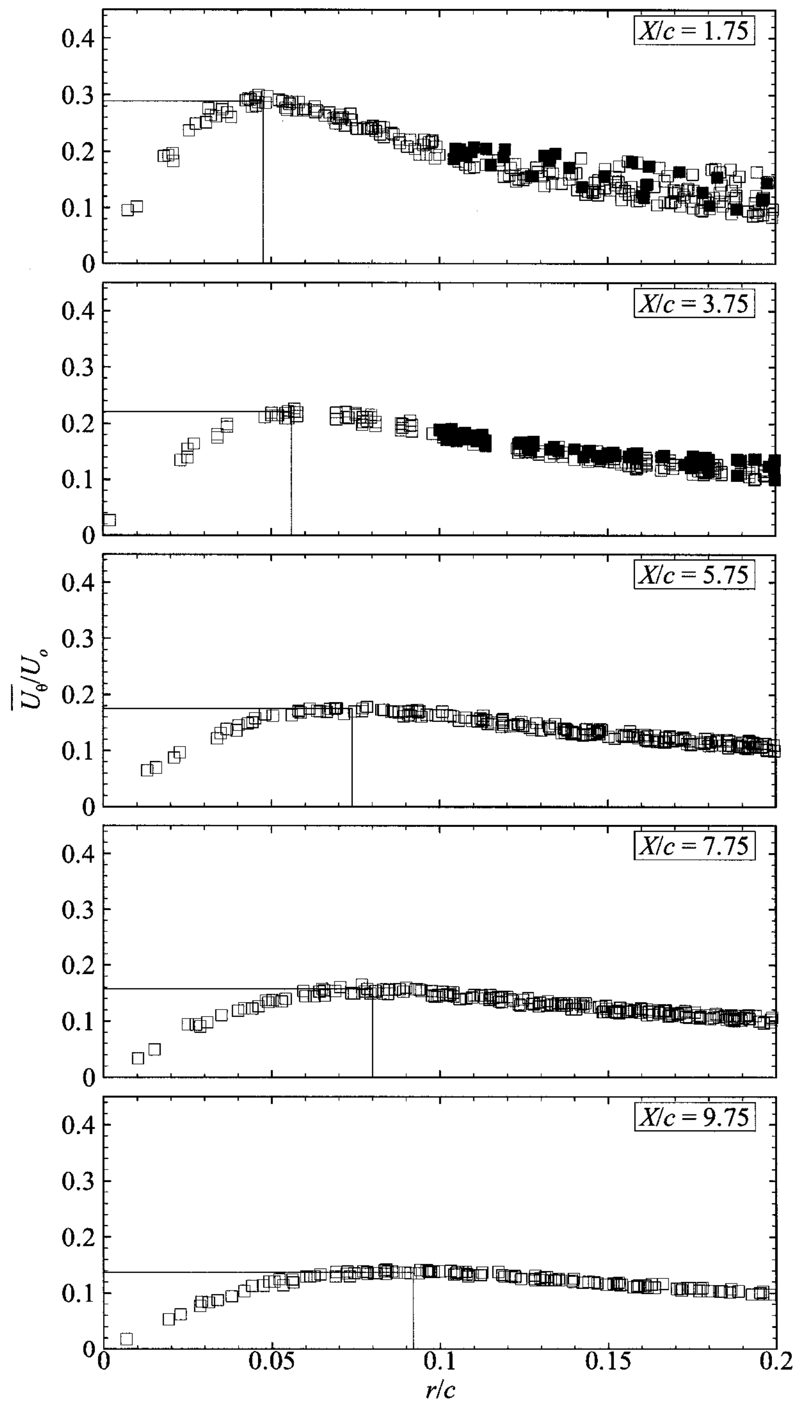

Figure 5.46: Radial variation of the mean circumferential velocity normalized by local free-stream velocity $\overline{U}_\theta/U_o$ for the large-grid-upstream case. Solid squares indicate data points located in the spiral wake.

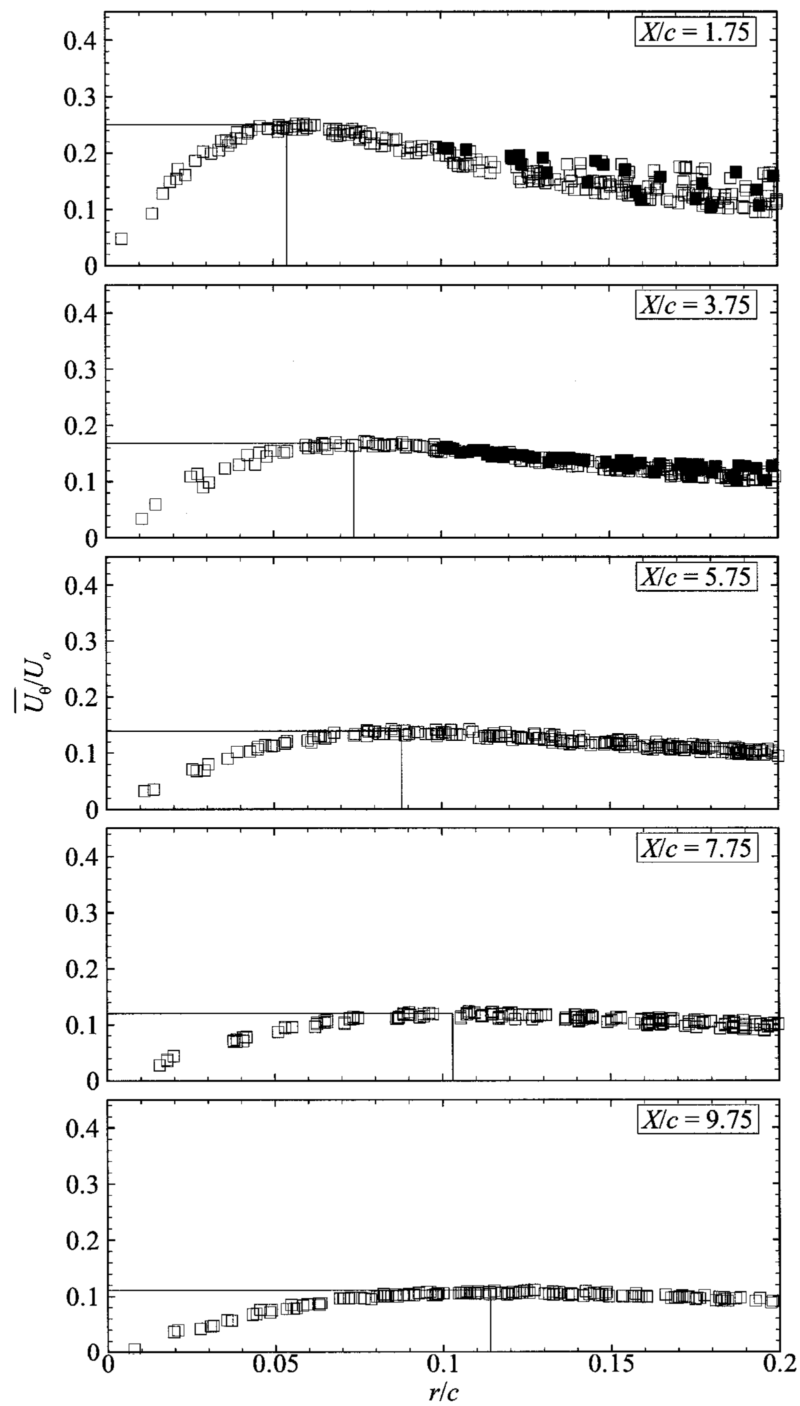

Figure 5.47: Radial variation of the mean circumferential velocity normalized by local free-stream velocity $\overline{U}_\theta/U_o$ for the large-grid case. Solid squares indicate data points located in the spiral wake.

wise distance for the three free-stream conditions are illustrated in Figure 5.48a-b. In the no-grid case, these parameters changed only very slightly, if at all, which indicates that the corresponding profiles were essentially free of wandering effects. Vortex wandering would appear as an apparent diffusion of these profiles, causing $\overline{U}_{\theta\,\max}$ to decay and $\overline{r}_{\theta\,\max}$ to grow, with both effects intensified with increasing free-stream turbulence. The changes of both parameters with streamwise distance could be well represented by fitted power laws as

$$\overline{U}_{\theta\,\max}/U_o = A\,(X/c)^{-m} \tag{5.16}$$

$$\overline{r}_{\theta\,\max}/c = B\,(X/c)^{n} \tag{5.17}$$

with the coefficients and exponents summarized in Table 5.1.

Case	A	m	B	n
small grid upstream	0.36	0.15	0.04	0.04
small grid	0.35	0.18	0.04	0.06
large grid upstream	0.38	0.43	0.04	0.39
large grid	0.32	0.48	0.04	0.43

Table 5.1: Fitted power law coefficients.

Time-averaged radial profiles of the circumferential velocity are subjected to the effects of vortex wandering, which become stronger with increasing free-stream turbulence. This can be further illustrated by considering the change in the angular momentum of the fluid contained in the apparent core. Away from the origin there is no source of external torque that would increase this angular momentum, so one would expect that, if the measured value represented well the corresponding value in the wandering vortex, it would have to remain constant, or most likely decrease due to viscous actions. The apparent core angular momentum, estimated using the fit of Phillips (1981), was found to be proportional

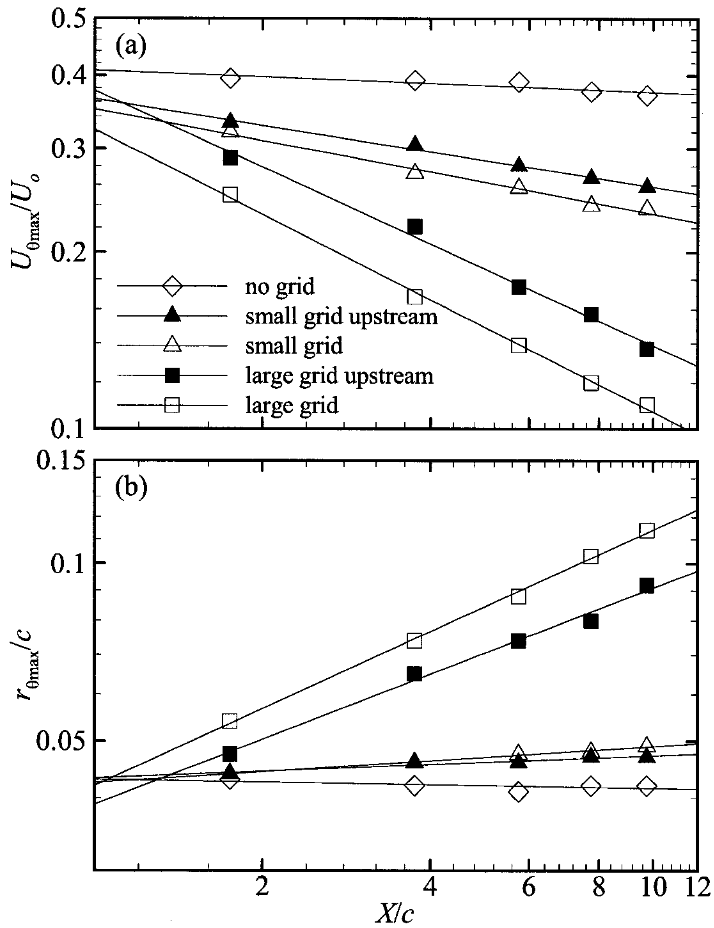

Figure 5.48: Streamwise development of (a) $\overline{U}_{\theta\,\mathrm{max}}/U_o$ and (b) $\overline{r}_{\theta\,\mathrm{max}}/c$. Solid line indicates fitted power law.

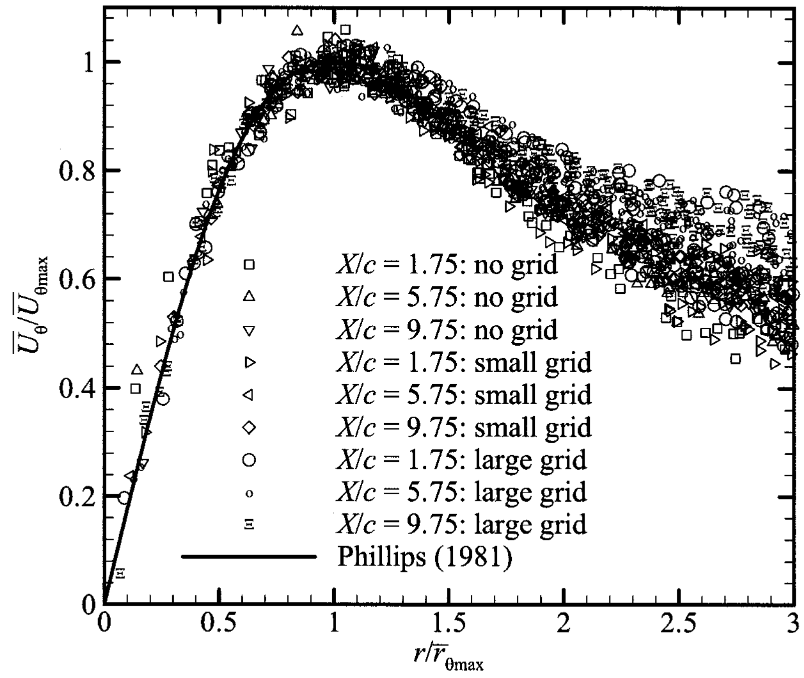

Figure 5.49: Radial profiles of the mean circumferential velocity in normalized axes; the solid line is a self-similar curve proposed by Phillips.

to $\overline{r}^3_{\theta\,\max}\overline{U}_{\theta\,\max}$ and increased for the large-grid cases. These results clearly demonstrate an increasing influence of vortex meandering on the circumferential velocity profiles.

The circumferential velocity profiles in the apparent cores of wing-tip vortices in non-turbulent free streams are expected to develop in a self-similar fashion, if $\overline{U}_\theta$ and r are normalized by the peak value $\overline{U}_{\theta\,\max}$ and the peak radius $\overline{r}_{\theta\,\max}$, respectively (Phillips (1981)). Figure 5.49 shows that this applies not only to the present no grid case but also to profiles in cases of grid turbulence. In all cases, collapse of the data was fairly consistent within the range $r/\overline{r}_{\theta\,\max} < 1.2$, but the scatter increased with increasing dimensionless radius outside that range.

The data within the apparent vortex core were described fairly well by the curve fit proposed by Phillips (1981), who also noted that, for $r/\overline{r}_{\theta\,\mathrm{max}} \gtrsim 1.2$, the circumferential velocity profile would not be self-similar, but its shape would depend on the conditions occurring during vortex formation. It is interesting to note that the mean velocity profiles for the turbulent free streams develop in self-similar fashions, despite the fact that they are strongly influenced by vortex meandering and could, therefore, be quite different from the corresponding instantaneous velocity profiles. It is not clear whether this would be the case if the free stream had an arbitrary turbulence structure, as grid turbulence also develops self-similarly.

5.10 Time-averaged circulation

In the present study, the mean time-averaged circulation was found by interpolating U_θ/U_o to a circular mesh with linearly spaced nodes in both the r/c and θ directions centred on the time-averaged vortex axis. Circulation as a function of radial distance was then estimated from

$$\overline{\Gamma}\,(r) = \int_0^{2\pi} \overline{U}_\theta\,(r)\, r\mathrm{d}\theta\ , \tag{5.18}$$

where the integration was performed numerically. Radial profiles of $\overline{\Gamma}/U_o c$ are presented at $X/c = 1.75, 3.75, 5.75, 7.75$ and 9.75 in Figure 5.50 for each of the five free-stream conditions.

The radial profiles of circulation in the no-grid case, shown in Figure 5.50a, change only slightly as the vortex develops downstream. Within the vortex core, the circulation remains essentially unchanged, whereas, at larger radii, there is a small but measurable increase in circulation with increasing streamwise distance. Most likely this can be attributed to the observation that vorticity from the spiral shear layer is gradually being

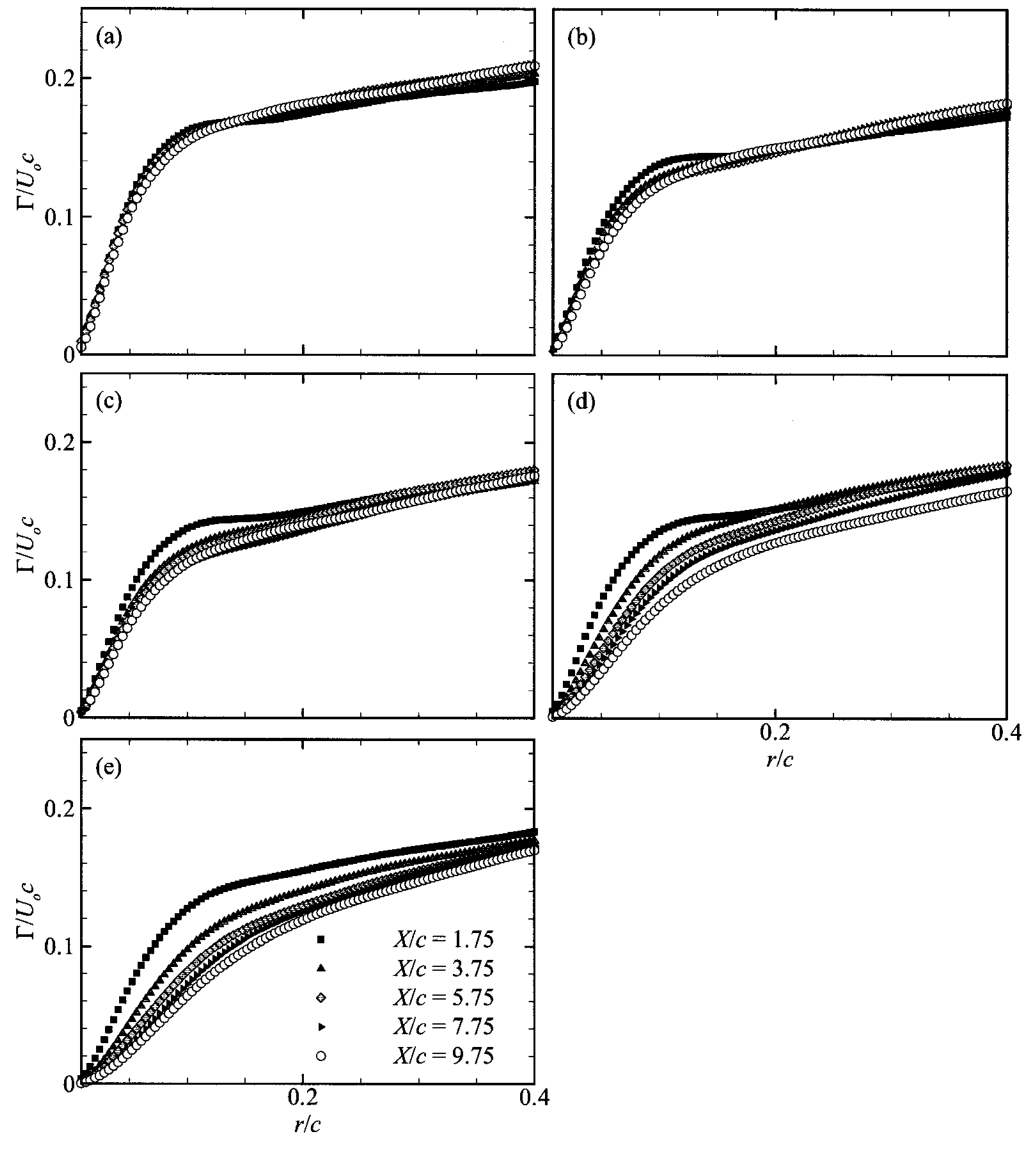

Figure 5.50: Radial variation of $\overline{\Gamma}/U_o c$ at each streamwise measurement location for the (a) no-grid, (b) small-grid-upstream, (c) small-grid, (d) large-grid-upstream and (e) large grid cases.

wrapped around the vortex and becomes drawn into the region of integration as the vortex evolves downstream.

For the cases with grid turbulence, the circulation is noticeably lower than for the no-grid case over the entire radial range considered, which is somewhat surprising considering the similarity of the lift distributions shown in Figure 5.26. The small-grid-upstream case, shown in Figure 5.50b, reflects similar behaviour as that of the no-grid case at large radii. Near the time-averaged vortex centre, there is a decrease in circulation with increasing streamwise distance. This decrease in circulation is also evident in the other grid turbulence cases and reflects the diffusion of the apparent vortex core discussed above. At large radii, the small-grid case and large-grid upstream cases, Figure 5.50c and Figure 5.50d, respectively, show an initial increase in circulation, followed by a decrease as streamwise distance increases. The large-grid case, Figure 5.50e , indicates a decrease in circulation over all radii. Although the radial profiles of $\overline{U}_\theta$ are strongly influenced by wandering, this influence decreases as r increases (Devenport et al. (1996)), hence the decrease in $\overline{\Gamma}$ observed for the grid cases at large r is expected to be minimally affected by wandering.

5.11 Time-averaged turbulent kinetic energy and Reynolds stresses

The time-averaged turbulent kinetic energy and Reynolds stresses were found to be strongly affected by vortex wandering. For this reason, these results are not presented in detail and discussed in the main part of the thesis. However, because the distributions of the turbulent kinetic energy and Reynolds stresses would be of value as a reference to both numerical modelers and experimentalists, they are presented in Appendix A. A brief summary of the main observations based on these results is as follows.

Three-dimensional plots of the distributions of the turbulent kinetic energy, k/U_o^2, and Reynolds normal stresses, $\overline{u_x^2}/U_o^2$, $\overline{u_y^2}/U_o^2$ and $\overline{u_z^2}/U_o^2$, on transverse planes demonstrate that the wing wake can be identified as a thin region in which the velocity fluctuations were greater than the free-stream level. The fluctuations in the wing wake were observed to decrease with streamwise distance. The amplitude of velocity fluctuations for the two large-grid cases essentially reached the free-stream level at $X/c = 9.75$.

Peaks of k, $\overline{u_x^2}$, $\overline{u_y^2}$ and $\overline{u_z^2}$ considerably greater than values observed in the free-stream and the spiral wake were observed at the time-averaged vortex axis. These peaks could be entirely attributed to vortex wandering. The relationship between the amplitudes and distributions of the peaks and the wandering amplitude is discussed in Appendix A.

Due to the spiralling nature of the wake, Reynolds shear stresses calculated using a Cartesian coordinate system do not have much physical relevance within the spiral wake and therefore are not presented in this document. However the Reynolds shear stresses $\overline{u_x u_y}/U_o^2$, $\overline{u_x u_z}/U_o^2$ and $\overline{u_y u_z}/U_o^2$ measured near the vortex axis during the high-resolution core-centred measurements at $X/c = 9.75$ are presented in Appendix A. As with the Reynolds normal stresses, the shapes of the distributions of the Reynolds shear stresses near the vortex axis are attributed to vortex wandering.

5.12 Frequency spectra

Frequency spectra (previously defined in Equation 5.13 for the streamwise direction) of the three velocity components were measured at various locations along the line $z \approx 0$ and at the streamwise locations $X/c = 1.75$, 5.75 and 9.75 at $\mathrm{Re}_c = 2.4 \times 10^5$. These spectra are not easy to interpret as, besides conventional turbulence within the vortex, they also contain the effects of wandering, especially near the time-averaged vortex axis. In addition to low frequency energy caused by the vortex wandering, wandering will also act to average the spectra spatially as the probe will be moving in time relative to the instantaneous vortex centre. Due to the influence of vortex wandering, features evident in the frequency spectra that are observed for the no-grid case might be obscured in the corresponding spectra for the small-grid and large-grid cases, even though the physical process that causes these features could also exist for these cases. Due to this difficulty of interpretation, only sample frequency spectra F_{yy} of U_y are shown in this section. Frequency spectra of U_x and U_z were also calculated and but are not shown for brevity. Although the details of F_{xx} and F_{zz} are slightly different from F_{yy}, the interpretation of the spectra is the same as described below for F_{yy}.

Spectra at $X/c = 1.75$: Sample frequency spectra F_{yy} of U_y are shown in Figures 5.51, 5.52 and 5.53 for the no-grid, small-grid and large-grid cases, respectively. First, let us examine the spectra at the locations furthest away from the time-averaged vortex axis, within the range $y/c < -0.15$. In the no-grid case, the spectra was quite similar to that measured for the empty wind-tunnel (Figure 4.5) and thus can be attributed mostly to fluctuations of the wind tunnel speed rather than turbulence or vortex wandering effects. Correspondingly, the spectra for $y/c < -0.15$ in the two grid cases were comparable to those in the corresponding grid turbulence without the wing (Figures 5.17b and d).

As the measurement location approached the time-averaged vortex axis, the spectra changed dramatically. In the no-grid case, a large increase in energy for $f > 1\,\mathrm{kHz}$, including broad-band peaks near $3\,\mathrm{kHz}$ evident in the spectra at $y/c = -0.10$ and $y/c = -0.07$ were observed. This broadband peak has an appearance similar to those measured by Devenport et al. (1996) and Miranda and Devenport (1998) who associated the peak with dominant eddies in the spiral wake. Examination of Figures 5.28 and A.7 indicate that the location $y/c = -0.10$ could also be within the spiral wake, which indicates that the broadband peak observed in Figure 5.51 is probably also due to spiral wake eddies.

Within the range $-0.10 < y/c < 0$, there was also an order of magnitude increase in energy within the range $0 < f \lesssim 100\,\mathrm{Hz}$ for all three cases, most noticeably for the small-grid and large-grid cases. In both cases, the spectra exhibited plateaux within the range $0 < f \lesssim 100\,\mathrm{Hz}$,, followed by a power-law drop-off with an exponent of approximately -2.1 for $f \gtrsim 100\,\mathrm{Hz}$. This region is most likely associated with energy contributions caused by wandering of the wing tip vortex and is investigated in more detail in Section 6.2.2.

Spectra at $X/c = 5.75$: Sample frequency spectra F_{yy} of U_y are shown in Figures 5.54, 5.55 and 5.56 for the no-grid, small-grid and large-grid cases, respectively. Again, at the measurement locations furthest from the time-averaged vortex axis, $y/c < -0.25$, the power spectra for all three cases were comparable to those measured without the wing in the tunnel (Figures 4.5, and 5.17b,d). As the time-averaged vortex axis is approached, the no-grid case spectra show increasing energy with decreasing radius for $f > 1\,\mathrm{kHz}$ until $|y| < \overline{r}_{\theta\,\mathrm{max}}$, where the energy in this range decreases. This could indicate the relaminarization of turbulent eddies entrained in the vortex core during formation. A broadband peak was also evident for $|y| < \overline{r}_{\theta\,\mathrm{max}}$ with the central frequency of the peak varying between approximately 800 Hz and 1 kHz. Within the vortex core, this peak is most likely associated with an instability in the vortex as discussed by Singh and Uberoi (1976), Bandyopadhyay et al. (1991), Jacquin et al. (2001) and others. Thorough examination of this instability is beyond the scope of the current study and, as a result, is only briefly discussed in Section 7.2.

For $y/c > -0.10$, an increase of low frequency energy in the range $10 < f \lesssim 100\,\mathrm{Hz}$ was evident, with the spectra in Figure 5.54 appearing to plateaux for $10 < f \lesssim 60Hz$. This plateaux is expected to be associated with vortex wandering and will be further addressed in 6.2.2. As the time-averaged vortex centre was approached, the amount of energy in this range increased and a roll-off with a slope of approximately -2.1 becomes evident. This increase in low frequency energy was also evident at $X/c = 5.75$ in the small-grid and large-grid cases for $y/c > -0.13$. For the small-grid case, the roll-off occurred for $f \gtrsim 100\,\mathrm{Hz}$ and had a slope of approximately -2.8 whereas for the large-grid case, the roll-off occurred for $f \gtrsim 80\,\mathrm{Hz}$ at a slope of approximately -2.4.

Spectra at $X/c = 9.75$: Sample frequency spectra F_{yy} of U_y are shown in Figures 5.57, 5.58 and 5.59 for the no-grid, small-grid and large-grid cases, respectively. The same characteristics were evident at $X/c = 9.75$ as for $X/c = 1.75$ and $X/c = 5.75$, although the details are slightly different. An increase in energy at $f > 1\,\mathrm{kHz}$ for $-0.2 < y/c < -0.04$

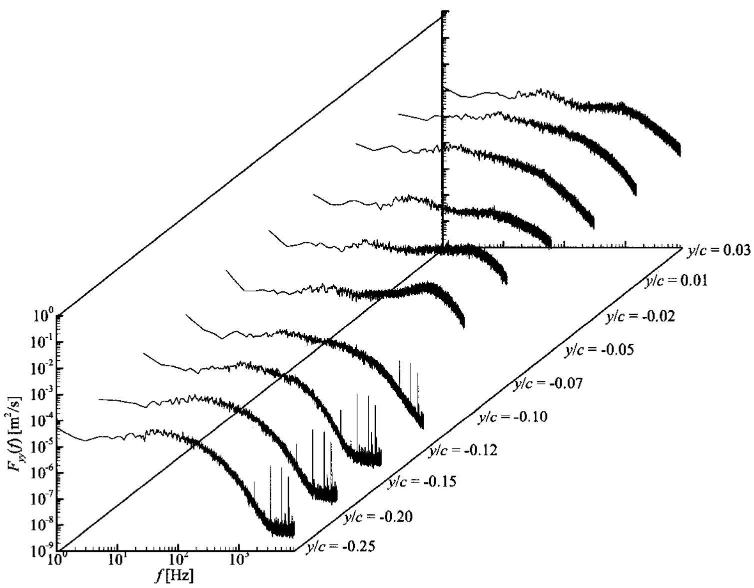

Figure 5.51: Frequency spectra $F_{yy}(f)$ at various y/c locations along a line through the time-averaged vortex centre for the no-grid case at $X/c = 1.75$.

was observed for the no-grid case, with a decrease in energy in this high frequency range evident for $|y| < r_{\theta\,\mathrm{max}}$ indicating relaminarization of the core. A broadband peak, possibly associated with instability in the vortex core, is evident for the no-grid case for $y/c > -0.07$ in Figure 5.57. This peak is centred between approximately 800 Hz and 1 kHz . The low frequency energy increase associated with vortex wandering occurred for $f \lesssim 60$ Hz with a slope of approximately -2.8 for both the no-grid and small-grid cases, and for $f \lesssim 60$ Hz with a slope of approximately -2.1 for the large-grid case.

5.13 Anisotropy tensor

To further investigate changes to the turbulent flow field surrounding the vortex, each component of the anisotropy tensor was calculated using Equation 5.3 and the distri-

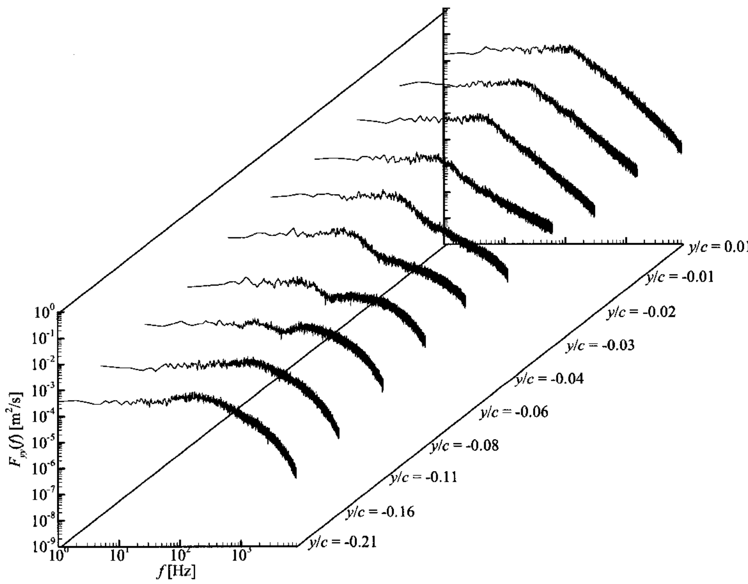

Figure 5.52: Frequency spectra $F_{yy}(f)$ at various y/c locations along a line through the time-averaged vortex centre for the small-grid case at $X/c = 1.75$.

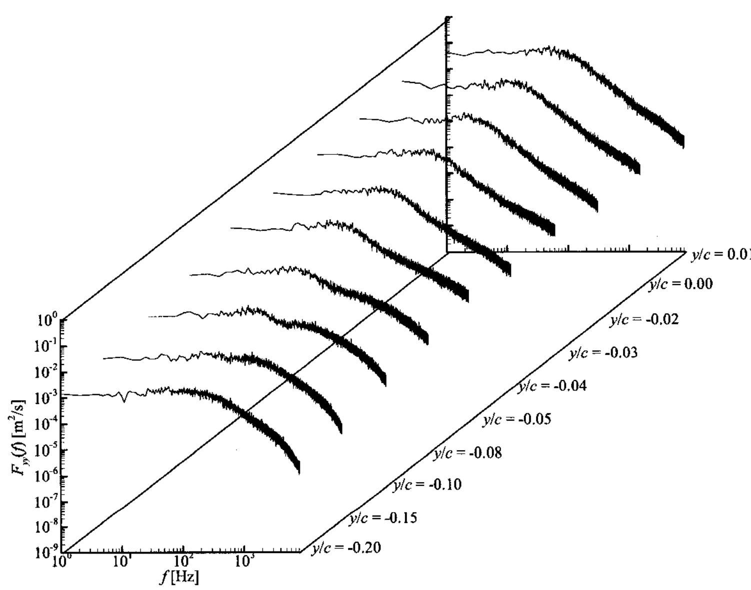

Figure 5.53: Frequency spectra $F_{yy}(f)$ at various y/c locations along a line through the time-averaged vortex centre for the large-grid case at $X/c = 1.75$.

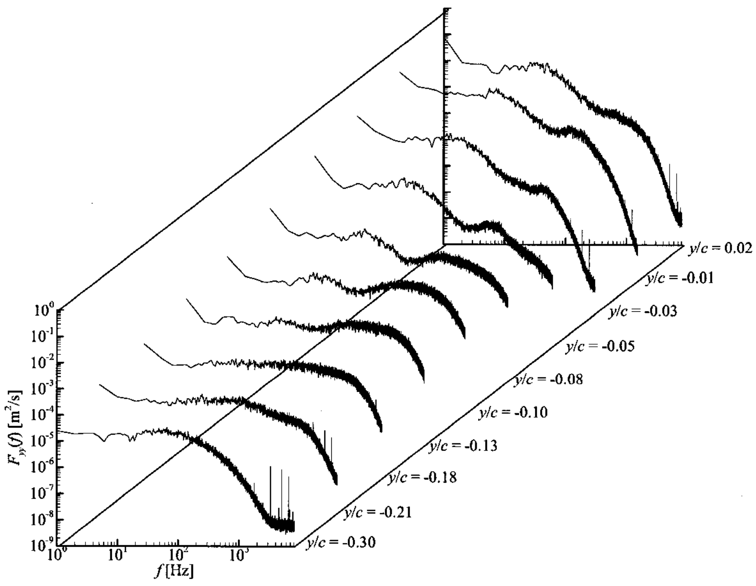

Figure 5.54: Frequency spectra $F_{yy}(f)$ at various y/c locations along a line through the time-averaged vortex centre for the no-grid case at $X/c = 5.75$.

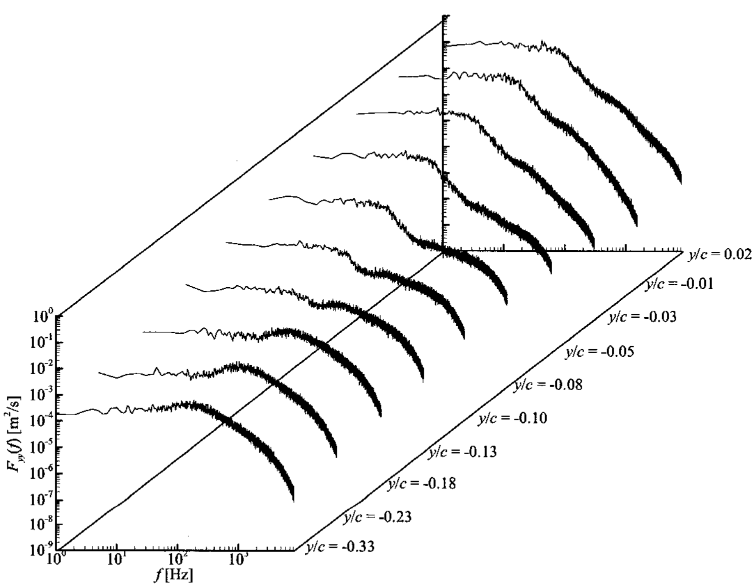

Figure 5.55: Frequency spectra $F_{yy}(f)$ at various y/c locations along a line through the time-averaged vortex centre for the small-grid case at $X/c = 5.75$.

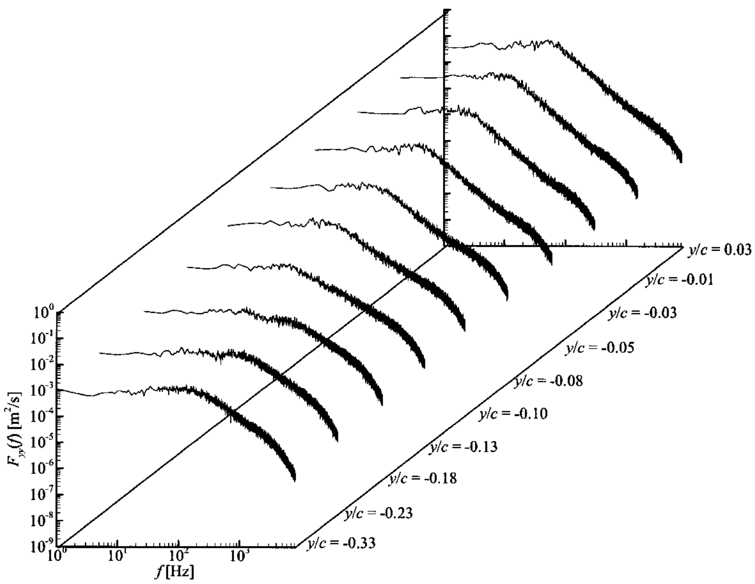

Figure 5.56: Frequency spectra $F_{yy}(f)$ at various y/c locations along a line through the time-averaged vortex centre for the large-grid case at $X/c = 5.75$.

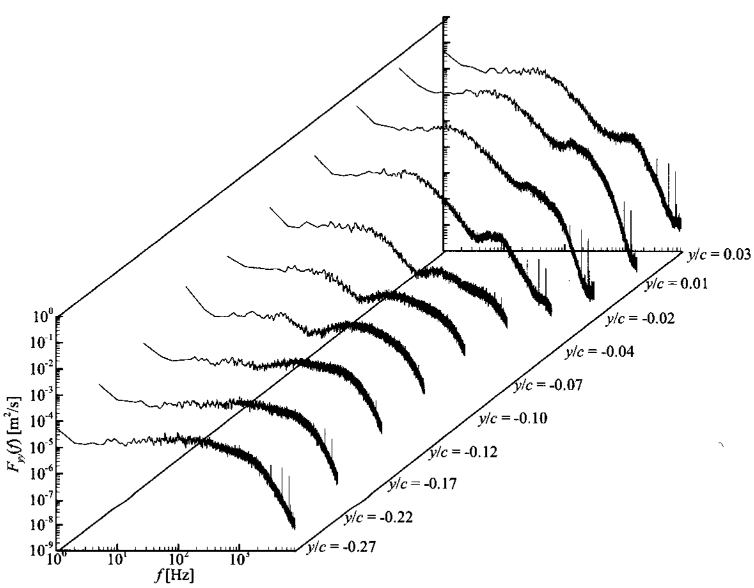

Figure 5.57: Frequency spectra $F_{yy}(f)$ at various y/c locations along a line through the time-averaged vortex centre for the no-grid case at $X/c = 9.75$.

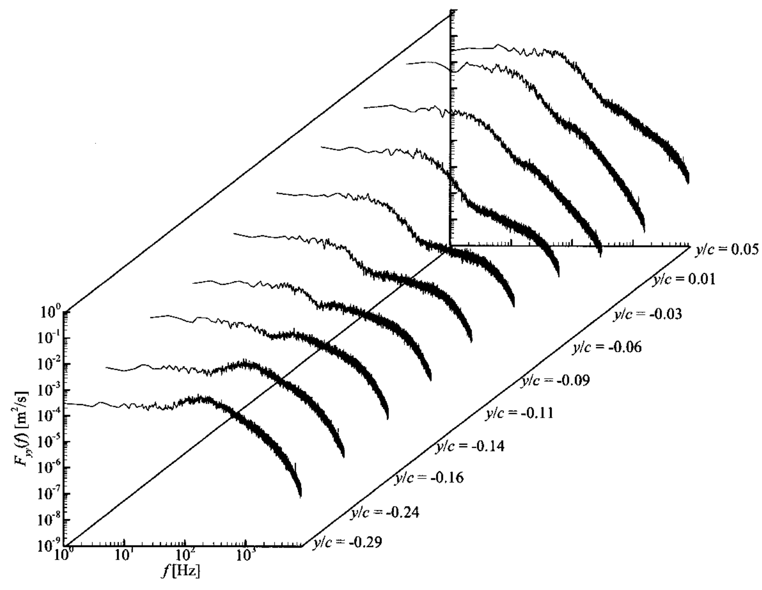

Figure 5.58: Frequency spectra $F_{yy}(f)$ at various y/c locations along a line through the time-averaged vortex centre for the small-grid case at $X/c = 9.75$.

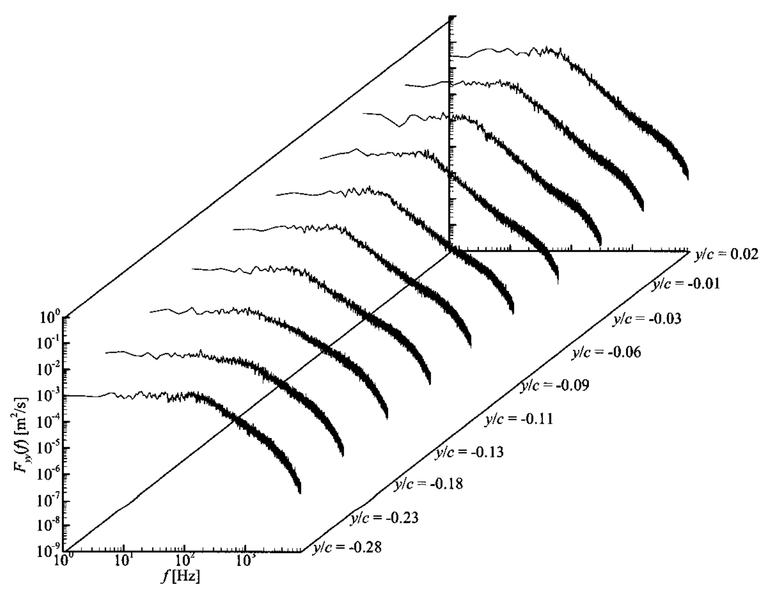

Figure 5.59: Frequency spectra $F_{yy}(f)$ at various y/c locations along a line through the time-averaged vortex centre for the large-grid case at $X/c = 9.75$.

bution of the component across the yz plane examined. The distribution of a_{xx} for the no-grid, small-grid and large-grid cases at $X/c = 1.75$, 5.75 and 9.75 is shown as isocontours of a_{xx} in Figure 5.60. Similar contour plots of a_{yy}, a_{zz}, a_{xy}, a_{xz} and a_{yz} are shown in Figures 5.61-5.65, respectively. In these plots, the range $-0.02 < a_{ij} < 0.02$, the approximate range of a_{ij} measured in the grid turbulence with the wing removed, is left white to show the regions of nearly isotropic fluctuations. For the no-grid case, components of a_{ij} measured outside the spiral wake and the vortex have little physical significance due to the lack of turbulence in this region.

The distributions of a_{xx} shown in Figure 5.60 are similar for all three cases at all streamwise positions; they consist of an axi-symmetric region of negative a_{xx} at the time-averaged vortex axis and a region of positive a_{xx} at the edge of the spiral wake. Negative values within the vortex core are consistent with the expected anisotropy caused by vortex wandering, because within the vortex the radial gradients of U_y and U_z are higher than that of U_x. Hence, as the vortex position changes in time, the contribution of wandering to $\overline{u_y^2}$ and $\overline{u_z^2}$ measured at a fixed point will be larger than the contribution to $\overline{u_x^2}$. The region that is influenced strongly by vortex wandering grows with streamwise distance and with free-stream turbulence intensity, indicating that the wandering amplitude and/or the velocity deficit in the core grows with streamwise distance and with increasing free-stream turbulence intensity. Similarly, the streamwise fluctuations within the spiral wake will be higher at the edge of the spiral wake when compared to those in the transverse directions, resulting in positive a_{xx} values.

Both the small-grid and large-grid cases in the free-stream have slightly positive

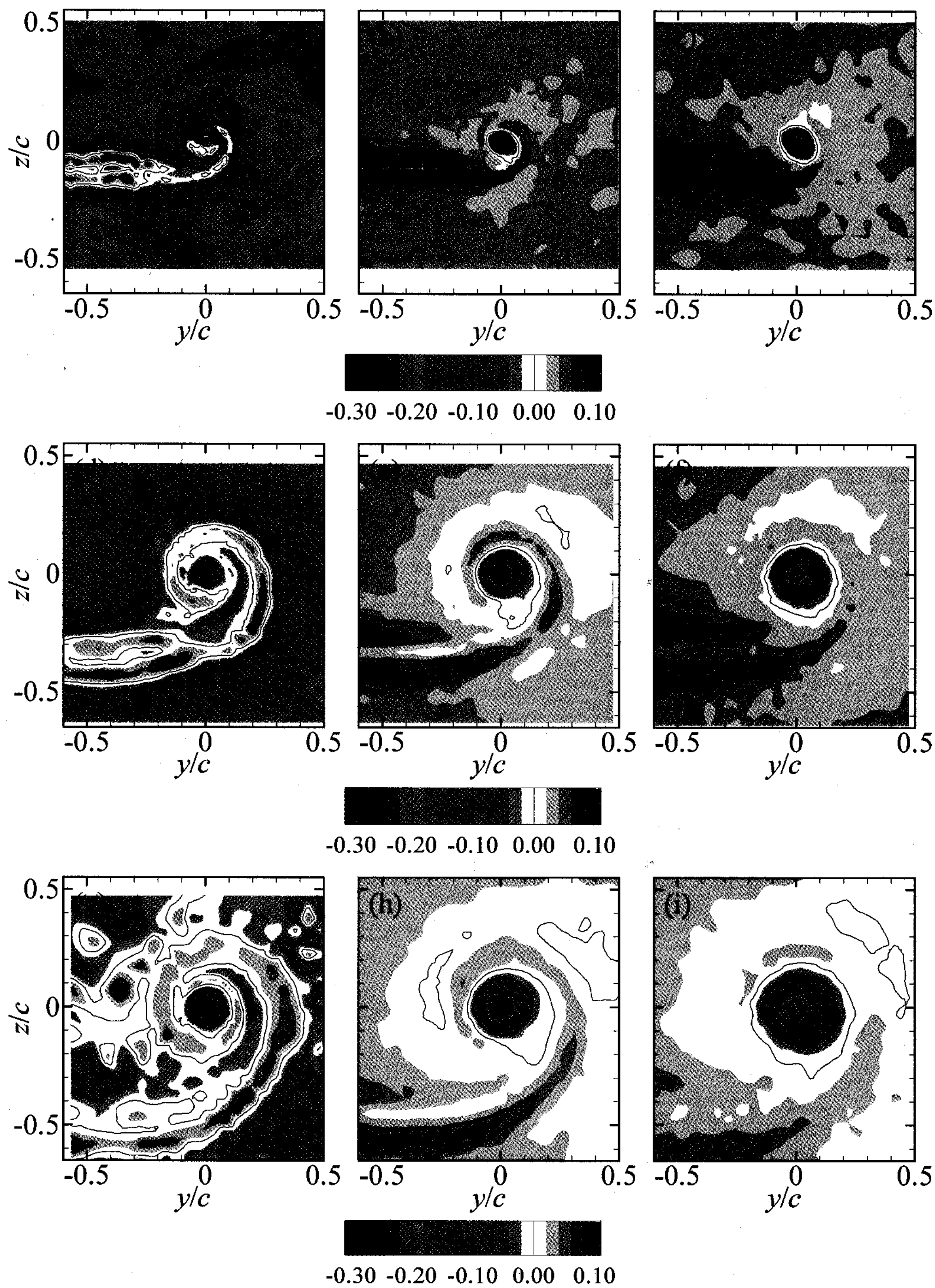

Figure 5.60: Distribution of a_{xx} for the (a) no-grid case at $X/c = 1.75$, (b) the small-grid case at $X/c = 1.75$, (c) the large-grid case at $X/c = 1.75$, (d) the no-grid case at $X/c = 5.75$, (e), the small-grid case at $X/c = 5.75$, (f) the large grid case at $X/c = 5.75$, (g) the no-grid case at $X/c = 9.75$, (h), the small-grid case at $X/c = 9.75$ and (i) the large grid case at $X/c = 9.75$.

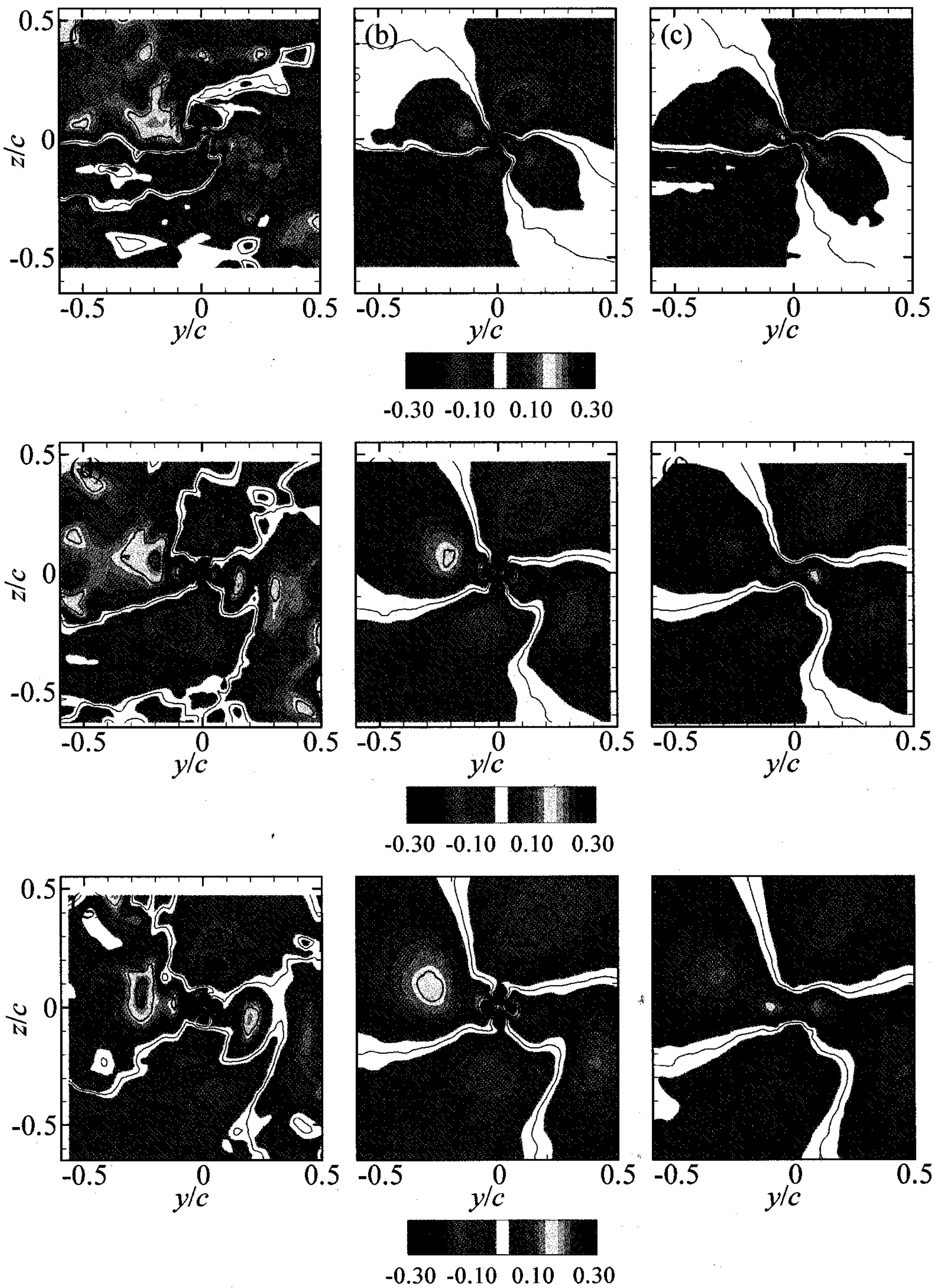

Figure 5.61: Distribution of a_{yy} for the (a) no-grid case at $X/c = 1.75$, (b) the small-grid case at $X/c = 1.75$, (c) the large-grid case at $X/c = 1.75$, (d) the no-grid case at $X/c = 5.75$, (e), the small-grid case at $X/c = 5.75$, (f) the large grid case at $X/c = 5.75$, (g) the no-grid case at $X/c = 9.75$, (h), the small-grid case at $X/c = 9.75$ and (i) the large grid case at $X/c = 9.75$.

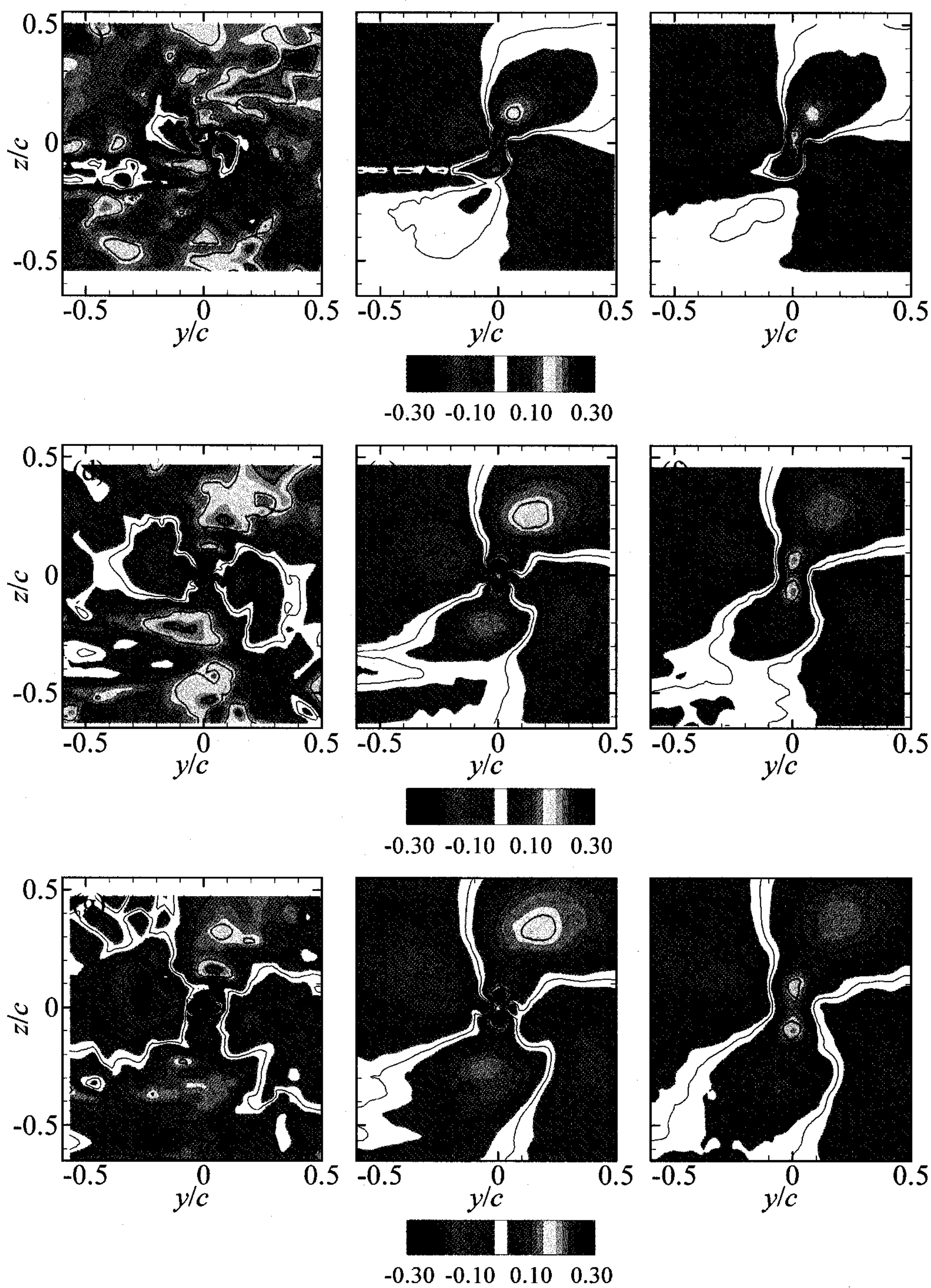

Figure 5.62: Distribution of a_{zz} for the (a) no-grid case at $X/c = 1.75$, (b) the small-grid case at $X/c = 1.75$, (c) the large-grid case at $X/c = 1.75$, (d) the no-grid case at $X/c = 5.75$, (e), the small-grid case at $X/c = 5.75$, (f) the large grid case at $X/c = 5.75$, (g) the no-grid case at $X/c = 9.75$, (h), the small-grid case at $X/c = 9.75$ and (i) the large grid case at $X/c = 9.75$.

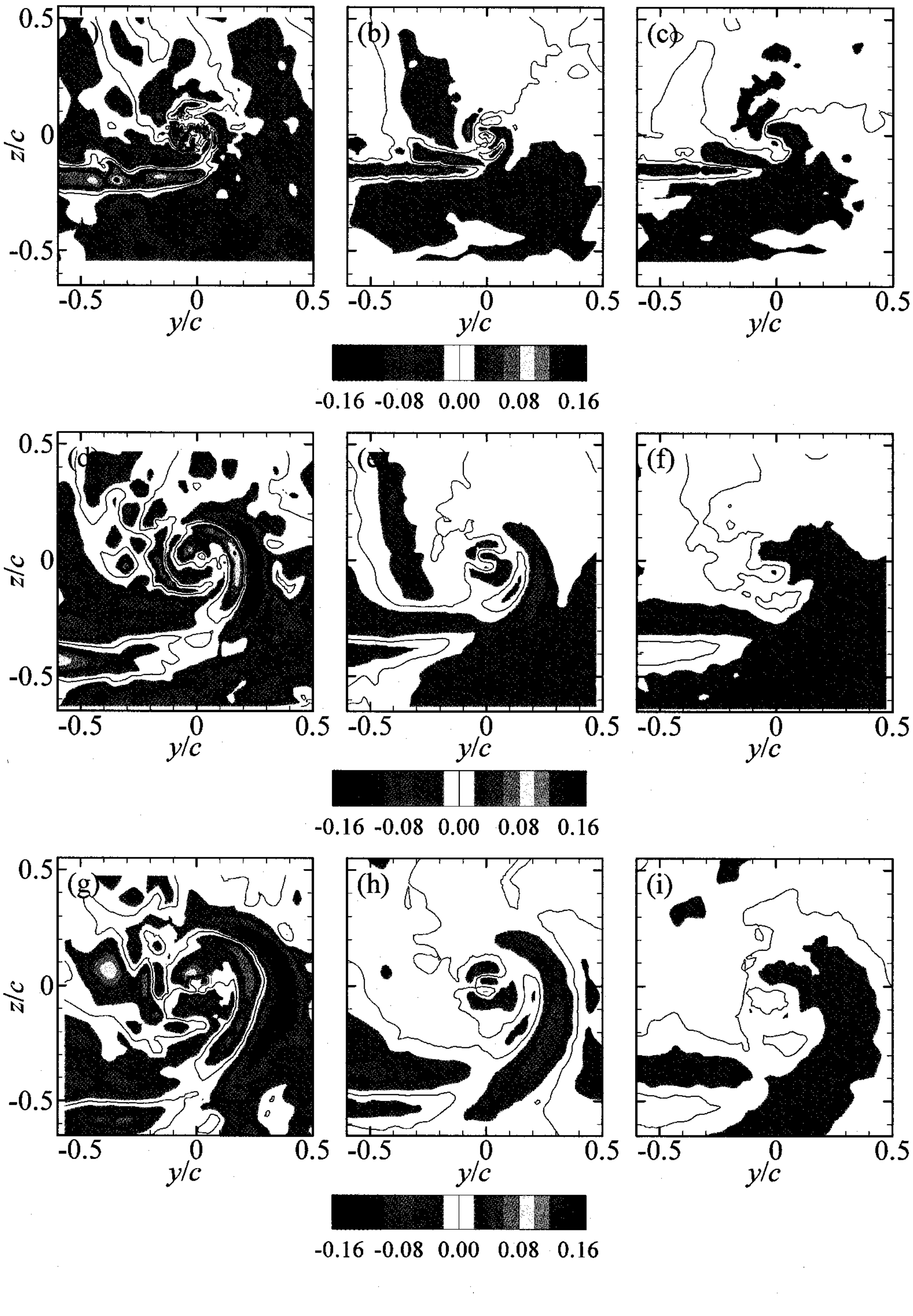

Figure 5.63: Distribution of a_{xy} for the (a) no-grid case at $X/c = 1.75$, (b) the small-grid case at $X/c = 1.75$, (c) the large-grid case at $X/c = 1.75$, (d) the no-grid case at $X/c = 5.75$, (e), the small-grid case at $X/c = 5.75$, (f) the large grid case at $X/c = 5.75$, (g) the no-grid case at $X/c = 9.75$, (h), the small-grid case at $X/c = 9.75$ and (i) the large grid case at $X/c = 9.75$.

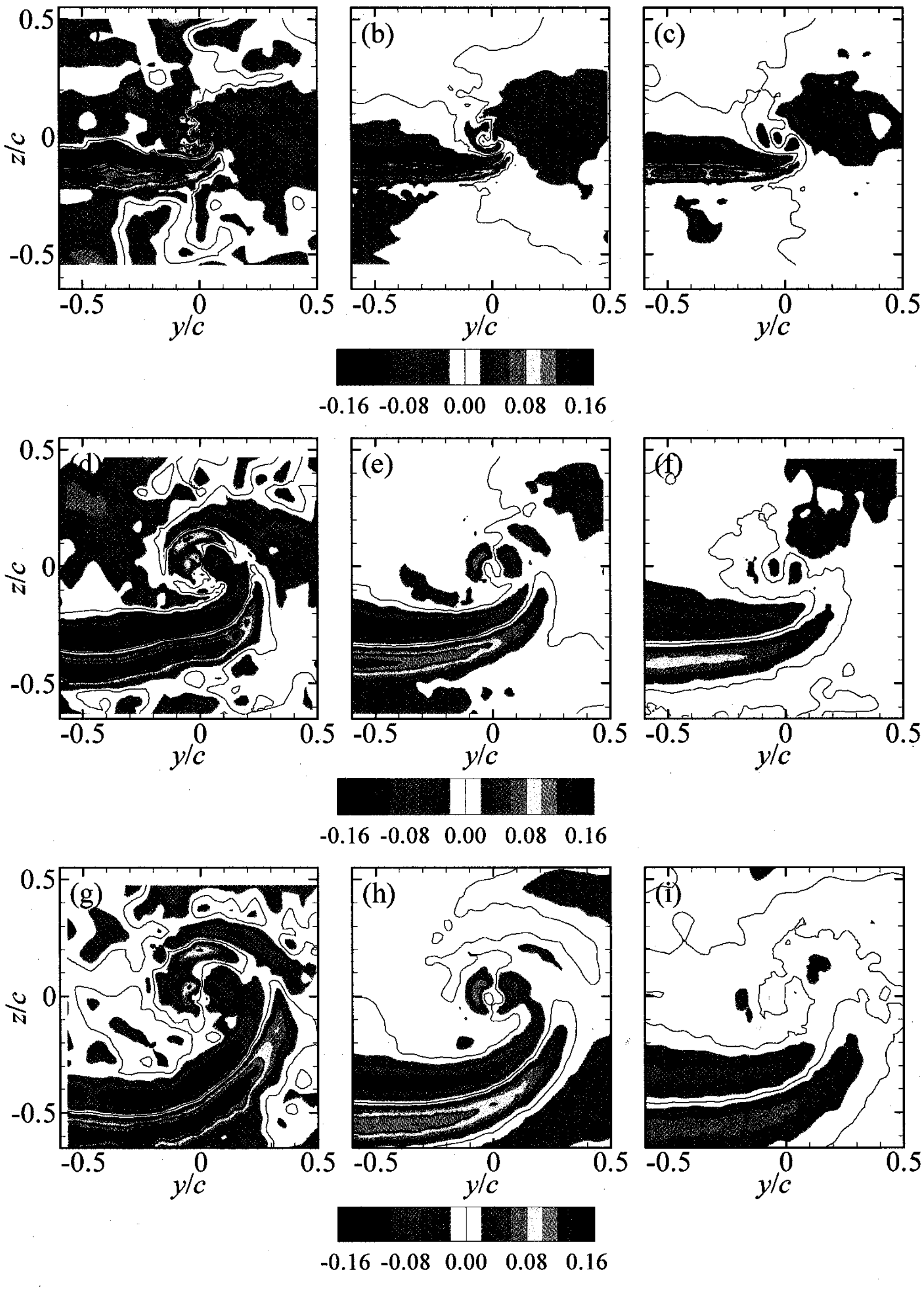

Figure 5.64: Distribution of a_{xz} for the (a) no-grid case at $X/c = 1.75$, (b) the small-grid case at $X/c = 1.75$, (c) the large-grid case at $X/c = 1.75$, (d) the no-grid case at $X/c = 5.75$, (e), the small-grid case at $X/c = 5.75$, (f) the large grid case at $X/c = 5.75$, (g) the no-grid case at $X/c = 9.75$, (h), the small-grid case at $X/c = 9.75$ and (i) the large grid case at $X/c = 9.75$.

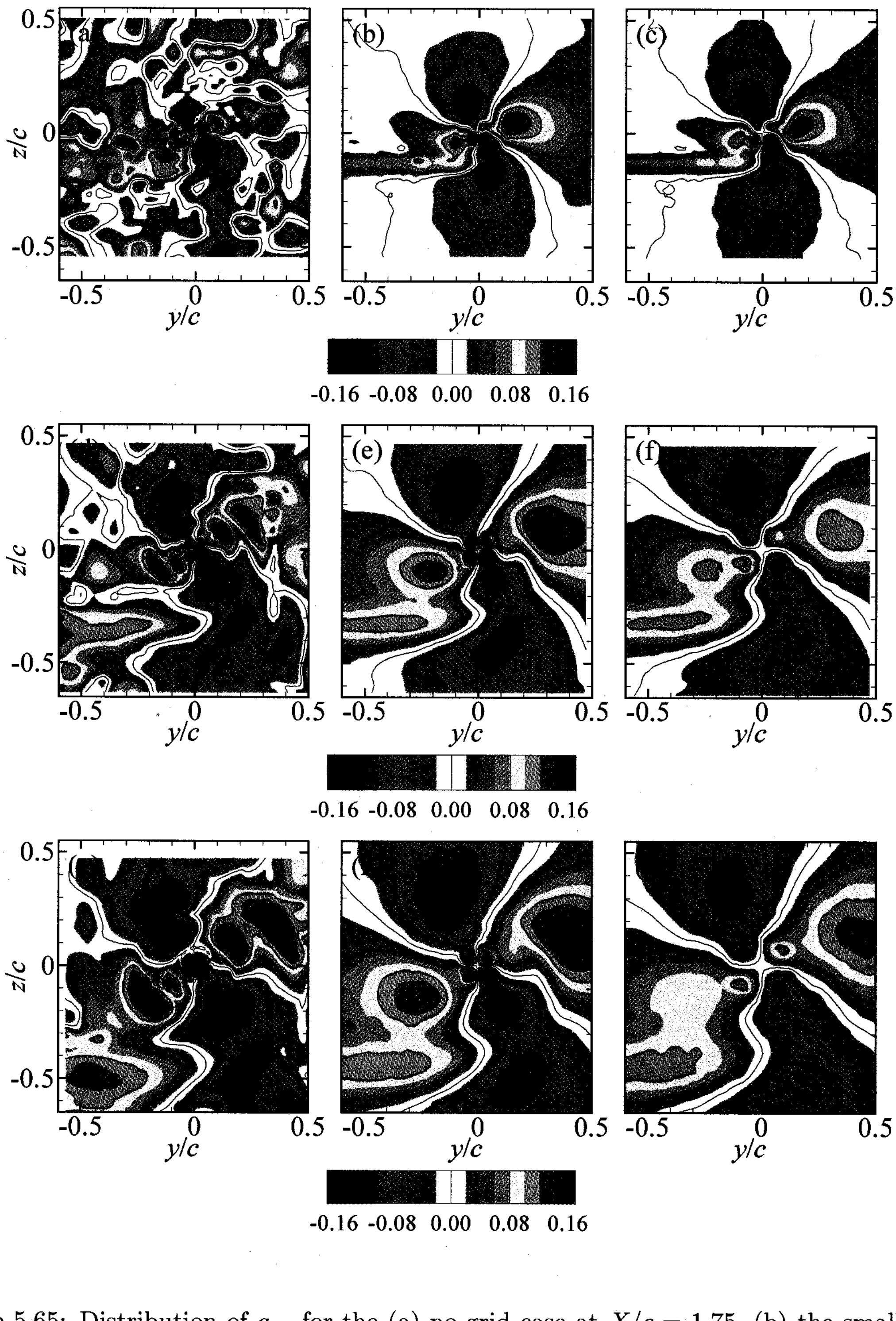

Figure 5.65: Distribution of a_{yz} for the (a) no-grid case at $X/c = 1.75$, (b) the small-grid case at $X/c = 1.75$, (c) the large-grid case at $X/c = 1.75$, (d) the no-grid case at $X/c = 5.75$, (e), the small-grid case at $X/c = 5.75$, (f) the large grid case at $X/c = 5.75$, (g) the no-grid case at $X/c = 9.75$, (h), the small-grid case at $X/c = 9.75$ and (i) the large grid case at $X/c = 9.75$.

values of a_{xx}, consistent of the values of a_{xx} measured in the grid turbulence with the wing removed (Figure 5.5). Therefore, the development of a region around the vortex where $a_{xx} \approx 0$ suggests some reorganization of the free-stream turbulence.

The distribution of a_{yy} shown in Figure 5.61 is very different from that observed for a_{xx} with all cases at all streamwise locations having similar patterns. This pattern is similar to the cloverleaf distribution of $\overline{u_y u_z}$ observed in Figure A.31, with regions of positive a_{yy} roughly aligned with quadrants of negative yz and regions of negative a_{yy} roughly aligned with regions of positive yz with the definition of the pattern much less evident for the no-grid case. In each region of positive and negative a_{yy}, two peaks are evident; one peak was located relatively far from the core, at $r/c \approx 0.15, 0.2$ and 0.35 at $X/c = 1.75$, 5.75 and 9.75, respectively. The second peak was located along the z and y axes for the positive and negative a_{yy}, respectively, at $r/c \approx 0.03$ for the no-grid case, $r/c \approx 0.04$ for the small-grid case and $r/c \approx 0.05$ for the large-grid case at $X/c = 1.75$. This second peak is less evident for the regions of negative a_{yy} and moves radially outward with streamwise distance. The peak values decreased with streamwise distance and increasing free-stream turbulence.

An almost identical pattern as that observed for a_{yy} in Figure 5.61 was observed for a_{zz} in Figure 5.62, except in inverse, with regions of positive a_{zz} occurring at locations of negative a_{yy} and vice versa.

In comparison with the a_{xx}, a_{yy} and a_{zz} components of the anisotropy tensor, the a_{xy} and a_{xz} components appear much more disorganized with nearly isotropic values everywhere except in the spiral wake. The arrangement of their isocontours is consistent with the arrangement of the isocontours of Reynolds shear stresses in a two-dimensional wake ,with greater anisotropy values measured in the direction perpendicular to the wake axis. As the wake diffuses with increasing streamwise distance and with increasing free-stream turbulence, the anisotropy decreases.

The distribution of the a_{yz} component of the anisotropy tensor is very similar to those observed for a_{yy} and a_{zz} except that the pinwheel pattern has shifted in such a way that regions of highest and lowest a_{yz} occur in regions of near-zero a_{yy} and a_{zz}.

The arrangement of a_{yy}, a_{zz} and a_{yz} is consistent with a reorganization of the turbulence due to the wrapping of free-stream eddies around the vortex, as discussed in Section 6.1. However, this interpretation appears to be inconsistent with the existence of the pattern in the no-grid case, where there are no free-stream eddies to be re-organized. Therefore, the distributions of a_{yy}, a_{zz} and a_{yz} could be results of contamination by vortex wandering. Whether due to reorganization of turbulent eddies or due to vortex wandering, the appearance of Figures 5.61, 5.62 and 5.65 indicates that the entire measurement plane is affected.

To determine whether or not the patterns in Figures 5.61, 5.62 and 5.65 are due to turbulence or contamination due to wandering, frequency spectra were calculated at specific locations and the frequency distribution of a_{ij} was calculated from

$$\zeta_{ij}(f) = \frac{F_{ij}(f)}{F_{kk}(f)} \ . \tag{5.19}$$

The frequency spectra F_{xx}, F_{yy} and F_{zz} and the frequency distributions of ζ_{xx}, ζ_{yy} and ζ_{zz} are shown for the small-grid case at $X/c = 9.75$ without the wing in place and three locations with the wing in place: $(y, z) = (-0.29c, 0.08c)$ corresponding to a local maximum of a_{yy} and a minimum of a_{zz}, $(y, z) = (0.13c, 0.33c)$ corresponding to a local maximum of

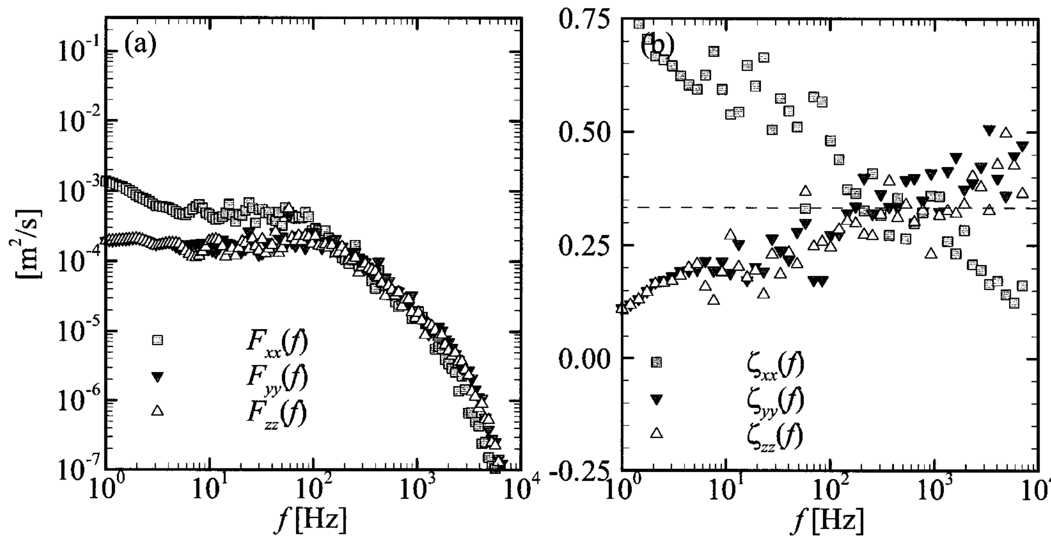

Figure 5.66: (a) Frequency spectra F_{xx}, F_{yy} and F_{zz} and (b) frequency distribution of ζ_{xx}, ζ_{yy} and ζ_{zz} for the small-grid case without the wing at $X/c = 9.75$. Dashed line indicates a constant value of 1/3.

a_{zz} and a minimum of a_{yy}, $(y, z) = (-0.05c, 0.00c)$ corresponding to the local maximum of a_{yy} near the time-averaged vortex axis. The four frequency spectra and corresponding frequency distributions of ζ_{xx}, ζ_{yy} and ζ_{zz} are shown in Figures 5.66-5.69 respectively.

The frequency spectra and frequency distributions of a_{xx}, a_{yy} and a_{zz} without the wing in place, Figure 5.66, shows that the high ζ_{xx} values of the grid turbulence is due to more energy at low frequency, $f < 100\,\text{Hz}$. Between $f \approx 100\,\text{Hz}$ and $f \approx 1000\,\text{Hz}$, the energy appears to be approximately equally distributed between the three Cartesian directions. At high frequencies, $f > 1000\,\text{Hz}$, the fluctuations in the transverse directions have more energy than fluctuations in the streamwise direction. With the wing in place, there is an increase in energy at all frequencies. At $(y, z) = (-0.29c, 0.08c)$ the frequency spectra and anisotropy frequency distributions shown in Figure 5.67b indicate that the slight decrease in ζ_{xx} around the vortex in Figure 5.60 is due to a greater increase in fluctuations

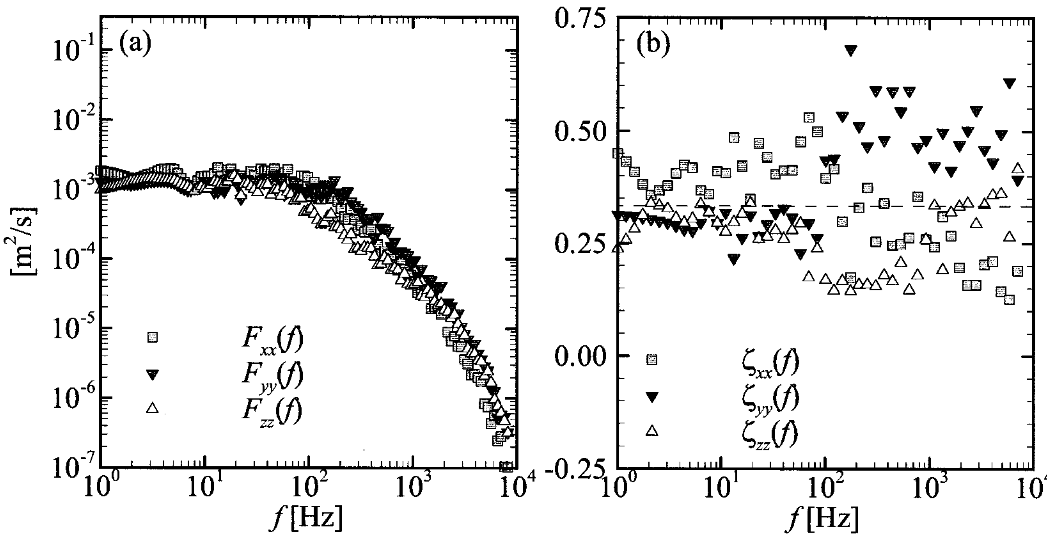

Figure 5.67: (a) Frequency spectra F_{xx}, F_{yy} and F_{zz} and (b) frequency distribution of ζ_{xx}, ζ_{yy} and ζ_{zz} for the small-grid case at $X/c = 9.75$ and $(y, z) = (-0.29c, 0.08c)$. Dashed line indicates a constant value of 1/3.

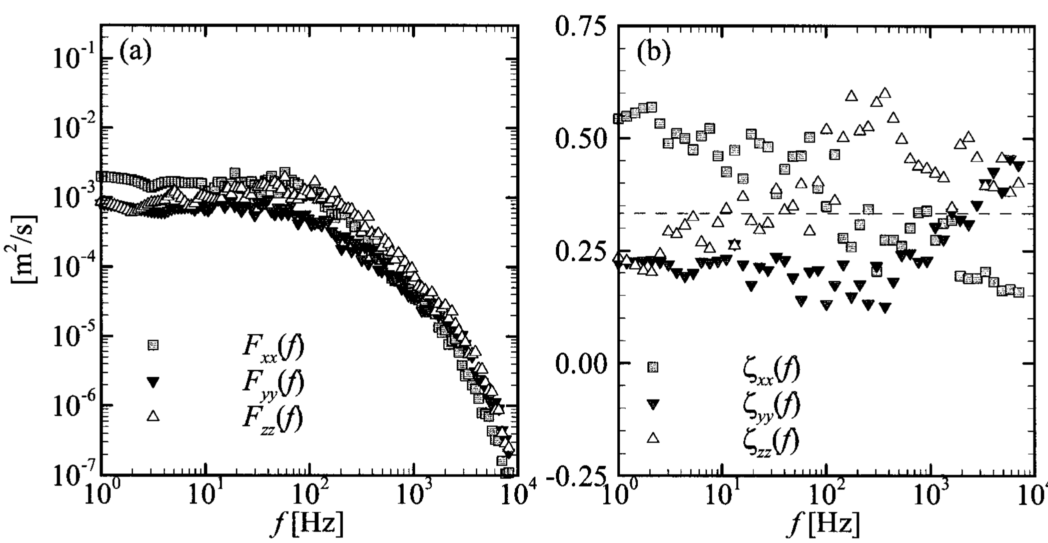

Figure 5.68: (a) Frequency spectra F_{xx}, F_{yy} and F_{zz} and (b) frequency distribution of ζ_{xx}, ζ_{yy} and ζ_{zz} for the small-grid case at $X/c = 9.75$ and $(y, z) = (0.13c, 0.33c)$. Dashed line indicates a constant value of 1/3.

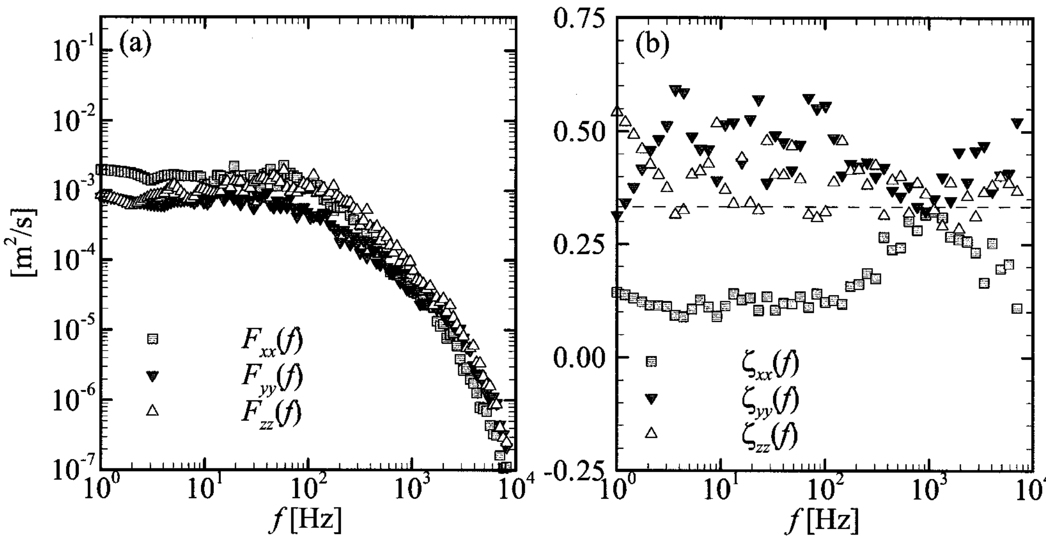

Figure 5.69: (a) Frequency spectra F_{xx}, F_{yy} and F_{zz} and (b) frequency distribution of ζ_{xx}, ζ_{yy} and ζ_{zz} for the small-grid case at $X/c = 9.75$ and $(y, z) = (-0.05c, 0.00c)$. Dashed line indicates a constant value of 1/3.

in both U_y and U_z at frequencies $f < 1000\,\text{Hz}$ compared to U_x. Positive values of ζ_{yy} and negative values of ζ_{zz} are due to a greater increase in fluctuations in U_y when compared to U_z over the same frequency range. The results shown in Figure 5.68 show the same behaviour as in Figure 5.67, except with the greatest increase in fluctuations occurring for U_z rather than U_y. Figure 5.69 indicates that the increase in ζ_{yy} at $(y, z) = (-0.05c, 0.00c)$ is also due to a large increase in velocity fluctuations in the transverse directions relative to the increase in fluctuations of U_x for $f < 1000\,\text{Hz}$.

Figures 5.66 to 5.69 indicate that what appears to be reorganization of turbulence in Figures 5.61, 5.62 and 5.65 occurs at frequencies $f < 1000\,\text{Hz}$. At this low frequency range, the most likely source of the anisotropy is contamination due to vortex wandering. Two interesting points arise from this analysis, the first is that vortex wandering affects the entire measurement plane, indicating that the vortex moves almost as a solid body and that the wandering appears to have less influence over the measurements at frequencies $f > 1000\,\mathrm{Hz}$.

5.14 Integral length scales

The integral length scale was defined by Equation 5.5, which makes use of Taylor's frozen flow approximation. However, this approximation is not valid in the spiralling flow field in the proximity of the vortex, because the local eddies are not convected in the streamwise direction. Instead, these eddies are, in the mean, convected at some inclined direction with respect to the x axis, with this inclination increasing as $r_{\theta\,\mathrm{max}}$ is approached. A more realistic length scale for the eddies in the proximity of the vortex can be defined as

$$L_x^* = \frac{\overline{U}_x^*}{u_x^{*\prime} u_x^{*\prime}} \int_0^{\tau_o} R_{x^*x^*}(\tau)\,\mathrm{d}\tau \;, \tag{5.20}$$

where $\overline{U}_x^*$ was the mean convection velocity of the eddies, determined by rotating the (U_x, U_y, U_z) coordinate system at each measurement location to (U_x^*, U_y^*, U_z^*) such that $\overline{U}_y^*$, $\overline{U}_z^* = 0$ so that the x^*-axis was aligned with the local mean flow direction.

Taylor's approximation would be invalid near the vortex core due to the continual change in the direction of the eddy convection at the measurement point caused by vortex wandering. However, at measurement locations far enough away from the time-averaged vortex axis, where the radial profiles of the velocity components change relatively slowly, the effect of wandering on the mean velocity direction would be reduced. As will be shown in Section 6.3, the effect of vortex wandering on the measured $\overline{U}_\theta$ and hence the inclination of the mean velocity vector may be neglected for $r/c > 0.08$ for the small grid case and $r/c > 0.15$ for the large grid case. Therefore, at sufficiently large radii (i.e. larger than

$r/c = 0.15$ for the large-grid case and larger than $r/c = 0.08$ for the small grid case), the integral length scale calculated using Equation 5.20 is approximately correct. However, considering the inaccuracy of the Taylor approximation in shear flows and the influence of wandering on measurements, these results will only be used for comparative purposes.

The integral length scales calculated using Equation 5.20 are presented as radial profiles in Figures 5.70-5.73 normalized by L_{x_o}, the integral length scale determined in the grid turbulence on the same streamwise cross-section. As expected, measurements in the spiral wake are distinct from those in the vortex and appear as scatter; to distinguish them from the rest, such measurements have been indicated by solid symbols in Figures 5.70-5.73. At $X/c = 1.75$, all four figures show an azimuthal ring of $L_x^*/L_{x_o} < 1$ in the range $0 \lesssim r/c \lesssim 0.3$ with a minimum of approximately $L_x^*/L_{x_o} = 0.5$ centred at $r/c \approx 0.1$. As streamwise distance increases, this azimuthal ring grows and moves radially outward to encompass the radial range $0.1 \lesssim r/c \lesssim 0.8$ at $X/c = 9.75$. The location of minimum L_x^*/L_{x_o} also moves radially outward, reaching $r/c \approx 0.2$ for the small-grid-upstream and small-grid cases and $r/c \approx 0.3$ for the large-grid-upstream and large-grid cases. Smaller length scales of approximately $L_x^*/L_{x_o} = 0.5$ are also measured in the spiral wake.

The regions with smaller length scales could be traced to the wing boundary layer, which is shed from the wing to form the spiral wake. Examination of the small-grid-upstream and large-grid-upstream cases shows that, initially, the minimum integral length scales in the wake were quite close to the minimum in the azimuthal ring. It is possible that the azimuthal ring is the result of boundary layer fluid that has been entrained around the vortex during formation. If this is the case, it is interesting to note that the L_x^*/L_{x_o} values

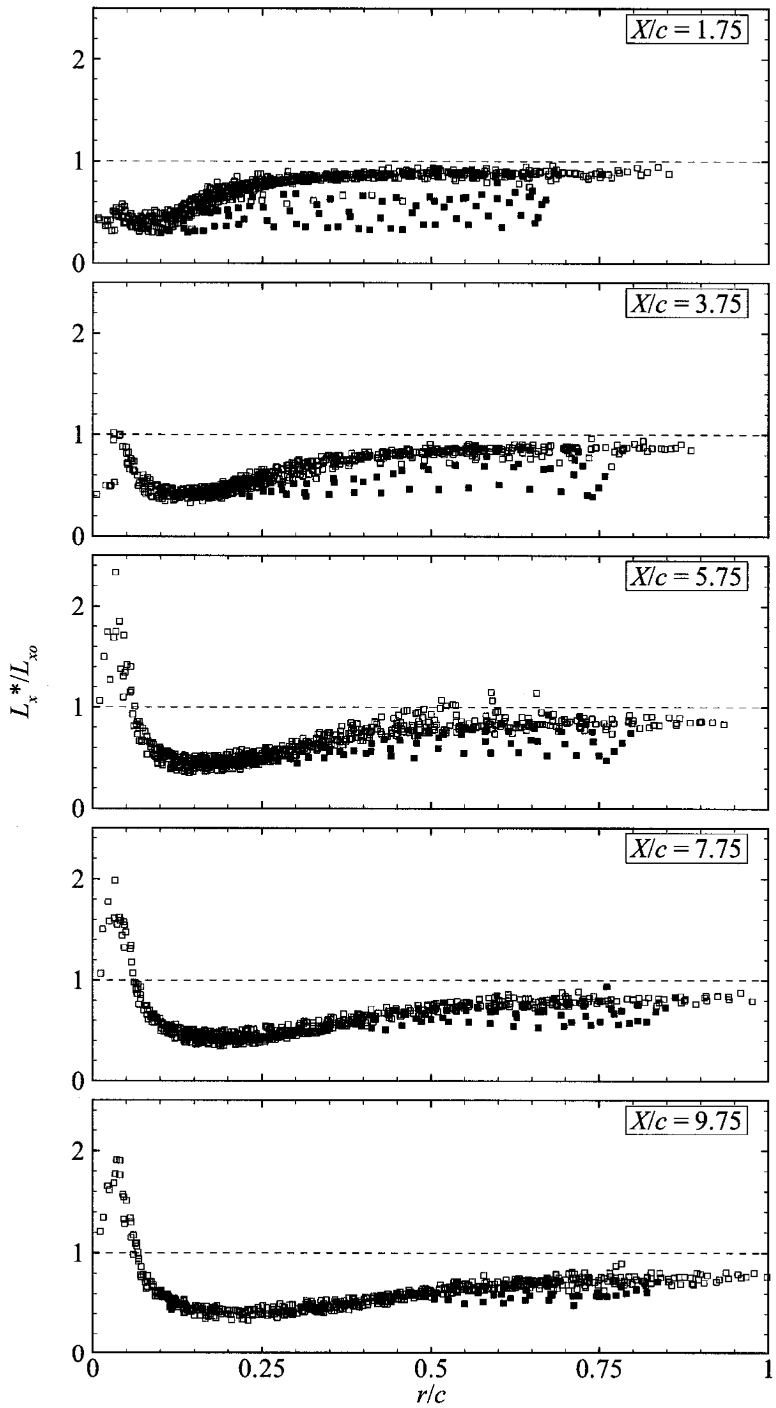

Figure 5.70: Radial variation of the integral length scale normalized by the integral length scale measured at the same streamwise location without the wing in place L_x^*/L_{x_o}, for the small-grid-upstream case. Solid squares indicate data points located in the spiral wake.

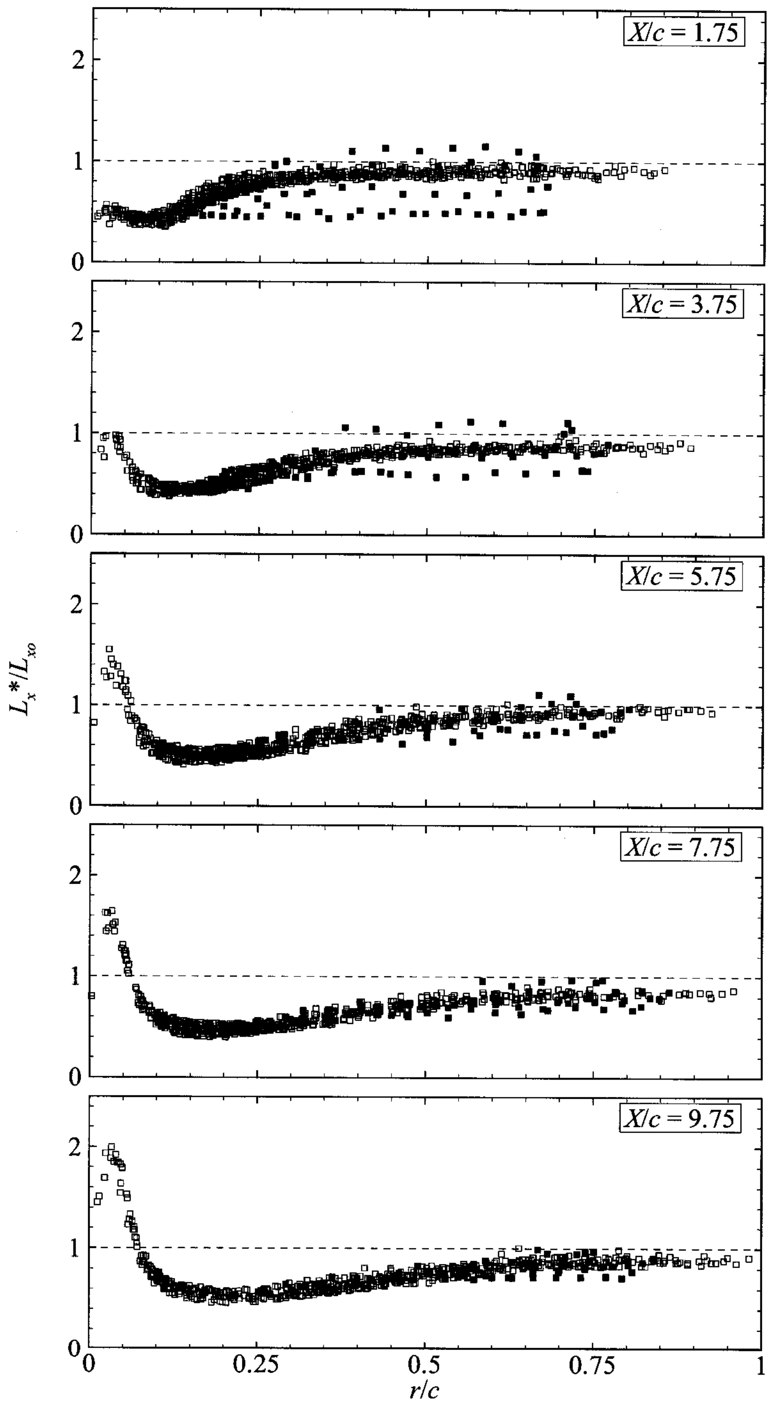

Figure 5.71: Radial variation of the integral length scale normalized by the integral length scale measured at the same streamwise location without the wing in place L_x^*/L_{x_o}, for the small-grid case. Solid squares indicate data points located in the spiral wake.

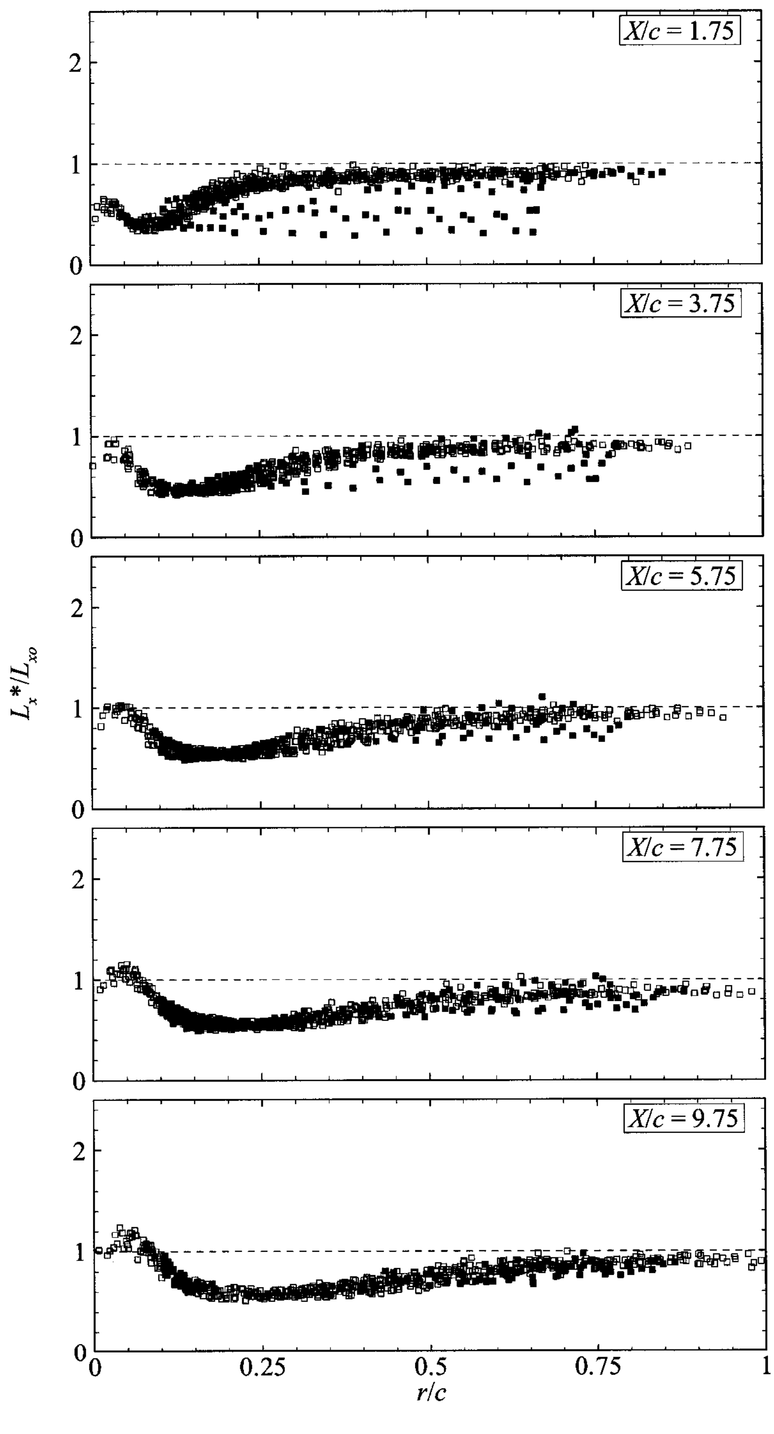

Figure 5.72: Radial variation of the integral length scale normalized by the integral length scale measured at the same streamwise location without the wing in place L_x^*/L_{x_o}, for the large-grid-upstream case. Solid squares indicate data points located in the spiral wake.

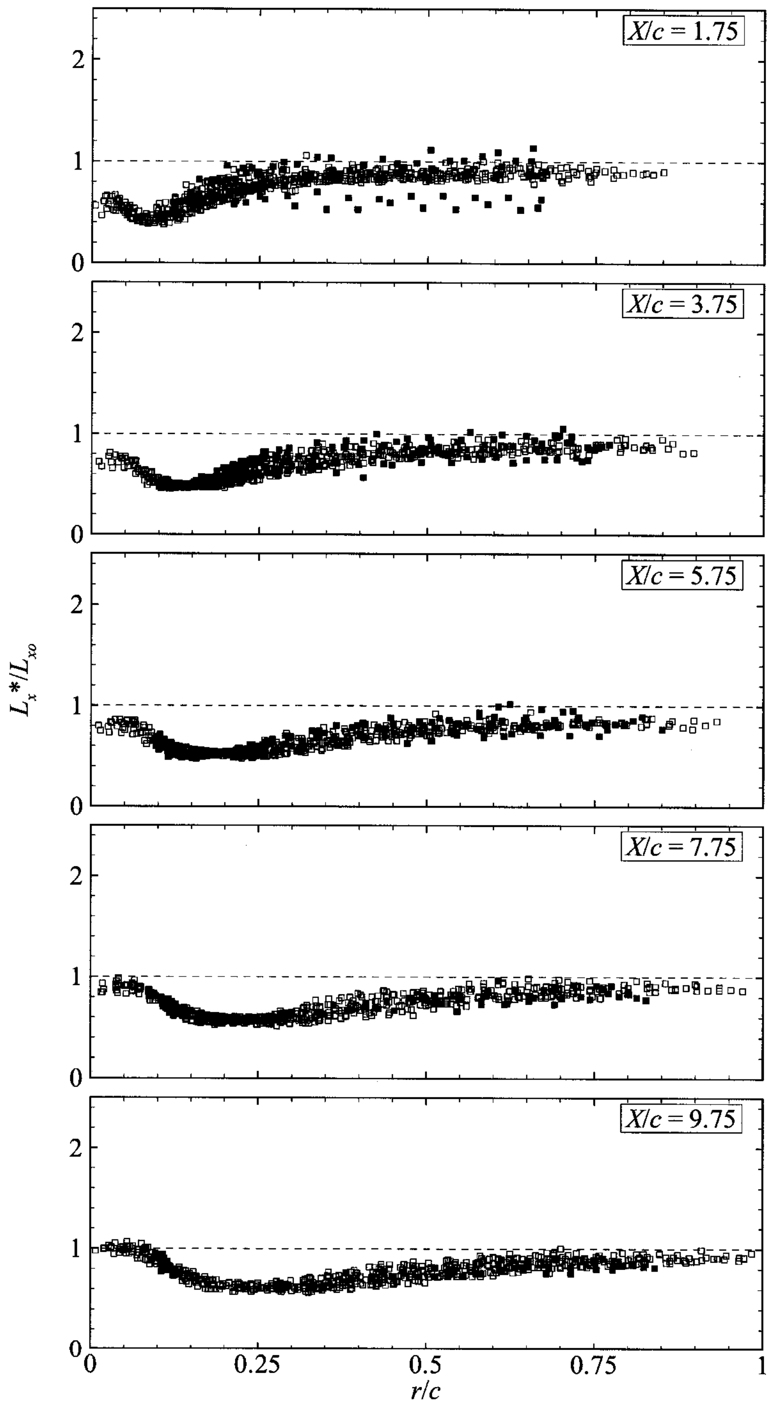

Figure 5.73: Radial variation of the integral length scale normalized by the integral length scale measured at the same streamwise location without the wing in place L_x^*/L_{x_o}, for the large-grid case. Solid squares indicate data points located in the spiral wake.

at measurement locations within the spiral wake increase with X/c to reach approximately the same values as those outside the wake at $X/c = 9.75$. In contrast, the minimum value of L_x^*/L_{x_o} measured within the azimuthal ring remains relatively unchanged. This could be an indication that the vortex is inhibiting the process by which the length scales within the spiral wake grow or is deforming and reorienting them so that the streamwise length scale is smaller. Using two-point measurements in the spiral wake, Miranda and Devenport (1998) observed that the integral length scale in the transverse direction increased as the wake spiralled closer to the vortex core. This suggests that the eddies were becoming re-oriented in the azimuthal direction. A corresponding decrease in the streamwise integral length scale could therefore be expected (as illustrated in Figure 6.10).

Near the time-averaged vortex axis, the time-series are dominated by vortex wandering, which, by comparison to the turbulence in the spiral wake and the vortex core, represents a large-scale motion (Heyes et al. (2004), Devenport et al. (1996)). Hence the longer length scales near $r/c = 0$ are likely to be associated with this motion. Near the axis, $L_x^*/L_{x_o} \approx 2$ for the two small-grid cases, but $L_x^*/L_{x_o} \approx 1$ for the two large-grid cases. Considering that L_{x_o} for the large-grid cases is approximately twice that of the small-grid cases, this indicates that L_x^* at $r/c < 0.1$ is approximately the same for all cases, and hence the length scale of the wandering appears to be independent of the integral length scale of the grid turbulence.

5.15 Strain rate fluctuations

The rate of strain fluctuations form a second-order tensor s_{ij}, defined as (Tennekes and Lumley (1972))

$$s_{ij} = \frac{1}{2}\left(\frac{\partial u_i}{\partial x_j} + \frac{\partial u_j}{\partial x_i}\right) \tag{5.21}$$

This tensor is related to the dissipation rate of turbulent kinetic energy through

$$\varepsilon = 2\nu\overline{s_{ij}s_{ij}} \ . \tag{5.22}$$

Tennekes and Lumley (1972) also note that, at high Reynolds numbers, it is related to the turbulent enstrophy as

$$\overline{\omega_i\omega_i} \approx 2\overline{s_{ij}s_{ij}} \ , \tag{5.23}$$

This relationship shows the connection between fine-scale fluctuations of vorticity and energy dissipation. Therefore, s_{ij} can be used to describe the fine-scale dynamics of the turbulence near the vortex. The full s_{ij} tensor cannot be determined from the present measurements. However, assuming local isotropy of the fine-scale turbulence, one may estimate ε as (Tennekes and Lumley (1972))

$$\varepsilon \approx 15\nu\overline{\left(\frac{\partial u_x}{\partial x}\right)^2} \ . \tag{5.24}$$

Further employing Taylor's frozen flow approximation, one may estimate the magnitude s of the turbulent strain rate as

$$s = \overline{s_{ij}s_{ij}}^{\frac{1}{2}} \approx \frac{2.74}{\overline{U}_x}\left[\overline{\left(\frac{\partial u_x}{\partial t}\right)^2}\right]^{\frac{1}{2}} \ . \tag{5.25}$$

As described in the previous section, when the flow is spiralling, the local eddies are not convected in the streamwise direction and the frozen flow hypothesis is not valid. To improve the estimate of the turbulent strain rate, the Cartesian coordinate system at each measurement system was rotated such that the x-axis was aligned with the mean direction of eddy convection (as described in the previous section) and the turbulent strain rate was estimated as

$$s^* \approx \frac{2.74}{\overline{U}_x^*} \left[\overline{\left(\frac{\partial u_x^*}{\partial t} \right)^2} \right]^{\frac{1}{2}} , \tag{5.26}$$

where * indicates a value calculated in the rotated frame. Again, considering the inaccuracy of the Taylor approximation in shear flows and the influence of wandering on measurements, these results will only be used for comparative purposes.

The turbulent strain rate calculated in this manner is presented as radial profiles in Figures 5.74-5.77 with s^* normalized by s_o, the magnitude of the turbulent strain rate measured in the grid turbulence with the wing removed at the same streamwise cross-section. Results are presented for each of the four grid turbulence cases. To clarify the contribution of measurements in the spiral wake to the overall scatter, such measurement locations have been indicated by solid symbols in Figures 5.74-5.77.

Figures 5.74-5.77 indicate that s^*/s_o was much higher both within the spiral wake and near the time-averaged vortex axis. As the vortex develops downstream, s^*/s_o in the spiral wake decays to free-stream levels, however near the time-averaged vortex axis s^* remains over three times higher than the free-stream value for all X/c. For the small-grid and small-grid-upstream cases, Figures 5.75 and 5.74, respectively, the higher s^*/s_o occurs in an azimuthal ring with a peak in the range $r/c = 0.05$ to 0.1. As will be shown later, this is just outside the vortex core as $r_{\theta\,\max} \approx 0.04$ for all cases. For the small-grid-upstream case at $X/c = 1.75$, this peak value within the azimuthal ring was $s^*/s_o \approx 6$, however, for

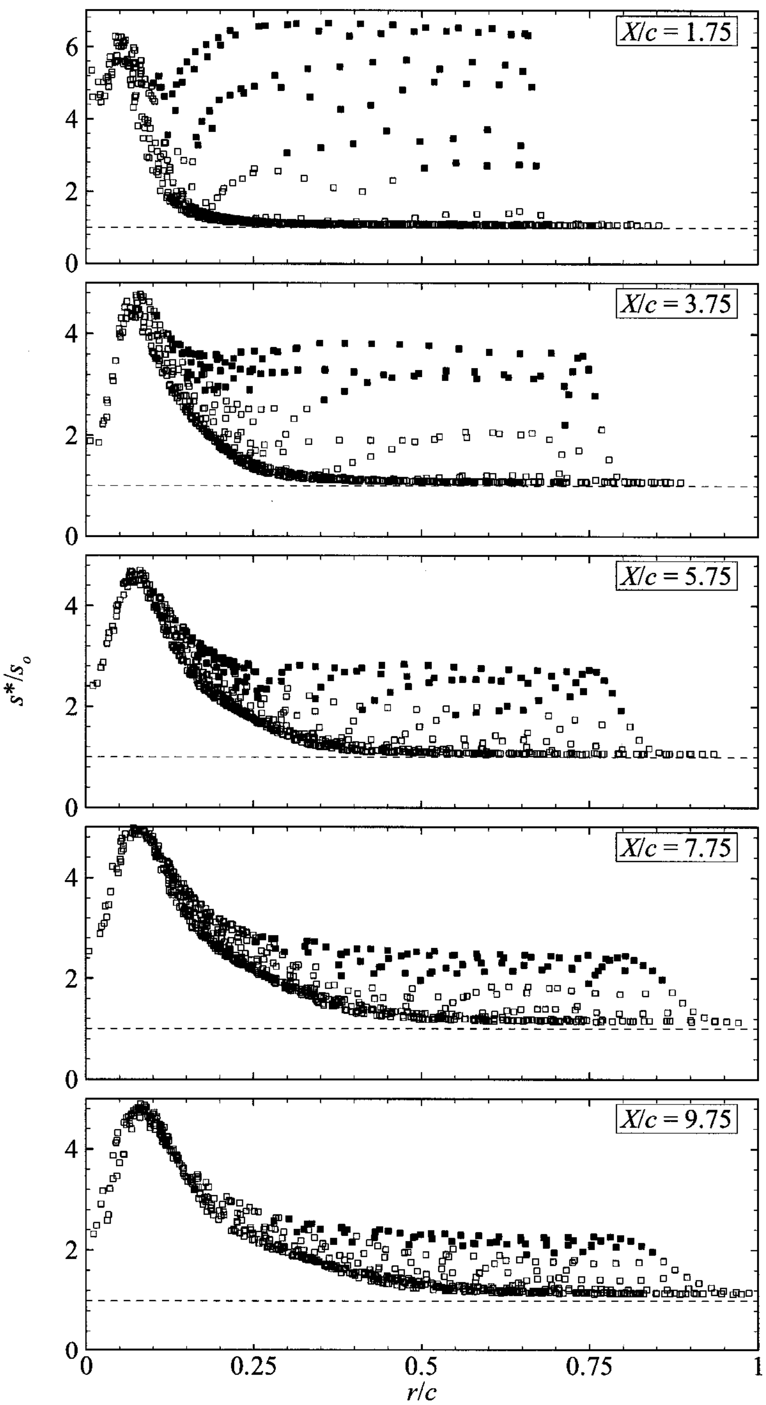

Figure 5.74: Radial variation of the turbulent strain rate s^* for the small-grid-upstream case. normalized by the turbulent strain rate measured at the same streamwise location without the wing in place, s_o. Solid squares indicate data points located in the spiral wake.

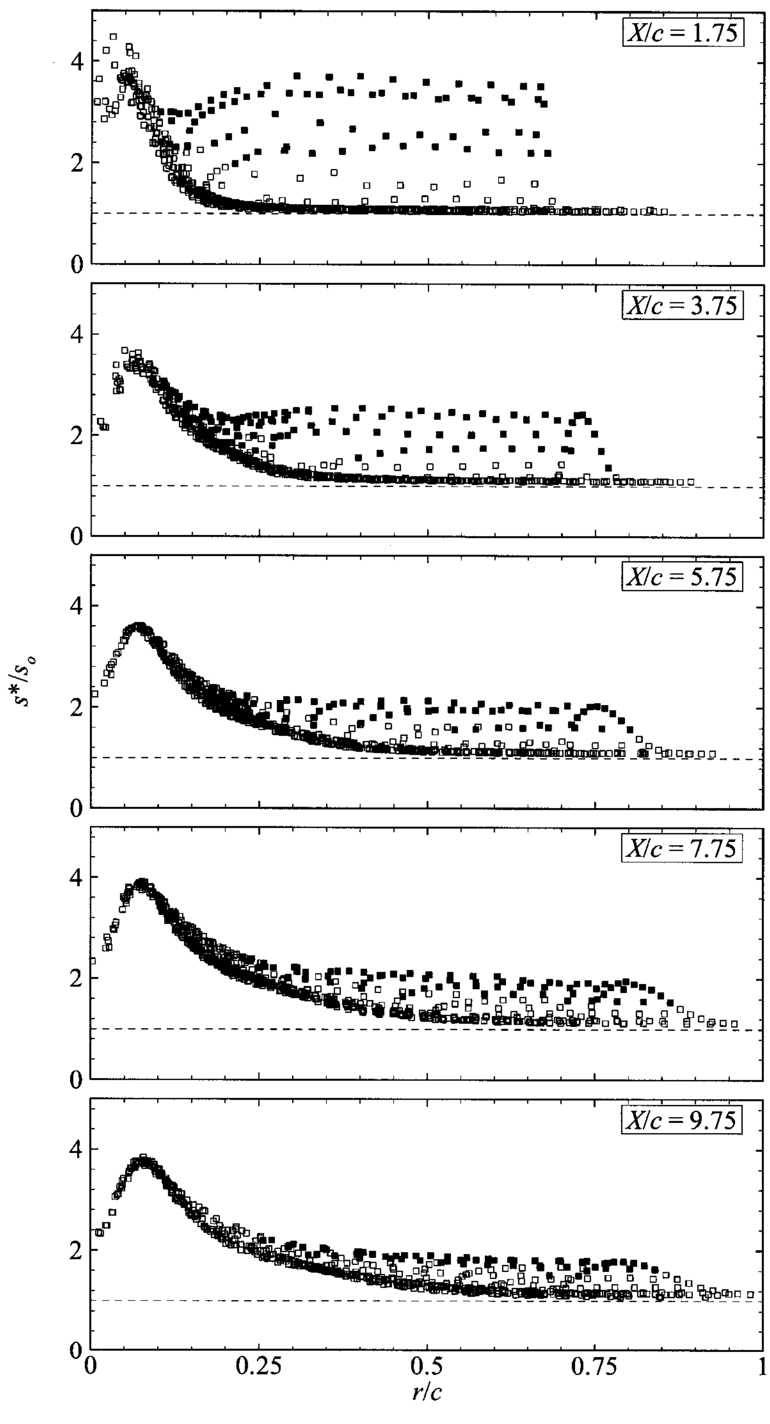

Figure 5.75: Radial variation of the turbulent strain rate s^* for the small-grid case. normalized by the turbulent strain rate measured at the same streamwise location without the wing in place, s_o. Solid squares indicate data points located in the spiral wake.

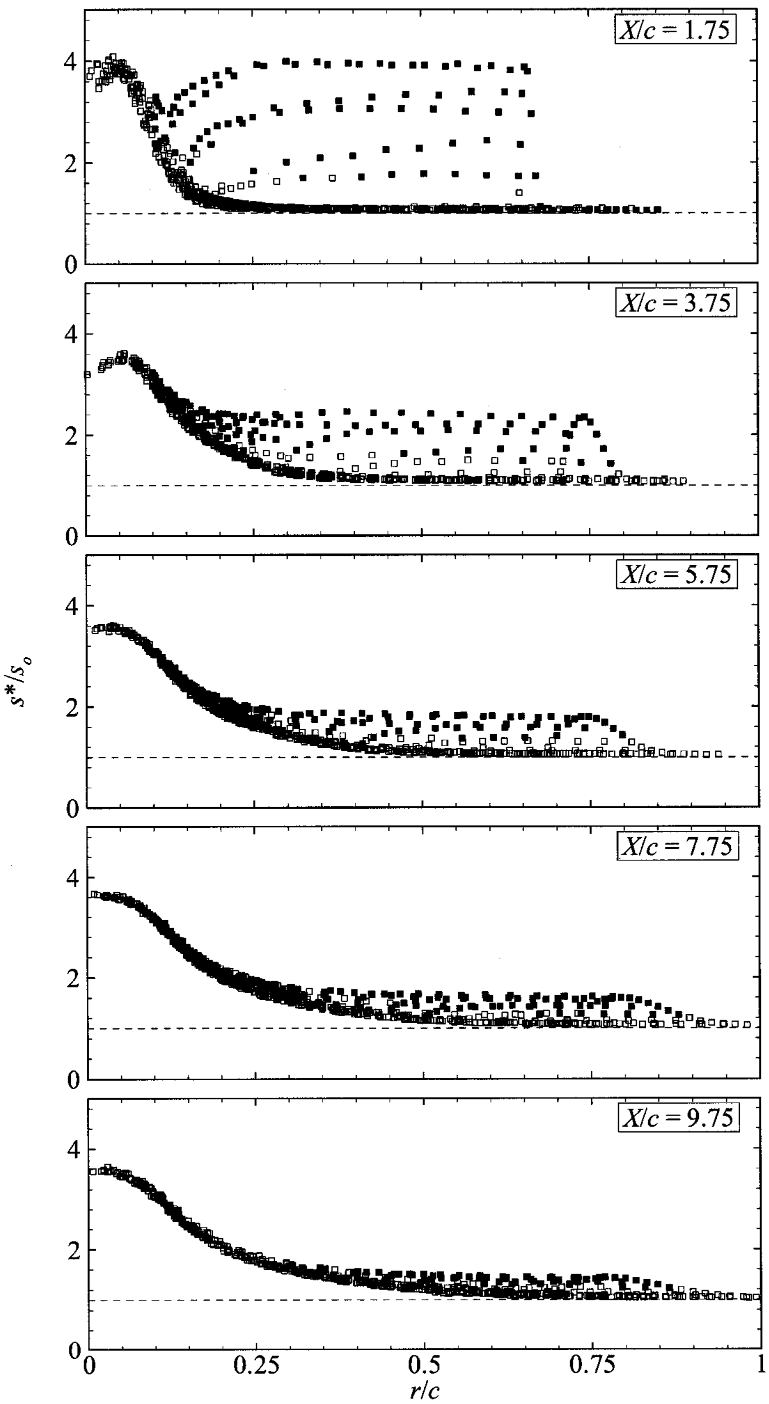

Figure 5.76: Radial variation of the turbulent strain rate s^* for the large-grid-upstream case. normalized by the turbulent strain rate measured at the same streamwise location without the wing in place, s_o. Solid squares indicate data points located in the spiral wake.

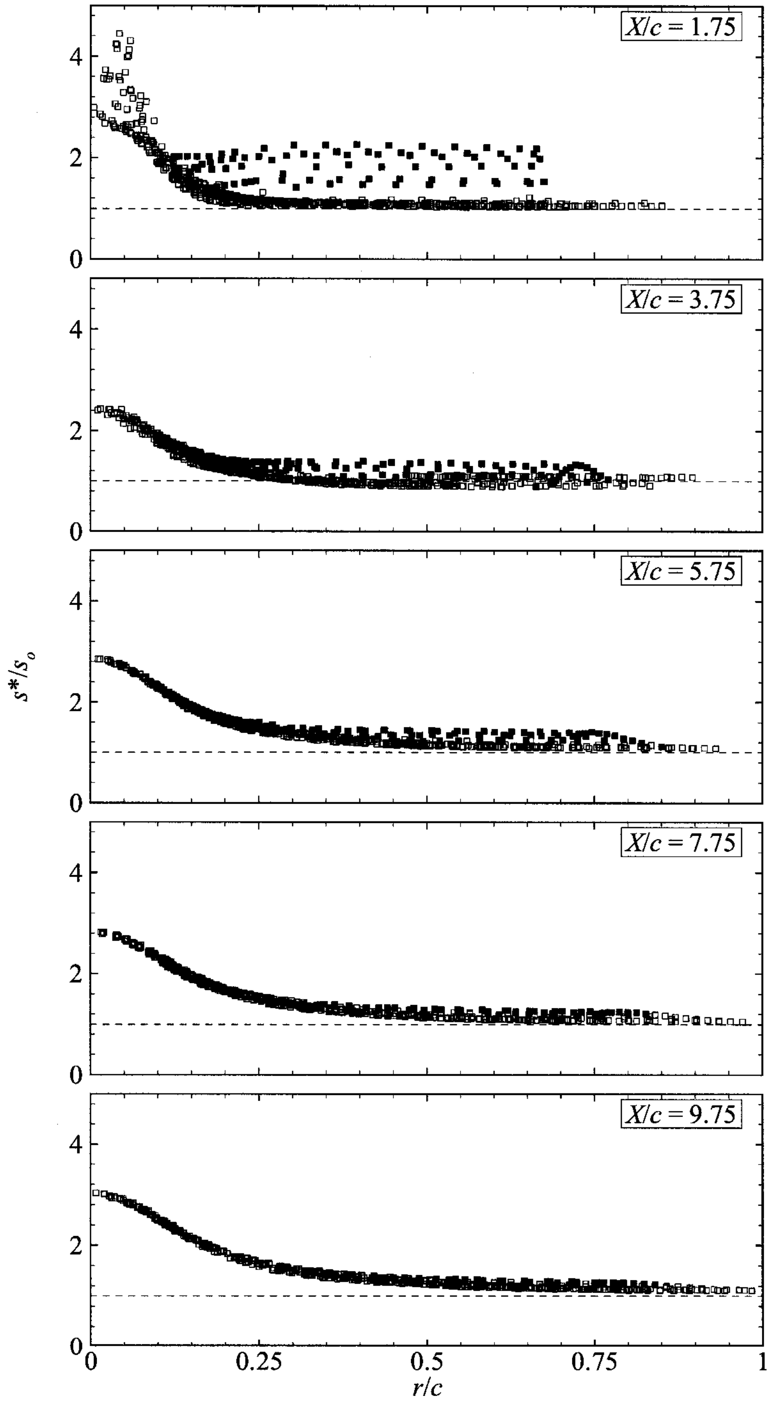

Figure 5.77: Radial variation of the turbulent strain rate s^* for the large-grid case. normalized by the turbulent strain rate measured at the same streamwise location without the wing in place, s_o. Solid squares indicate data points located in the spiral wake.

$X/c = 3.75$ to 9.75 the peak decreased to $s^*/s_o \approx 5$. The peak value of s^*/s_o within the azimuthal ring for the small-grid case was slightly lower, with a peak value of $s^*/s_o \approx 4$ at $X/c = 1.75$, remaining at $s^*/s_o \approx 4$ up to $X/c = 9.75$.

An azimuthal ring of high ε was observed by Melander and Hussain (1993) in their DNS simulations; they found that it was uncorrelated with the presence of azimuthally oriented coherent structures of high enstrophy at the same radius, but offered no explanation for the higher dissipation surrounding the vortex core. Analytically investigating the dissipation in spiral shear layers wrapping around a vortex, Kawahara (2005) observed increased dissipation of kinetic energy ($\frac{1}{2}\overline{U_i U_i}$ as opposed to $\frac{1}{2}\overline{u_i u_i}$) both in the shear layers and in an azimuthal ring around the vortex where the time-averaged velocity gradients (and hence the time-averaged strain rate) are highest.

In general, for the large-grid and large-grid upstream cases, Figures 5.77 and 5.76, respectively, the peak s^*/s_o occurs at the time-averaged vortex centre, with peak values $s^*/s_o \approx 4$ for the large-grid-upstream case and $s^*/s_o \approx 3$ for the large-grid case. Some evidence of an azimuthal ring is evident in Figure 5.76 for the large-grid-upstream case at $X/c = 1.75$ and $X/c = 3.75$. In fact, it is quite possible that s^*/s_o is highest in azimuthal rings for the large-grid and large-grid-upstream cases as well but this organization is obscured by vortex wandering. Vortex wandering, which tends to smoothen spatially the time-averaged statistics, is significantly higher for the two large-grid cases than for the two-small-grid cases. This implies that in the large-grid cases, due to wandering, the peak value s^*/s_o would be reduced and the azimuthal ring could appear at smaller radii, compared to the small-grid cases, thus obscuring the formation of an azimuthal ring.

Chapter 6

Analysis

6.1 Bandpass filtered Reynolds normal stresses

Filtering of the velocity signals has been used by previous vortex investigators to separate the velocity fluctuations within different frequency bands. Devenport et al. (1996) used high-pass filtering to show that there was little high frequency energy in the vortex core, relative to the innermost spirals of the spiral wake which surround the core, thus supporting the hypothesis that the core flow was laminar. Beninati and Marshall (2005) investigated the energy content in the low-frequency range below a cut-off frequency by integrating the power spectra up to this cut-off frequency and used these results to demonstrate that the motion of the vortex was induced by secondary, azimuthally-aligned coherent structures. In the following, we will use bandpass filtering to determine the contributions of fluctuations within different frequency ranges to the Reynolds normal stresses.

To calculate the filtered normal stresses, the time series of U_x, U_y and U_z were first bandpass filtered at the desired range of frequencies using a 6th order bandpass Butterworth filter twice, first in a forward pass and then in reverse to ensure that the filtered signals had zero phase shift. After the filtering was performed, the bandpass Reynolds stresses were calculated from the filtered data. The frequency bands considered were the ranges 0-500 Hz, 500-1000 Hz, 1000-1500 Hz, 1500-2000 Hz, 2000-2500 Hz, 2500-3000 Hz, 3000-4000 Hz, 4000-5000 Hz, 5000-6000 Hz, 6000-7000 Hz and 7000-8200 Hz. As examples, the Reynolds normal stresses in the frequency ranges 0-500 Hz, 1000-1500 Hz and 7000-8200 Hz are presented as contours of $\widehat{u_x^2}/U_o^2$, $\widehat{u_y^2}/U_o^2$ and $\widehat{u_z^2}/U_o^2$ (the $\widehat{\ }$ is used to indicate a bandpass filtered average) in Figures 6.1, 6.2, 6.3 for the no-grid, small-grid and large-grid cases at $X/c = 5.75$ and in Figures 6.4, 6.5 and 6.6 for the no-grid, small-grid and large-grid cases at $X/c = 9.75$.

Normal stresses in the 0-500 Hz frequency range

For all cases shown in Figures 6.1a-c to 6.6a-c, the largest stresses in the frequency range 0-500 Hz occur for $\widehat{u_y^2}/U_o^2$ and $\widehat{u_z^2}/U_o^2$ on the time-averaged vortex axis, with the isocontours appearing oval shaped as observed in Figures A.26 and A.27. These patterns of isocontours can be directly attributed to vortex wandering, which, as discussed in the previous section, predominantly affects the low frequency range of transverse motions. Consistent with the observations of Section A.3, the streamwise stresses due to wandering are much smaller than the transverse stresses. For the no-grid case, the streamwise stress is too small to appear in the contour scale used. For the small-grid and large-grid cases, the streamwise stresses are evident, appearing at the time-averaged vortex axis and are axisymmetric, consistent with vortex wandering.

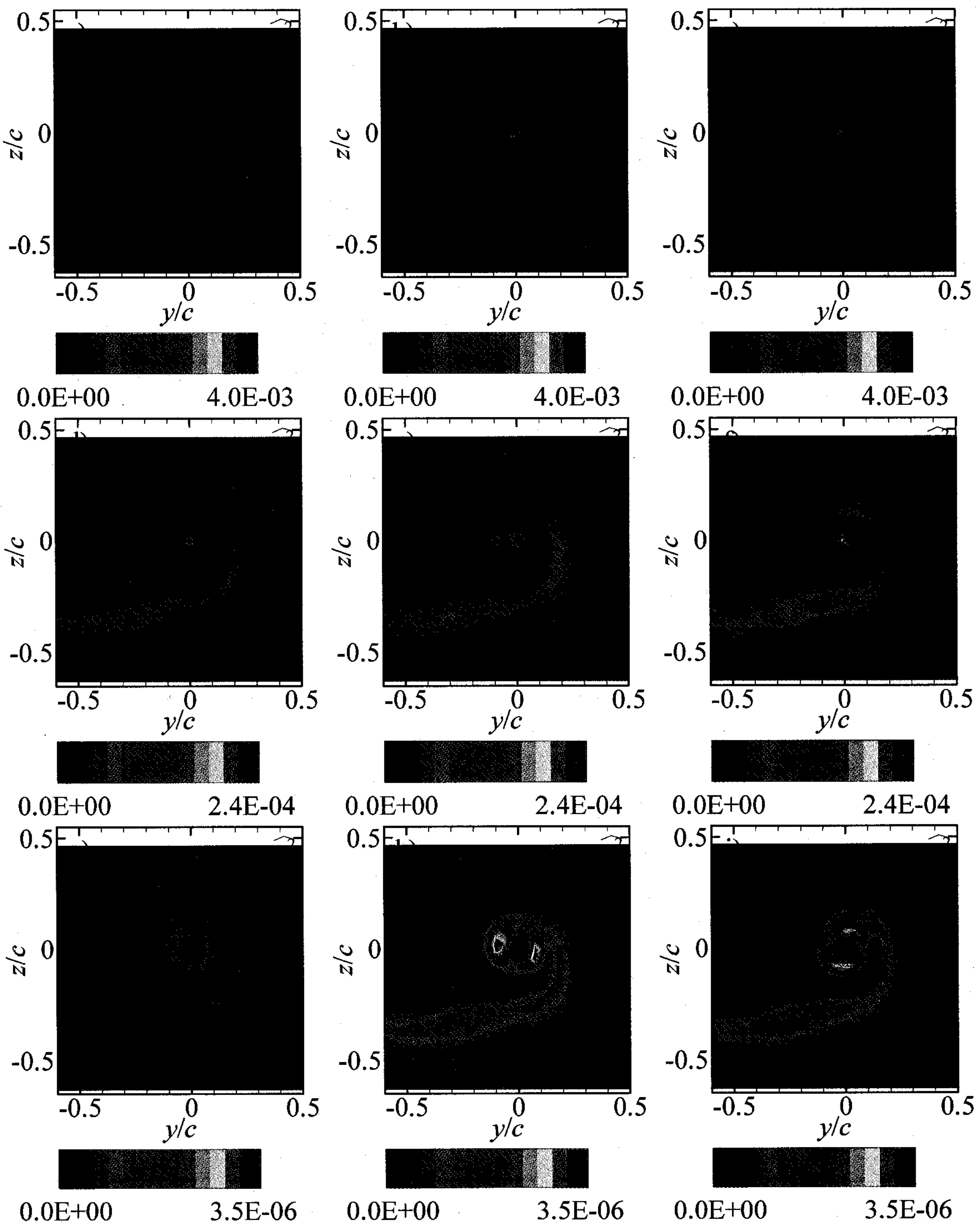

Figure 6.1: Band-pass filtered Reynolds stresses for the no-grid case at $X/c = 5.75$. (a) $\widehat{u_x^2}/U_o^2$ in range 0-500 Hz, (b) $\widehat{u_y^2}/U_o^2$ in range 0-500 Hz, (c) $\widehat{u_z^2}/U_o^2$ in range 0-500 Hz, (d) $\widehat{u_x^2}/U_o^2$ in range 1.0-1.5 kHz, (e) $\widehat{u_y^2}/U_o^2$ in range 1.0-1.5 kHz, (f) $\widehat{u_z^2}/U_o^2$ in range 1.0-1.5 kHz, (g) $\widehat{u_x^2}/U_o^2$ in range 7-8.2 kHz, (h) $\widehat{u_y^2}/U_o^2$ in range 7-8.2 kHz and (i) $\widehat{u_z^2}/U_o^2$ in range 7-8.2 kHz.

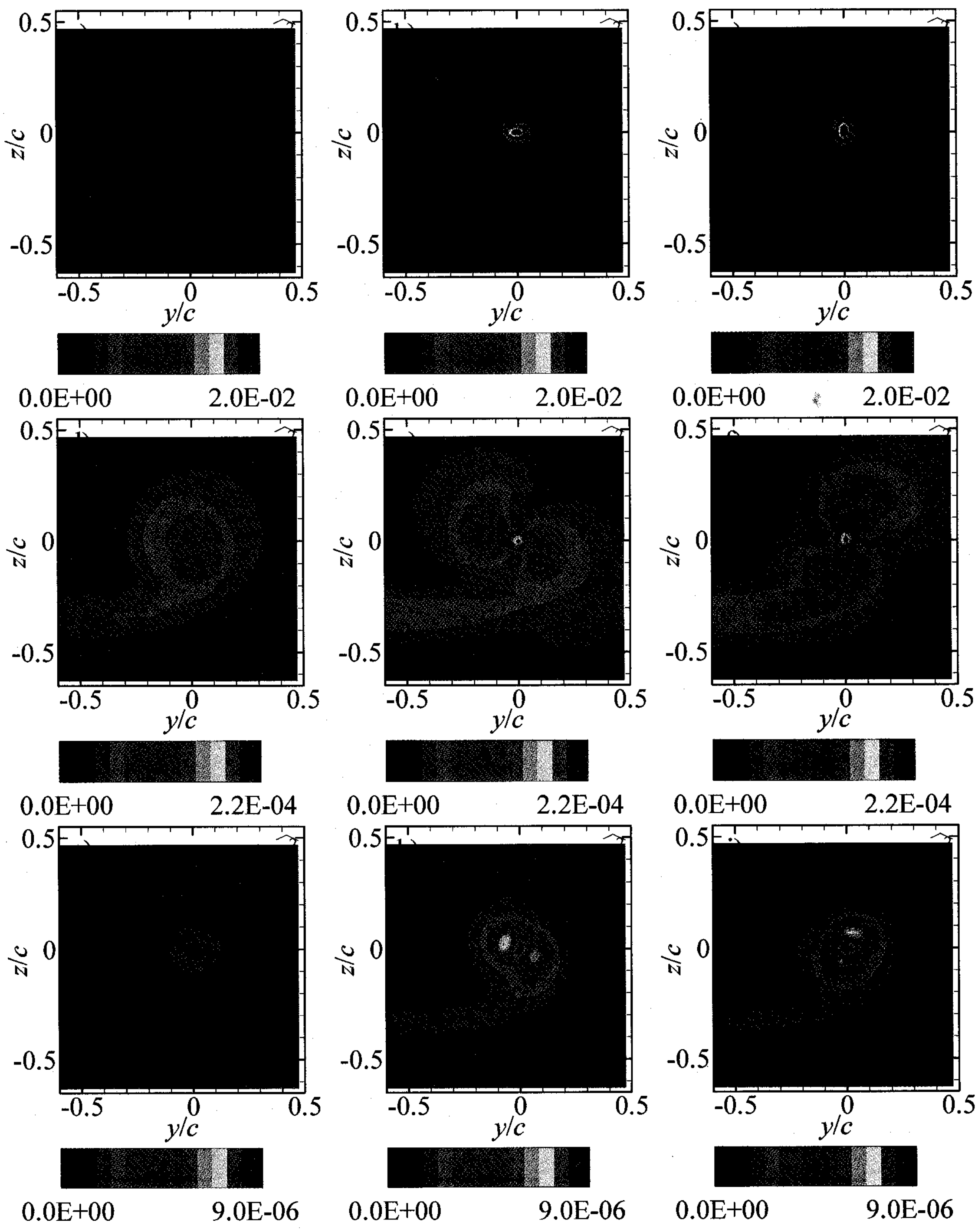

Figure 6.2: Band-pass filtered Reynolds stresses for the small-grid case at $X/c = 5.75$. (a) $\widehat{u_x^2}/U_o^2$ in range 0-500 Hz, (b) $\widehat{u_y^2}/U_o^2$ in range 0-500 Hz, (c) $\widehat{u_z^2}/U_o^2$ in range 0-500 Hz, (d) $\widehat{u_x^2}/U_o^2$ in range 1.0-1.5 kHz, (e) $\widehat{u_y^2}/U_o^2$ in range 1.0-1.5 kHz, (f) $\widehat{u_z^2}/U_o^2$ in range 1.0-1.5 kHz, (g) $\widehat{u_x^2}/U_o^2$ in range 7-8.2 kHz, (h) $\widehat{u_y^2}/U_o^2$ in range 7-8.2 kHz and (i) $\widehat{u_z^2}/U_o^2$ in range 7-8.2 kHz.

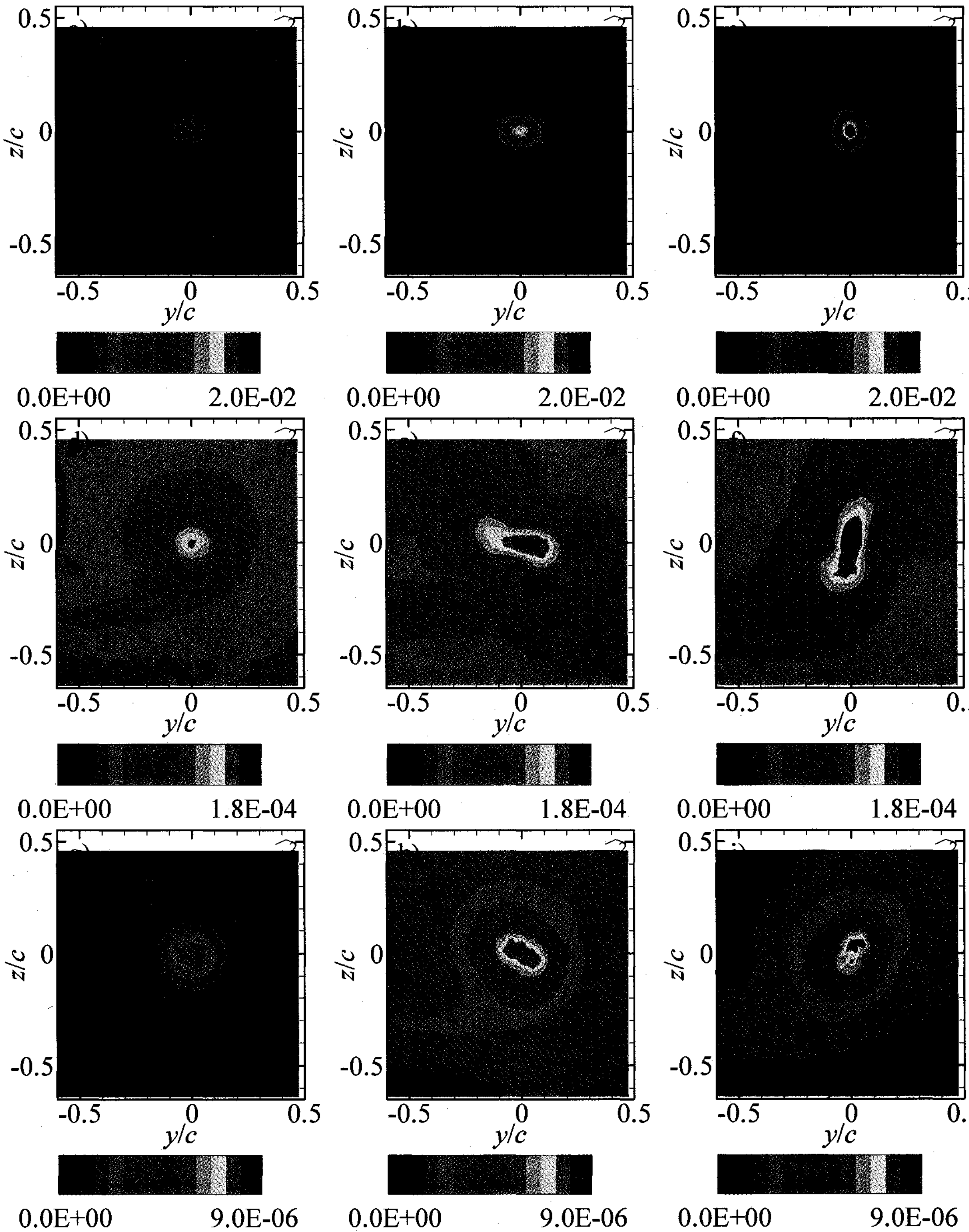

Figure 6.3: Band-pass filtered Reynolds stresses for the large-grid case at $X/c = 5.75$. (a) $\widehat{u_x^2}/U_o^2$ in range 0-500 Hz, (b) $\widehat{u_y^2}/U_o^2$ in range 0-500 Hz, (c) $\widehat{u_z^2}/U_o^2$ in range 0-500 Hz, (d) $\widehat{u_x^2}/U_o^2$ in range1.0-1.5 kHz, (e) $\widehat{u_y^2}/U_o^2$ in range 1.0-1.5 kHz, (f) $\widehat{u_z^2}/U_o^2$ in range 1.0-1.5 kHz, (g) $\widehat{u_x^2}/U_o^2$ in range 7-8.2 kHz, (h) $\widehat{u_y^2}/U_o^2$ in range 7-8.2 kHz and (i) $\widehat{u_z^2}/U_o^2$ in range 7-8.2 kHz.

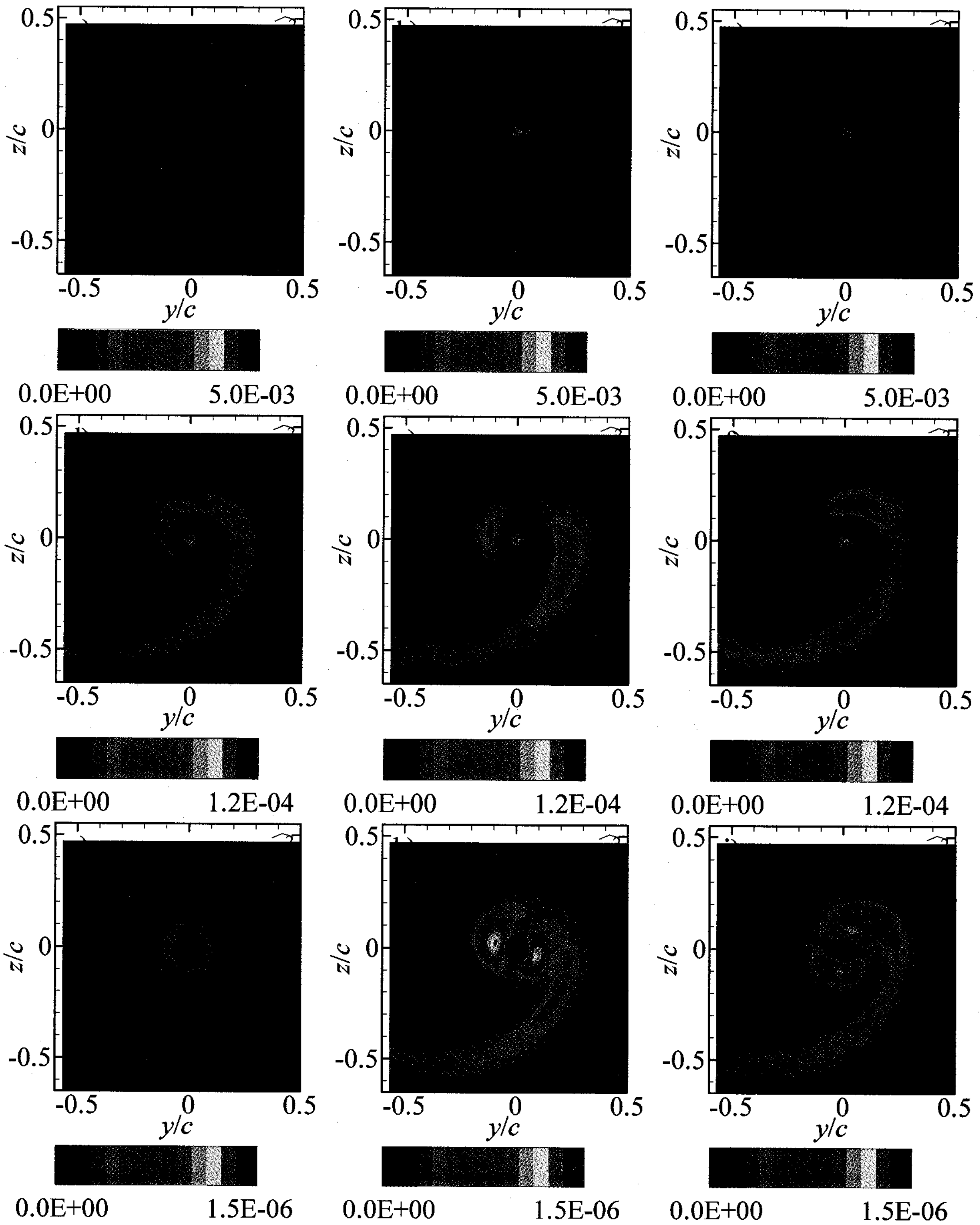

Figure 6.4: Band-pass filtered Reynolds stresses for the no-grid case at $X/c = 9.75$. (a) $\widehat{u_x^2}/U_o^2$ in range 0-500 Hz, (b) $\widehat{u_y^2}/U_o^2$ in range 0-500 Hz, (c) $\widehat{u_z^2}/U_o^2$ in range 0-500 Hz, (d) $\widehat{u_x^2}/U_o^2$ in range 1.0-1.5 kHz, (e) $\widehat{u_y^2}/U_o^2$ in range 1.0-1.5 kHz, (f) $\widehat{u_z^2}/U_o^2$ in range 1.0-1.5 kHz, (g) $\widehat{u_x^2}/U_o^2$ in range 7-8.2 kHz, (h) $\widehat{u_y^2}/U_o^2$ in range 7-8.2 kHz and (i) $\widehat{u_z^2}/U_o^2$ in range 7-8.2 kHz.

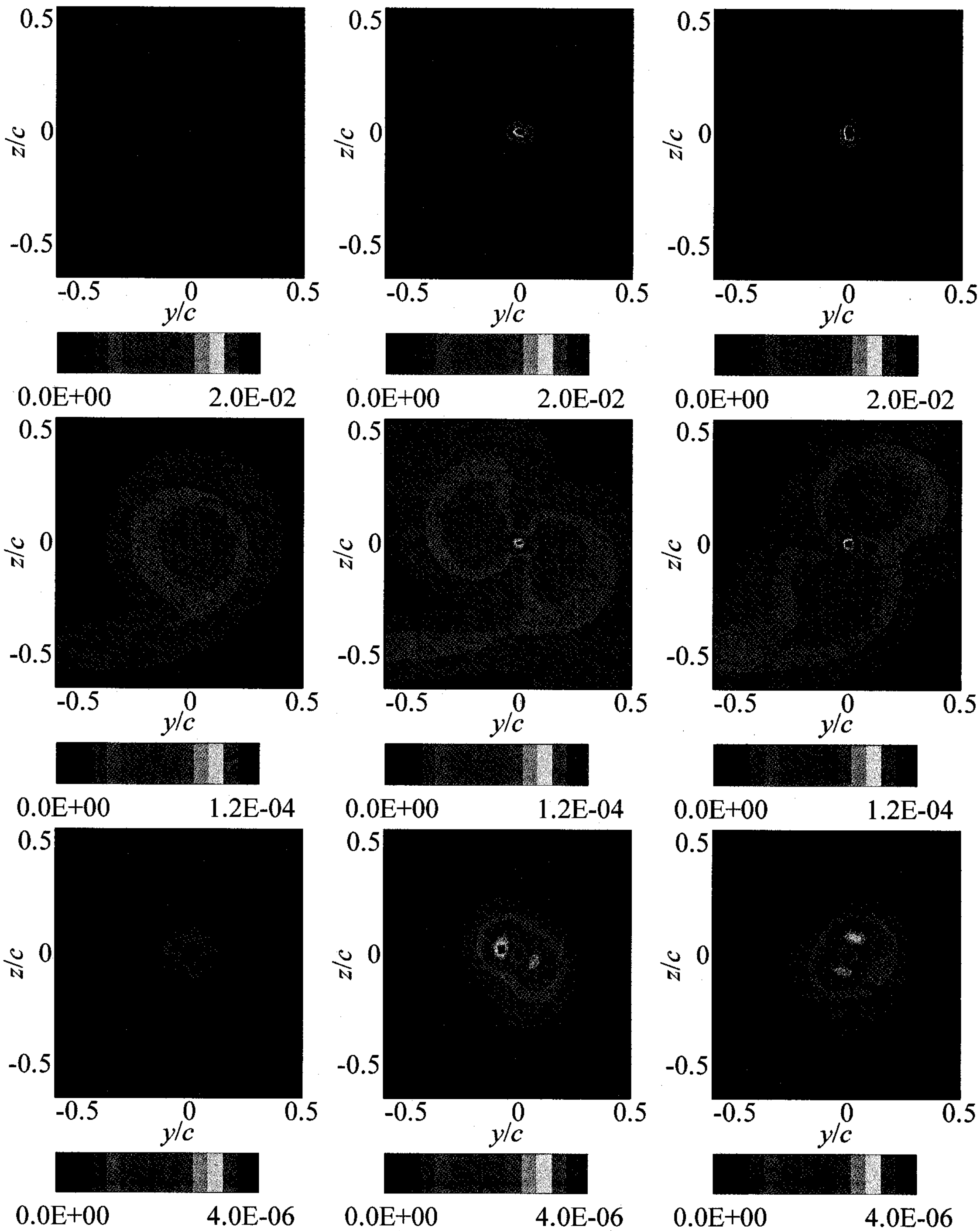

Figure 6.5: Band-pass filtered Reynolds stresses for the small-grid case at $X/c = 9.75$. (a) $\widehat{u_x^2}/U_o^2$ in range 0-500 Hz, (b) $\widehat{u_y^2}/U_o^2$ in range 0-500 Hz, (c) $\widehat{u_z^2}/U_o^2$ in range 0-500 Hz, (d) $\widehat{u_x^2}/U_o^2$ in range 1.0-1.5 kHz, (e) $\widehat{u_y^2}/U_o^2$ in range 1.0-1.5 kHz, (f) $\widehat{u_z^2}/U_o^2$ in range 1.0-1.5 kHz, (g) $\widehat{u_x^2}/U_o^2$ in range 7-8.2 kHz, (h) $\widehat{u_y^2}/U_o^2$ in range 7-8.2 kHz and (i) $\widehat{u_z^2}/U_o^2$ in range 7-8.2 kHz.

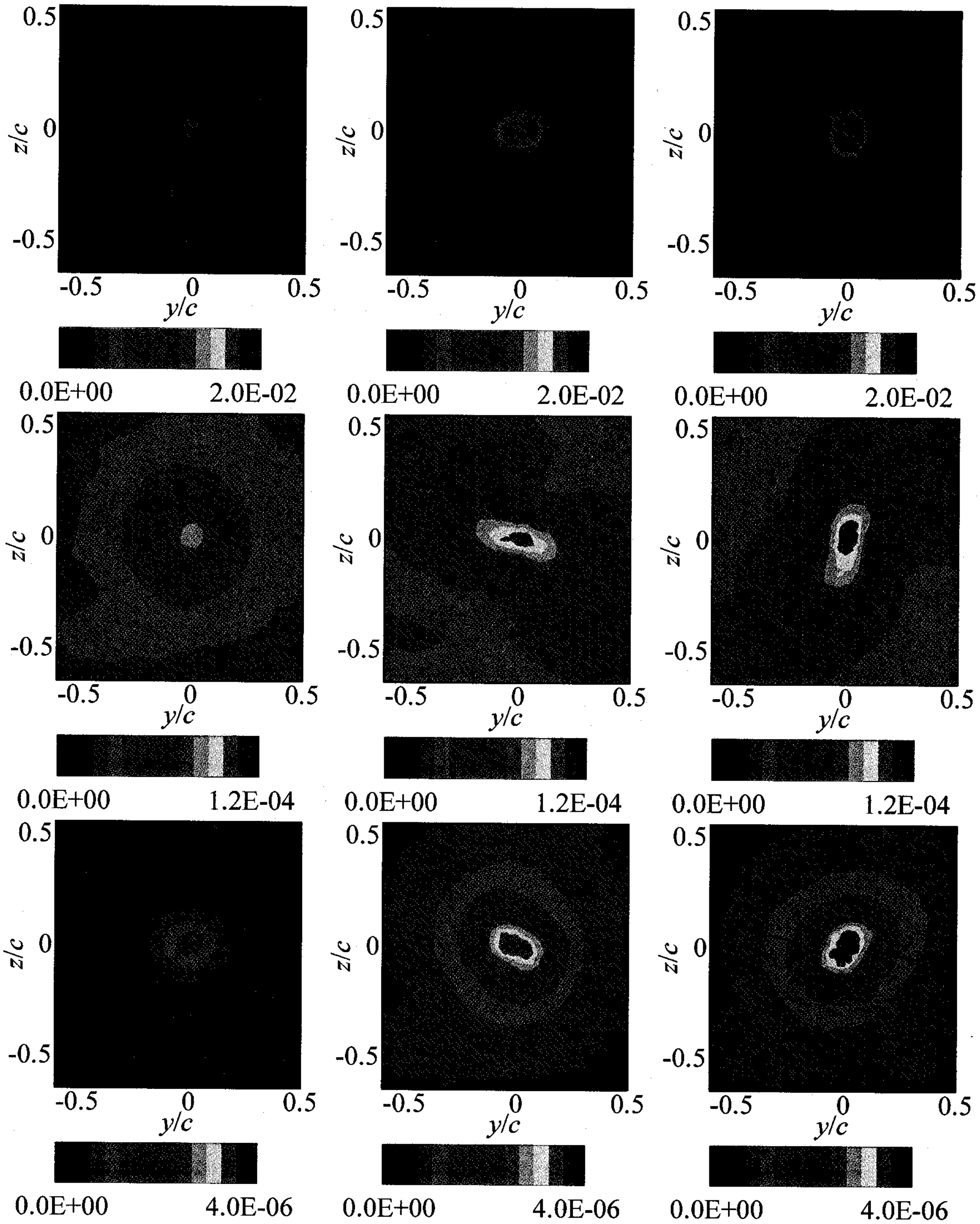

Figure 6.6: Band-pass filtered Reynolds stresses for the large-grid case at $X/c = 9.75$. (a) $\widehat{u_x^2}/U_o^2$ in range 0-500 Hz, (b) $\widehat{u_y^2}/U_o^2$ in range 0-500 Hz, (c) $\widehat{u_z^2}/U_o^2$ in range 0-500 Hz, (d) $\widehat{u_x^2}/U_o^2$ in range 1.0-1.5 kHz, (e) $\widehat{u_y^2}/U_o^2$ in range 1.0-1.5 kHz, (f) $\widehat{u_z^2}/U_o^2$ in range 1.0-1.5 kHz, (g) $\widehat{u_x^2}/U_o^2$ in range 7-8.2 kHz, (h) $\widehat{u_y^2}/U_o^2$ in range 7-8.2 kHz and (i) $\widehat{u_z^2}/U_o^2$ in range 7-8.2 kHz.

Normal stresses in 1.0-1.5 kHz frequency range

For the no-grid case at $X/c = 5.75$ and $X/c = 9.75$ in the frequency range 1.0-1.5 kHz (Figures 6.1d-f and 6.4d-f), the wandering influence is still apparent on the time-averaged axis, however the Reynolds stresses in the spiral wake are of comparable magnitude with increasing magnitude in the stresses as the spiral approaches the core. The spiral wake is clearly evident in the contours of all three normal stresses (Figures 6.1d-f and 6.4d-f). Each of the transverse stresses have two peaks in the radial range $0.1 < r/c < 0.2$; the peaks of $\widehat{u_y^2}/U_o^2$ occurred near the y axis and those of $\widehat{u_z^2}/U_o^2$ near the z axis with the peak on the innermost portion of the spiral slightly weaker. It is interesting to note that, except in the range $0.1 < r/c < 0.2$, $\widehat{u_y^2}/U_o^2$ and $\widehat{u_z^2}/U_o^2$ have comparable magnitudes in the spiral wake, whereas on the innermost spirals the organization of the transverse stresses suggests that fluctuations in the radial direction are more important than in the azimuthal direction. As streamwise distance increases from $X/c = 5.75$ to 9.75, the contours appear more diffuse and the magnitude of the Reynolds stresses decreases.

For the small-grid case at $X/c = 5.75$ and $X/c = 9.75$ in the frequency range 1.0-1.5 kHz (Figures 6.2d-f and 6.5d-f), the magnitude of the wandering influence is reduced on the time-averaged vortex axis. High transverse Reynolds normal stresses are now evident in the radial range $0.1 \lesssim r/c \lesssim 0.3$, with the $\widehat{u_x^2}/U_o^2$ occurring for $r/c \lesssim 0.2$. The contours of the transverse stresses $\widehat{u_y^2}/U_o^2$ and $\widehat{u_z^2}/U_o^2$ have a double-peak appearance, similar to the one observed for the no-grid case, however, they spread over a much larger area. As with the no-grid case, as streamwise distance increases from $X/c = 5.75$ to $X/c = 9.75$, the contours appear more diffuse and the magnitude of the Reynolds stresses decreases.

For the large-grid case at $X/c = 5.75$ and $X/c = 9.75$ in the frequency range 1.0-1.5 kHz (Figures 6.3d-f and 6.6d-f), the peak Reynolds normal stresses occur on the time-averaged vortex axis, as observed for the lower frequency band. However, the $\widehat{u_y^2}/U_o^2$ and $\widehat{u_z^2}/U_o^2$ stresses are of comparable magnitude in the free-stream and have an ovoid appearance organized in such a way as the fluctuations in the radial direction are higher than in the tangential direction. Again, as streamwise distance increases, the magnitude of the Reynolds normal stresses decreases and the contours appear more diffuse.

Normal stresses in 7-8.2 kHz frequency range

For the no-grid case at $X/c = 5.75$ and $X/c = 9.75$ in the frequency range 7-8.2 kHz (Figures 6.1g-i and 6.4g-i), the Reynolds stresses within the vortex core ($r/c \lesssim 0.04$) are much smaller than in the surrounding fluid, consistent with the observations of Devenport et al. (1996). The distribution of the stresses is similar to that observed in the 1.0-1.5 kHz frequency range, however the highest streamwise normal stresses now occur in an azimuthal ring; it is worth noting that a similar ring was also observed in the high-pass filtered results of Devenport et al. (1996). Also, for $X/c = 9.75$, as the wake spirals closer to the vortex there is an increase in normal stresses.

For the small-grid case at $X/c = 5.75$ and $X/c = 9.75$ in the frequency range 7-8.2 kHz (Figures 6.2g-i and 6.5g-i) the distribution of Reynolds normal stresses are concentrated in an azimuthal ring around the vortex core and the spiral wake is no longer evident in the contours of $\widehat{u_x^2}/U_o^2$. As with the previous bandpass range, two peaks are evident along the $y = 0$ and $z = 0$ axis when the transverse normal stress is in the radial direction.

As with the small grid cases, the large-grid case at $X/c = 5.75$ and $X/c = 9.75$ in the frequency range 7-8.2 kHz (Figures 6.3g-i and 6.6g-i) show a concentration of Reynolds normal stresses near the time-averaged vortex axis. However the stresses are not arranged in an azimuthal ring, as the peak values are located on the time-avearged vortex axis. Similar to the observations made for the small-grid case, the region in which the Reynolds stresses are greater than those in the free-stream appears to be smaller than in the 1.0-1.5 kHz frequency range, suggesting that the presence of the vortex intensifies the small scale eddies.

To investigate the azimuthal ring at high frequency pass-bands further, profiles along the line $z = 0$ were examined. These profiles for the no-grid and small-grid cases at $X/c = 9.75$ (where the azimuthal ring is prominant) are shown in Figures 6.7 and 6.8 respectively for $\widehat{u_x^2}/U_o^2$, $\widehat{u_y^2}/U_o^2$ and $\widehat{u_z^2}/U_o^2$. Along the $z = 0$ axis, $\widehat{u_y^2}/U_o^2$ is the Reynolds stress in the radial direction and $\widehat{u_z^2}/U_o^2$ is the Reynolds stress in the circumferential direction. Figures 6.7a-b show that as the frequency pass-band increases, the peak streamwise and radial stresses moves towards the centre of the vortex. At small frequency pass-bands, the peak circumferential stress (Figure 6.7c) is at approximately the same radial location as the radial and streamwise stresses, however, at higher pass-bands the peak stress is radially further away from the vortex axis. Similar behaviour was also observed in the small grid case (Figure 6.5a-c).

This distribution of stresses in the azimuthal ring appears to be consistent with the wrapping of the spiral wake around the vortex, as discussed by Devenport et al. (1996) and Miranda and Devenport (1998). As the wake becomes wrapped around the vortex, it

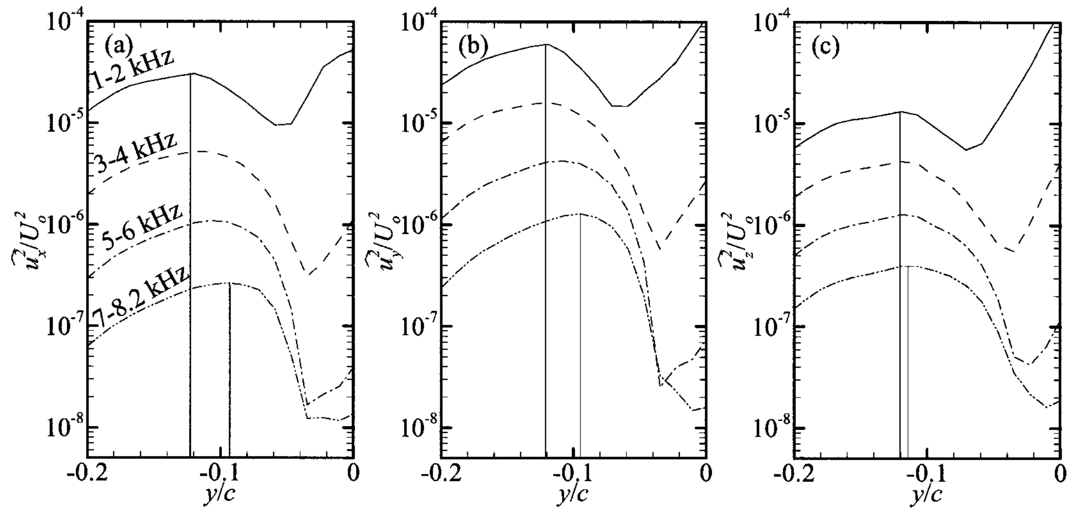

Figure 6.7: Reynolds normal stresses, (a) $\widehat{u_x^2}/U_o^2$, (b) $\widehat{u_y^2}/U_o^2$ and (c) $\widehat{u_z^2}/U_o^2$ in selected pass-bands along the $z = 0$ axis for the no-grid case at $X/c = 9.75$.

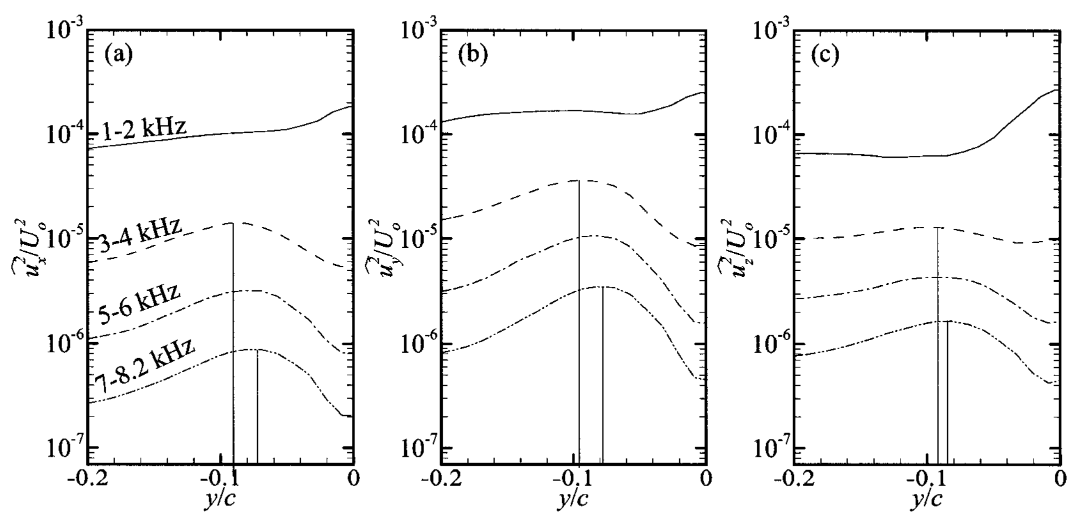

Figure 6.8: Reynolds normal stresses, (a) $\widehat{u_x^2}/U_o^2$, (b) $\widehat{u_y^2}/U_o^2$ and (c) $\widehat{u_z^2}/U_o^2$ in selected pass-bands along the $z = 0$ axis for the small-grid case at $X/c = 9.75$.

undergoes stretching, which becomes stronger as the core is approached. This stretching process can be illustrated using a simple model consisting of a Lamb-Oseen vortex placed at $(y, z) = (0, 0)$ and a series of points placed along the line $z = const$ at a time t_o, at locations corresponding to the near wake of the wing. During a small time increment δt, the induced velocity field of the vortex would displace each point on the y, z plane by a distance $U_\theta \delta t$ along the local circumferential direction. By time-integration, one may identify the location of each point at different times. The results of this integration for two selected times t_1 and $2t_1$are illustrated in Figure 6.9, in which the core radius $r_{\theta\,\max}$ of the vortex is denoted by a circle. This figure illustrates that the distance between each neighbouring pair of points increases (i.e., the line connecting these points is stretched) with time and that the greatest stretching occurs in the innermost spiral, where $\partial U_\theta / \partial r$ was the highest. Similar behaviour is also observed when modeling the roll-up of a trailing vortex sheet using point vortices (Heyes et al. (2003)). Note that this stretching is primarily in the azimuthal direction as the distance traveled by the points in the streamwise direction will be $U_\infty \Delta t$ and remain the same for all points.

A similar process could be expected to occur in the presence of free-stream turbulence, whereby the free-stream eddies become wrapped around the vortex. Stretching would tend to increase the azimuthal scale of the eddies and to decrease the radial and streamwise scales, which thus become smaller towards the vortex core where the stretching is highest, as sketched in Figure 6.10. As these eddies get convected past the probe, their turbulent kinetic energy would appear to shift to higher frequencies, due to their smaller scale.

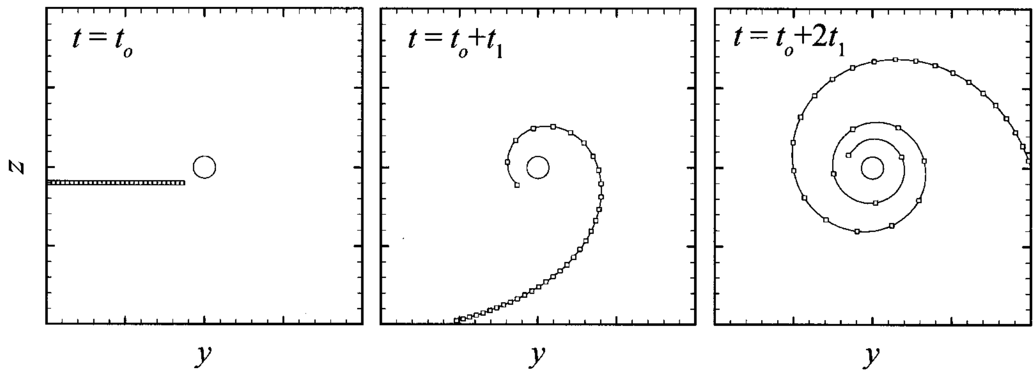

Figure 6.9: Illustration of stretching undergone by wake due to the vortex.

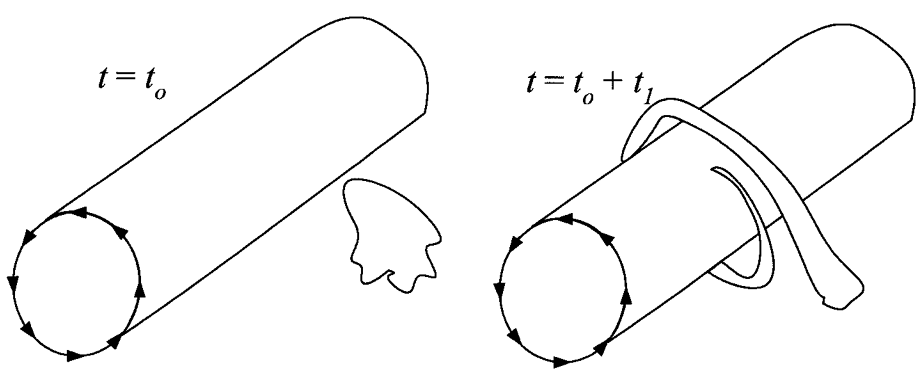

Figure 6.10: Sketch illustrating the influence of stretching on a free-stream eddy.

This eddy stretching has been observed in the numerical simulations of Miyazaki and Hunt (2000), Holzäpfel et al. (2003), Takahashi et al. (2005) and Marshall and Beninati (2005) and has been linked to the formation of secondary coherent structures through merger of eddies with like-signed azimuthal vorticity. Marshall and Beninati (2005) describes the appearance of the secondary structures as vortex loops, with the legs of the loop aligned in the azimuthal direction. The radial component of Reynolds stresses was found to be enhanced relative to the other two directions through velocity induced by the pairing of the legs of these loops. This description is consistent with present observations based on Figures 6.7 and 6.8, which show that the component of Reynolds stress in the radial direction has the greatest magnitude, compared to the streamwise and azimuthal directions.

Marshall and Beninati (2005) also estimate that the typical core size of these coherent structures is approximately $0.7r_{\theta\,\max}$. For the conditions of the present experiment, this would correspond to approximately $0.03c$. Assuming that the structures are convected by the velocity U_o, one would expect that the frequency of the most energetic fluctuations would be near 4 kHz, which is consistent with the approximate frequency range for which the azimuthal ring becomes prominent for the small-grid case (3-4 kHz in Figure 6.8). In the spiral wake, the most energetic eddies for the no-grid case would have a scale comparable to the wake width, which from Figure 5.28 can be estimated to be approximately $0.2c$ for $X/c = 9.75$ and thus corresponding to a frequency of 0.2 kHz. This frequency value is consistent with the ring being evident at lower frequencies for the no-grid case (at 1-2 kHz in Figure 6.7). As the eddies are increasingly stretched azimuthally, their radial scales will further decrease and hence the frequency range at which these eddies are most dominant will increase as well. This is consistent with the radially inward movement of the peak in the Reynolds stresses at higher frequency pass-bands in both Figures 6.7 and 6.8.

Although the arrangement of the Reynolds stresses into azimuthal rings was not evident for the large-grid case, it does not necessarily mean that this same reorganization did not occur in this case. Due to the large amplitude of vortex wandering (see Section 6.2), even when the probe is at the time-averaged vortex core, it spends more time measuring outside the core than inside. Hence, the stresses at $(y, z) = (0, 0)$ could contain contributions from a very large region around the vortex.

6.2 Quantifying vortex wandering

6.2.1 Wandering amplitude

Vortex wandering was found to be significant in the grid cases. In order to achieve a correct interpretation of the vortex properties it is necessary to quantify the vortex wandering and to assess its effects on the measurements.

Method of Devenport et al.

Devenport et al. (1996) used an iterative technique, detailed in Appendix B, to recover the corrected velocity profile, $U_{\theta c}(r)$, from the time-averaged velocity profile, $\overline{U}_\theta(r)$. This technique assumes that the joint probability distribution of vortex position in the y and z directions is bi-normal and therefore described by the standard deviations, σ_y and σ_z, of the distributions in the y and z direction respectively. These two values are estimates of the amplitudes of wandering in the y and z directions.

Application of Devenport et al.'s technique to the current measurements for the no-grid case (results shown in Figure 6.11) showed that the effect of wandering was essentially negligible for this case (compare Figure 5.43 to Figure 6.11a) with very little development of the velocity profile in the streamwise direction such that $r_{\theta\,\mathrm{max}} = 0.04c$ and $U_{\theta\,\mathrm{max}} = 0.4U_o$ for all streamwise cases except at $X/c = 9.75$. At $X/c = 9.75$ the peak circumferential velocity was $U_{\theta\,\mathrm{max}} = 0.37U_o$ at $r_{\theta\,\mathrm{max}} = 0.04c$. The corrected small-grid velocity profiles (Figure 6.11b) showed little change in $r_{\theta\,\mathrm{max}} = 0.04c$ with streamwise distance whereas $U_{\theta\,\mathrm{max}}$ decreased from $0.35U_o$ at $X/c = 1.75$ to $0.31U_o$ at $X/c = 9.75$.

The rms wandering amplitudes σ_y and σ_z determined while correcting the profiles are shown in Figure 6.12. The wandering amplitude was found to grow with streamwise distance for both the no-grid and small-grid cases with the wandering amplitude of the no-grid case remaining lower than $0.006c$ (1 mm), which is consistent with the previous observation of essentially negligible effect of wandering.

When attempting to apply Devenport et al.'s correction to the large-grid cases, it was found that after one or two iterations, the corrected series fits became unrealistic, containing oscillations and values of $U_{\theta\,\mathrm{max}}$ near U_o (see Figure 6.11c). It was discovered that the most likely source of this inconsistency was a limitation in the correction (the minimum realizable radial position of the series fit in Equation B.3). As the assumed wandering amplitude iterated to large amplitudes for the large-grid cases, the minimum radius at which the corrected profile could be accurately predicted exceeded the radial location of peak circumferential velocity, which introduced an ambiguity in the location of this peak. Because the location of the peak affects the magnitude of the velocity gradients

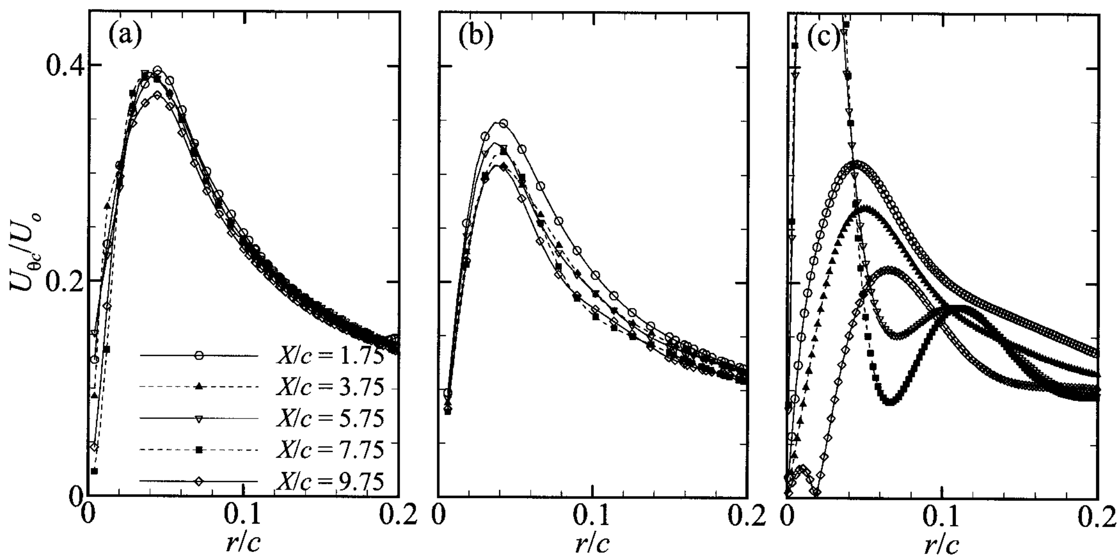

Figure 6.11: Radial profiles of circumferential velocity corrected for wanderng using the method of Devenport et al. (1996) for (a) the no-grid (b) small-grid and (c) large-grid cases.

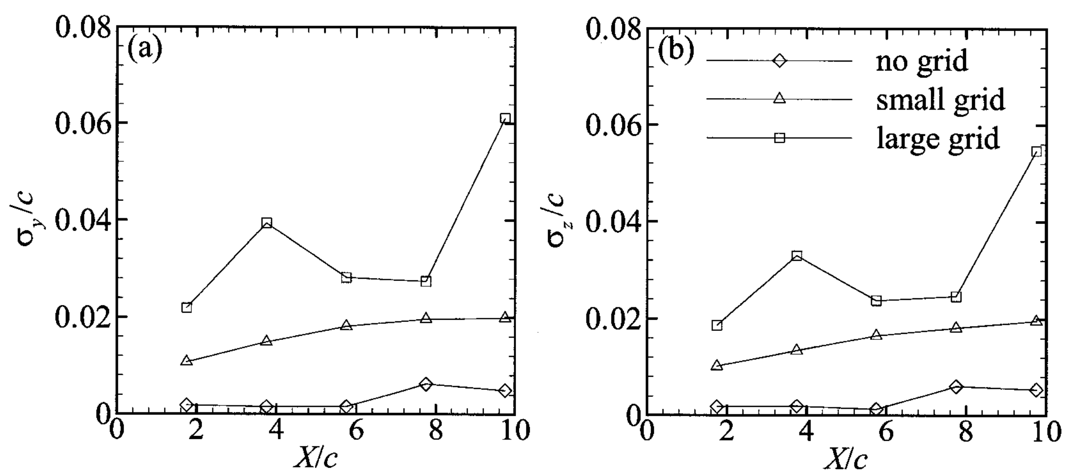

Figure 6.12: Wandering amplitudes (a) σ_y/c and (b) σ_z/c determined using the correction technique of Devenport et al.

in the vortex core, there is a corresponding ambiguity in the determination of the estimated contribution of wandering to the Reynolds stresses, which is used to correct the assumed wandering amplitude.

Zero-crossing technique

Because Devenport et al.'s technique was found to result in improbable velocity profiles for large amplitudes of vortex wandering, it is possible that the technique also could contain undetected errors for corrections required for smaller amplitudes of wandering. Another complication arising from using Devenport et al.'s correction technique is the possibility of turbulence within the vortex core, which, in Devenport's correction, is assumed to have a negligible contribution to $\overline{u_y^2}$, $\overline{u_z^2}$, $\overline{u_y u_z}$ compared to the influence of vortex wandering. However, in the strong free-stream turbulence cases under consideration, there is a possibility of non-negligible contributions of turbulence to the Reynolds stresses within the core. The existence of these additional contributions could result in over-correction of the profiles. Finally, Spalart (1998) suggests that the correction could include errors introduced by the assumption of a binormal probability distribution of vortex position. In light of these statements, it was felt that if a different technique could be developed to quantify the vortex wandering, greater confidence could be provided in the correction of Devenport et al. (1996).

Consider a laminar vortex with its axis intersecting the measuring plane at position (y_v, z_v) and a probe located at position (y_p, z_p) and measuring velocity components U_{yv} and U_{zv} on this plane, as shown in Figure 6.13.

It can be observed that, as the vortex wanders in y and z, there could be instances

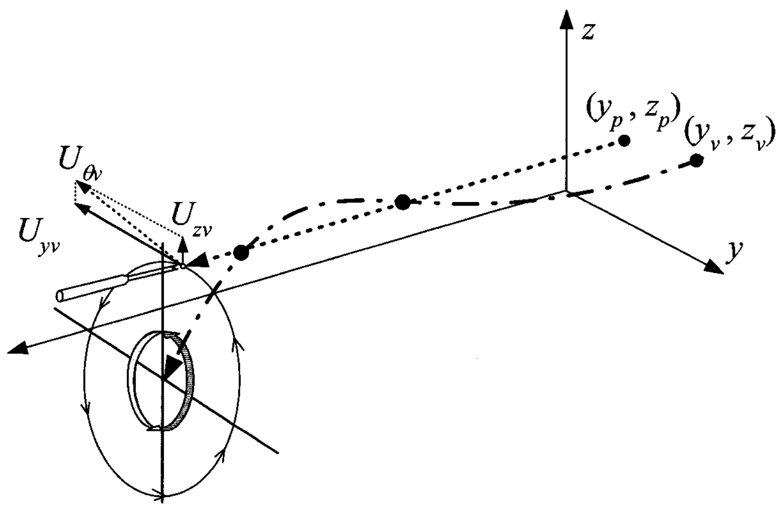

Figure 6.13: Sketch defining vortex position in the yz plane (y_v, z_v), probe position in the yz plane (y_p, z_p) and the velocity components induced by the vortex at the probe position U_{yv}, U_{zv} as the vortex wanders in time.

at which the measurement probe is on the axis of the vortex, such that $(y_v, z_v) = (y_p, z_p)$. At these instances, the measured transverse velocity components must vanish, i.e., $U_{yv} = U_{zv} = 0$. By quantifying the instances when $U_{yv} = U_{zv} = 0$ for a yz plane of (y_p, z_p) measurement positions, an estimate of the joint probability distribution function of (y_v, z_v) can be determined, such that the probability of the vortex axis being at position (y, z) in the measurement plane is proportional to the number of simultaneous zero crossings for U_y and U_z. The "width" of the joint probability density function can then be used as a measure of the vortex wandering amplitude.

In practice, this approach is contaminated by two complications. First, the velocity components measured by the probe are with respect to the laboratory frame, whereas the velocity induced by the vortex is considered to be in a frame attached to the wandering axis. This effect would be negligible if the transverse velocity of the vortex axis were very small compared to the local induced velocity. Second, if there were turbulence in the vortex core, it would cause fluctuations of the local velocity, which would introduce zero crossings at locations different from the vortex axis. Because there is no way to determine accurately the contributions of these two effects on the velocity measurements, the best one can do is to estimate the uncertainty that they would introduce to the determination of the vortex axis location.

It seems reasonable to assume that, in a strongly turbulent free-stream, the wandering of the vortex would be largely attributed to convection by the free-stream eddies. As the vortex resists deformation, its wandering velocity would likely be significantly lower than the local transverse velocity fluctuation in the free stream (in the absence of the vortex). Therefore, the amplitude of free-stream fluctuations may be considered as an upper bound for the amplitude of wandering velocity. For the purposes of estimating uncertainty, we consider as upper bound the value $2u'_y$, which is larger in magnitude than the free-stream fluctuations 95% of the time. The amplitude of turbulent fluctuations in the vortex core is even more challenging to estimate. It is known that internal turbulence production within the vortex core is small (Devenport et al. (1996)), and that the stabilizing effects of rotation would tend to eliminate turbulence within the vortex (Bradshaw (1969)). On the other hand, it is possible that the "beating about" of the vortex by the free stream turbulence and induction by nearby turbulent eddies might result in velocity fluctuations in the core, which may make a contribution to the local velocity measurement before they get eliminated by rotation. Again, it seems that a reasonable estimate of the upper limit of such motions would be $2u'_y$. In the worst case, velocity fluctuations caused by both effects would have an amplitude of approximately $2.8u'_y$.

As an illustration of the uncertainty evaluation process, consider the large-grid case at $X/c = 9.75$, for which the free-stream had $u'_y \approx 0.025U_o$. Then, the upper bound of the velocity fluctuation uncertainty would be $2.8u'_y \approx 0.07U_o$. Assuming that the radial gradients of circumferential velocity in the vortex core for the turbulent free-stream cases are not very different from that in the no-grid case, one may estimate the radial gradient of the circumferential velocity near the axis as $\frac{\partial U_\theta}{\partial r} \approx 0.1U_o/\,\mathrm{mm}$ (see Figure 6.11a for example). Then, one could infer that the previously estimated velocity uncertainty would introduce an uncertainty in the determination of the vortex axis location equal to $2.8u'_y/\left(\frac{\partial U_\theta}{\partial r}\right) \approx 0.7\,\mathrm{mm}$. This uncertainty is significantly smaller than the estimated amplitude of the wandering motion, to be discussed in following sections. The actual uncertainty is expected to be significantly smaller than this value, which is considered to be an upper bound.

A different problem in this axis determination process arises when the probe is far away from the vortex axis, so that the measured velocity is essentially grid-generated turbulence. Then, the amplitude of the velocity fluctuations becomes of the order of u'_y and zero-crossings that are unrelated to the passage of the vortex axes would be encountered. To remove a part of the turbulent fluctuations from the measured time series, while leaving wandering contributions unaffected, the time series was first digitally low-pass filtered before the zero-crossing count was conducted. The filter used was a double-pass fifth order Butterworth filter with a cut-off frequency of 500 Hz with guidance in selecting the cut-off frequency provided by visual inspection of the filtered time series. Moreover, the probability that a zero-crossing represented vortex axis passage and not free-stream turbulence was increased significantly by applying the following condition on the streamwise velocity U_x. Time-averaged velocity profiles, such as those shown in Figures 5.33 to 5.37 indicate that, in general, $\overline{U}_x$ decreases with r. For example, in the no-grid case at $X/c = 9.75$, for which the effect of wandering on the profile is expected to be small within the core, $U_x < 0.98U_o$ for $r/c < 0.08$. The condition for accepting a zero-crossing as representing passage of the vortex axis was selected as $U_x < 0.97U_o$. The value of this threshold was initially selected using $1 - u'_y$ and then adjusted by trial and error as not to reject an excessive number of axis passages. It was found that, if the threshold were too low, for example if $U_x \lesssim 0.90U_o$, the maximum number of axis passages captured fell to around 0.05% of the time-series length and confidence could not be provided that the instances captured were not outliers. If the threshold was increased, the number of zero-crossings observed at large radii (e.g., $r/c \gtrsim 0.2$ for the large-grid case at $X/c = 9.75$) would increase at rates greater than that for smaller radii (e.g., $r/c \lesssim 0.2$ for the large-grid case at $X/c = 9.75$).

Finally, to account for the spatial resolution of the probe, a zero-crossing was defined as an instance in the time series where $|U_y|$ and $|U_z|$ were $\leq 0.05U_o$. Using $\frac{\partial U_\theta}{\partial r} \approx 0.1U_o/\,\mathrm{mm}$ this equates to a spatial range of 0.5 mm, which is approximately the width of the probe measurement volume, therefore when $|U_y|$ and $|U_z| \leq 0.05U_o$ the vortex axis is assumed to be within the probe measurement volume.

As an example of this analysis, Figure 6.14 shows isocontours of zero-crossings for the no-grid, small-grid and large-grid cases at $X/c = 9.75$. Zero-crossing counts were used to estimate the probability density function (PDF) of the instantaneous vortex axis position relative to its time-averaged position. Such PDFs along the $z = 0$ and $y = 0$ axes, determined from zero-crossings counted from data points within a range of $0.01c$ of each axis, are presented in Figure 6.15. This figure clearly shows that, in all cases, the time-averaged vortex axis position has the maximum probability of being also the instantaneous axis position. It also illustrates a dramatic increase of axis wandering with increasing free-stream turbulence. The good agreement of Gaussian curve fits with the measurements, also shown in Figure 6.15, is strong evidence that vortex wandering is approximately Gaussian in all directions. This observation extends Devenport et al. (1996)'s assumption for vortex wandering in low-turbulence free streams to the case of free-streams with isotropic turbulence. The wandering amplitude for each measurement case can be confidently represented by the standard deviation σ of the distance between the instantaneous and time-averaged vortex axis positions, as determined by the zero-crossing method, and conveniently estimated from the fitted Gaussian curves. To illustrate the soundness of this approach, it is noted that the high-resolution measurements for the no-grid case at $X/c = 9.75$ gave $\sigma \approx 0.8\,\mathrm{mm}$, which was not too far from the value 0.6 mm, estimated using Devenport et al.'s technique. The difference between these two values is within the expected uncertainties of the zero-crossing technique and the probe positioning system and smaller than the spatial resolution of the hot-wire probe.

As an example of the effect of conditioning we can examine the large-grid case at $X/c = 9.75$. Far away from the core, at $(y, z) = (-0.15c, -0.15c)$, the filtering was found to decrease the accepted zero-crossings by 1.5% of the time series length, and the threshold of $U_x < 0.97U_o$ decreased the accepted zero crossings by a further 7.5% of the time series length. On the time-averaged vortex axis, filtering decreased the accepted zero-crossings

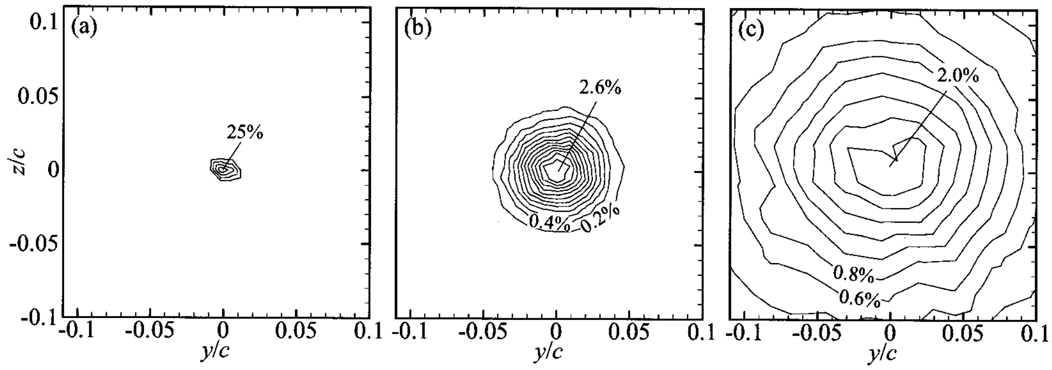

Figure 6.14: Isocontours of zero-crossing count as a percentage of time series length for the (a) no-grid, (b) small-grid and (c) large-grid cases ($X/c = 9.75$). Contour spacing 5% for the no-grid case and 0.2% for the small-grid and large-grid cases.

by less than 0.1% of the time series length, while the U_x threshold decreased the accepted data points by only 0.5% of the time-series length.

The dependence of the wandering amplitude σ on streamwise distance for the three cases is presented in Figure 6.16. In this figure, σ_y and σ_z were estimated from fitted Gaussian curves to probability distributions such as shown in Figure 6.15 from data points along the $z = 0$ and $y = 0$ axes respectively. Due to the dependence of quality of the Gaussian curve fit on the density of measurement points, only data sets with high measurement point density near the time-averaged vortex axis provided dependable results. Hence, the analysis could only be performed on the no-grid, small-grid and large-grid cases at $X/c = 3.75$, 5.75, 7.75 and 9.75.

Some confidence in the zero-crossing technique can be provided when comparing the wandering amplitude for the small-grid case in Figure 6.16 to the wandering amplitude of the small-grid case calculated using the technique of Devenport et al. (1996) shown in Figure 6.12. For example, using the zero crossing count, σ_y was found to be 2.6 mm,

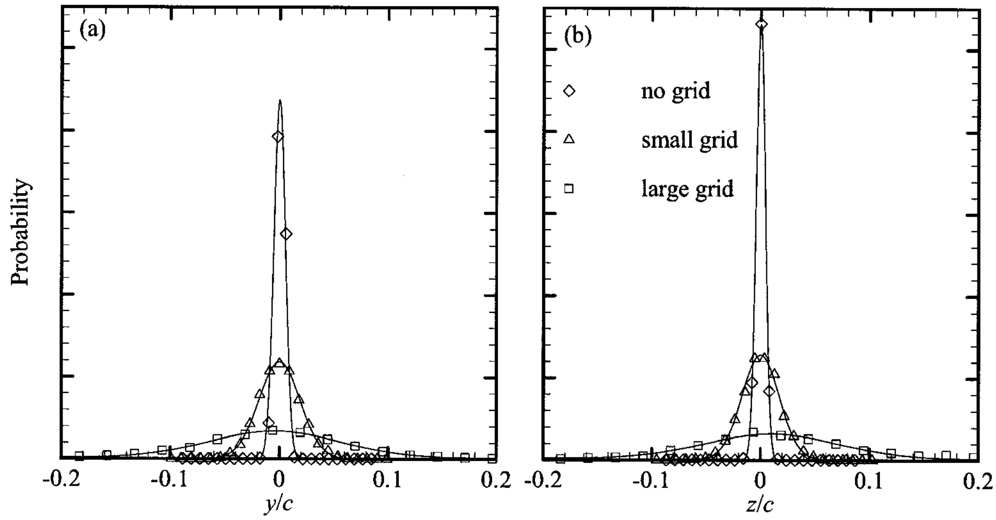

Figure 6.15: Probability density functions of vortex axis position relative to its time average in the (a) y and (b) z directions at $X/c = 9.75$ for the no-grid, small-grid and large-grid cases.

3.1 mm, 3.1 mm and 3.6 mm with increasing X/c, whereas the corresponding values from the technique of Devenport et al. (1996) were 2.6 mm, 3.2 mm, 3.5 mm and 3.5 mm. This agreement is well within the expected error for the zero-crossing technique.

Figure 6.16 reveals a slight anisotropy of σ_y and σ_z for the large-grid and no-grid cases. This isotropy is more closely examined in Figure 6.17 which shows the streamwise development of σ_y/σ_z for the three-cases shown in 6.16.

For the measurement cases with lower measurement point resolution, and shorter measurement lengths, data scatter reduced the confidence in the Gaussian curve-fits. To reduce the restriction on data point acceptance, the technique was modified. Examining Figure 6.13, it can be observed that, when the vortex crosses the horizontal axis of the probe ($y_p = y_v$), $U_{zv} = 0$. Similarly, when $z_p = z_v$, $U_{yv} = 0$. Therefore, by counting the zero-crossings of U_z along the y-axis, an estimate of the probability distribution of vortex

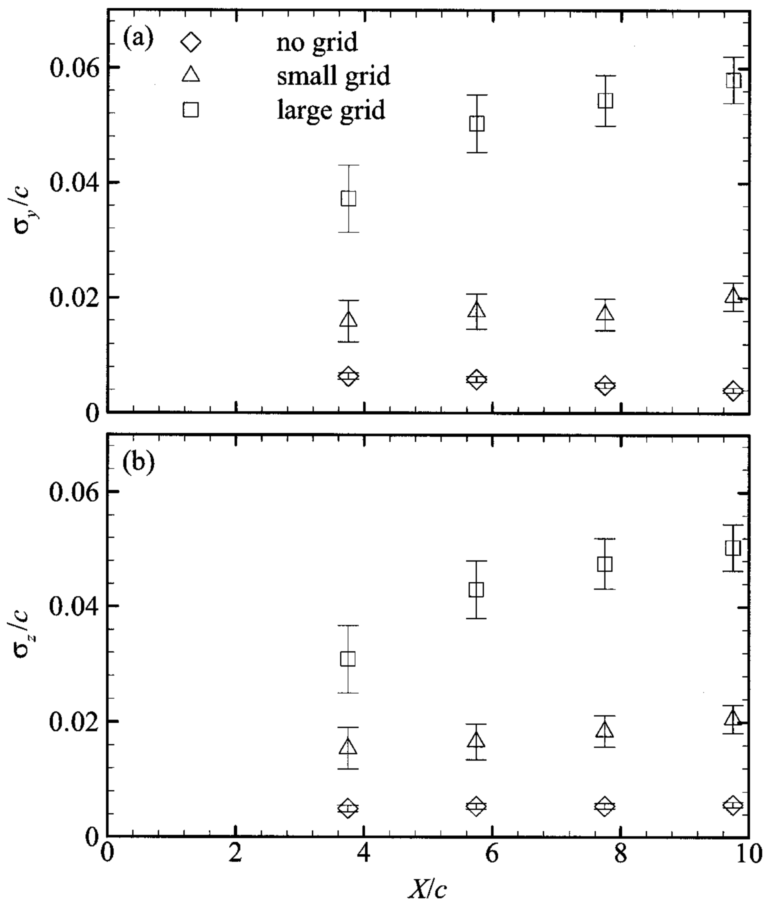

Figure 6.16: Estimated wandering amplitude in (a) y and (b) z directions using simultaneous zero-crossings. Error bars represent estimated uncertainty in identifying the instances when the probe and vortex centre are coincident due to internal turbulence and convective velocity of the vortex.

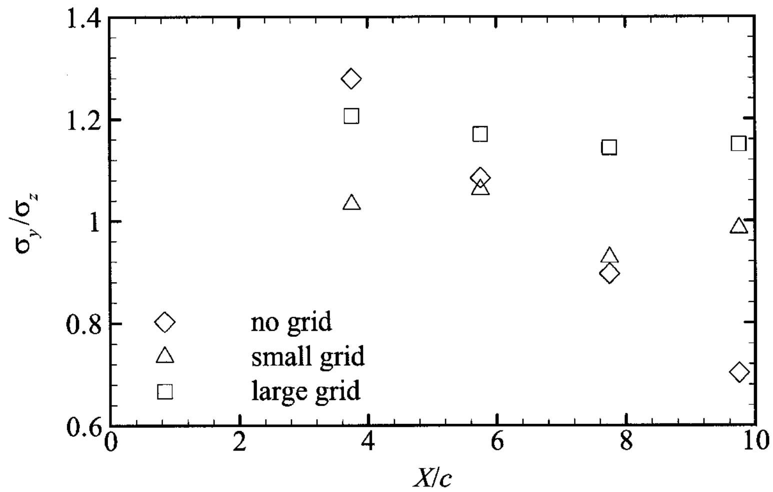

Figure 6.17: Streamwise development of σ_y/σ_z determined using simultaneous zero-crossing technique.

position in the y direction can be obtained with a similar estimate possible along the z-axis. An order of magnitude increase in detected zero-crossings was observed using the new criterion.

The dependence of the wandering amplitude σ on streamwise distance for all measurement cases is presented in Figure 6.18. In this figure, profiles along the y- (Figure 6.18a) and z- (Figure 6.18b) axes were examined separately for zero-crossings in U_y and U_z, respectively, and the corresponding σ_y and σ_z were estimated from fitted Gaussian curves. Comparison of Figure 6.18 to Figure 6.16 shows that values of σ_y and σ_z determined using the zero-crossings for only one component of velocity compare well with the corresponding results determined from the simultaneous zero-crossing of both velocity components.

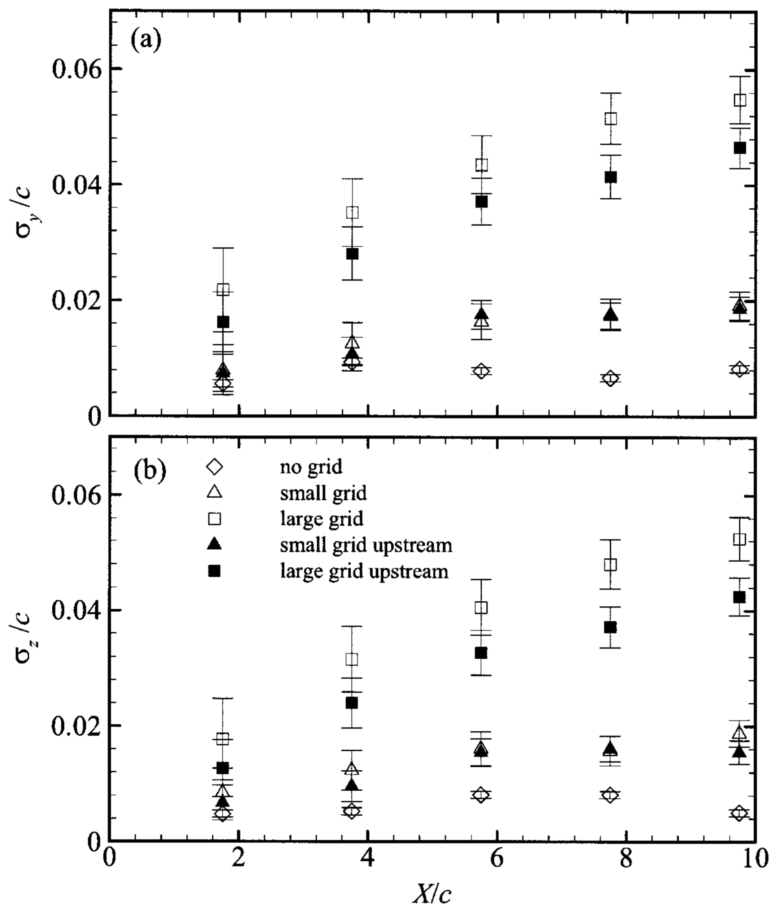

Figure 6.18: Estimated wandering amplitudes in (a) y and (b) z directions as determined by zero crossings of (a) U_z and (b) U_y. Error bars represent estimated uncertainty in identifying the instances when the probe and vortex centre are coincident due to internal turbulence and convective velocity of the vortex.

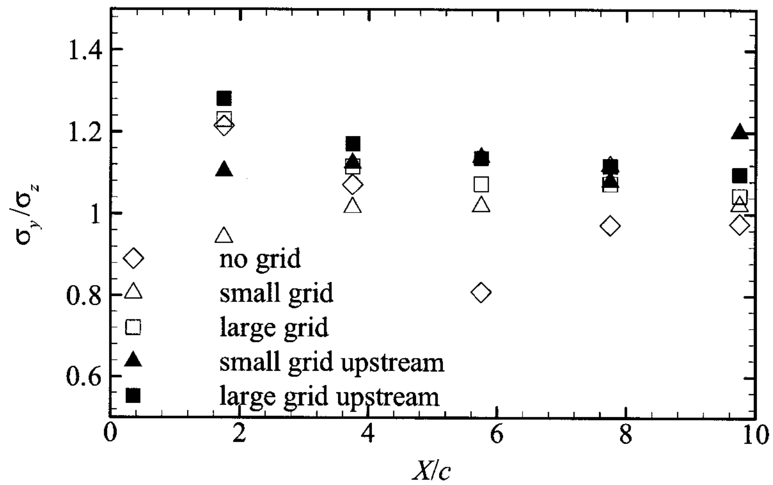

Figure 6.19: Ratio σ_y/σ_z of wandering amplitude in y and z directions as determined by zero crossings of U_z and U_y, respectively.

Comparison with plume dispersion

Vortex wandering in a turbulent stream has some macroscopic analogy with the turbulent dispersion of the plume of a passive scalar, emitted continuously by a point source. Nevertheless, there are some fundamental differences between the two systems: the plume does not affect the flow and poses no resistance to its dispersion, whereas the vortex is a coherent entity, inducing a velocity field in its surroundings and requiring an external torque for its strength and direction to be changed. Even so, the analogy becomes more apparent when examining the analytical treatment of dispersion of a passive scalar in homogeneous isotropic turbulence. Typically, this treatment models the trajectory of a single particle fluid from a point or line source using Lagrangian statistics to model the turbulence. The concentration of the passive scalar after a specified time is then determined as a probability distribution of the possible locations of the particle at that time. The analogy to vortex wandering arises if one models the vortex as an idealized line vortex being emitted from the tip of the wing. If the vortex line is modeled as consisting of many points ("nodes"), separated by sufficient distances for each node to move approximately independently of each other (i.e., neglecting Biot-Savart induction), they can be treated in the same manner as the particles of a passive scalar with no molecular diffusivity. As $t \to \infty$, the probability distribution of vortex position will therefore be analogous to the long-time distribution of passive scalar concentration.

The concentration of a passive scalar emitted from a point source located along the x-axis in homogeneous isotropic turbulence with negligible molecular diffusivity can be approximated as (Csanady (1973))

$$c(x, y, z) \approx \frac{\dot{m}}{4\pi\gamma_T x} \exp\left(-\frac{\left(y^2 + z^2\right) U_x}{4\gamma_T x}\right) , \tag{6.1}$$

where γ_T is the eddy diffusivity and $\dot{m}$ is the mass flow rate of the passive scalar at the point source. The resulting radial distribution of concentration is therefore a Gaussian distribution with standard deviation $2\sqrt{\gamma_T x / U_x}$. The difficulty with using Equation 6.1 is the determination of the eddy diffusivity. Although there are approximations which can be applied to homogeneous isotropic turbulence, these approximations are based on a constant integral length scale, which is not consistent with the characteristic turbulent decay of grid turbulence.

Dispersion of a passive scalar from a line source in decaying homogeneous turbulence has been examined by Shlien and Corrsin (1974) experimentally and by Anand and Pope (1985) theoretically, using a Langevin-type formulation. Although the dispersion of a passive scalar from a line source has a different concentration distribution than dispersion from a point source, the width of the plume should remain the same. The analytical solution for the concentration of a passive scalar from emitted from a line source in homogeneous isotropic turbulence with negligible molecular diffusivity is (Roberts and Webster (2002))

$$c(x,y) \approx \frac{\dot{m}_u}{\sqrt{4\pi\gamma_T x U_x}} \exp\left(-\frac{y^2 U_x}{4\gamma_T x}\right) , \tag{6.2}$$

where $\dot{m}_u$ is the mass flow rate of the passive scalar per unit span of the line source. The concentration distribution in y is again a Gaussian distribution of standard deviation $2\sqrt{\gamma_T x/U_x}$. It therefore seems reasonable to approximate the radius of the plume from a point source using the width of the wake from a line source.

Using the normalized curves fit of Anand and Pope (1985) and scaled experimental results of Shlien and Corrsin (1974) for the dispersion of heat from a heated wire in decaying grid turbulence as a function of streamwise distance from the source, the expected dispersion of a passive scalar emitted from $X/c = 0$ was estimated for each measurement case using the corresponding grid turbulence statistics measured without the wing in place. Additionally, molecular diffusion was neglected so that only the effects of turbulent dispersion are highlighted. The standard deviation of the passive scalar dispersion is compared to the estimated wandering standard deviation of the scaled results of both Anand and Pope, Figure 6.20a, and Shlien and Corrsin, Figure 6.20b.

Although there are some slight differences between the model of Anand and Pope and the scaled measurements of Shlien and Corrsin, both show comparable amplitudes of dispersion with streamwise distance and both are significantly higher than the estimated wandering shown in Figure 6.18. This implies that the vortex is not transported as a passive scalar. One possible explanation for this difference is that the vortex is far from passive as

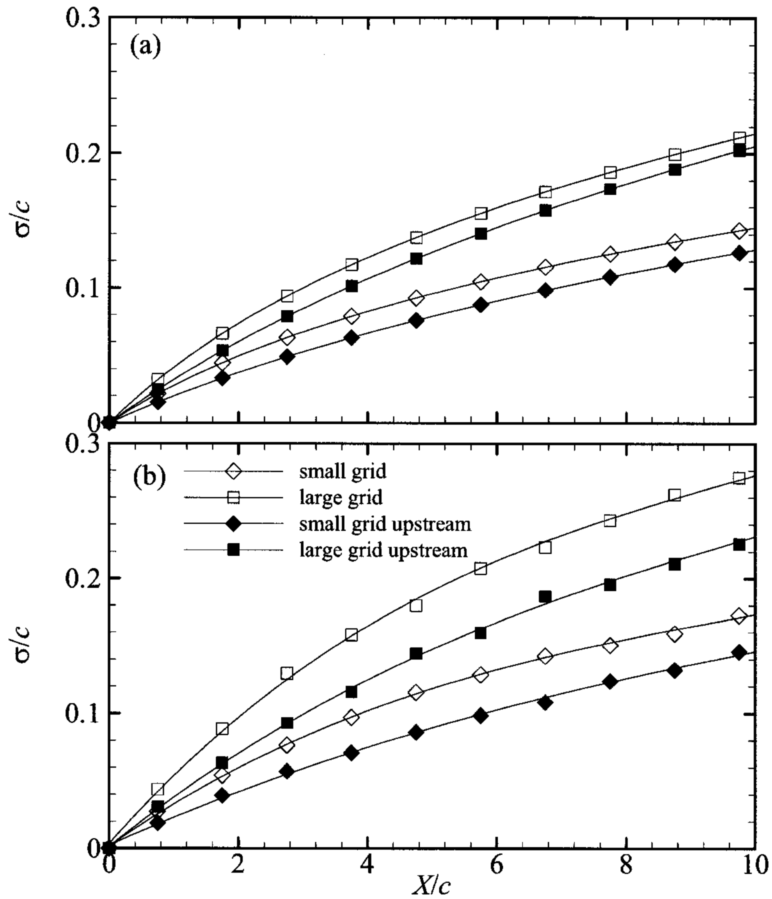

Figure 6.20: Estimated diffusion of a passive scalar using the model of (a) Anand and Pope (1985) and scaled fit of (b) Shlien and Corrsin (1974) for each free-stream turbulence case.

it actively reorganizes and alters the structure of the surrounding turbulence, which in turn reduces the effectiveness of the turbulent transport on the vortex.

6.2.2 Frequency characteristics of vortex motion

Temporal characteristics of the vortex wandering were examined using frequency spectra of U_y and U_z on the time-averaged vortex axis, where the contribution of wandering to the total fluctuation energy is the greatest. Sample spectra, measured at $(y, z) = (0c, 0c)$ for the no-grid, small-grid and large-grid cases at $X/c = 3.75$, 5.75, 7.75 and 9.75 are shown in Figure 6.21. In general, the frequency spectra of U_y and U_z are very similar on and near the time-averaged vortex axis, but their differences increase with increasing radial position. The peak at 30 Hz for the no-grid case is associated with vibration of the probe due to wind tunnel vibrations, as described in Section 4.7.

The variation of power spectra in this flow is difficult to associate with particular causes because they contain contributions from several sources, including:

- vortex wandering, which is expected to act at relatively low frequencies; its relative contribution to the frequency spectra depends on both the local instantaneous velocity gradient, as well as the wavelength, amplitude and path of the vortex wandering

- free-stream turbulence, which is expected to act at relatively high frequencies; frequency spectra within the vortex would be different from those in the free-stream, but should approach them as radius increases

- turbulence in the spiral wake, which contains energetic eddies with length scales of the order of the wake width

- possible instabilities within the vortex core, which would likely express themselves as peaks at characteristic frequencies (Jacquin et al. (2003))

To confuse matters more, the wandering will act to spatially average the spectra, because, as the vortex wanders in space, the probe would measure energy contributions from a range of locations in the flow. For this reason, it is possible that spectra measured with a fixed probe could contain contributions from patterns that dominate different parts of the flow, including the vortex core, the spiral wake, and the free-stream. Even so, vortex wandering effects are expected to be prevalent in spectra measured in the vortex core.

The frequency spectra at $(y, z) = (0c, 0c)$, shown in Figure 6.21, are significantly different for the three cases considered. The no-grid case (Figure 6.21a) has the highest energy level at frequencies lower than 1 Hz, followed by a plateau in the range from 1 to 100 Hz. Between 100 and 400 Hz, these spectra show a roll-off with constant slope, followed by another plateau in the range from 400 to 1000 Hz. At frequencies above 1 kHz, the energy decreases at a continuously increasing rate. A spike of energy is observed at about 1 kHz, which is found to grow with increasing streamwise distance. This spike was previously observed in Section 5.12, and is believed to be associated with an instability in the vortex core, evident for the no-grid case only (similar peaks have been observed and associated with instability by, for example, Singh and Uberoi (1976) and Bandyopadhyay et al. (1991)).

Frequency spectra for the small-grid case (Figure 6.21b) show a relatively flat region for $f \lesssim 100\,\mathrm{Hz}$, followed by a roll-off of constant slope in the range $100\,\mathrm{Hz} \lesssim f \lesssim 300\,\mathrm{Hz}$. At $f \approx 300\,\mathrm{Hz}$, there is a "kink" in the spectra, followed by a roll-off of increasing

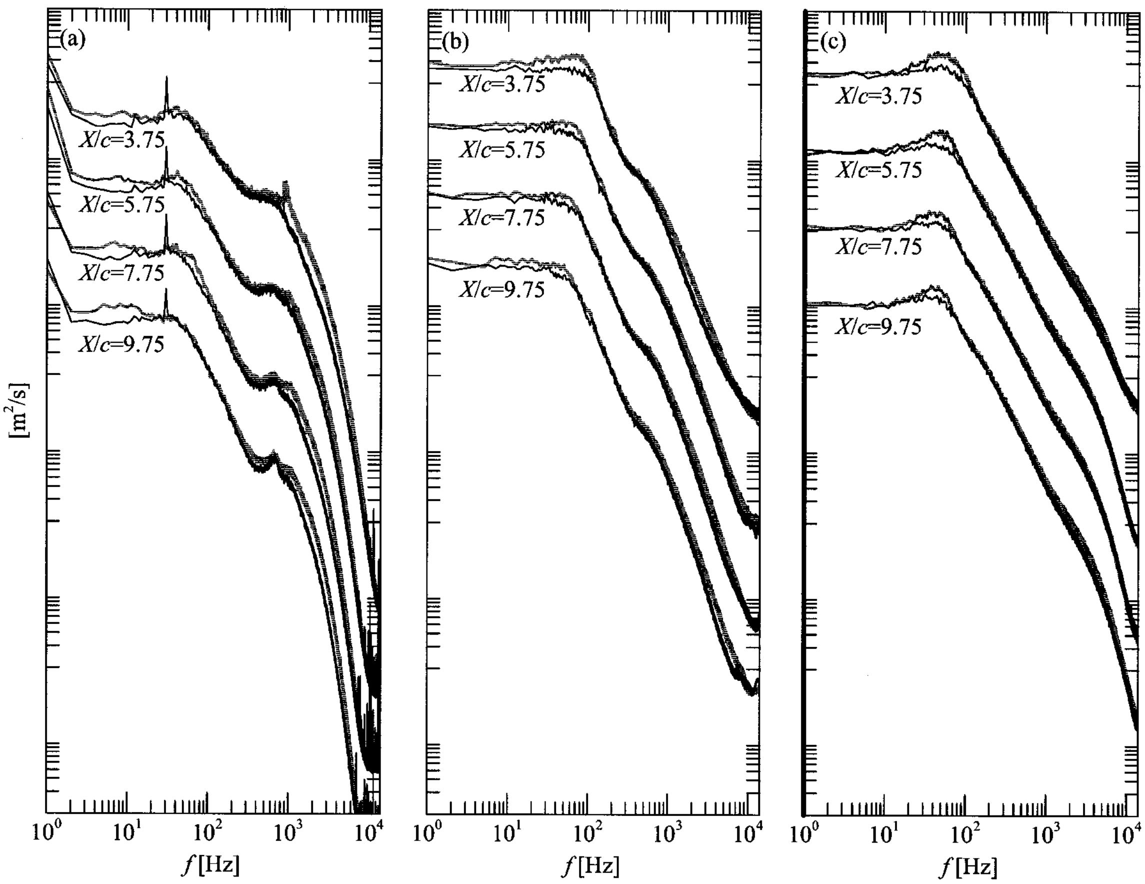

Figure 6.21: Frequency spectra of U_y (black) and U_z (grey) at $(y, z) = (0.0c, 0.0c)$ for (a) no-grid, (b) small-grid and (c) large-grid cases at $X/c = 3.75$, 5.75, 7.75 and 9.75. Each measurement location downstream of $X/c = 3.75$ has been shifted down by a decade to increase clarity. Axes for (a), (b) and (c) are identical.

slope with increasing frequency. Frequency spectra for the large-grid case (Figure 6.21b) appear generally similar to the small-grid case, with the kink appearing at $f \approx 1.2\,\mathrm{kHz}$. Also evident in the large-grid case is a broadband peak centred at $f \approx 40\,\mathrm{Hz}$.

Comparing the spectra in the three cases, one may readily observe that they all display a plateau in the low frequency range ($f \lesssim 100\,\mathrm{Hz}$), followed by a roll-off of constant slope up to some frequency where there is a kink in the spectra. It is believed that this plateau and roll-off are the signature of vortex wandering. If the wandering and turbulence were independent, the fluctuations of the two effects would result in spectra which have the general appearance as illustrated in Figure 6.22. The actual slope of the roll-off is slightly different for each of the cases, however, this is attributed to differences in the relative contribution of wandering to the velocity signal.

In order to investigate the possible connection between the broad-band peak observed for the large-grid case and the dominant wavelengths of vortex wandering the cross-spectrum (Bendat and Piersol (2000)) of U_y and U_z was examined

$$G_{yz}(f) = 2 \int_{-\infty}^{\infty} R_{yz}\left(\tau\right) \exp\left(-i2\pi f \tau\right) \mathrm{d}\tau \tag{6.3}$$

where

$$R_{yz}\left(\tau\right) = \frac{1}{T} \int_{0}^{T} u_y\left(t\right) u_z\left(t+\tau\right) \mathrm{d}t \tag{6.4}$$

is the corresponding cross-correlation function. Cross-spectra were calculated using MATLAB's *cpsd* function for the same conditions as those for the power spectra in Figure 6.21 and their magnitudes are shown in Figure 6.23 in semi-log scales. Because wandering affects both components of velocity simultaneously, the cross-spectra are expected to show more prominently the frequency range of wandering than power spectra would. Figure 6.23

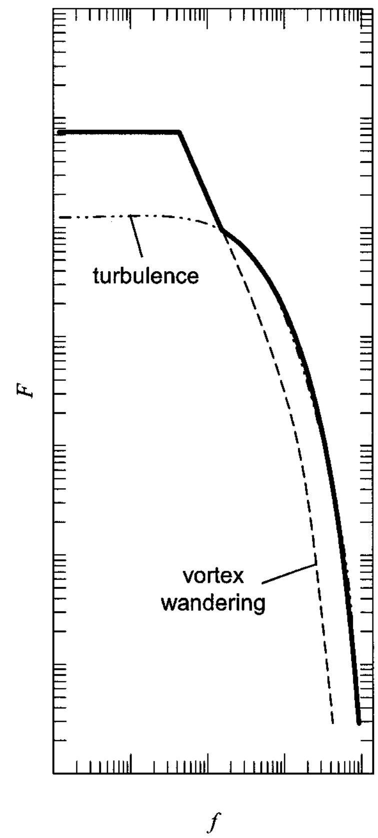

Figure 6.22: Sketch illustrating separate contributions to spectra from turbulence and vortex wandering.

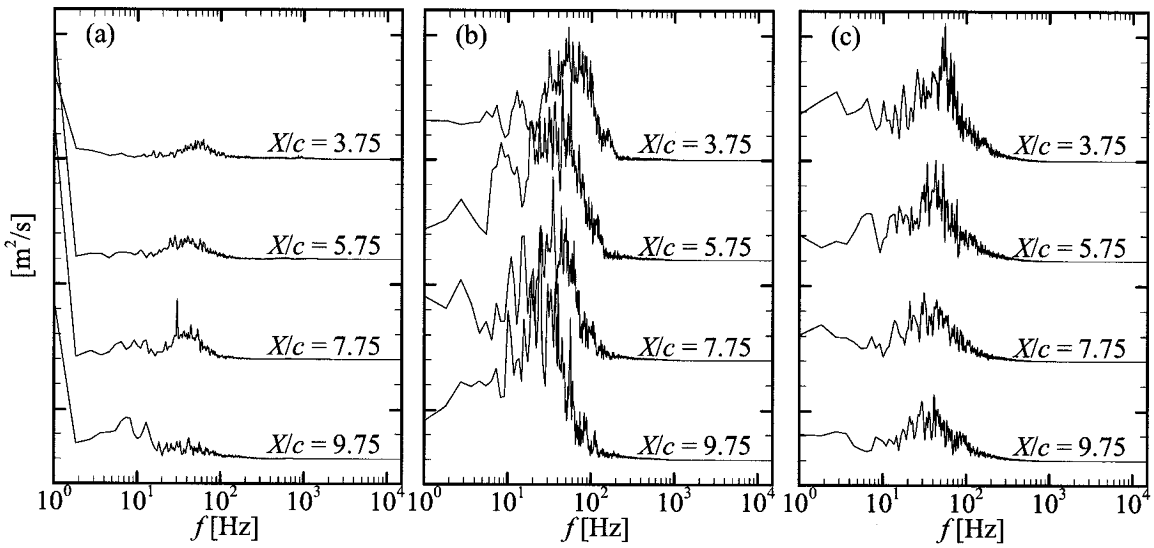

Figure 6.23: Cross-power spectra of U_y and U_z measured at $(y, z) = (0c, 0c)$ and $X/c = 3.75$, 5.75, 7.75 and 9.75 for (a) no-grid, (b) small-grid and (c) large-grid cases. Axes are semi-log, with each successive streamwise case downstream of $X/c = 3.75$ shifted downwards by 0.00004 for clarity.

indicates that a broad-band peak in frequency exists for all cases between about 30 and 50 Hz. The peak frequency f_p in this range was identified using a 40$^{\text{th}}$ order polynomial fit (where the polynomial was defined as $A\,(\log(f)) + B(\log(f))^2 + \ldots$ etc.) and is plotted in Figure 6.24. Even taking into consideration that the uncertainty of this procedure would be significant, one may conclude from this figure that the peak frequency decreases with streamwise distance and that differences in peak frequencies for the three cases are not very large.

Although the peak evident in the cross-spectra of U_y and U_z is clearly the result of vortex wandering, its frequency is not necessarily equal to the dominant frequency of wandering. This can be illustrated by the following example. Assume, for simplicity, that the wandering consists of a sinusoidal wave-like motion at a specific frequency f_w and an

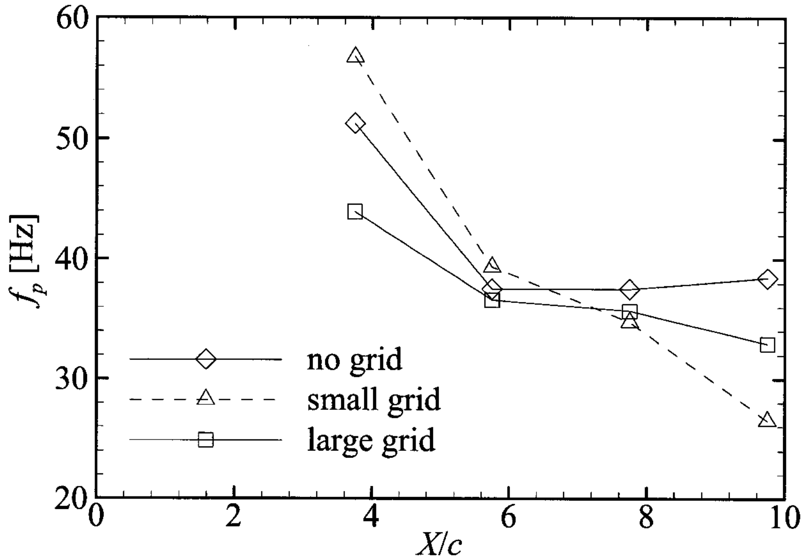

Figure 6.24: Peak frequency in the 30 to 60 Hz range identified from cross-spectra of U_y and U_z at $(y, z) = (0c, 0c)$.

amplitude that is greater than the radius $r_{\theta\,\max}$ of maximum circumferential velocity. Then, as the vortex would oscillate across the position of the probe, the dominant frequency of velocity fluctuations measured by the probe would be effectively $2f_w$, because of the change in sign of $\partial U_\theta/\partial r$ at $r_{\theta\,\max}$. If the wandering amplitude were sufficient for the probe to move across the entire core, the frequency of fluctuations measured by the probe would be effectively $4f_w$ because $\partial U_\theta/\partial r$ would change sign twice across the vortex core. Hence, when the amplitude of wandering is relatively large, the influence of the wandering on the measurements could be expected to bias the measured frequency peaks towards higher frequencies.

The previous point was investigated further using a simple model of vortex wandering. The objective of this simple analysis was to determine if the peak observed in the frequency spectra of velocity could be due to biasing to higher frequencies caused by the process described above. By modelling the change in vortex position (y_v, z_v) due to wandering as a Langevin process (Pope (2000)), one may estimate future positions as

$$y_v\left(t+\Delta t\right) = y_v\left(t\right) - y_v\left(t\right)\frac{\Delta t}{T_L} + \left(\frac{2\sigma_y^2 \Delta t}{T_L}\right)^{1/2} \xi\left(t\right) \tag{6.5}$$

and

$$z_v\left(t+\Delta t\right) = z_v\left(t\right) - z_v\left(t\right)\frac{\Delta t}{T_L} + \left(\frac{2\sigma_z^2 \Delta t}{T_L}\right)^{1/2} \xi\left(t\right) \ , \tag{6.6}$$

where $\xi\left(t\right)$ is a Gaussian random variable with unity standard deviation and T_L is the Lagrangian integral time-scale of the vortex wandering; wandering motions in the y and z directions are assumed to be uncorrelated and to have rms amplitudes σ_y and σ_z, respectively. In Equations 6.5 and 6.6, the second and third terms represent, respectively, the relaxation of the motion towards the original position due to the time-dependence and the random diffusion of the particle away from the original position. The frequency spectrum of y_v (the spectrum of z_v was identical to it), is shown in Figure 6.25. To determine the corresponding velocity spectrum, the velocity induced at $(y, z) = (0, 0)$ by a Lamb-Oseen vortex at $(y, z) = (y_v\left(t\right), z_v\left(t\right))$ was estimated. The Lamb-Oseen vortex parameters were set as $U_{\theta\,\mathrm{max}} = 0.2U_o$ and $r_{\theta\,\mathrm{max}} = 0.007\,\mathrm{m}$, which are approximately equal to the corresponding large-grid case values. The wandering was assumed to have $\sigma_y = \sigma_z = 0.01\,\mathrm{m}$ and $T_L = 0.014\,\mathrm{s}$ and, following Section 6.2.1, the vortex convection velocity was assumed to be negligible. Using these conditions, the frequency spectrum of vortex position shown in Figure 6.25a was found to result in the frequency spectrum of velocity at $(y, z) = (0, 0)$ shown in Figure 6.25b. Examination of Figure 6.25b indicates that the velocity spectrum is qualitatively similar to the position spectrum and bears no evidence of a peak forming at higher frequencies. This process was repeated for a variety of different values of $r_{\theta\,\mathrm{max}}/\sigma_y$

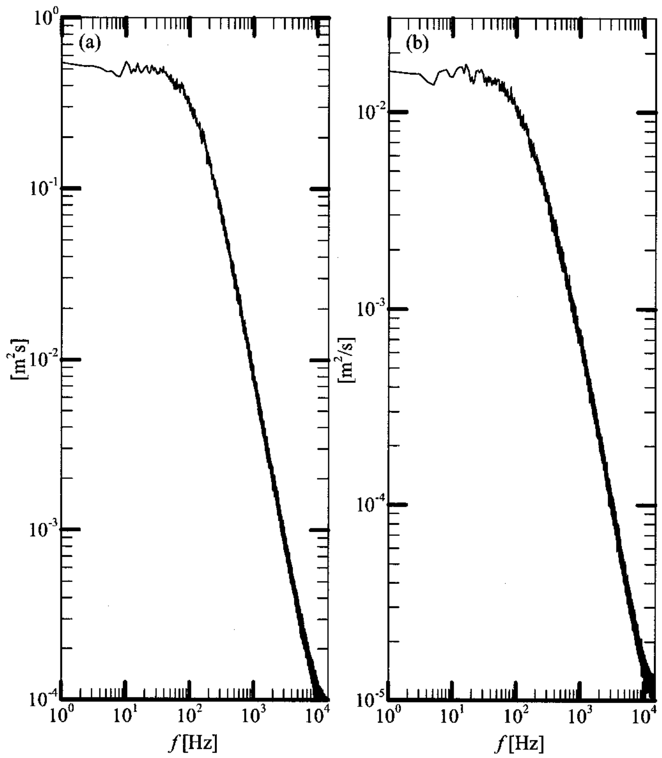

Figure 6.25: Frequency spectrum of (a) y position of model vortex position and (b) y component of velocity induced at $(y, z) = (0, 0)$ due to a Lamb-Oseen vortex with position described by (a).

and $U_{\theta\,\max}$ for the same y_v and z_v series and, although there were differences in the magnitudes and roll-offs of the resulting velocity spectra, no peaks at higher frequencies were observed. Hence, the peaks observed in Figure 6.23 appear to be caused by some quasi-periodic activity associated with wandering and are not an artifact of the transformation of power spectra from a spatial frame to a velocity frame. The most likely reason for this is that, as the vortex wanders in the y and z directions, the probe does not cross $r_{\theta\,\max}$ frequently enough to have statistical significance, hence biasing to higher frequencies was unnoticable.

Also evident for the no-grid case (Figure 6.23a) is a peak at a frequency near

7 Hz. This peak increases in energy with streamwise distance, such that, at $X/c = 9.75$, it contains more energy than the peak between 30 and 50 Hz. Also evident is significant energy for $f \lesssim 2$ Hz. These observations seem to indicate that for the no-grid case there are multiple sources of the wandering, each of which may have a different range of dominant frequencies. Although these sources may also be present in the grid-turbulence cases, their effects are not visible in the spectra, which are dominated by the main source of wandering, namely the grid turbulence.

The peak frequency f_p observed in the cross-spectra can be combined with an appropriate convection velocity to provide an estimate of the characteristic wavelength of vortex wandering. Choosing U_o as the convection velocity, one may estimate this wavelength as U_o/f_p. The streamwise development of this parameter for all cases are shown in Figure 6.26. Due to the relatively low sampling rate and short time-series length (compared to the two-probe data set used to calculate the spectra in Figure 6.21), there is significant uncertainty in f_p, which introduces appreciable data scatter. The wavelength U_o/f_p appears to grow with streamwise distance for all the grid cases, whereas the no-grid case wavelength remains relatively constant for $X/c \geq 3.75$. Although the two small-grid cases have smaller starting values of U_o/f_p, at $X/c = 9.75$ all grid cases have comparable U_o/f_p. It is also interesting to note that U_o/f_p is an order of magnitude larger than the longitudinal integral length scale of the free-stream grid turbulence measured without the wing (Figure 5.8). Moreover, U_o/f_p grows at a faster rate than the wandering amplitude (Figure 6.18) and is one to two orders of magnitude greater than it. A comparison of these three length scales is provided in Figure 6.27.

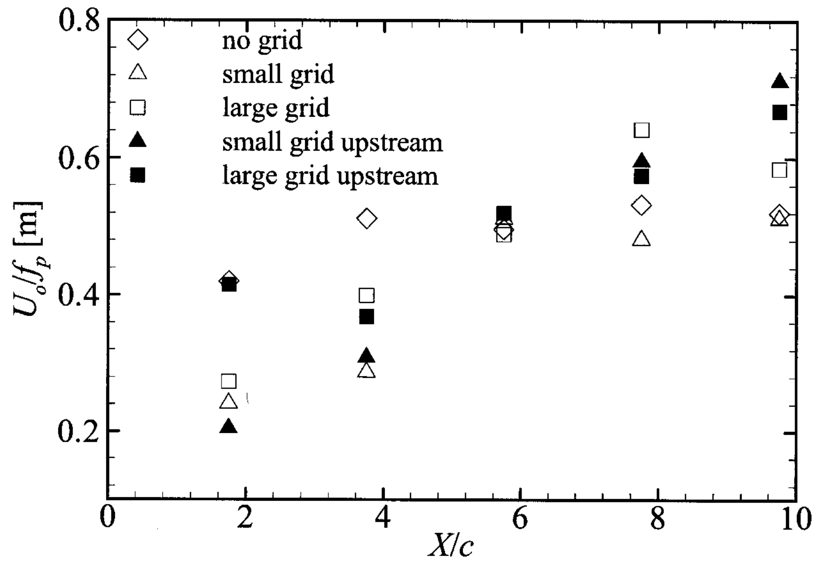

Figure 6.26: Streamwise development of U_o/f_p.

Although the wavelength of wandering appears to be much larger than the grid turbulence length scales, the timescale $1/f_p$ is compared to the "eddy turnover time" (or "eddy lifetime") $\tau_E = L_x/u'_x$ in Figure 6.28. This figure indicates, with considerable scatter, that the timescale of wandering decreases at the same rate as the eddy turnover time, with $1/f_p$ being approximately $0.4\tau_E$.

6.3 Reconstruction of the circumferential velocity profile in the wandering frame

6.3.1 Overview

The vortex wandering analysis has demonstrated that, as the free-stream turbulence increases, so too does the amplitude of vortex wandering. When wandering becomes

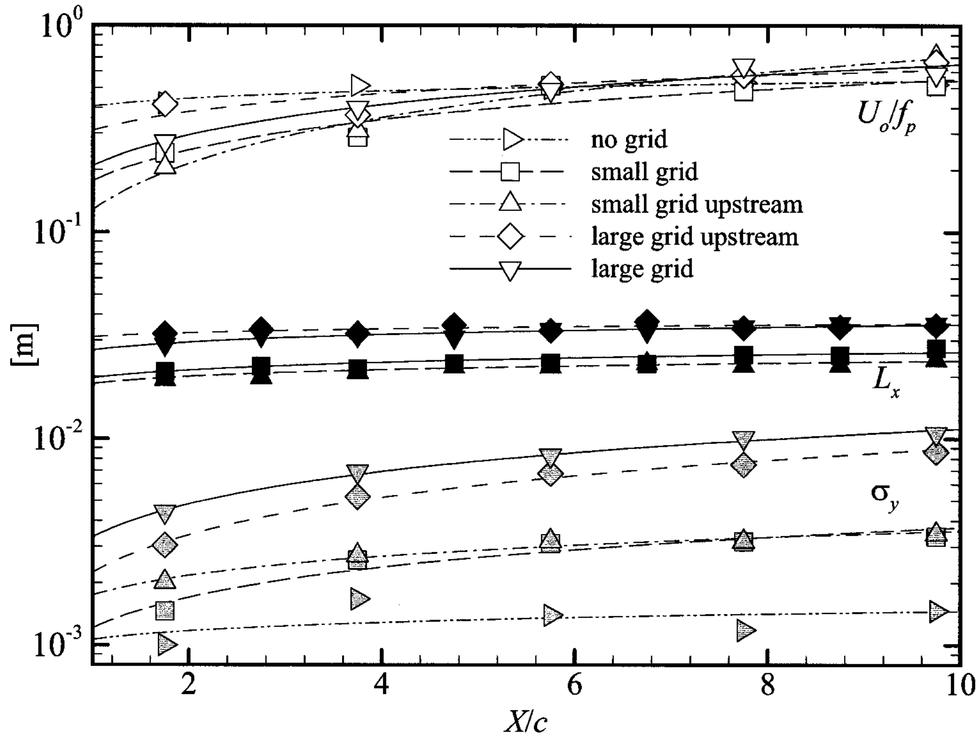

Figure 6.27: Comparison of different length scales. The wandering amplitude σ_y is shown by grey symbols. The integral length scale L_x measured with the wing removed is shown by black symbols and U_o/f_p is shown by white symbols.

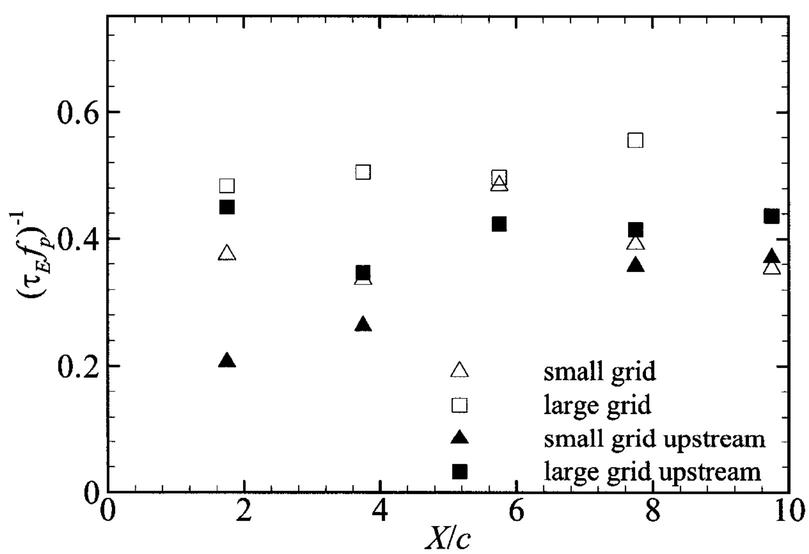

Figure 6.28: Comparison of wandering timescale $1/f_p$ to the eddy turnover time $\tau_E = L_x/u'_x$ calculated for the grid turbulence with the wing out of the tunnel.

intense, time-averaged profiles of the velocity and other properties measured by a fixed probe would deviate significantly from corresponding properties of the vortex that would be measured by a probe following the vortex axis in its motion. The objective of this section is to reconstruct radial profiles of vortex properties in a frame of reference that is attached to the wandering vortex axis.

To determine the average velocity at different radial positions in a frame of reference wandering with the vortex, two four-sensor hot-wire probes were used. The probes were separated in the y direction by a spacing S, which could be varied between 7.1 mm and 27.6 mm. In the following discussion, subscripts 1 and 2 will denote the probe used. Measurements were performed at $\mathrm{Re}_c = 2.4 \times 10^5$ and $\alpha = 5°$ at $X/c = 3.75$, 5.75, 7.75 and 9.75, for the no-grid, small-grid and large-grid cases. First the two probes were separated by $S = 7.1$ mm and measurements were taken in a yz plane, around the time-averaged vortex axis estimated from previous single-point measurements. These data were then analyzed to determine a more exact location of the time-averaged vortex axis as well as the orientation of each probe with respect to this axis. Probe 1 was then fixed on the time-averaged vortex axis and probe 2 was traversed such that its distance from probe 1 spanned the range from $S = 7.1$ mm to 27.6 mm at 0.5 mm increments.

To determine the velocity at a given radial position from the instantaneous vortex axis, the measurements of each probe were sorted upon a condition applied to the measurements of the other probe. The challenge in this procedure was to identify the locations of the two probes relative to the vortex axis. As an initial step, only parts of the time series were considered by requiring that the vortex axis would intersect the line joining the two probe measurement volumes. These instances can be identified by $U_{y1} \approx 0$, as illustrated in Figure 6.29 (where U_{yv} and U_{zv} are the components of velocity induced by the vortex in the y and z directions, respectively, as introduced in Figure 6.13). Note that a stricter condition would be $U_{y1} \approx U_{y2} \approx 0$. In a laminar vortex, this additional restriction would be unnecessary because the probes are separated along the y axis. However, in a turbulent vortex, non-zero radial velocity could be measured by one probe when the other one reads a zero radial component. To explore whether applying the stricter condition would affect the results, the reconstruction was repeated with the stricter condition as well, but the only difference between this and the simpler condition was that the latter produced a slightly smoother profile due to the inclusion of more data points. The threshold below which a transverse velocity was considered to be negligible was set at $0.03U_o$, which corresponds to an uncertainty of 0.3 mm in locating the vortex axis in the no-grid case. Thus, the data set considered only included cases with $-0.03U_o < U_{y1} < 0.03U_o$. Then, the instantaneous circumferential velocity in the vortex could be determined from $U_{\theta 1} \approx |U_{z1}|$ and $U_{\theta 2} \approx |U_{z2}|$.

The next step in the analysis was to determine the radial location of each of the probes. To do this, the joint probability density functions (JPDF) of U_{z1} and U_{z2}, conditioned on $U_{y1} \approx 0$, were used to investigate the relationship between the circumferential velocities measured by the two probes. Figure 6.30 shows examples of these JPDF for the no-grid, small-grid and large-grid cases at $X/c = 9.75$ with $S = 7.1$ mm. JPDF isocontours follow a distinct pattern, which can be attributed to the velocity induced by the vortex at different positions with respect to the probe locations. Different regions of this JPDF pattern identify distinct regimes of the instantaneous locations of the probes with respect

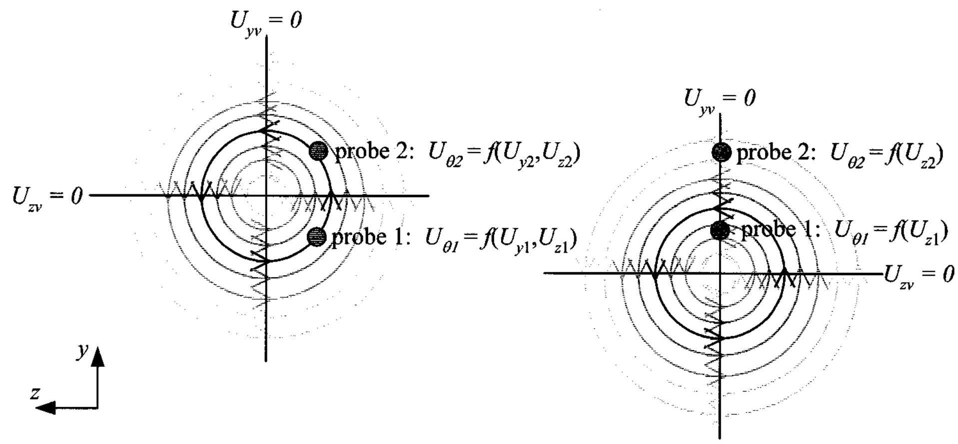

Figure 6.29: Sketch illustrating the relationship between velocity components induced by the vortex (U_{yv}, U_{zv}) and the velocity components measured by the two probes. When U_{y1} or $U_{y2} = 0$, $U_{z1} = U_{\theta 1}$ and $U_{z2} = U_{\theta 2}$.

to the vortex axis, as illustrated in Figure 6.31 with the regimes defined in Figure 6.32. The full pattern is not evident in the no-grid JPDF because the wandering amplitude was too small for probe 1 to travel outside the vortex core. As the wandering amplitude increased, however, the probes measured velocities at increasingly larger distances from the instantaneous vortex axis and hence the pattern becomes evident for the small-grid case and even more pronounced for the large-grid case, for which the wandering amplitude was sufficiently large for the entire vortex to wandered past both probes.

As probe spacing increases, the pattern of the JPDF isocontours changes slightly from that shown in Figure 6.31, because, as the probe spacing increases, the probability of both probes being within the vortex core at the same time decreases. Instead, there is a new regime that is apparent when both probes are on either side of the core. In addition, the possible U_{z1} and U_{z2} combinations change. For example, when probe 1 is at the location of maximum U_{zv}, or probe 2 is at the location of minimum U_{zv}, the velocity measured by

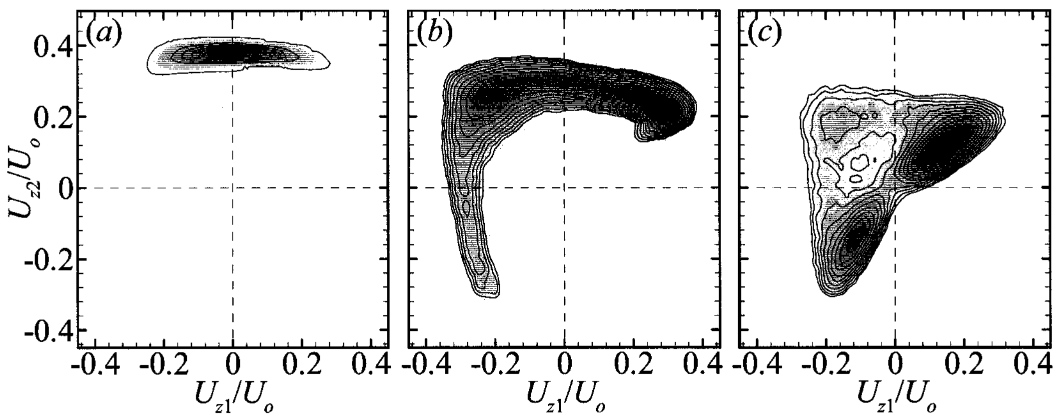

Figure 6.30: Joint probability density functions of U_{z1} and U_{z2} conditioned on $U_{y1} \approx 0$ for the (a) no-grid, (b) small-grid and (c) large-grid cases at $X/c = 9.75$ and with $S = 7.1\,\mathrm{mm}$. Darker shading indicates higher probability. Isocontours logorithmically spaced to highlight low-probability events.

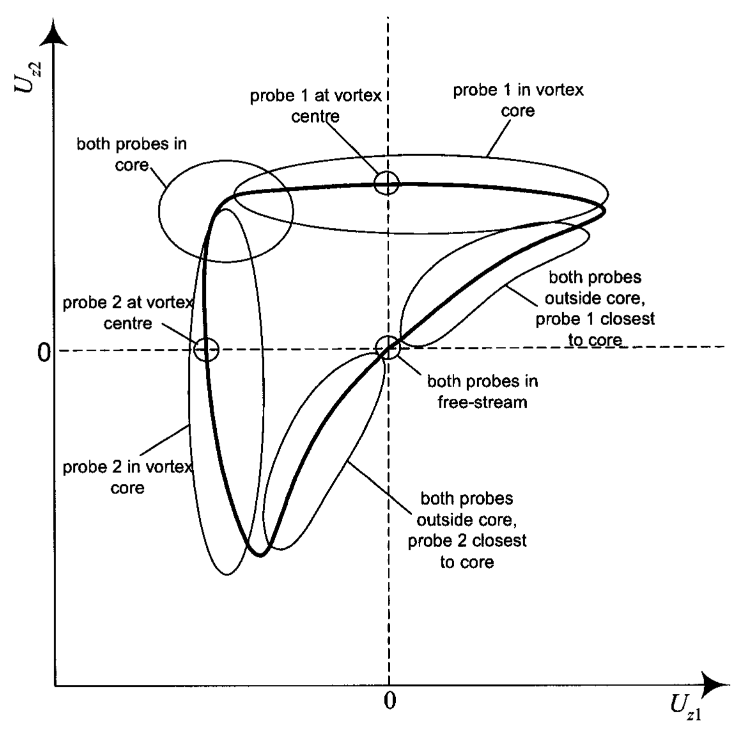

Figure 6.31: Sketch illustrating locations of different regimes on JPDF of U_{z1} and U_{z2} which have been conditioned such that $U_{y1} \approx 0$ for small values of S.

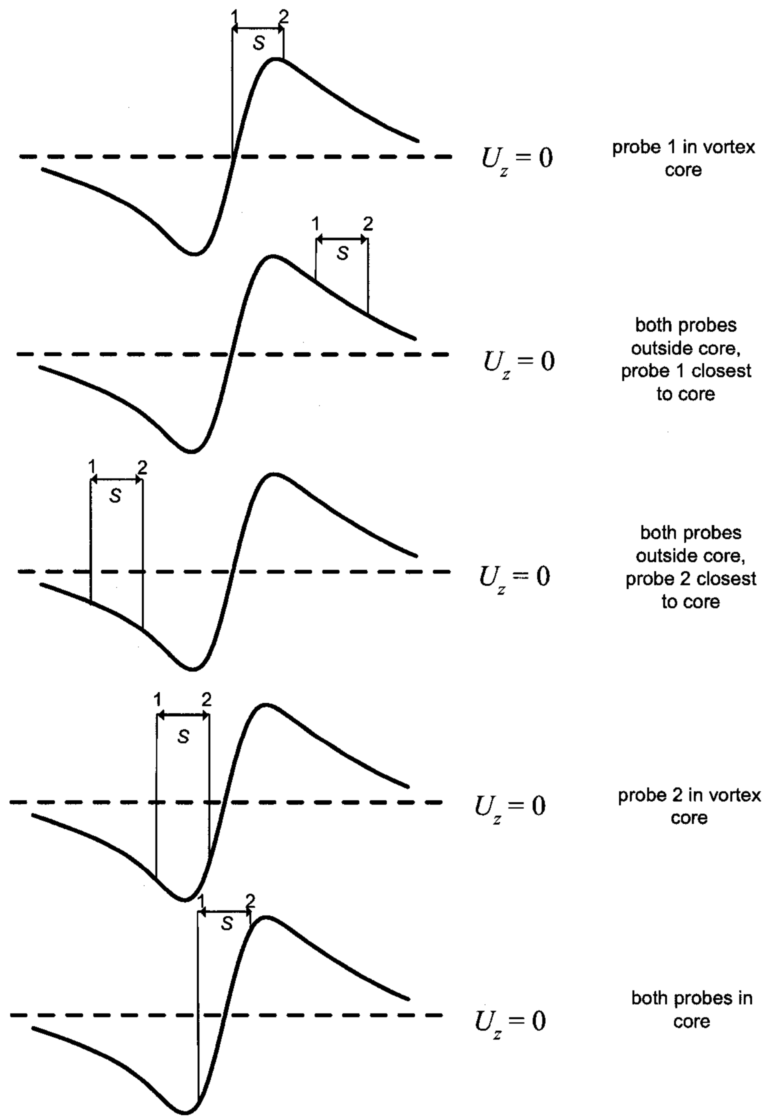

Figure 6.32: Sketch defining different regimes of probe position for small values of S.

the other probe will decrease with increasing S. Hence, the pattern of isocontours depends on the ratio of S to the vortex core radius. Examples of JPDF isocontours for the probe spacing of $S = 19.6\,\text{mm}$ are shown in Figure 6.33 for the no-grid, small-grid and large-grid cases at $X/c = 9.75$. As with Figure 6.30, a distinct pattern is evident, however, the pattern of the JPDF contours is slightly different from the one shown in Figure 6.31. Nevertheless, different regimes can still be identified as illustrated in Figure 6.34 with the regimes defined in Figure 6.35. Thus, by careful examination of these JPDF plots, the relationship between the probe position and the vortex circumferential velocity can be estimated.

6.3.2 Outer Profile Reconstruction

The outer portions of the radial profiles of the circumferential velocity were reconstructed as follows. First, instances at which $U_{y1} \approx U_{z1} \approx 0$ were identified. These instances occurred when the axis of the vortex passed through probe 1 and correspond to the line $U_{z1} = 0$ on the JPDF of U_{z1} and U_{z2} with the condition $U_{y1} \approx 0$ (indicated by a dashed line in Figures 6.30 and 6.33). In other words, the values of U_{z2} intersecting the line $U_{z1} = 0$ are the values of U_{z2} measured when probe 1 is on the instantaneous vortex axis. Thus, the cross-sectional profile of the JPDF along this line is assumed to approximately represent the probability density function (PDF) of the circumferential velocity at a radial distance from the instantaneous vortex axis that is equal to the probe spacing. The average value of U_{z2}, determined from the PDF, should therefore be $\widetilde{U}_\theta\,(r = S)$ where $\widetilde{\ }$ indicates the average value in the wandering frame. The cross-sectional profiles at $U_{z1} = 0$ of the JPDFs shown in Figure 6.30 are shown in Figure 6.36a-c. For the no-grid and small-grid cases, the profiles appear to be Gaussian. Note that due to the large wandering amplitude

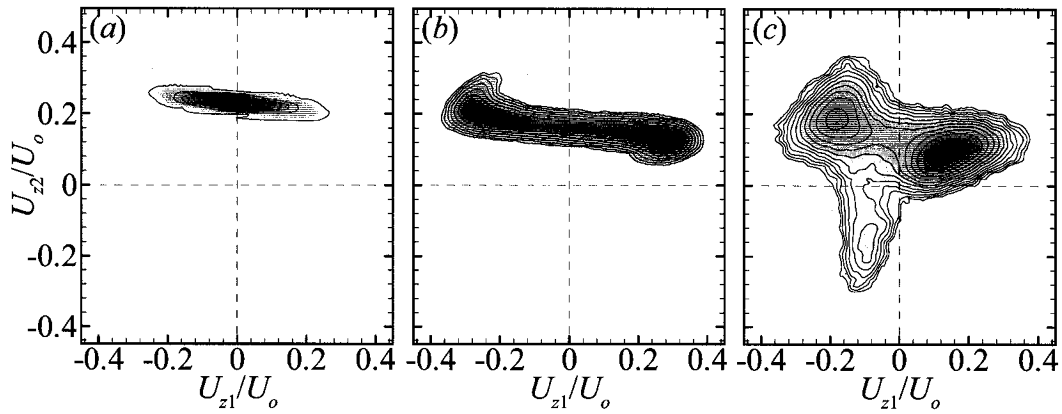

Figure 6.33: Joint probability density functions of U_{z1} and U_{z2} conditioned on $U_{y1} \approx 0$ for the (a) no-grid, (b) small-grid and (c) large-grid cases at $X/c = 9.75$ and $S = 19.6\,\text{mm}$. Darker greyscales indicate higher probability. Isocontours logorithmically spaced to highlight low-probability events.

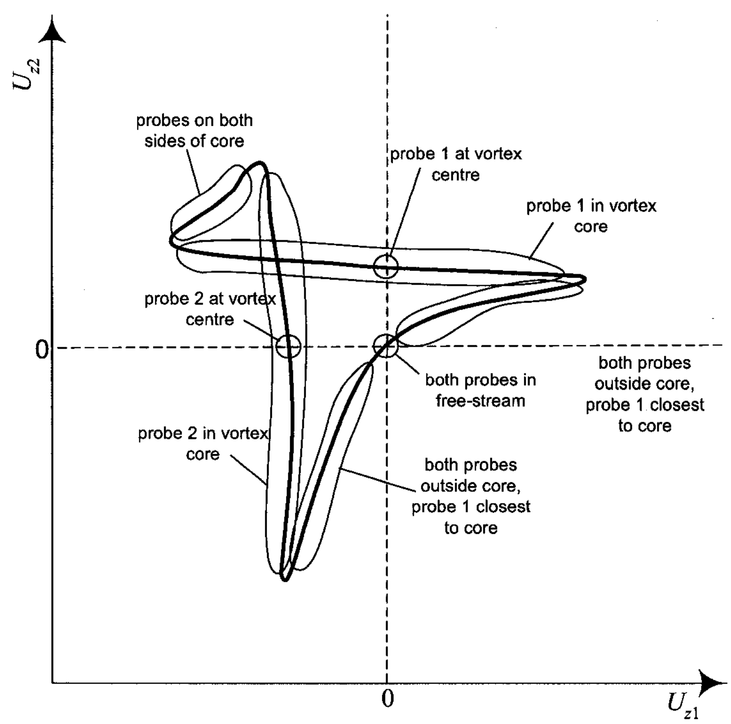

Figure 6.34: Sketch illustrating locations of different regimes on JPDFs of U_{z1} and U_{z2} which have been conditioned such that $U_{y1} \approx 0$ at large values of S.

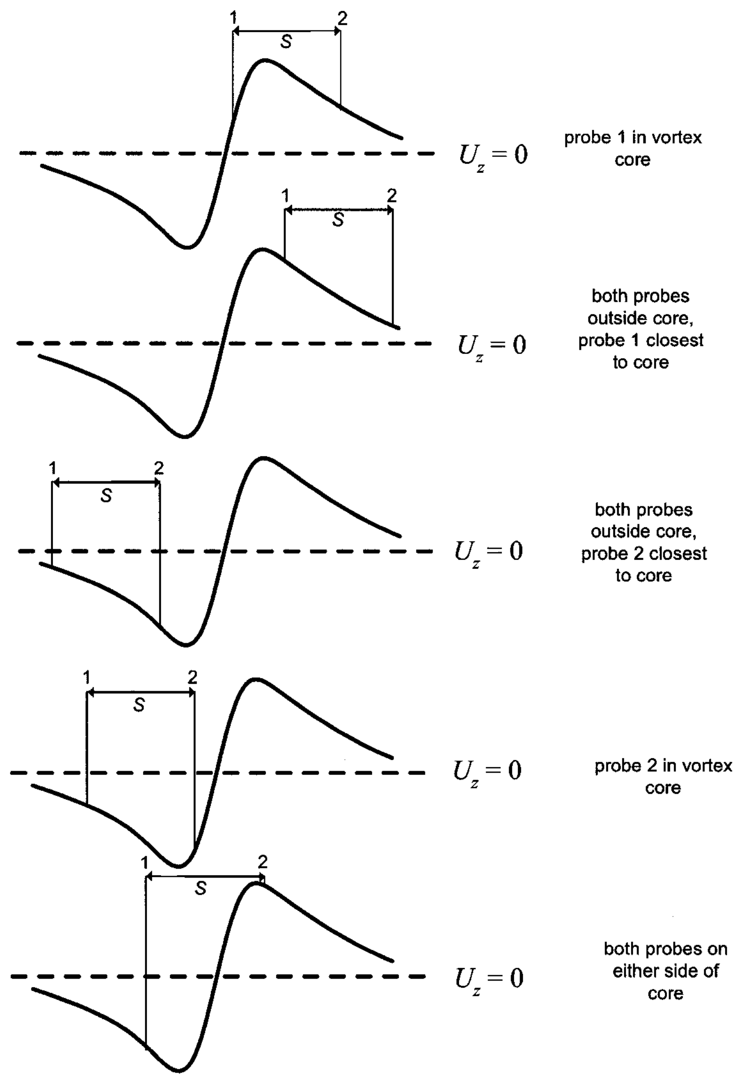

Figure 6.35: Sketch defining different regimes of probe positions for large values of S.

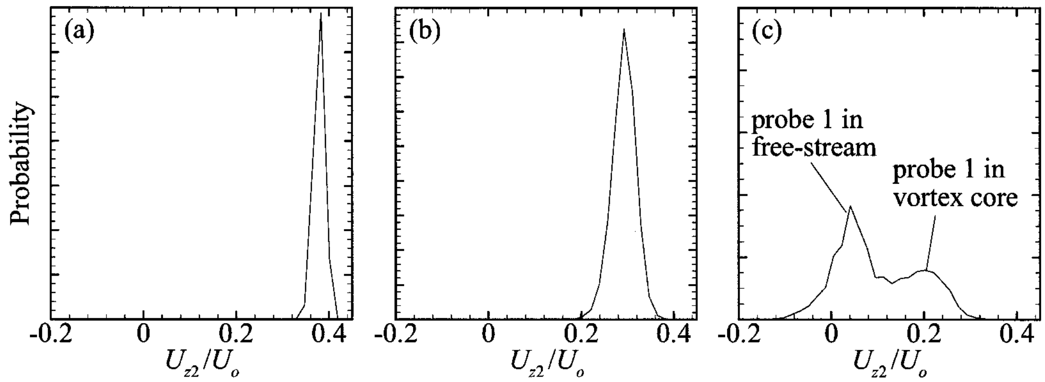

Figure 6.36: Cross-sections at $U_{z1} = 0$ of JPDFs measured at $X/c = 9.75$ and $S = 7.1\,\text{mm}$ for (a) no-grid, (b) small-grid and (c) large-grid cases.

for the large-grid case, averaging the PDF results in an inaccurate estimate of $\widetilde{U}_\theta$ due to a large number of measurement instances when probe 1 and probe 2 were in the free-stream (compare Figure 6.30c to Figure 6.31). Therefore, for the large-grid case, the appropriate peak value (identified as illustrated in Figure 6.36) was selected.

By determining $\widetilde{U}_\theta$ for different values of S, the average radial profile of the vortex circumferential velocity, relative to the vortex axis, was reconstructed for the range $7.1\,\text{mm} \leq r \leq 27.6\,\text{mm}$. As an example of the reconstruction, the portions of the radial profiles determined using this technique for the no-grid, small-grid and large-grid cases at $X/c = 9.75$ are indicated by solid symbols in Figure 6.37 for all three cases. Also indicated in Figure 6.37 are the corresponding time-averaged profiles $\overline{U}_{z2}(S)$, indicated by hollow symbols. The noticeably increased scatter in the large-grid case is due to a decrease in the population of instances at which probe 1 coincided with the vortex axis.

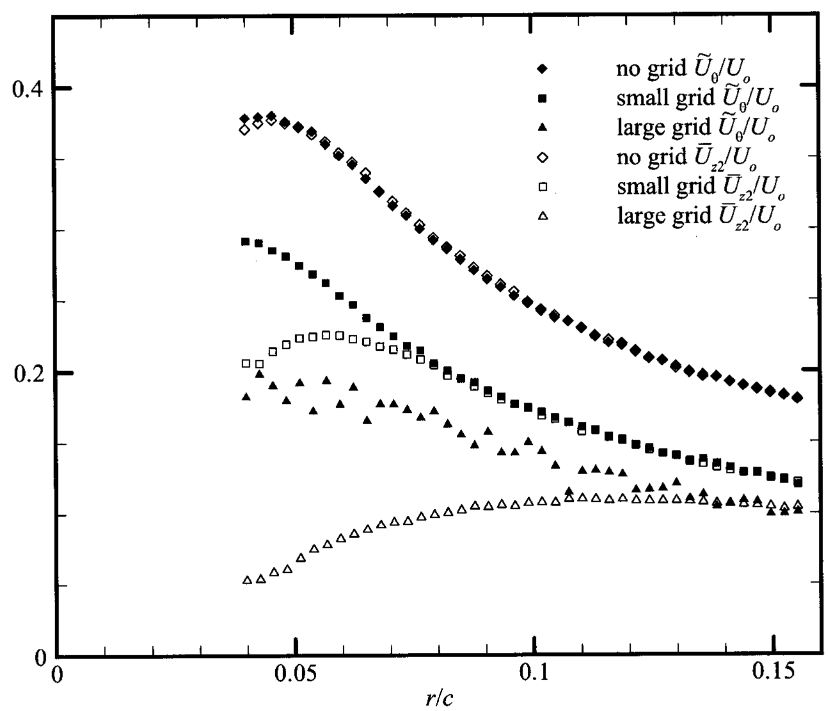

Figure 6.37: Comparison of $\widetilde{U}_\theta\,(S)$ to $\overline{U}_{z2}\,(S)$ in the range $7.1\,\text{mm} \leq S \leq 27.6\,\text{mm}$ for the no-grid, small-grid and large-grid cases at $X/c = 9.75$.

6.3.3 Inner profile reconstruction

The method described above could not reconstruct the circumferential velocity in the inner vortex core, because the probe separation could not be reduced below 7.1 mm. To reconstruct the inner portion of the velocity profile, the most probable combinations of U_{z1} and U_{z2} were combined with the reconstructed outer profile and the probe spacing to find $U_{z1}(r_1) = \widetilde{U}_\theta(r)$.

The procedure started by determining $U_{z2} = f(U_{z1})$ using the following procedure. First, the JPDF of U_{z1} and U_{z2} conditioned by $U_{y1} \approx 0$ was determined at $S = 14.1$ mm. At 40 discrete values of $U_{z1} \geq 0$, the probability density of U_{z2} was determined by taking slices of the JPDF at U_{z1}. For each discrete value of U_{z1} the value of U_{z2} corresponding with peak probability was determined using quadratic interpolation.

Then, for each of the 40 discrete values of U_{z1}, the corresponding radial position r_1 at which U_{z1} was measured was determined. To do this, the outer portion of the velocity profile (previously determined) was fitted with a fourth order polynomial to determine $r_2 = g(U_{z2})$. Thus, from $U_{z2} = f(U_{z1})$, the radial position of probe 2 corresponding to the measured value of U_{z1} could be determined from $r_2 = g(f(U_{z1}))$. Knowing the probe spacing, S, meant that the value of r_1 at which U_{z1} was measured could be found from $r_1 = g(f(U_{z1})) - S$. Hence $U_{z1}(r_1) = \widetilde{U}_\theta(r)$ could be found from the discrete values of U_{z1}.

Examples of the resulting reconstruction are shown in Figure 6.38 for the no-grid and small-grid cases at $X/c = 9.75$ with the inner profile reconstruction shown as open symbols and the outer profile reconstruction by closed symbols.

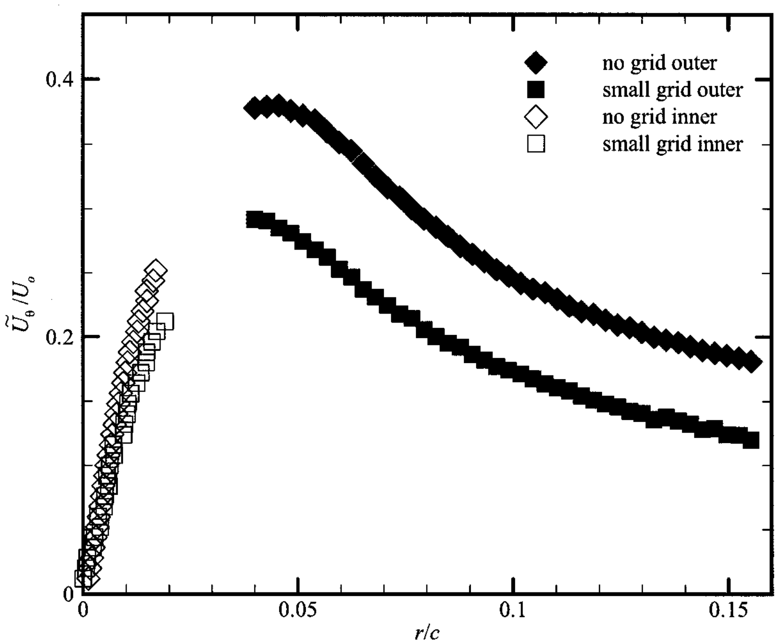

Figure 6.38: Comparison of the outer to inner portions of the reconstructed velocity profile for the no-grid and small-grid cases at $X/c = 9.75$.

Unfortunately, the applicability of this method was limited, since identifying $U_{z2} = f(U_{z1})$ became impossible as U_{z1} increased and the distinction between measurement instances when probe 1 was within the vortex core and the instances when it was outside the core became increasingly difficult. For the large-grid case this occurred at very small values of U_{z1} and hence this method could not be applied. This problem is illustrated in Figure 6.39, which examines slices of the JPDF shown in Figure 6.30c along axes representing $U_{z1} = 0.0U_o$ (Figure 6.39a), $0.035U_o$ (Figure 6.39b) and $0.07U_o$ (Figure 6.39c). In Figure 6.39a, two peaks are clearly evident, corresponding to probe 1 being in the free-stream and probe 1 being in the vortex core. As U_{z1} increases, the peak corresponding to the probe being within the vortex core becomes increasingly obscured by the free-stream values. At $U_{z1} = 0.07U_o$, the peak corresponding to probe 1 being within the core is no longer evident.

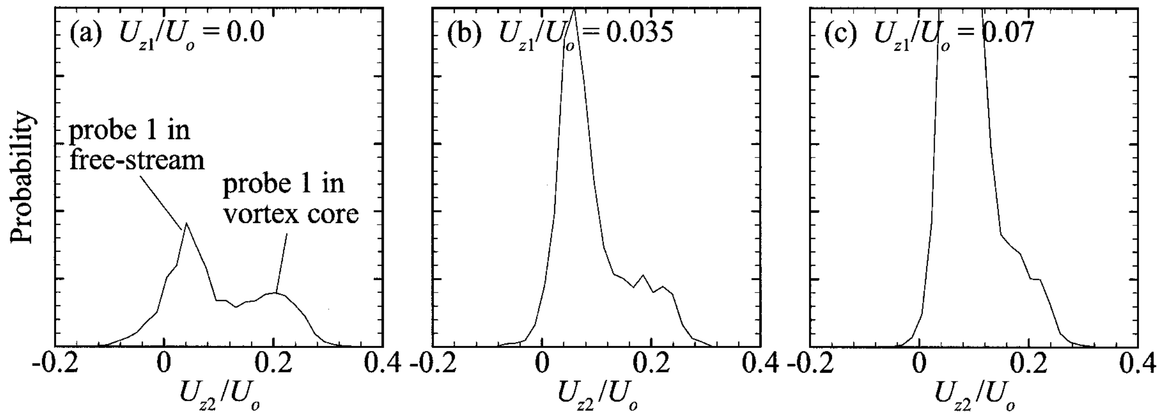

Figure 6.39: Slices of JPDF of U_{z1} and U_{z2} (conditioned on $U_{y1} \approx 0$) measured for the large-grid at $X/c = 9.75$ and $S = 7.1\,\mathrm{mm}$. Slices along (a) $U_{z1} = 0.0$, (b) $U_{z1} = 0.035U_o$ and (c) $U_{z1} = 0.07U_o$ are shown.

As U_{z1} approached the peak circumferential velocity, this problem also became evident for the no-grid and small-grid cases as well. Hence, the reconstruction of the inner profile was limited to $U_{z1} < 0.25U_o$ for the no-grid case and $U_{z1} < 0.22$ for the small-grid case. Within this range, the results were found to be insensitive to S. This insensitivity is illustrated in Figure 6.40.

6.3.4 Completing the profile

The value of peak circumferential velocity $U_{\theta\,\max}$ and the radial location $r_{\theta\,\max}$ at which it occurs are characteristic velocity and spatial scales of a vortex and their temporal evolutions are representative of changes in the vortex velocity profile. Unfortunately, these scales cannot be determined with certainty from the previous method, as it appears from Figure 6.37 that $r_{\theta\,\max}$ was either very close to or slightly less than the minimum probe spacing. Therefore, it is necessary to reconstruct the full velocity profile. For the no-grid and small-grid cases, for which the inner portions of the profiles was reconstructed, the

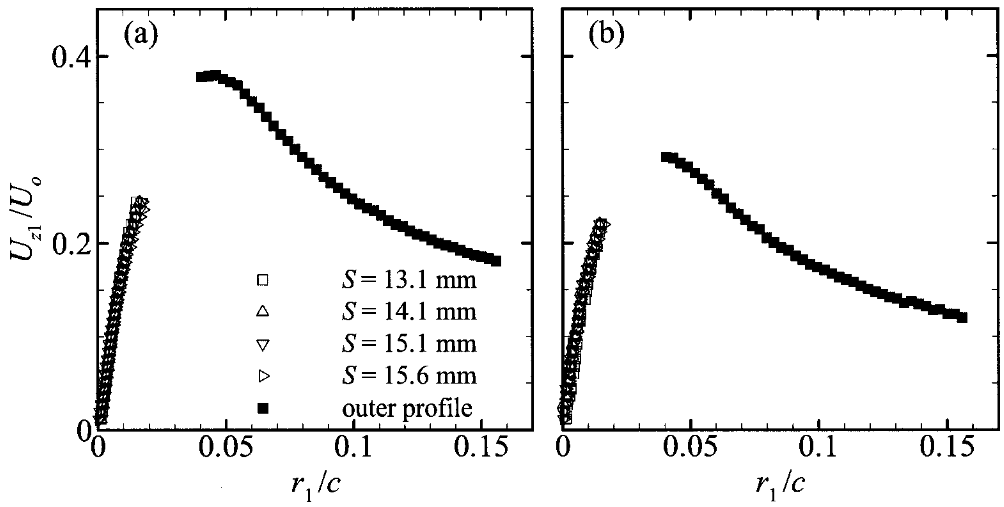

Figure 6.40: Comparison of inner profile reconstructed using different probe spacings for (a) no-grid case and (b) small-grid case at $X/c = 9.75$.

missing portions were estimated by interpolating the corresponding circulation profiles. By assuming the velocity profiles to be axi-symmetric, the circulation profiles in a wandering frame were estimated from

$$\widetilde{\Gamma}(r) = 2\pi r \widetilde{U}_\theta(r). \tag{6.7}$$

Examples of the resulting circulation profiles are shown in Figure 6.41a for the no-grid and small-grid cases at $X/c = 9.75$. It is obvious by looking at the reconstructed parts of these profiles that the missing portions are monotonically increasing with radius at a nearly constant rate. Interpolation was performed using a fourth order polynomial fit, determined using the four nearest points of the outer and the four nearest points of the inner portions of the reconstructed profile. The resulting fit is shown as a solid line in Figure 6.41a. Then, the corresponding missing portions of the radial profiles of circumferential velocity were determined by inverting Equation 6.7, as shown in Figure 6.41b .

To reconstruct the inner portion of the velocity profile for the large-grid case, the

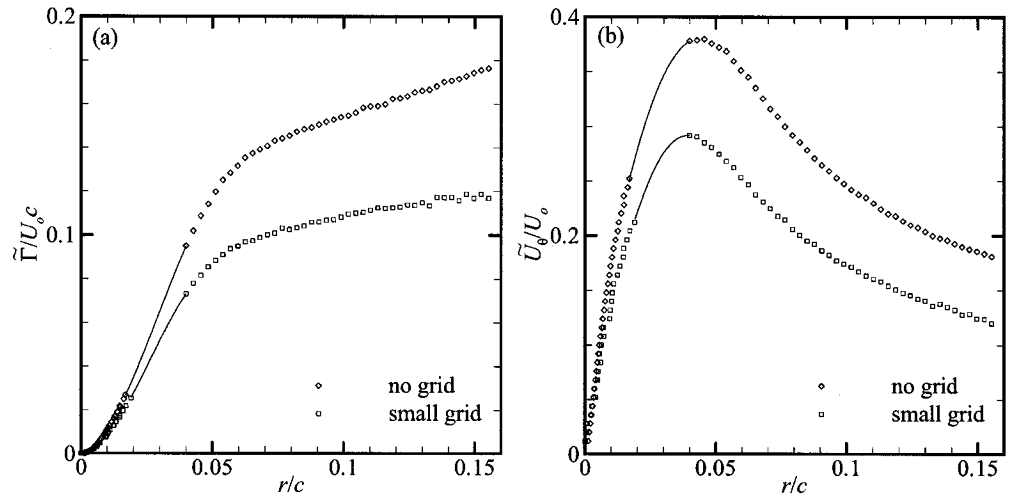

Figure 6.41: Example of curve fit used to connect the inner and outer portions of the reconstructed profiles of (a) $\widetilde{\Gamma}$ and the corresponding profiles of (b) $\widetilde{U}_\theta$ for the no-grid and small-grid cases at $x/c = 9.75$.

following empirical expression describing the velocity profile (Phillips (1981))

$$\frac{U_\theta}{U_{\theta\,\max}} = \left[1.772\left(\frac{r}{r_{\theta\,\max}}\right)^2 - 1.0467\left(\frac{r}{r_{\theta\,\max}}\right)^4 + 0.2747\left(\frac{r}{r_{\theta\,\max}}\right)^6\right]\frac{r_{\theta\,\max}}{r} \quad r/r_{\theta\,\max} \leq 0.92 \tag{6.8a}$$

$$\frac{U_\theta}{U_{\theta\,\max}} = \left[\ln\left(\frac{r}{r_{\theta\,\max}}\right) + 1\right]\frac{r_{\theta\,\max}}{r} \quad 0.92 \leq r/r_{\theta\,\max} \leq 1.2 \tag{6.8b}$$

was used instead of interpolation. Phillips (1981) demonstrates that the inner portion ($r < 1.2r_{\theta\,\max}$) of a fully formed vortex is self-similar and described by a combination of the log-log law of Hoffman and Joubert (1963) (Equation 6.8b) and a polynomial fit that has been structured using appropriately selected boundary conditions (Equation 6.8a). Therefore, by appropriately scaling Phillips' curve to match the reconstructed outer portion of the previously determined profiles, an estimate of $\widetilde{r}_{\theta\,\max}$ and $\widetilde{U}_{\theta\,\max}$ can be obtained.

It was found that it was easier to match Phillips' expression to the experimental results by using $\widetilde{\Gamma}(r)$ to estimate $\widetilde{U}_{\theta\,\max}$ and $\widetilde{U}_\theta(r)$ to estimate $\widetilde{r}_{\theta\,\max}$. This process of matching the profiles is illustrated in Figure 6.42a-d for the large grid case at $X/c =$ 9.75. Figure 6.42a compares the experimentally determined large-grid $\widetilde{\Gamma}(r)$ profile to three Phillips circulation profiles calculated using an assumed value of $\widetilde{r}_{\theta\,\max}$ and three different values of $\widetilde{U}_{\theta\,\max}$. It was discovered that small changes in $\widetilde{U}_{\theta\,\max}$ cause large changes in the comparison between the Phillips profiles and the experimental profiles. Comparatively, as illustrated in Figure 6.42c, the comparison between the Phillips profile and the experimental profile was found to be relatively insensitive to the selected value of $\widetilde{r}_{\theta\,\max}$. As Figure 6.42c shows, the $\widetilde{\Gamma}(r)$ from Phillips' profile is relatively insensitive to the precise value of $\widetilde{r}_{\theta\,\max}$. Therefore, it was found that it was possible to find a value of $\widetilde{U}_{\theta\,\max}$ which provided a good match between Phillips profile and the experimental profile with the matching of the curves insensitive of the selection of $r_{\theta\,\max}$. Hence, it is estimated that $U_{\theta\,\max}$ could be found by direct experimentation to within an accuracy of $\pm 0.002U_o$. Once $\widetilde{U}_{\theta\,\max}$ was determined using the radial profiles of circulation, the value of $\widetilde{r}_{\theta\,\max}$ was estimated by determining the best match of the circumferential velocity profile. Estimated accuracy of the process to determine $\widetilde{r}_{\theta\,\max}$ was ± 0.3 mm.

The reconstructed velocity profiles in the yz plane for the no-grid, small-grid and large-grid cases at $X/c = 3.75$, 5.75, 7.75 and 9.75 are shown in Figure 6.43. The reconstructed profiles of the no-grid case were found to be quite similar to the time-averaged profiles with little change with streamwise distance. At $X/c = 3.75$, the profile exhibits a distinctly different appearance, with an inflection point appearing near $r_{\theta\,\max}$. Although it is possible that this inflection indicates some uncertainty in the reconstruction, careful examination of Figure 6.11a reveals a similar inflection in the profile corrected using the

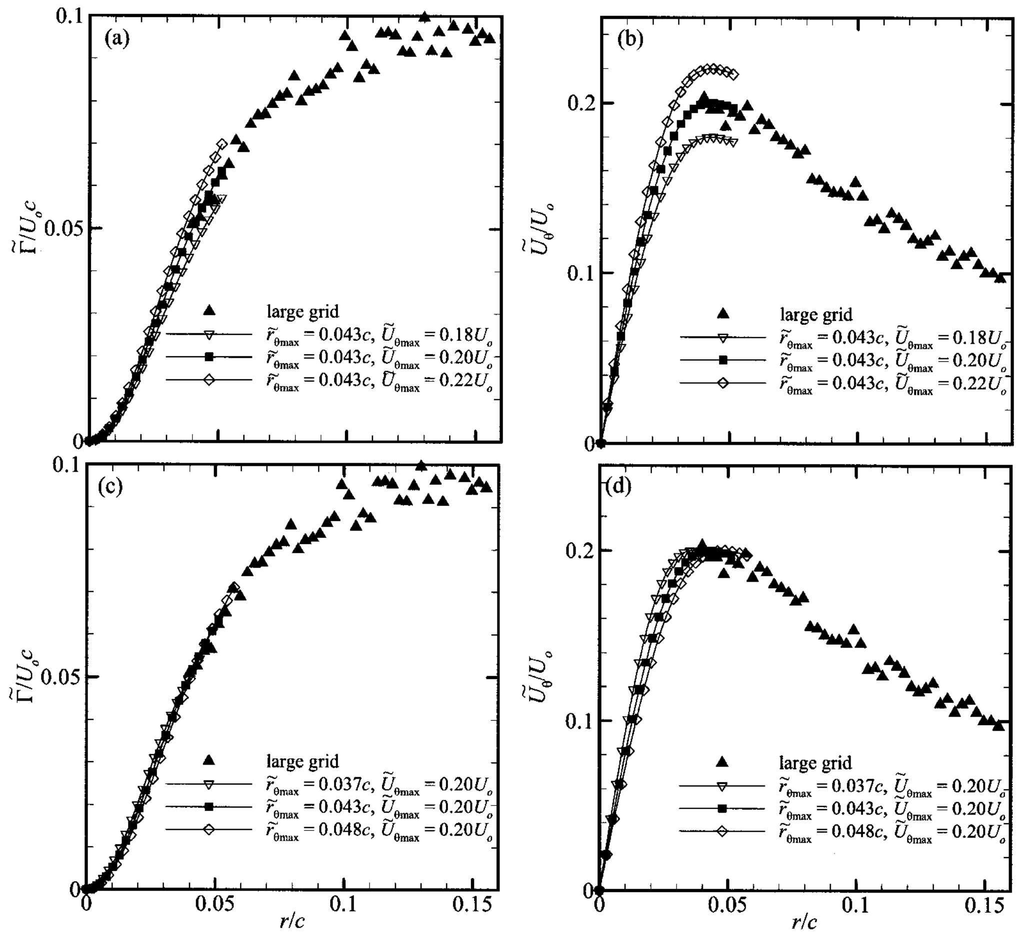

Figure 6.42: Radial profiles of (a),(c) $\widetilde{\Gamma}/U_o c$ and (b),(d) $\widetilde{U}_\theta/U_o$ comparing the results of the outer profile reconstruction to the Phillips profile with (a),(b) constant $\widetilde{r}_{\theta\,\mathrm{max}}$ and varying $\widetilde{U}_{\theta\,\mathrm{max}}$ and (c),(d) varying $\widetilde{r}_{\theta\,\mathrm{max}}$ and constant $\widetilde{U}_{\theta\,\mathrm{max}}$.

correction of Devenport et al. (1996). In addition, a similar inflection was also observed at $X/c = 4.75$ by Devenport et al. (1996), who attribute it to remnants of vorticity from the formation of the vortex from multiple vortices at the tip of the wing (similar vortices were also observed in the current study). The reconstructed small-grid case compares well with the profiles corrected using Devenport's method (Figure 6.11b), which also showed little change in $r_{\theta\,\max} = 0.04c$ while $U_{\theta\,\max}$ decreased from $0.35U_o$ at $X/c = 1.75$ to $0.31U_o$ at $X/c = 9.75$. The streamwise evolution of the large-grid case in Figure 6.43 also shows a decrease in $U_{\theta\,\max}$ with streamwise distance while little corresponding change in $r_{\theta\,\max}$ can be detected.

The streamwise developments of $\widetilde{r}_{\theta\,\max}$ and $\widetilde{U}_{\theta\,\max}$ are shown in Figures 6.44a and b respectively. It is interesting to note that there appears to be no significant systematic dependence of $\widetilde{r}_{\theta\,\max}$ on either streamwise distance or free stream turbulence level, although there are appreciable uncertainty and scatter. In contrast, there is a noticeable decrease of $\widetilde{U}_{\theta\,\max}$ both with increasing streamwise distance and increasing free-stream turbulence. The streamwise evolution of $\widetilde{U}_{\theta\,\max}$ may be represented by the fitted power law

$$\widetilde{U}_{\theta\,\max}/U_o = A\,(X/c)^{-n} \tag{6.9}$$

with the coefficients for each case given in Table 6.1.

Case	A	n
no grid	0.4	0.04
small grid	0.4	0.1
large grid	0.4	0.3

Table 6.1: Fitted power law coefficients for reconstructed velocity profiles.

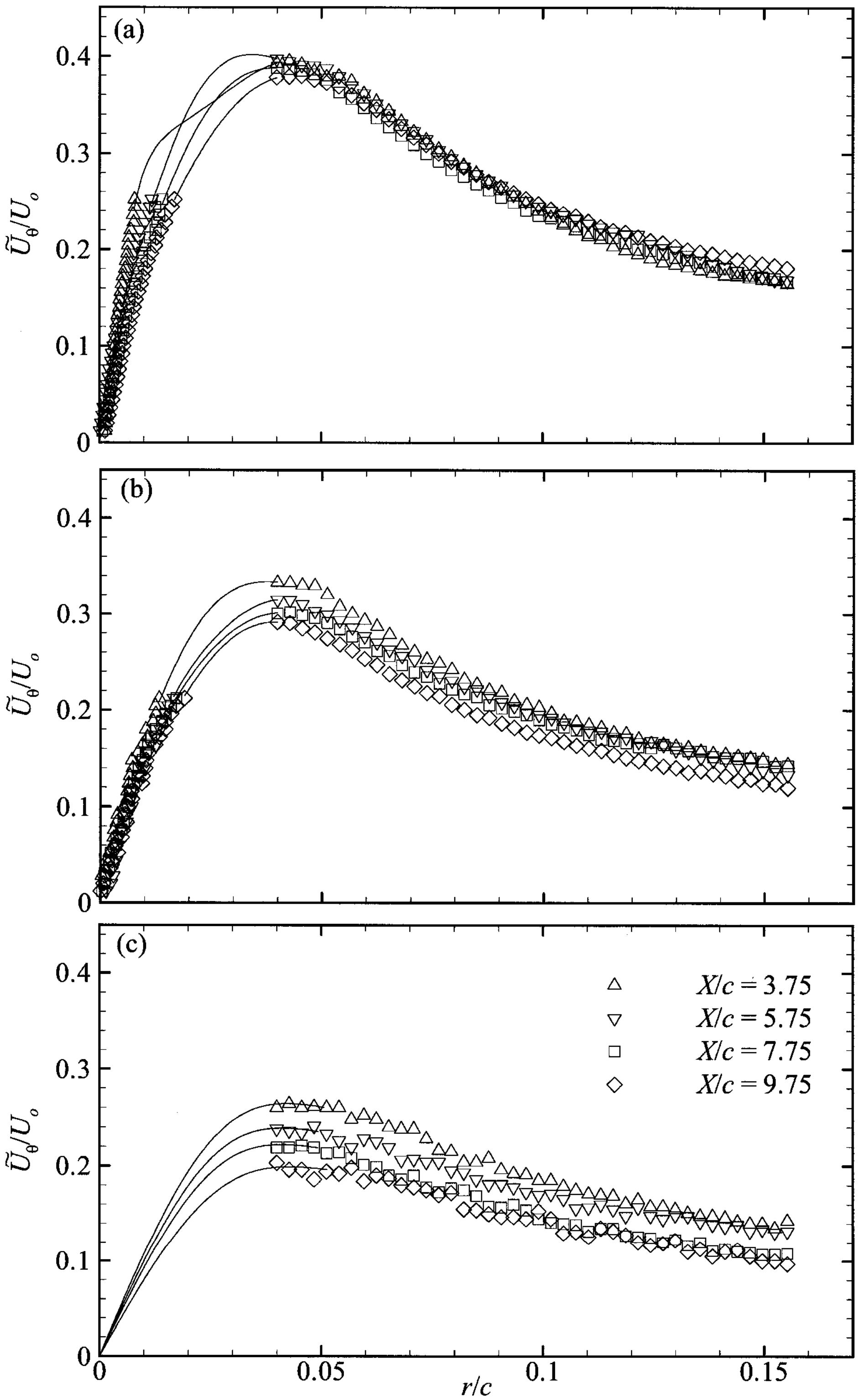

Figure 6.43: Radial profiles of $\widetilde{U}_\theta$ at X/c = 3.75, 5.75, 7.75 and 9.75 for (a) no-grid, (b) small-grid and (c) large-grid cases.

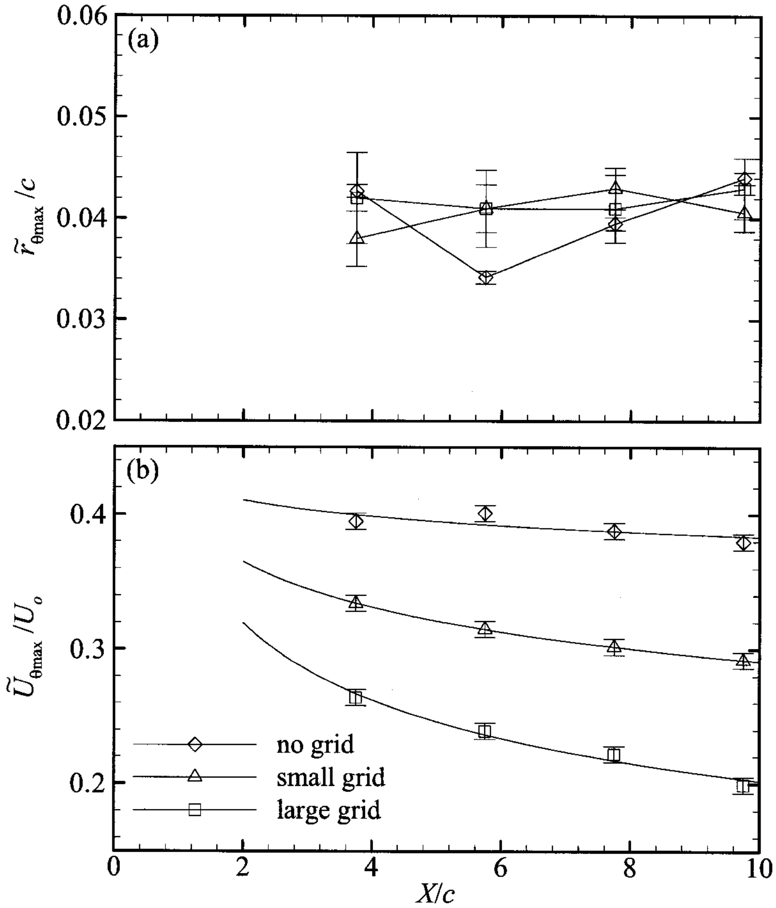

Figure 6.44: Streamwise development of (a) $\widetilde{r}_{\theta\,\max}/c$ and (b) $\widetilde{U}_{\theta\,\max}/U_o$. Error bars in (a) indicate the estimated error in the instances where probe 1 is coincident with vortex centre (see Figure 6.18). Error bars in (b) indicate the estimated uncertainty of the four-wire probe velocity. Solid lines in (b) indicate power law fit.

6.3.5 Vortex bending

The velocity profiles reconstructed by using the method described above were based on the assumption that the instantaneous vortex axis is always perpendicular to the yz plane, which was determined from average data. However, it is obvious that vortex wandering also changes temporally the orientation of this axis. As illustrated by the simulations of Marshall and Beninati (2005), the instantaneous angle between the vortex line and the yz plane might not necessary be negligible at high free-stream turbulence intensities. If the orientation of the vortex line with respect to the yz plane fluctuated sufficiently, it would introduce an apparent diffusion into $\widetilde{U}_\theta(r)$ in a manner similar to that of transverse motion due to vortex wandering. Hence, it is necessary to determine whether the radial profile of the vortex in its actual cross-sectional plane would be significantly different from the reconstructed profile in the yz plane and, if this was found to be true, to estimate appropriate corrections. This was done as follows.

First, following the reconstruction technique described above, probe 1 is always assumed to be located on the instantaneous vortex axis. Then, pitch and yaw angles were defined for the vortex axis with respect to the x-axis. The vortex pitch angle ψ_χ was defined as the projected angle of the vortex axis on the xy plane, as illustrated in Figure 6.45. In this figure, the position of probe 1 and probe 2 are also defined as (y_1, z_1) and (y_2, z_2). The vortex yaw angle ϕ_χ was defined as the projected angle of the vortex axis on the xz plane, as illustrated in Figure 6.46. In this section, the subscript χ indicates values associated with the cross-sectional plane of the vortex.

The influence of vortex bending by ψ_χ and ϕ_χ angles on the velocity measured

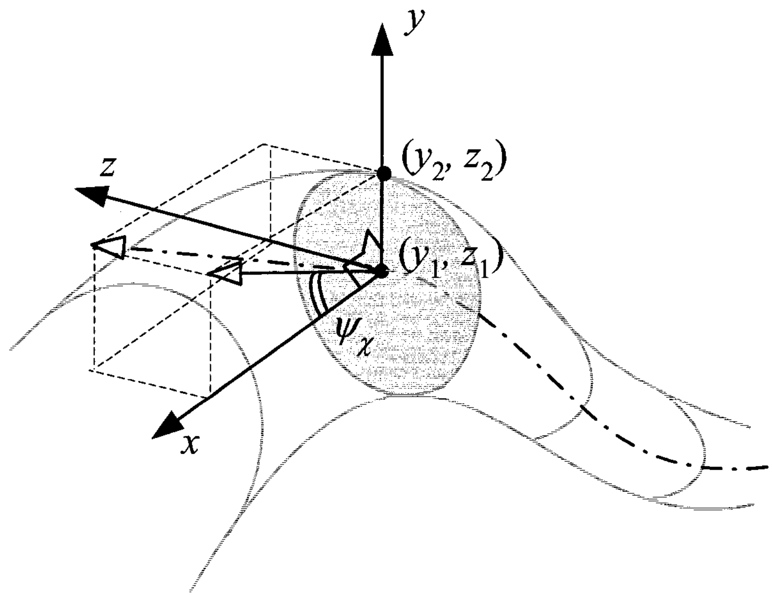

Figure 6.45: Sketch illustrating the definition of vortex pitch, ψ_χ.

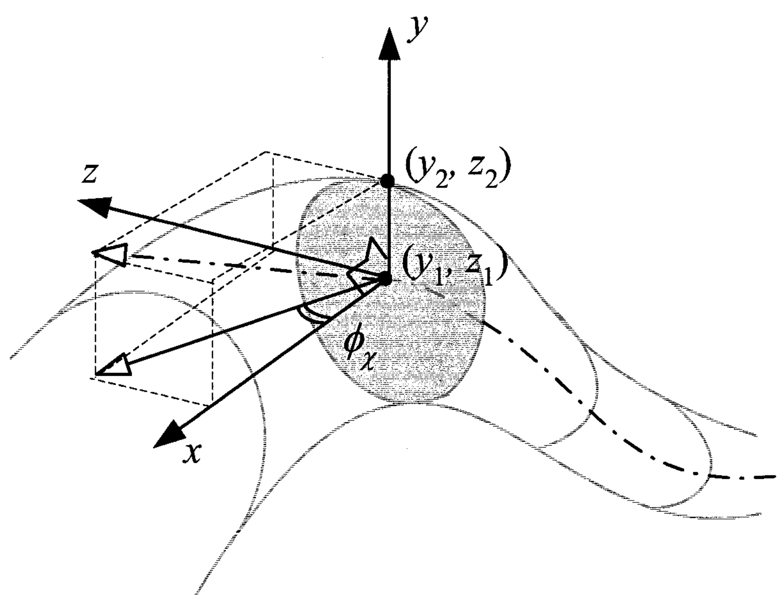

Figure 6.46: Sketch illustrating the definition of vortex yaw, ϕ_χ.

by probe 2 is illustrated in Figure 6.47. The difference between the instantaneous radial position of probe 2 (equal to the probe spacing S) in the yz plane and the instantaneous radial position of probe 2 in the vortex cross-sectional plane depends on the magnitude of ψ_χ. In the reconstruction, it was assumed that $U_{z2}\left(S = r_2\right) \approx U_{z2}\left(r_\chi\right)$. As the amplitude of bending increases, however this assumption would become invalid. Also, the circumferential velocity in the vortex cross-sectional plane, when projected on the yz plane, would be reduced due to the magnitude of ϕ_χ. However, if the bending angle is known, a correction can be determined from Figure 6.47 as

$$r_\chi = \frac{r_2}{\cos\psi_\chi} \tag{6.10a}$$

$$U_{\theta\chi} = \frac{U_{z2}}{\cos\phi_\chi} \tag{6.11a}$$

where r_2 is the radial position of probe 2 with respect to the instantaneous vortex centre in the yz plane, r_χ is the radial position of the probe with respect to the instantaneous vortex axis in the vortex cross-sectional plane, $U_{\theta\chi}$ is the circumferential velocity in the yz plane and U_{z2} is the corresponding component of velocity projected on the yz plane in the z direction and measured by probe 2. Therefore, if the average bending angle can be estimated, the conditionally averaged profiles can be corrected accordingly.

To estimate the average bending angle, the wandering motion was modeled as a sinusoidal wave in the xy plane with wavelength and amplitude equal to values estimated in Sections 6.2.2 and 6.2.1, respectively. It was also assumed that the average pitch and yaw angles are approximately equal, namely that $\overline{\psi}_\chi \approx \overline{\phi}_\chi$. The assumption of equal pitch and yaw average angles appears to be reasonable due to the approximately isotropic natures of both the free-stream turbulence and the vortex wandering.

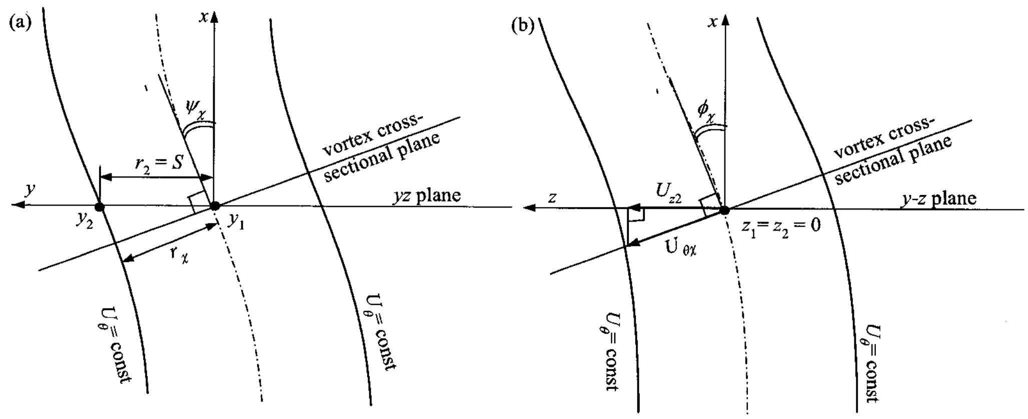

Figure 6.47: Sketch illustrating effect of (a) ψ_χ and (b) ϕ_χ on reconstruction of instantaneous velocity profiles.

To estimate the amplitude of the average sinusoidal wave, the standard deviation σ of the wandering amplitude (Section 6.2.1) was used. Here σ was taken to be the average value of σ_y and σ_z. the values of σ used in this analysis have been presented in Table 6.2.

The average wavelength λ of the sine wave was estimated from the peak frequency f_p of wandering as determined from cross-spectra measured on the time-averaged vortex axis as described in Section 6.2.2 and U_o as the convection velocity of the vortex past the probe. The resulting values for the wavelength are also presented in Table 6.2. With the values for σ and λ given in Table 6.2, the average value of the angle $\arctan(|y|/x)$ for the sine wave $y = \sigma \sin(2\pi x/\lambda)$ was estimated numerically.

The resulting estimates of bending angles are presented in Table 6.3.

As can be observed in Table 6.3, the estimates of the average angle between the vortex and the probe indicate that this angle was less than 4° in all cases. Thus, according to the corrections of Equations 6.10, the corresponding uncertainty in the r and $\widetilde{U}_\theta$ values of the reconstructed circumferential velocity profiles was quite small, as indicated in Table

	no grid			small grid			large grid		
X/c	σ [m]	f_p [Hz]	λ [m]	σ [m]	f_p	λ [m]	σ [m]	f_p [Hz]	λ [m]
3.75	0.0010	51	0.39	0.0026	57	0.35	0.0064	44	0.46
5.75	0.0014	38	0.53	0.0031	39	0.51	0.0080	37	0.55
7.75	0.0013	38	0.53	0.0031	35	0.57	0.0098	36	0.56
9.75	0.0012	38	0.53	0.0034	26	0.75	0.010	33	0.61

Table 6.2: Table of values used to estimate vortex pitch and yaw angles

	no grid			small grid			large grid		
X/c	$\overline{\psi}_\chi$ or $\overline{\phi}_\chi$	Δr	$\Delta\widetilde{U}_\theta$	$\overline{\psi}_\chi$ or $\overline{\phi}_\chi$	Δr	$\Delta\widetilde{U}_\theta$	$\overline{\psi}_\chi$ or $\overline{\phi}_\chi$	Δr	$\Delta\widetilde{U}_\theta$
3.75	0.6°	0.01%	0.01%	1.7°	0.05%	0.05%	3.2°	0.2%	0.2%
5.75	0.6°	0.01%	0.01%	1.4°	0.03%	0.03%	3.4°	0.2%	0.2%
7.75	0.6°	0.01%	0.01%	1.2°	0.02%	0.02%	4.0°	0.2%	0.2%
9.75	0.5°	0.01%	0.01%	1.0°	0.01%	0.01%	3.8°	0.2%	0.2%

Table 6.3: Estimated vortex pitch and yaw angles and corresponding estimated uncertainty in r and $\widetilde{U}_\theta$

6.3 and therefore negligible. Consequently, there was no need to apply any corrections to the results.

6.3.6 Comparison of reconstructed and time-averaged velocity profiles

Having reconstructed the average velocity profile in a wandering frame, and estimated the wandering amplitude, it is possible to compare it to the time-averaged profile on a fixed frame. This was done by enforcing a transverse motion of the reconstructed profile in a manner that is statistically described by the experimentally determined JPDFs of vortex position (Figure 6.14) and determining the resulting velocity components induced by the vortex at discrete locations in the yz plane. The vortex motion was simulated using a number generator which generated normally distributed random numbers. Two series of random values were generated with standard deviations σ_y and σ_z to represent the vortex position y_v and z_v for each measurement case. Discrete positions were selected along the y axis at which to calculate point statistics to represent the probe positions (y_p, z_p). For each instance of the series, the U_{yv} and U_{zv} velocity components were found from interpolation of the $\widetilde{U}_\theta$ profile using

$$r_p = \left((y_p - y_v)^2 + (z_p - z_v)^2\right)^{0.5} \tag{6.12}$$

$$\theta_p = \arctan\left(\frac{(z_p - z_v)}{(y_p - y_v)}\right) \tag{6.13}$$

$$U_{yv} = -\widetilde{U}_\theta\left(r_p\right)\sin\left(\theta_p\right) \tag{6.14}$$

$$U_{zv} = \widetilde{U}_\theta\left(r_p\right)\cos\left(\theta_p\right). \tag{6.15}$$

Point statistics were then calculated from the series of U_{yv} and U_{zv} for comparison with the time averaged statistics along the line $z = 0$. Mean values of U_z are compared in Figure 6.48, second moments of U_y are compared in Figure 6.49, second moments of U_z are compared in Figure 6.50, skewnesses of U_z are compared in Figure 6.51 and kurtoses are compared in Figure 6.52.

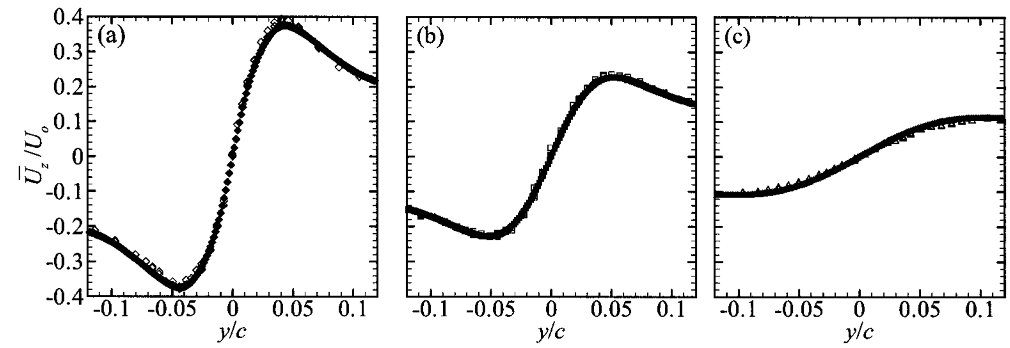

Figure 6.48: Comparison of $\overline{U}_z/U_o$ determined from measurements (hollow symbols) with values calculated using reconstructed velocity profile and measured wandering amplitude (solid symbols) for (a) no-grid, (b) small-grid and (c) large-grid cases at $X/c = 9.75$.

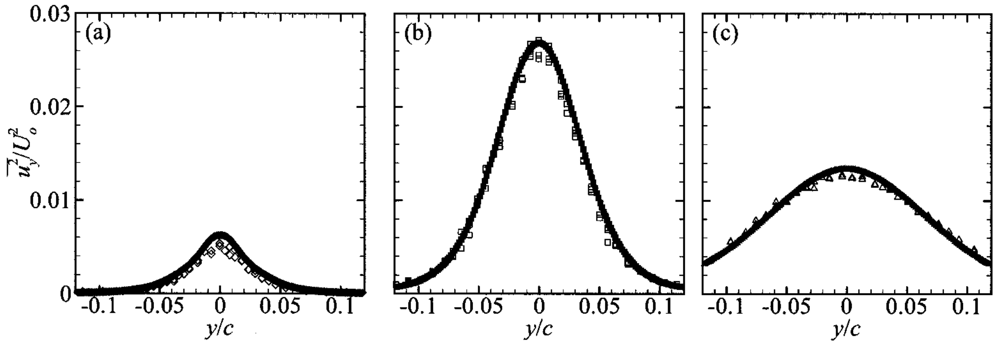

Figure 6.49: Comparison of $\overline{u_y^2}/U_o^2$ determined from measurements (hollow symbols) with values calculated using reconstructed velocity profile and measured wandering amplitude (solid symbols) for (a) no-grid, (b) small-grid and (c) large-grid cases at $X/c = 9.75$.

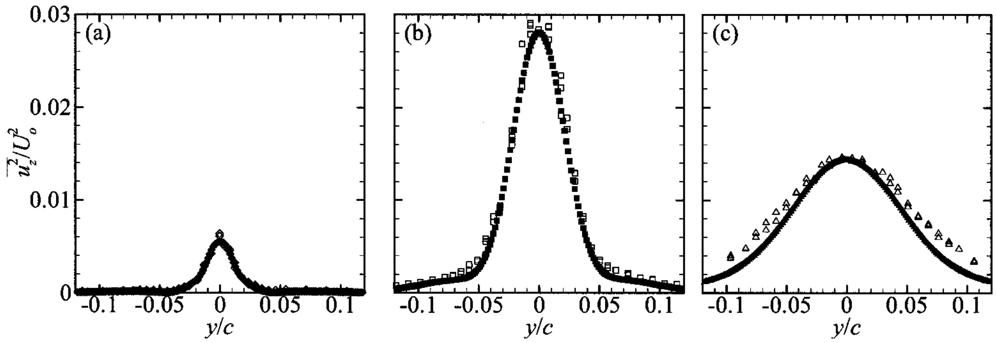

Figure 6.50: Comparison of $\overline{u_z^2}/U_o^2$ determined from measurements (hollow symbols) with values calculated using reconstructed velocity profile and measured wandering amplitude (solid symbols) for (a) no-grid, (b) small-grid and (c) large-grid cases at $X/c = 9.75$.

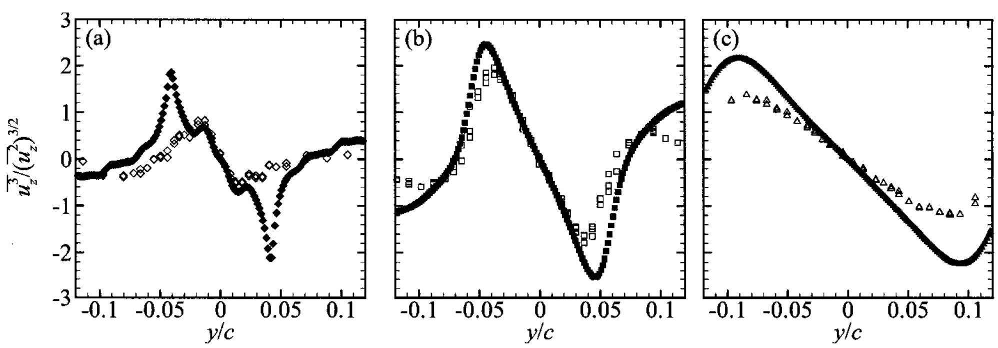

Figure 6.51: Comparison of $\overline{u_y^3}/\overline{u_y^2}^{3/2}$ determined from measurements (hollow symbols) with values calculated using reconstructed velocity profile and measured wandering amplitude (solid symbols) for (a) no-grid, (b) small-grid and (c) large-grid cases at $X/c = 9.75$.

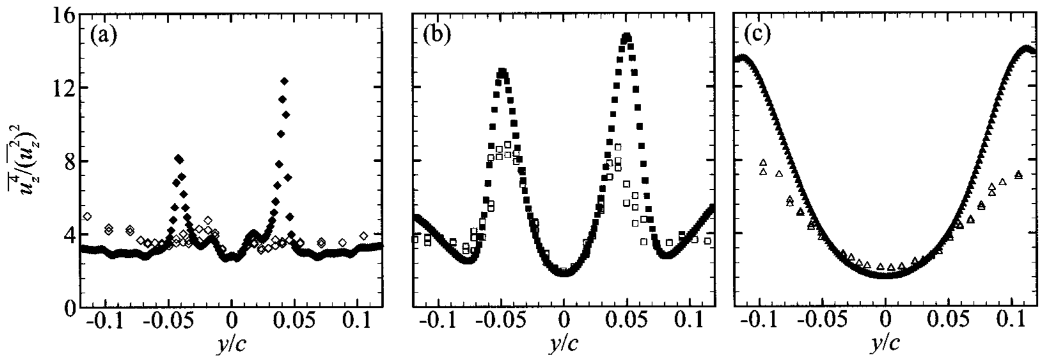

Figure 6.52: Comparison of $\overline{u_y^4}/\overline{u_y^2}^2$ determined from measurements (hollow symbols) with values calculated using reconstructed velocity profile and measured wandering amplitude (solid symbols) for (a) no-grid, (b) small-grid and (c) large-grid cases at $X/c = 9.75$.

Excellent comparisons were observed for the first and second moments, providing confidence in both the zero-crossing technique used to determine the vortex wandering amplitude and in the accuracy of the reconstructed profiles. Although the third and fourth moments show increasing differences between the time-averaged measurements and the reconstructed results, both variations have comparable orders of magnitude and shapes. As well as providing confidence in the analysis techniques developed, the comparisons provided by Figures 6.48 to 6.52 reinforce the observations of Devenport et al. (1996) and Heyes et al. (2004) that the time-averaged statistics near the vortex core are dominated by the influence of vortex wandering.

6.3.7 Time dependence of the reconstructed profile

The reconstructed profiles of $\widetilde{U}_\theta(r)$ shown in Figure 6.43 were determined using the average or most probable values of $U_{z2}(S)$. These profiles showed a measurable decrease in $\widetilde{U}_{\theta\,\max}$ with increasing free-stream turbulence, however it is possible that, if the velocity profile were time dependent, there could be instances when the velocity profile of the small-grid and large-grid cases would be comparable to the one in the no-grid case. To investigate this possibility, the outer profile was reconstructed as described in Section 6.3.2, except that, instead of selecting the average or most probable value of $U_{z2}(S)$ when $U_{z1} = 0$, the maximum value was selected. To avoid contamination of the results by outliers, the maximum was determined using a set of conditions. To minimize the inclusion of instances at which probe 1 was within the free-stream, only values of $U_{z2}(S)$ greater than the value with the peak probability were considered. For the large-grid case, for which two peaks are evident, this peak was the one associated with probe 1 being in the core. The value selected as the maximum was the value below which $U_{z2}(S)$ has a 99% probability of occurring when $U_{z1} = 0$. This value was determined by examining the probability distribution of values greater than the peak value associated with probe 1 being within the vortex core and selecting the value at 99%, which, following Section 6.3.2, allows the estimation of a radial profile from $U_{z2(99\%)}(S) \approx \widetilde{U}_{\theta(99\%)}(r = S)$. The resulting profiles are shown in Figure 6.53 for the no-grid (Figure 6.53a), small-grid (Figure 6.53b) and large-grid (Figure 6.53c) cases at $X/c = 3.75$, 5.75, 7.75 and 9.75.

Figure 6.53 indicates that it is unlikely that the small-grid and large-grid cases have instantaneous circumferential velocity profiles that match the no-grid profile at the same streamwise position. This indicates that the decay observed in Figure 6.43 is not due to averaging of an unsteady velocity profile.

The possible unsteadiness of the velocity profile was investigated further by examining the difference $\widetilde{U}_{\theta(99\%)}(r) - \widetilde{U}_{\theta}(r)$. This difference is shown normalized by u'_{zo} in Figure 6.54, where u'_{zo} is the rms of transverse velocity fluctuations measured at the same

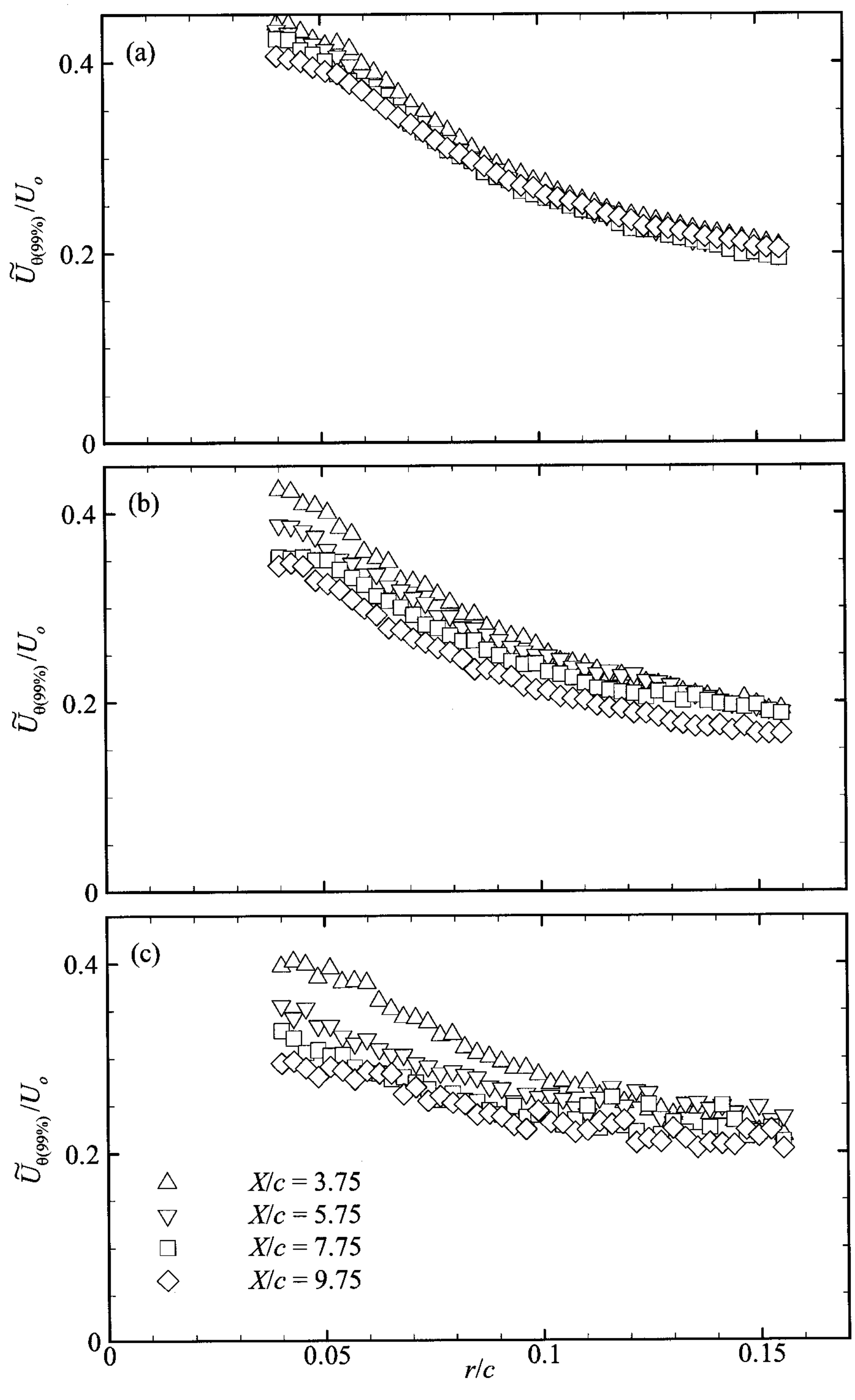

Figure 6.53: Radial profiles of $\widetilde{U}_{\theta(99\%)}$ at X/c = 3.75, 5.75, 7.75 and 9.75 for (a) no-grid, (b) small-grid and (c) large-grid cases.

streamwise position with the wing removed from the tunnel.

For the no-grid case, Figure 6.54a, the value of u'_{xo} was an order of magnitude smaller than $\widetilde{U}_{\theta(99\%)}(r) - \widetilde{U}_{\theta}(r)$. A streamwise decrease of $\widetilde{U}_{\theta(99\%)}(r) - \widetilde{U}_{\theta}(r)$ was evident, indicating a decay of the velocity fluctuations with streamwise distance. At $X/c = 3.75$ and 5.75, the spiral wake appeared as a region with a higher level of unsteadiness for $r/c > 0.9$ and 1.2, respectively, and was not evident for $X/c = 7.75$ and 9.75. There is also an increase in $\widetilde{U}_{\theta(99\%)}(r) - \widetilde{U}_{\theta}(r)$ with decreasing r. This increase could be evidence of some residual effect of wandering on the reconstruction process, however, observing that the value of $\left(\widetilde{U}_{\theta(99\%)}(r) - \widetilde{U}_{\theta}(r)\right)/u'_{zo}$ at $r/c < 0.05$ decreases with streamwise distance, wandering does not appear to be a likely source. Thus, it appears that the increase in $\widetilde{U}_{\theta(99\%)}(r) - \widetilde{U}_{\theta}(r)$ is due to unsteadiness. However, it is unclear whether this unsteadiness is due to large-scale unsteadiness in the vortex core or due to small-scale turbulent fluctuations.

The small-grid case unsteadiness, shown in Figure 6.54b, appears to be nearly self-similar because the profiles of $\widetilde{U}_{\theta(99\%)}(r) - \widetilde{U}_{\theta}(r)$ approximately collapse when scaled by u'_{xo}. Similar to the no-grid case, the values of $\left(\widetilde{U}_{\theta(99\%)}(r) - \widetilde{U}_{\theta}(r)\right)/u'_{zo}$ increases as r decreases with values of $\left(\widetilde{U}_{\theta(99\%)}(r) - \widetilde{U}_{\theta}(r)\right)/u'_{zo} \approx 4$ at $r/c = 0.04$ and values of $\left(\widetilde{U}_{\theta(99\%)}(r) - \widetilde{U}_{\theta}(r)\right)/u'_{zo} \approx 3$ at $r/c = 0.15$ (except at $X/c = 3.75$, where it is $\approx$ 2.2). Noting that homogeneous and isotropic turbulence has velocity fluctuations which are Gaussian, a 99% range of values is in the range $2.6u'_{zo}$, which is indicated in Figure 6.54 as a dashed line. For $r/c > 0.1$, the values of $\widetilde{U}_{\theta(99\%)}(r) - \widetilde{U}_{\theta}(r)$ were within $0.4u'_{zo}$ of this value, indicating that the fluctuations in this range are due to free-stream turbulence. For $r/c < 0.1$ the increase could indicate an increase in turbulent fluctuations or large-scale

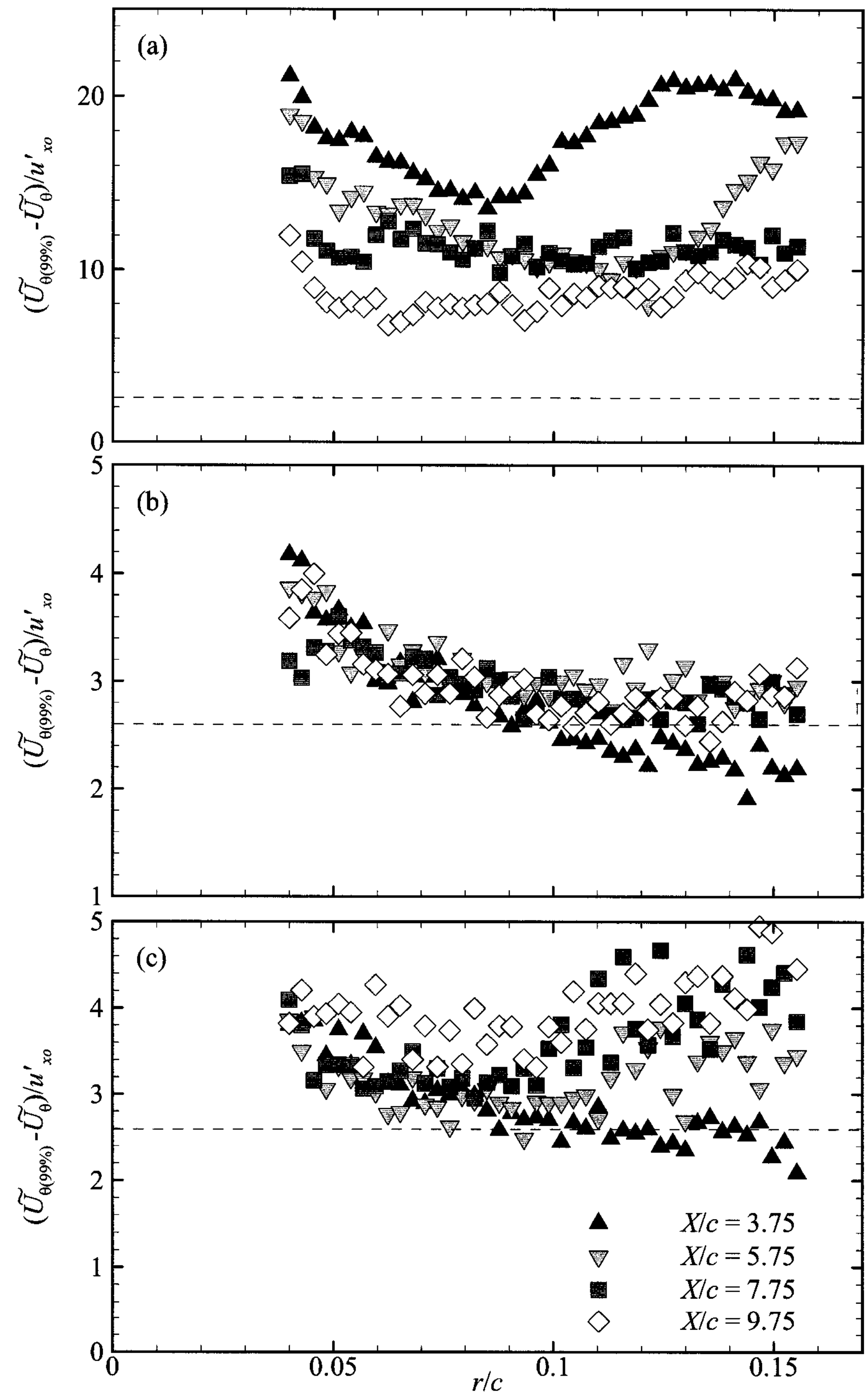

Figure 6.54: Radial profiles of $\left(\widetilde{U}_{\theta(99\%)} - \widetilde{U}_{\theta}\right)/u'_{zo}$ at X/c = 3.75, 5.75, 7.75 and 9.75 for (a) no-grid, (b) small-grid and (c) large-grid cases. Dashed line indicates a value of 2.6.

distortions of the vortex core.

Nearly identical behaviour was observed for the large-grid case (Figure 6.54c) at $X/c = 3.75$. At $X/c = 5.75$, the profile is similar for $r/c < 0.1$, however the unsteadiness increases with increasing r for $r/c > 0.1$. At $X/c = 7.75$, this increase occurs for $r/c > 0.08$. At $X/c = 9.75$, $\left(\widetilde{U}_{\theta(99\%)}(r) - \widetilde{U}_{\theta}(r)\right)/u'_{zo}$ was between 4 and 5, with higher values at larger radii. This increase in unsteadiness is not associated with the spiral wake, as can be observed by comparing it to that in the no-grid case wake (for which the wake appears at $r/c > 0.09$ at $X/c = 3.75$ and $r/c > 1.2$ at $X/c = 5.75$). Instead, it is probable that the increase in unsteadiness is due to some other source.

Chapter 7

Discussion

7.1 Effect of free-stream turbulence on vortex formation

The flow visualization and single sensor hot-wire results indicate that free-stream turbulence did not introduce any apparent qualitative change in the vortex formation process, although it affected the initial turbulence level in the vortex core and resulted in increased distortion and meandering of the formed vortices. The negligible effect of free-stream turbulence on the loading of the wing is demonstrated by the fact that the section lift coefficient c_L showed a negligible variation with increasing free-stream turbulence level (Section 5.6).

Within the range of the reconstruction of velocity profiles ($X/c = 3.75$ to 9.75), the $\widetilde{r}_{\theta\,\max}$ values show that the small-grid and large-grid cases had approximately the same core radius, however the uncertainty in determining $\widetilde{r}_{\theta\,\max}$ (within 10%) prevents one from making a definitive statement concerning the effect of free-stream turbulence on the initial radius of the vortex core. Within the same streamwise range, $\widetilde{U}_{\theta\,\max}$ for the small-grid case and large-grid case are lower than no-grid case (by approximately 20% and 40% respectively). If the decay of $\widetilde{U}_{\theta\,\max}$ were linear, extrapolating the $\widetilde{U}_{\theta\,\max}$ values to $X/c = 0$ would indicate that the small-grid case $\widetilde{U}_{\theta\,\max}$ would be approximately 12% lower than the no-grid case and the large-grid case 24% lower at the approximate location of vortex formation, which could be interpreted as the formation of an initially weaker vortex core for the grid cases. However, if the decay is modeled using the power law shown in Figure 6.44, $\widetilde{U}_{\theta\,\max}$ for all three cases converges at $X/c = 0.75$, the trailing edge of the wing, which would indicate an initially similar value of $\widetilde{U}_{\theta\,\max}$ for all three cases. Support for this possibilty can be found in the streamwise development of $\overline{r}_{\theta\,\max}$ and $\overline{U}_{\theta\,\max}$ (Figures 5.48a and b). For all measurement cases, these quantities appear to converge to the no-grid case values at small X/c. It therefore appears that the effect of free-stream turbulence on the initial radial profile of circumferential velocity profile is small.

7.2 Streamwise velocity within the vortex core

An issue of interest is to determine whether, for the different free-stream conditions, the time-averaged streamwise velocity in the vortex core is jet-like or wake-like, namely whether the peak streamwise velocity U_p in the core is greater or smaller than U_o (Chow et al. (1997), Devenport et al. (1996), Anderson and Lawton (2003)). The measurements in the no-grid and small-grid upstream case at $X/c = 1.75$ (Figures 5.33 and 5.34) appear to conform with neither of these patterns. Instead, the axial velocity profile has a local maximum at the vortex center, roughly equal to the local free-stream velocity, surrounded by an annular region with a velocity deficit. As the vortex develops downstream, both the central maximum and the annular deficit decrease and the axial velocity profile approaches a wake-like form. Considering that lateral vortex motion would generally tend to smoothen the time-averaged velocity profile, one may not assert the degree, if any, by which the observed changes in the mean profile are caused by vortex wandering or whether they are the result of changes in the instantaneous profiles.

To illuminate this issue, a simple model was created by introducing a random transverse motion of the velocity profile indicated by a solid line in Figure 5.33 for $X/c = 1.75$, which is an approximation of the measured mean profile. Time series representing the instantaneous displacements in the y and z directions of the vortex axis from the fixed origin with zero means and standard deviations σ_y and σ_z, respectively, were generated using a Gaussian random number generator. A series of points along a radial line were chosen to represent locations of the fixed measuring probe, and a time series of the velocity U_x at each point was formed by selecting appropriate values from the velocity profile of the randomly moving vortex. Mean values U_x were calculated from the series for different values of $\sigma_y = \sigma_z = \sigma$, which correspond to the amplitudes of wandering motion. The results for $\sigma = 0.005c\,(= 1\,\mathrm{mm})$ and $\sigma = 0.017c\,(= 3\,\mathrm{mm})$ are presented in Figure 5.33 for $X/c = 5.75$ and 9.75, respectively as dashed lines. Despite its crudeness, this model reproduces fairly well the profiles measured at $X/c = 5.75$ and 9.75 for the no-grid case. In other words, the shapes of the mean profiles measured downstream are approximately the same as the mean profiles that would be observed by a fixed probe, if a vortex with a fixed instantaneous profile equal to the mean profile at $X/c = 1.75$ were set in Gaussian-type vortex wandering. Note that the rms amplitudes of wandering estimated at each location are actually conservative, because they are based on the assumption that the profile at $X/c = 1.75$ is not itself subjected to wandering. However these values are significantly larger than predicted using the correction techniques of both Devenport et al. (1996) and the current study, which implies that either the correction is inaccurate or the streamwise development shown in Figures 5.33 and 5.34 is due to effects other than vortex wandering. Due to the agreement of the current wandering estimate and that of Devenport et al. (1996), it appears more likely that the development is due to effects other than vortex wandering, such as viscous or turbulent diffusion.

An annular profile, such as measured for the no-grid case at $X/c = 1.75$, can be expected to produce instability within the vortex core (Marshall and Beninati (2000), Fabre and Jacquin (2004)). Indeed, there is a peak evident in the no-grid case power spectra within the vortex core (Figures 5.54, 5.57 and 6.21a). Such peaks are commonly associated with vortex instabilities (Singh and Uberoi (1976), Bandyopadhyay (1990), Jacquin et al. (2003)). Turbulence produced by these instabilities will act to decrease the streamwise velocity gradients within the core through momentum transport, which could explain the decrease in U_p with streamwise distance observed in Figure 5.33 and evolution of the radial profile of $\overline{U}_x$ towards a more Gaussian form.

For the turbulent free-stream cases, for which vortex wandering was found to be much stronger than that in the no-grid case, one would anticipate that instantaneous radial profiles of the streamwise velocity could be even more different in shape from the mean profiles measured by a fixed probe. It is thus clear that vortex wandering could possibly obscure the measurement of an annular velocity profile by smoothening velocity differences, reducing peak values and spreading the profile radially, in a process that could be termed as apparent radial diffusion. It appears at least possible that the annular profile could also exist for the grid cases immediately following vortex formation as slight annularity was observed in the small-grid-upstream case at $X/c = 1.75$.

Considering that for the grid turbulence cases a greater amount of turbulence was observed within the vortex during flow visualization of the vortex formation and within the boundary layers in the single-sensor hot-wire measurements, it appears likely that there is a higher level of turbulence entrained into the core from both the boundary layers and the free stream during vortex formation. Therefore, it is likely that there will be increased turbulent diffusion of streamwise momentum in these cases, which, in turn, would rapidly reduce any annularity of the streamwise velocity profile. This would tend to result in a rapid evolution in time towards the more Gaussian shape observed in the radial profile of streamwise velocity for the grid cases and could explain the differences observed between the no-grid and grid cases. Thus, differences in the observed time-averaged profiles of $\overline{U}_x$ for different free-stream conditions could be due partly to differences in the instantaneous profiles and partly to differences in wandering effects.

7.3 Effect of free-stream turbulence on the spiral wake

An increase in free-stream turbulence appeared to increase the rate of diffusion of the streamwise momentum within the spiral wake, as observed in Figures 5.28 to 5.32. This was expressed as both an increase in the wake width and a corresponding decrease in velocity deficit. Moreover, increasing free-stream turbulence resulted in a decrease in the curvature of the wake, which may be interpreted as a reduction in the strength of the velocity field induced by the vortex. This reduction in wake curvature is not an artefact of the measuring procedure, as it cannot be attributed to vortex wandering.

Within the shear layer, isotachs of circumferential velocity across the spiral wake are oriented at an angle to the wake (Figures 5.38 to 5.42), indicating that the wake is undergoing both stretching and shearing, in agreement with discussion by Devenport et al. (1996) and Miranda and Devenport (1998). For all five free-stream conditions, the angles between the velocity contours and the wake trajectory are comparable, which indicates that the relative strength of stretching compared to skewing remains unaffected by free-stream turbulence. However, also apparent in Figures 5.38 to 5.42 is a decrease in the density of the isotachs of $\overline{U}_\theta$ along the wake with increasing free-stream turbulence, indicating a decrease in the magnitude of rates of both stretching and shearing in the wake with increased free-stream turbulence. Stretching along the length of the spiral tends to increase the azimuthal vorticity component, whereas shearing tends to produce additional turbulence in the wake. As these effects appear to weaken with increasing free-stream turbulence, one would expect that the influence of the wake on the vortex would also weaken.

Lateral spreading of the shear layer shed from the wing was observed, which would decrease the rates of shearing in the wake and appeared to be caused by an increase in turbulent diffusion. Such increases in diffusion occur both with increasing streamwise distance and increasing free-stream turbulence. Phillips (1981) describes the process of the innermost spirals of the shear layer merging together through viscous diffusion to form the vortex core. This process, combined with an increased rate of diffusion due to more intense free-stream turbulence, provides a mechanism for an increase in the vortex core radius at distances far downstream of the wing, where the vortex roll-up is complete, however no such increase was observed in the streamwise distance examined in this study.

7.4 Vortex wandering

Measurements of time-averaged Reynolds stresses (Section 5.11) were found to be strongly contaminated by vortex wandering, with the greatest effect appearing as very high local Reynolds stresses near the time-averaged vortex axis. Examination of the a_{yy}, a_{zz} and a_{yz} component of the anisotropy tensor in Section 5.13 indicated that wandering of the vortex contaminated the entire measurement region. Therefore, caution must be exercised when analyzing time-averaged turbulence statistics in the presence of wandering.

A novel analysis was performed in Section 6.2.1 to quantify the amplitude of vortex wandering by determining the joint probability density function (JPDF) of vortex position in y and z using the zero-crossings of U_y and U_z. It was found that, for the isotropic grid turbulence, the vortex position on the yz plane could be described by a bi-normal distribution with roughly circular organization of the JPDF isocontours of probability around the time-averaged axis of the vortex, indicating that there is little preferential bias in the wandering direction. Devenport et al. (1996) also assumed a bi-normal distribution and found that there was a measurable correlation between the y and z directions. For the grid cases, no such correlation could be observed in the JPDFs. For the no-grid case, however, because of the relatively coarse spacing of the measurement grid and the relatively low amplitude of wandering, the effectiveness of the zero-crossing technique was reduced and, therefore, the existence of a correlation between y and z directions of wandering observed by Devenport et al. could not be established.

The results of the wandering analysis do not appear to support the hypothesis that the wandering of an isolated vortex in free-stream turbulence is the result of an instability excited by the turbulent eddies. Such types of motion are incompatible with the observed bi-normal JPDF of vortex position, which indicates that the vortex motion is random rather than organized, as would be the case if it were the result of either sinusoidal or helical instabilities. For example, for a helical instability, the greatest number of zero-crossings would occur in a ring around the mean vortex axis, which would trace the path of the instantaneous vortex axis, whereas, for a sinusoidal (bending wave) instability, the greatest number of zero-crossings would occur at the peaks of the sine wave. Rossow (1999) notes that an isolated vortex undergoing a bending wave instability will tend to rotate about its own axis and for such behaviour the greatest number of zero-crossings would occur at the time-averaged vortex axis, however, the general appearance of the JPDF of vortex position would be closer to a "Mexican hat" shape than a Gaussian shape, with increased probability at the edge of the range of motion.

The amplitude of vortex wandering was found to be well described using the standard deviations σ_y and σ_z of the bi-normal distribution in the y and z directions. The wandering amplitude was found to increase both with streamwise distance and increased free-stream turbulence. A weak directional dependence was observed in the wandering, as σ_y was found to be slightly larger than σ_z, particularly for the large-grid case. However, close examination of the Reynolds normal stresses $\overline{u_y^2}$ and $\overline{u_z^2}$ shows that the grid-generated turbulence itself was not perfectly isotropic, with $\overline{u_y^2}$ being slightly larger than $\overline{u_z^2}$, possibly due to the difference in width and height of the wind tunnel. Consistency of the anisotropy between the Reynolds normal stresses and the wandering amplitude also supports the observation that wandering is the result of transport due to free-stream eddies.

This study confirms what other researchers (Devenport et al. (1996), Rokhsaz et al. (2000), Baker et al. (1974)) have observed, that the wandering amplitude grows with streamwise distance. The wandering was found to have the largest amplitude when the vortex was weakest, which indicates that the wandering was not self-induced. Of interest is a comparison of the sensitivity of vortex wandering to the turbulence kinetic energy and that to its length scale. As discussed in Section 6.2.1, the wandering amplitude is higher for the large-grid case with the grid in the downstream position when compared to corresponding case with the grid in the upstream position (the uncertainty for the small-grid and small-grid upstream cases prevents one from conducting a meaningful comparison between these two cases). It is reminded that, as the grid turbulence evolves downstream, its kinetic energy decays, whereas its integral length scale grows. Thus, the present observations indicate that the wandering amplitude depends in a stronger fashion on the turbulent kinetic energy than the turbulence length scale.

The wavelengths exhibited by the vortex wandering were estimated in Section 6.2.2 using frequency spectra of velocity on the time-averaged vortex axis. It was observed that the spectral content of vortex wandering was wideband and appeared predominantly as a plateau in the spectra for $f < 100\,\text{Hz}$. Despite this broad range of frequencies, closer examination of the frequency contribution using cross-spectra revealed the existence of a dominant wandering frequency f_p, which was near 80 Hz at $X/c = 1.75$ and decreased with streamwise distance to approximately 30 Hz at $X/c = 9.75$. This decrease in frequency implies a growth in the wavelength of the wandering with streamwise distance (Figure 6.26). The wavelength U_o/f_p was not found to be comparable in magnitude with the integral length scale. The timescale $1/f_p$ corresponding to the peak frequency has been compared to the "eddy turnover time" (or "eddy lifetime") $\tau_E = L_x/u'_x$ in Figure 6.28. This figure indicates that the timescale of wandering decreases at the same rate as the eddy turnover time, with $1/f_p$ being approximately $0.4\tau_E$, which further supports the observation that wandering is the result of transport due to free-stream eddies.

7.5 Effect of free-stream turbulence on the vortex

Using a novel analysis of two-point three-component velocity measurements, the average circumferential velocity profile in the wandering frame was reconstructed in Section 6.3. A noticeable impact of free-stream turbulence was measured, with an increase in free-stream turbulence causing an increase in the rate decay of the peak circumferential velocity $\widetilde{U}_{\theta\,\max}$ of the reconstructed velocity profile. Interestingly, the radial location $\widetilde{r}_{\theta\,\max}$ at which $\widetilde{U}_{\theta\,\max}$ occurs did not show a corresponding increase, indicating a loss of angular momentum within the vortex core. Evidence in a reduction of circumferential velocity with increasing free-stream turbulence can also be found in the observed noticeable decrease in the curvature of the spiral wake with increasing free-stream turbulence, which may be interpreted as a reduction in the strength of the velocity field induced by the vortex.

Several possible mechanisms can be proposed to explain the mechanism leading to this loss of circumferential velocity:

- Turbulent diffusion due to entrainment of free-stream or boundary layer turbulence during vortex formation.

- Entrainment and diffusion of the vortex vorticity at the edge of the core by free-stream eddies, leading to transport of vorticity away from the vortex core.

- A vortex stripping mechanism, as suggested by Marshall and Beninati (2000). According to this hypothesis, secondary turbulent structures, which originate in grid turbulence, are wrapped around the vortex and gradually strip away parts of the core and its vorticity. Vortical fluid which is stripped from the core becomes wrapped around the vortex, such that its vorticity is re-oriented towards the azimuthal direction, thus adding to the strength of the coherent structures but reducing the circulation as measured on the transverse plane.

- Holzäpfel et al. (2003) suggest that it is the formation of these secondary structures that causes the reduction in core vorticity. According to this description, angular momentum is transferred from the core to the secondary structures as the latter wrap around the core. As the vortex stretches the secondary structures, work is performed by the vortex core on the structures, resulting in an increase of the rotational energy of the structures and a loss of the rotational energy of the vortex.

- Simulations (i.e. Holzäpfel et al. (2003)) have also observed that, under conditions with high free-stream turbulence, the vortex is rapidly deformed and broken up by the free-stream eddies.

Saffman (1995) describes that a Lamb-Oseen vortex undergoing viscous decay has a core radius $r_{\theta\,\max}$ which grows proportionately to $(\nu t)^{1/2}$. This prediction can be extended to a turbulent vortex to infer that the vortex core radius would roughly grow as $(\nu_t t)^n$, where ν_t is some eddy viscosity. The presently reconstructed velocity profiles show no evidence that $\widetilde{r}_{\theta\,\max}$ grows downstream. This lack of growth seems to imply that the vortex strength decay observed in the current study is due to a mechanism other than turbulent diffusion. Another possibility could be that the diffusion is competing with some other mechanism which counteracts the core growth.

The time-averaged radial profiles of circulation (Figure 5.50) also provide some information about the vortex decay. Near the vortex core, the time-averaged velocity used to calculate $\overline{\Gamma}$ was strongly influenced by wandering. However, as shown in Figure 6.37, the reconstructed velocity profiles match the time-averaged velocity profiles for the range $r/c \gtrsim 0.14$ (for the large-grid case at $X/c = 9.75$, the profiles were found to match at smaller radii for all other cases), hence the radial profiles of $\overline{\Gamma}$ should also be unaffected by wandering for this range.

The time-averaged radial profiles of circulation show that, for the grid turbulence cases, after an initial period of circulation increase (vortex formation and roll-up), there is a decrease in circulation at large radial distances. This decrease appears to occur over the entire range of measured radii, which is inconsistent with the diffusion of vorticity away from the vortex core, but could indicate a net reduction of axial vorticity. One possible explanation for the net loss of axial vorticity is the reorientation of vorticity vectors into the azimuthal direction, through stretching induced by the vortex. Alternately, the turbulent eddies could cause previously "organized" vorticity to become "disorganized" resulting in a reduction of axial vorticity. Thus, the behaviour of the radial profiles of circulation are consistent both with vortical fluid being stripped from the core and reorganized and the transfer of angular momentum from the core due to stretching of the azimuthal structures.

Holzäpfel et al. (2003) observed that after an initial period of decay, the vortex circulation remained relatively constant with time. They attribute this to an initial loss of vortex rotational energy during the formation of the secondary structures. Once the structures were fully formed, there was no more transfer of angular momentum to the structures and hence the decay in circulation ceases. Examination of Figure 6.44 shows that the rate of decay of $U_{\theta\,\max}$ decreases with X/c, which could indicate that the vortex is approaching a steady state. Heyes et al. (2004) also found that, at far downstream distances, the rate of decay of $U_{\theta\,\max}$ was small and similar to their no-grid case. This behaviour could indicate that the initial decay of $U_{\theta\,\max}$ is due to the formation of secondary structures and, once formed, $U_{\theta\,\max}$ could remain approximately constant. An alternate explanation, however, that the turbulent kinetic energy of the grid turbulence itself is decaying and that, as the turbulence decays, its influence on $U_{\theta\,\max}$ could be reduced.

It is important to note that the reconstructed velocity profiles produced in this study are only averages. Examination of the JPDFs of Figures 6.30 and 6.33 indicate that there is actually a range of U_{z2} values that are measured when probe 1 is at the instantaneous vortex axis. Although this U_{z2} variation could be due to uncertainty in the reconstruction technique, it is highly probable that the velocity profile in the wandering frame is unsteady, particularly because the streamwise evolution of the profile is due to turbulent effects. Hence, it is possible that the instantaneous field of the vortex is not precisely axi-symmetric. Non-axisymmetry may introduce instability and a mechanism for the detrainment of the core fluid into the free-stream.

The reconstructed velocity profiles were examined to obtain an estimate of unsteadiness in the profile in Section 6.3.7. These results indicated that, for the small-grid and large-grid cases, there was increasing unsteadiness as $\widetilde{r}$ decreased towards $\widetilde{r}_{\theta\,\mathrm{max}}$. This unsteadiness approximately scaled with the transverse velocity fluctuations of the free-stream turbulence measured with the wing removed at the same streamwise position. The simulations of Holzäpfel et al. (2003) indicate that secondary structures which wrap around the vortex can deform (bend) the vortex core and both stretch and squeeze the vortex. Thus the unsteadiness observed in the reconstructed profile could be due to large-scale deformation of the vortex by these secondary structures. If this is the case, the scaling of the unsteadiness by the transverse velocity fluctuations of the free-stream turbulence would indicate that velocity scales of the structures also scale with the velocity fluctuations of the free-stream turbulence.

Unfortunately, it was not possible with the current results to quantify turbulence and unsteadiness within the vortex core. However, some information can be found in the similarity between time-averaged Reynolds stresses and the reconstructed apparent Reynolds stresses caused by vortex wandering (Section 6.3.6). The similarity between the measured and reconstructed results indicate that any turbulence within the vortex core is relatively weak when compared to the apparent Reynolds stresses caused by wandering, which is consistent with the observations of Heyes et al. (2004). However, considering the magnitude of the vortex wandering, and the nature of the measurements, turbulence within the core cannot be ruled out. Only measurements of the temporal evolution of the vortex field in the wandering frame could resolve this issue.

7.6 Influence of the vortex on free-stream turbulence

In studies investigating the spiral wake, it has been found that, as the wake spirals to smaller radii, there are increased rates of stretching and skewing (Miranda and Devenport (1998), Devenport et al. (1996), Phillips (1981)). Simulations have also shown that, for a vortex in turbulence, the free-stream eddies become organized into azimuthal coherent structures (Marshall and Beninati (2005), Takahashi et al. (2005), Holzäpfel et al. (2003), Melander and Hussain (1993)). These studies clearly demonstrate that the vortex actively affects an initially isotropic free-stream turbulence, reorganizing it through shearing and straining to an anisotropic and inhomogeneous form.

Measurements presented in Section 5.14 revealed the existence of an azimuthal ring of integral length scales with a value equal to approximately half the integral length scale of the free-stream turbulence, which was found to grow with streamwise distance. Miranda and Devenport (1998) measured the transverse integral length scale in the spiral wake and found an increase in the transverse integral length scale along the spiral near the core when compared with measurements in a location where the wake had not yet begun to spiral around the vortex. This behaviour was attributed to the increased rate of stretching near the vortex and therefore a similar increase in transverse integral length scale could be expected in the free-stream eddies as they stretched and reoriented azimuthally. Coinciding with this increase in transverse integral length scale, would be a corresponding decrease in streamwise integral length scale due to mass conservation which would explain the decrease in streamwise integral length scale (compared to the grid turbulence with the wing removed) observed in Figures 5.70 to 5.73. The radial extent of this reorientation on the integral length scale was found to grow from $r < 6\widetilde{r}_{\theta\,\max}$ at $X/c = 1.75$ to a range to encompassing $r \lesssim 25\widetilde{r}_{\theta\,\max}$ by $X/c = 9.75$.

Closer to the vortex core within the range $\widetilde{r}_{\theta\,\max} \lesssim r \lesssim 6\widetilde{r}_{\theta\,\max}$, bandpass filtering performed in Section 6.1 revealed the existence of an azimuthal ring of high Reynolds stress at high frequencies, evident for both the no-grid and small-grid cases. This azimuthal ring had peak stresses at approximately $2.5\widetilde{r}_{\theta\,\max}$, which is near the radius of $2\widetilde{r}_{\theta\,\max}$ cited by Takahashi et al. (2005) at which secondary structures occur. The radial location of the peak was found to move inwards towards the vortex core as pass-band frequency was increased. This behaviour is consistent with the wrapping of the secondary structures around the core. As they do so, their streamwise length scale will decrease at each successive spiral.

At radii near $2\widetilde{r}_{\theta\,\max}$, a ring of enhanced turbulent strain rate was observed for the small-grid and small-grid-upstream cases in Section 5.15. Although the exact value was obscured by the effects of vortex wandering, the turbulent strain rate was several times greater than in the free-stream. As the eddies were stretched and wrapped around the vortex, their azimuthal vorticity would increase, resulting in higher overall enstrophy around the vortex core. Tennekes and Lumley (1972) show that at high Reynolds numbers, assuming approximately isotropic behaviour at small scales, enstrophy is related to dissipation through the action of viscosity and the turbulent strain rate. Both Takahashi et al. (2005)

and Melander and Hussain (1993) observed local regions of enhanced dissipation near the vortex core and found that these regions coexisted at the same radial range as the secondary structures, however Melander and Hussain (1993) could not statistically link the dissipation to the structures. However the higher dissipation of turbulent kinetic energy in this region could be due to stretching imposed by the vortex on small scale turbulent eddies causing them to stretch to increasingly smaller scales where they would be dissipated by viscosity.

For the large-grid and large-grid upstream cases, the highest Reynolds stresses in the bandpass filtered results and the location of peak turbulent strain rate occurred at the time-averaged vortex axis. However, at the high wandering amplitudes observed for the large-grid and large-grid-upstream cases, even at the time-averaged vortex axis the probe spends more time measuring velocity at radial locations outside the vortex core compared as opposed to inside the vortex core. As a result, for these cases, evidence of the organization of Reynolds stresses and turbulent strain rate into azimuthal rings was obscured by the wandering. Hence, little information about the organization of the turbulence by the vortex could be obtained for these cases.

Chapter 8

Conclusions and recommendations for future studies

The objective of this study was to observe and document the effects of free-stream turbulence on wing-tip vortex formation and streamwise development near the wing. Although recent simulations have provided some interesting insight into the interaction between a vortex and a turbulent free stream, there have been very few experimental studies which have attempted to measure this interaction, mainly because of difficulties arising from the unsteady wandering of the vortex. The present study has overcome these difficulties through the development of an analysis technique which can quantify the vortex wandering and by using simultaneous measurements of the velocity in magnitude and direction at two points combined with a specialized analysis procedure to reconstruct the velocity profile of the vortex in the wandering frame of reference. These results were combined with high quality time-averaged measurements and flow visualizations to provide a thorough overview of the vortex formation and development in the presence of free-stream turbulence.

Dye-injection flow visualization, combined with single-sensor hot-wire measurements and oil-film flow visualization revealed that the wing-tip vortex formed from three distinct co-rotating vortices whose positions were unaffected by free-stream turbulence. Moreover, flow visualization indicated that free-stream turbulence increased the turbulence within these vortices and the wandering amplitude.

Four-sensor hot-wire measurements of the velocity vector were performed in several cross-sectional planes downstream of the wing. It was observed that free-stream turbulence did not seem to introduce any measurable change in the mean trajectory of the vortex. The radial profile of the mean axial velocity had an axi-symmetric off-axis minimum in the no-grid case close to the wing, which developed towards a wake-like shape with increasing streamwise distance. All cases with grid turbulence in the free stream had wake-like mean axial profiles, which were found to be affected significantly by vortex wandering. The shear layer shed from the wing was found to both stretch and shear the wing wake. Increased free-stream turbulence resulted in reduced stretching and shearing, although the relative strengths of stretching and shearing remained in proportion. Time-averaged Reynolds stresses and circumferential velocity profiles near the mean vortex axis were found to be strongly affected by vortex wandering. Integral length scales were found to be approximately half of the integral length scale of the grid turbulence in an azimuthal ring around the vortex, with the ring radius growing with streamwise distance. At smaller radii, the turbulent strain rate was found to be significantly higher compared to the turbulent strain rate measured in the grid turbulence without the wing in place. Bandpass filtering of the Reynolds normal stresses indicated the presence of a ring of high Reynolds stresses around the vortex in high frequency pass-bands. The location of this ring was consistent with the location of the formation of azimuthally-aligned secondary structures observed in simulations by other authors.

Time-series analysis indicated that increasing the free-stream turbulence resulted in increased amplitude of vortex wandering. The vortex wandering was found to be well represented by a bi-normal distribution of vortex position. Combined with observations made from power spectra, these results indicated that the vortex wandering was caused by convective transport due to large-scale free-stream eddies.

Two point measurements were used to reconstruct the instantaneous velocity profile. Increasing free-stream turbulence was found to increase the rate of decay of the vortex peak circumferential velocity profile while not significantly affecting the radial location at which the peak occurs. These results, combined with time-averaged radial profiles of vortex circulation, indicate a net loss of axial vorticity and support the decay mechanisms proposed by other researchers who suggest that the vortex decay is due to three-dimensional effects such as vorticity stripping by secondary coherent structures which form azimuthally around the vortex (Marshall and Beninati (2000)) or to loss of angular momentum caused by the formation of these structures (Holzäpfel et al. (2003)).

The following recommendations for further work on the interaction between a vortex and free-stream turbulence can be made.

1. Flow visualization should be performed downstream of the wing to study the interaction between the turbulence and the vortex. In particular, this will provide insight

into the stretching of turbulent eddies around the vortex and will indicate whether there is any exchange of fluid between the vortex core and the free-stream.

2. Additional information could be provided on the instantaneous vortex core by repeating the two-probe measurements with probes that have been constructed in such a way as to decrease the minimum probe spacing. Alternately, performing experiments on a larger vortex will improve the spatial resolution of measurements in the core of the vortex.

3. Measurements could be taken with a PIV system, preferably time-resolved PIV. This measurement technique will verify the reconstruction technique and provide information about possible unsteadiness of the vortex velocity profile. In addition, measurements could be made in a plane including the streamwise axis to study the relationship between the vortex, the free-stream turbulence and secondary structures.

4. Introduction of shear into the free-stream will minimize the decay of the free-stream turbulence, as well as introducing vorticity into the flow. Minimizing the turbulent decay will indicate whether the observed decay of peak circumferential velocity is due to an event that occurs shortly after formation, such as the formation of secondary structures, or is due to a continual process such as vorticity stripping.

References

Anand, M. S. and S. B. Pope (1985). *Turbulent Shear Flows*, Chapter Diffusion Behind a Line Source in Grid Turbulence, pp. 46–61. Berlin: Springer-Verlag.

Anderson, E. and T. Lawton (2003). Correlation between vortex strength and axial velocity in a trailing vortex. *Journal of Aircraft 40*(4), 699–704.

Baker, G., S. Barker, K. Bofah, and P. Saffman (1974). Laser anemometer measurements of trailing vortices in water. *Journal of Fluid Mechanics 65*, 325–336.

Bandyopadhyay, P. (1990). AIAA 90-1625 the organized nature of a turbulent trailing vortex. In *AIAA 21st Fluid Dynamics, Plasma Dynamics and Lasers Conference*, Seattle, Washington, U.S.A., pp. 1–10. American Institute of Aeronautics and Astronautics.

Bandyopadhyay, P., D. Stead, and R. Ash (1991). Organized nature of a turbulent trailing vortex. *AIAA Journal 29*(10), 1627–1633.

Batchelor, G. (1964). Axial flow in trailing line vortices. *Journal of Fluid Mechanics 20*, 645–658.

Bendat, J. and A. Piersol (2000). *Random Data, Analysis and Measurement Procedures.* New York, U.S.A.: John Wiley and Sons, Inc.

Beninati, M. and J. Marshall (2005). An experimental study of the effect of free-stream turbulence on a trailing vortex. *Experiments in Fluids 38*, 244–257.

Bertin, J. and M. Smith (1989). *Aerodynamics for Engineers.* New Jersey, U.S.A.: Prentice-Hall, Inc.

Birch, D., T. Lee, F. Mokhtarian, and F. Kafyeke (2003). Rollup and near-field behavior of a tip vortex. *Journal of Aircraft 40*(3), 603–607.

Bradshaw, P. (1969). The analogy between streamline curvature and buoyancy in turbulent shear flow. *Journal of Fluid Mechanics 36*, 177–191.

Bradshaw, P. (1975). *An Introduction to Turbulence and its Measurement.* United Kingdom: Pergamon.

Bruun, H. (1995). *Hot-Wire Anemometry - Principles and Signal Analysis.* New York, U.S.A.: Oxford University Press.

Chow, J., G. Zilliac, and P. Bradshaw (1994). Turbulence measurements in the near-field of a wingtip vortex. In *Proceedings of Turbulence in Complex Flows*, pp. 61–78. ASME.

Chow, J., G. Zilliac, and P. Bradshaw (1997). Mean and turbulence measurements in the near field of a wingtip vortex. *AIAA Journal 35*(10), 1561–1567.

Comte-Bellot, G. and S. Corrsin (1966). The use of a contraction to improve the isotropy of grid-generated turbulence. *Journal of Fluid Mechanics 25*, 657–682.

Comte-Bellot, G. and S. Corrsin (1971). Simple eulerian time correlation of full and narrow-band velocity signals in grid-generated 'isotropic' turbulence. *Journal of Fluid*

Mechanics 48(2), 273–337.

Corsiglia, V., R. Schwind, and N. Chigier (1973). Rapid scanning, three-dimensional hot-wire anemometer surveys of wing-tip vortices. *Journal of Aircraft 10*(12), 752–757.

Cotel, A. and R. Breidenthal (1999). Turbulence inside a vortex. *Physics of Fluids 11*(10), 3026–3029.

Crow, S. (1970). Stability theory for a pair of trailing vortices. *AIAA Journal 8*, 2172–2179.

Csanady, G. (1973). *Turbulent Diffusion in the Environment.* Boston, U.S.A.: D. Reidel Publishing Company.

Dacles-Mariani, J., G. Zilliac, J. Chow, and P. Bradshaw (1995). Numerical / experimental study of a wingtip vortex in the near field. *AIAA Journal 33*(9), 1561–1568.

Devenport, W., M. Rife, I. Stergios, and G. Follin (1996). The structure and development of a wing-tip vortex. *Journal of Fluid Mechanics 312*, 67–106.

Döbbeling, K., B. Lenze, and W. Leuckel (1990). Basic considerations concerning the construction and usage of multiple hot-wire probes for highly turbulent three-dimensional flows. *Measurement Science and Technology 1*, 924–933.

Donaldson, C. and A. Bilanin (1975). *Vortex Wakes of Conventional Aircraft.* NATO Advisory Group for Aerospace Research and Development. AGARDograph No. 204.

Donaldson, C., R. Snedeker, and R. Sullivan (1974). Calculation of aircraft wake velocity profiles and comparison with experimental measurements. *Journal of Aircraft 11*, 547–555.

Dunn, W. (1997). Visualization of flow past a model of the CF-18 aircraft in a water tunnel. Master's thesis, University of Ottawa.

Etkin, B. and L. Reid (1996). *Dynamics of Flight - Stability and Control.* New York, U.S.A.: John Wiley and Sons, Inc.

Fabre, D. and L. Jacquin (2004). Viscous instabilities in trailing vortices at large swirl numbers. *Journal of Fluid Mechanics 500*, 239–262.

Ferchichi, M. and S. Tavoularis (2000). Reynolds number effects on the fine structure of uniformly sheared turbulence. *Physics of Fluids 12*(11), 2942–2953.

Gerz, T., F. Holzäpfel, and D. Darracq (2002). Commercial aircraft wake vortices. *Progress in Aerospace Sciences 38*, 181–208.

Green, S. (1995). *Fluid Vortices*, Chapter Wing Tip Vortices, pp. 427–470. Netherlands: Kluwer Academic Publishers.

Gursul, I. and W. Xie (1999). Origin of vortex wandering over delta wings. *Journal of Aircraft 37*(2), 348–350.

Heyes, A., S. Hubbard, A. Marquis, and D. Smith (2003). On the roll-up of a trailing vortex sheet in the very near field. *Proceedings of the Institute of Mechanical Engineers, Part G: Journal of Aerospace Engineering 217*(5), 263–269.

Heyes, A., R. Jones, and D. Smith (2004, July). Wandering of wing-tip vortices. In *Proceedings of the 12th International Symposium on the Applications of Laser Techniques to Fluid Mechanics*, Lisbon, Portugal.

Hoffman, E. and P. Joubert (1963). Turbulent line vortices. *Journal of Fluid Mechan-*

ics 16, 395–411.

Holzäpfel, F., T. Hofbauer, D. Darracq, H. Moet, F. Garnier, and C. Gago (2003). Analysis of wake vortex decay mechanisms in the atmosphere. *Aerospace Science and Technology 7*, 263–275.

Jacquin, L., D. Fabre, P. Geffroy, and E. Coustols (2001). The properties of a transport aircraft wake in the extended near field: An experimental study. AIAA Paper 2001-1038, Jan. 2001.

Jacquin, L., D. Fabre, D. Sipp, V. Theofilis, and H. Vollmers (2003). Instability and unsteadiness of aircraft wake vortices. *Aerospace Science and Technology 7*, 577–593.

Katz, J. and J. Galdo (1989). Effect of roughness on rollup of tip vortices on a rectangular hydrofoil. *Journal of Aircraft 26*(3), 247–253.

Kawahara, G. (2005). Energy dissipation in spiral vortex layers wrapped around a straight vortex tube. *Physics of Fluids 17*(5), 055111.1–055111.13.

Lavoie, P. and A. Pollard (2003). Uncertainty analysis of four-sensor hot-wires and their data-reduction schemes used in the near field of a turbulent jet. *Experiments in Fluids 34*, 358–370.

Lekakis, I. (1996). Calibration and signal interpretation for single and multiple hot-wire/hot-film probes. *Measurement Science and Technology 7*(10), 1313–1333.

Liebeck, R. (2004). Design of the blended wing body subsonic transport. *Journal of Aircraft 41*(1), 10–25.

Lugt, H. (1983). *Vortex Flow in Nature and Technology.* New York, U.S.A.: John Wiley and Sons, Inc.

Maciel, Y. and C. Gleyzes (2000). Survey of multi-wire probe data processing techniques and efficient processing of four-wire probe velocity measurements in turbulent flows. *Experiments in Fluids 29*, 66–77.

Marshall, J. (1997). The flow induced by periodic vortex rings wrapped around a columnar vortex core. *Journal of Fluid Mechanics 345*, 1–30.

Marshall, J. and M. Beninati (2000). Turbulence evolution in vortex-dominated flows. In *Nonlinear Instability, Chaos and Turbulence II*, pp. 1–40. Southampton, England: WIT Press.

Marshall, J. S. and M. L. Beninati (2005). External turbulence interaction with a columnar vortex. *Journal of Fluid Mechanics 540*, 221–245.

McInerny, S., W. Meecham, and P. Soderman (1990). Pressure fluctuations in the tip region of a blunt-tipped airfoil. *AIAA Journal 28*(1), 6–13.

Melander, M. and F. Hussain (1993). Coupling between a coherent structure and fine-scale turbulence. *Physical Review E 48*, 2669–2689.

Miranda, J. and W. Devenport (1998). Turbulence structure in the spiral wake shed by a lifting wing. *AIAA Journal 36*(4), 658–660.

Miyazaki, T. and C. R. Hunt, Julian (2000). Linear and nonlinear interactions between a columnar vortex and external turbulence. *Journal of Fluid Mechanics 402*, 349–378.

Phillips, W. (1981). The turbulent trailing vortex during roll-up. *Journal of Fluid Mechanics 105*, 451–467.

Pilette, D. (2000). Preliminary study of the tip vortex of a NACA 0012 wing. University of Ottawa internal document.

Pope, Stephen, B. (2000). *Turbulent Flows.* New York, U.S.A.: Cambridge University Press.

Pradeep, D. S. and F. Hussain (2001). Core dynamics of a strained vortex: Instability and transition. *Journal of Fluid Mechanics 447*, 247–285.

Rae, W. H. and A. Pope (1984). *Low Speed Wind Tunnel Testing, 2nd Ed.* New York, U.S.A.: John Wiley and Sons, Inc.

Ragab, S. and M. Sreedhar (1995). Numerical simulation of vortices with axial velocity deficits. *Physics of Fluids 7*(3), 549–558.

Ramaprian, B. and Y. Zheng (1997). Measurements in rollup region of the tip vortex from a rectangular wing. *AIAA Journal 35*(12), 1837–1843.

Roberts, P. and D. Webster (2002). Turbulent diffusion. In H. Shen, A. Cheng, K.-H. Wang, M. Teng, and C. Liu (Eds.), *Environmental Fluid Mechanics - Theories and Applications*, Chapter Turbulent Diffusion, pp. 7–45. Reston, Virginia: American Society of Civil Engineers.

Rokhsaz, K., S. Foster, and L. Miller (2000). Exploratory study of aircraft wake vortex filaments in a water tunnel. *Journal of Aircraft 37*(6), 1022–1027.

Rossow, V. (1999). Lift-generated vortex wakes of subsonic transport aircraft. *Progress in Aerospace Sciences 35*(6), 507–660.

Saffman, P. (1995). *Vortex Dynamics.* Cambridge, United Kingdom: Cambridge University Press.

Sarpkaya, T. and J. Daly (1987). Effect of ambient turbulence on trailing vortices. *Journal of Aircraft 6*, 399–404.

Shekarriz, A., T. Fu, J. Katz, and T. Huang (1993). Near-field behavior of a tip vortex. *AIAA Journal 31*(1), 112–118.

Shlien, D. and S. Corrsin (1974). A measurement of lagrangian velocity autocorrelation in approximately isotropic turbulence. *Journal of Fluid Mechanics 62 part 2*, 255–271.

Singh, P. and M. Uberoi (1976). Experiments on vortex stability. *Physics of Fluids 19*(12), 1858–1863.

Spalart, P. (1998). Airplane trailing vortices. *Annual Review of Fluid Mechanics 30*, 107–138.

Squire, H. (1965). The growth of a vortex in turbulent flow. *The Aeronautical Quarterly 16*(part 3), 302–306.

Sreedhar, M. and S. Ragab (1994). Large eddy simulation of longitudinal stationary vortices. *Physics of Fluids 6*(7), 2501–2514.

Sreenivasan, K., S. Tavoularis, R. Henry, and S. Corrsin (1980). Temperature fluctuations and scales in grid-generated turbulence. *Journal of Fluid Mechanics 100*(3), 597–621.

Takahashi, N., H. Ishii, and T. Miyazaki (2005). The influence of turbulence on a columnar vortex. *Physics of Fluids 17*(3), 035105.1–035105.14.

Tavoularis, S. (2005). *Measurement in Fluid Mechanics.* New York, U.S.A.: Cambridge University Press.

Tennekes, H. (1968). Simple model for the small-scale structure of turbulence. *Physics of Fluids 11*(3), 669–671.

Tennekes, H. and J. Lumley (1972). *A First Course in Turbulence.* Cambridge, U.S.A.: MIT Press.

Tsai, C. and S. Widnall (1976). The stability of short waves on a straight vortex filament in a weak externally imposed strain field. *Journal of Fluid Mechanics 73 part 4*, 721–733.

Vukoslavcevic, P. V., D. V. Petrovic, and J. M. Wallace (2004). An analytical approach to the uniqueness problem of hot-wire probes to measure simultaneously three velocity components. *Measurement Science and Technology 15*, 1848–1854.

Wallace, J. and J. Foss (1995). The measurement of vorticity in turbulent flows. *Annual Review of Fluid Mechanics 27*, 469–514.

Warhaft, Z. and J. L. Lumley (1978). An experimental study of the decay of temperature fluctuations in grid-generated turbulence. *Journal of Fluid Mechanics 88*(4), 659–684.

Wittmer, K., W. Devenport, and J. Zsoldos (1998). A four-sensor hot-wire probe system for three-component velocity measurements. *Experiments in Fluids 24*, 416–423.

Wyngaard, J. (1969). Spatial resolution of the vorticity meter and other hot-wire arrays. *Journal of Physics E: Scientific Instruments 2*(2), 983–987.

Appendix A

Time-averaged turbulent kinetic energy and Reynolds stresses

A.1 Time-averaged turbulent kinetic energy

The variations of measured velocity fluctuations are presented as three-dimensional contour plots of k/U_o^2 for each of the five free-stream conditions at $X/c = 1.75, 3.75, 5.75, 7.75$ and 9.75 in Figures A.1-A.5. These measurements were performed at $\alpha = 5°$ and $\mathrm{Re}_c = 2.4 \times 10^5$. In all figures, the wing wake can be identified as a thin region in which k/U_o^2 was greater than the free-stream level. Peaks of k/U_o^2 considerably greater than the free-stream value characterized the time-averaged centre of the vortex. In all cases, single axi-symmetric peaks were observed, except for the no-grid case at $X/c = 1.75$, where two peaks were evident.

Close to the wing, at $X/c = 1.75$, the magnitude of k/U_o^2 in the spiral wake was approximately the same for all cases. As the vortex developed downstream, the magnitude decreased monotonically with a more substantial decrease becoming evident as the free-stream turbulence intensity increased. At the last measuring station, $X/c = 9.75$, and with high levels of free-stream turbulence, the difference between the intensities of fluctuations in the spiral wake and the free stream was not very pronounced.

At the time-averaged centre of the vortex, the peak in k/U_o^2 was much greater in magnitude for the turbulent cases than for the no-grid case. The radial dimension of the peak increased monotonically with both free-stream turbulence intensity and streamwise distance. However, the streamwise trends of the magnitude of the measured peak k/U_o^2 varied depending on the free-stream conditions. Figure A.6 illustrates these trends for all five cases. The peak k/U_o^2 value for the no-grid case, initially at 0.027, rapidly decreased by an order of magnitude between $X/c = 1.75$ and $X/c = 3.75$, then gradually increased. The peak k/U_o^2 of the small-grid-upstream and small-grid cases did not initially decrease as observed for the no-grid case, but instead gradually increased with streamwise distance from their values at $X/c = 1.75$. An initial increase in peak k/U_o^2 was also evident in the large-grid-upstream case between $X/c = 1.75$ and $X/c = 3.75$, however, downstream of $X/c = 3.75$, the peak value decreased with X/c. Although the initial increase was not evident for the large-grid case, as X/c increased from $X/c = 1.75$, the peak magnitude k/U_o^2 decreased at the same rate as observed for the large-grid-upstream case for $X/c \geq 3.75$.

The trends observed in Figure A.6 can be explained almost entirely by considering the combination of vortex wandering and the variation of U_θ in the vortex. As shown in Section 6.2, the amplitude of vortex wandering increased with X/c and also with increasing

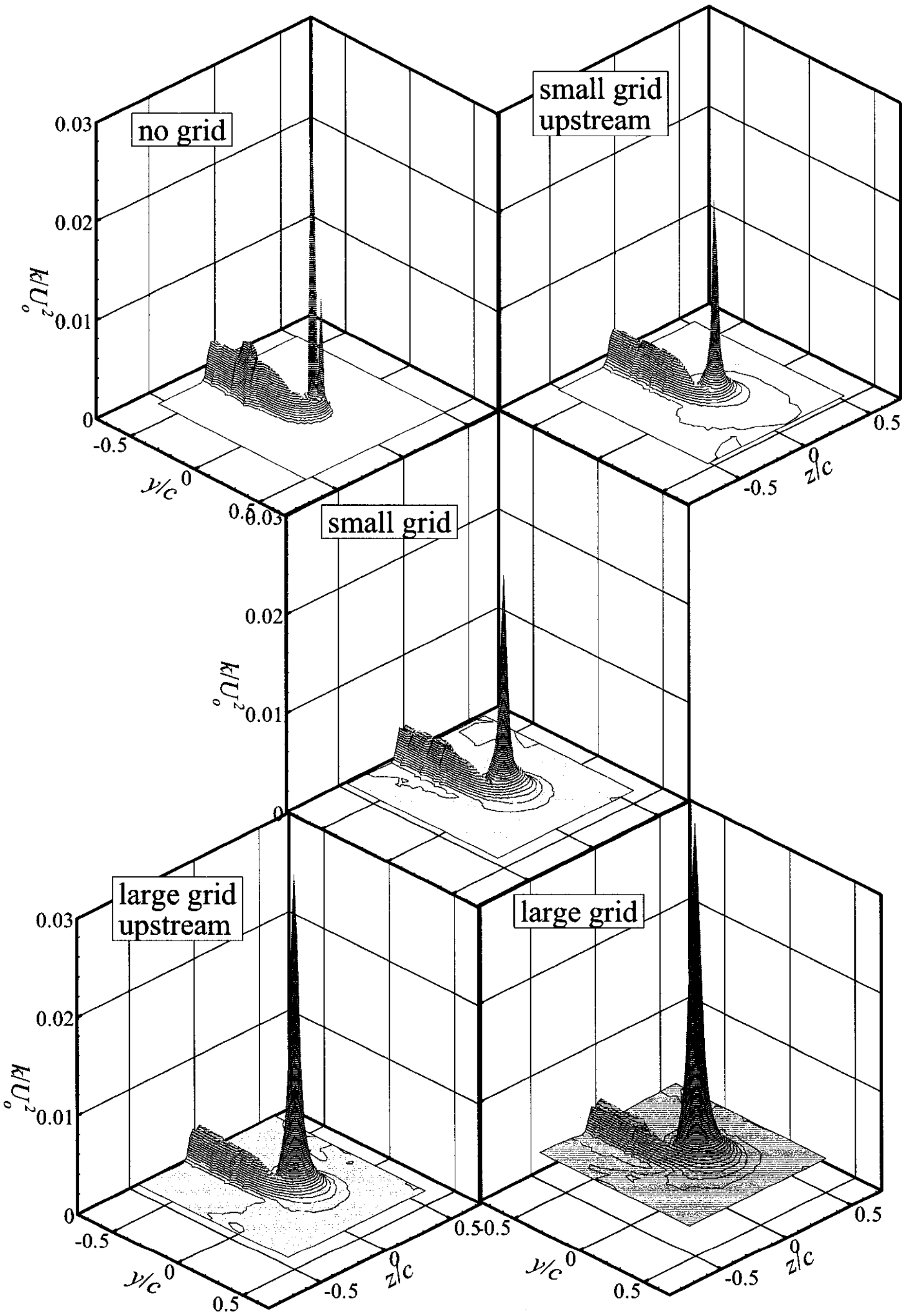

Figure A.1: Contours of k/U_o^2 at $X/c = 1.75$ for each measurement case. Contours are spaced 0.0002 apart.

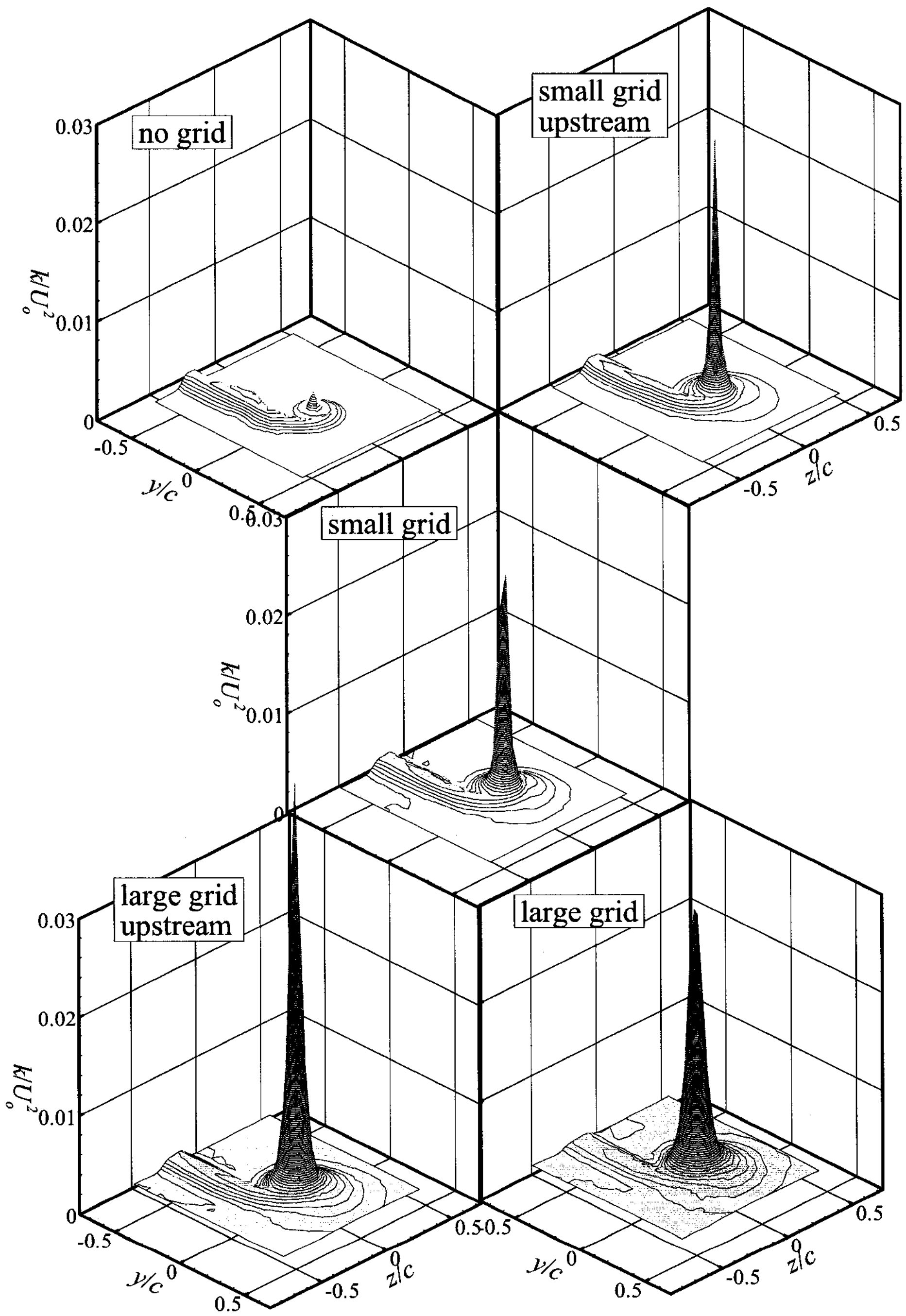

Figure A.2: Contours of k/U_o^2 at $X/c = 3.75$ for each measurement case. Contours are spaced 0.0002 apart.

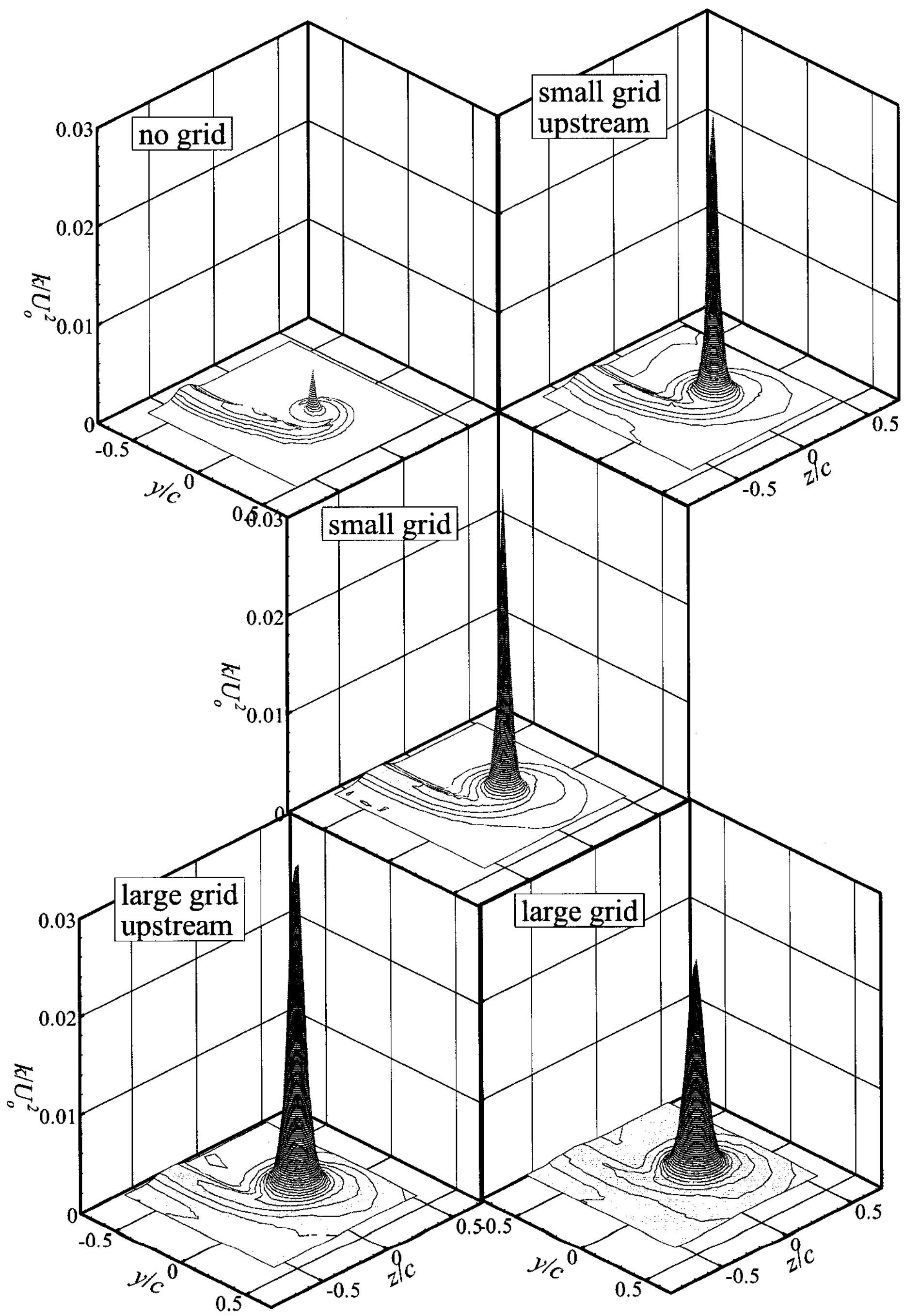

Figure A.3: Contours of k/U_o^2 at $X/c = 5.75$ for each measurement case. Contours are spaced 0.0002 apart.

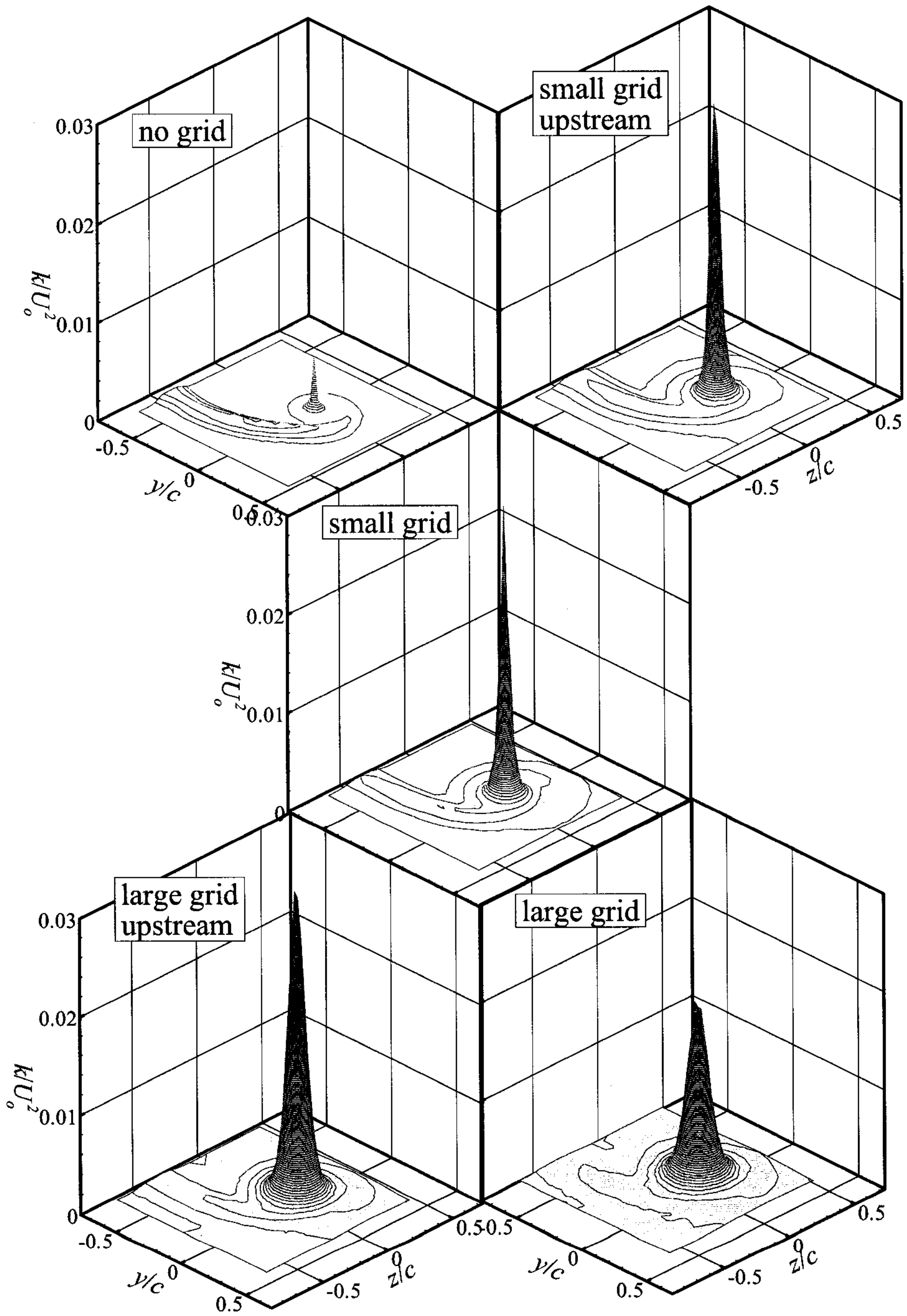

Figure A.4: Contours of k/U_o^2 at $X/c = 7.75$ for each measurement case. Contours are spaced 0.0002 apart.

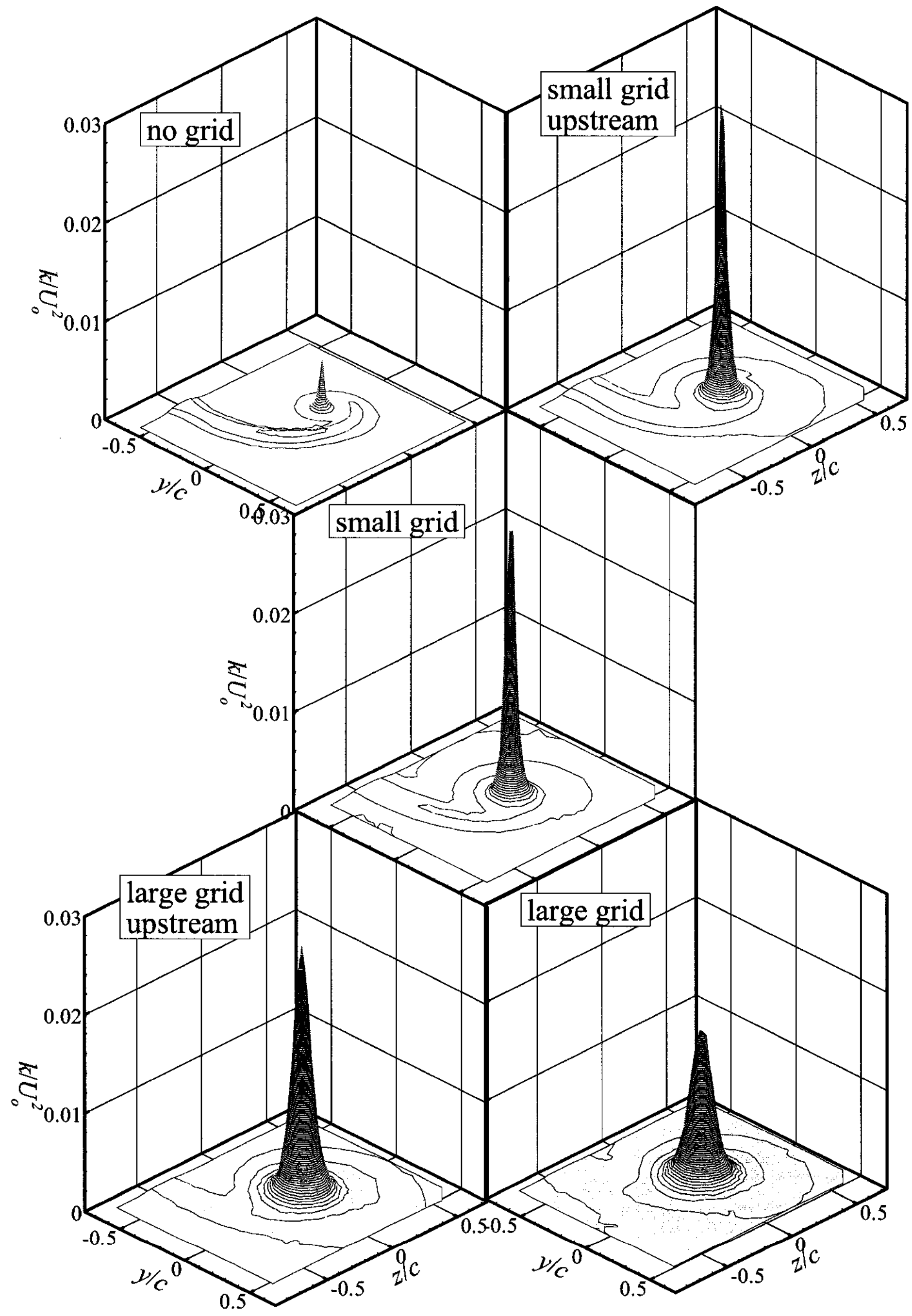

Figure A.5: Contours of k/U_o^2 at $X/c = 9.75$ for each measurement case. Contours are spaced 0.0002 apart.

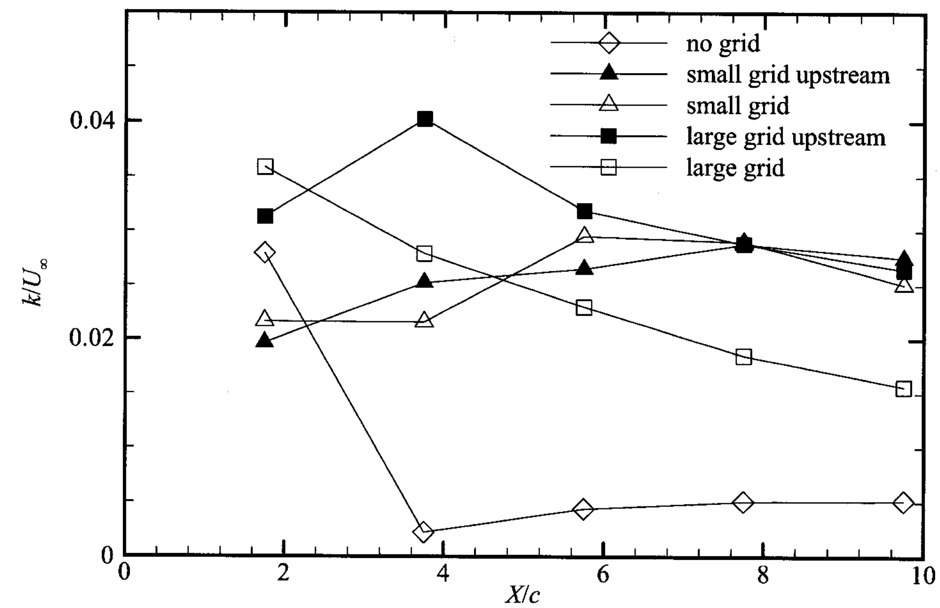

Figure A.6: Maximum k/U_o^2 measured for each of the measurement cases.

free-stream turbulence. The rms wandering amplitude was smaller than the core radius for the small-grid and small-grid-upstream cases and greater than the core radius for the large-grid and large-grid-upstream cases. Thus, the increases in maximum k/U_o^2 with X/c for the small-grid and small-grid-upstream cases were caused by the increase in wandering amplitude with X/c, because at $(y, z) = 0$ the probe was within the vortex core, where the velocity gradient is highest, for most of the measurement time. However, for the large-grid and large-grid-upstream cases, the probe was outside the vortex core, where the velocity gradient is smaller, for the majority of the measurement time. Hence, the decrease with X/c observed for the large-grid case and large-grid-upstream cases was caused by an increase in the time that the probe was outside the core due to increased wandering amplitude. For the no-grid case, the rapid decrease in peak k/U_o^2 from $X/c = 1.75$ to $X/c = 3.75$ is possibly caused by decay of turbulence entrained within the vortex core during formation. Downstream of $X/c = 3.75$, the maximum k/U_o^2 increases as the wandering amplitude increases.

A.2 Time-averaged Reynolds normal stresses in the streamwise direction

The variations of the measured streamwise normal stress $\overline{u_x^2}$ normalized by U_o^2 are shown in three dimensional contour form in Figures A.7-A.11 for $X/c = 1.75$, 3.75, 5.75, 7.75 and 9.75 at $\mathrm{Re}_c = 2.4 \times 10^5$ and $\alpha = 5°$. Similarities can be observed in these figures when they are compared to the turbulent kinetic energy distributions presented above, most notably high fluctuations in the spiral wake and a local peak at $(x, y) = (0, 0)$.

The spiral wake is evident in Figures A.7-A.11 as a thin region of $\overline{u_x^2}/U_o^2$ values slightly higher than those in the free-stream. The thickness of the spiral wake increased with both increasing free-stream turbulence and streamwise distance. As streamwise distance increased, there was a noticeable decrease in magnitude of $\overline{u_x^2}/U_o^2$ values in the wake, with the rate of decrease varying between the different cases. By $X/c = 9.75$ in the large grid case, the magnitude of $\overline{u_x^2}/U_o^2$ within the spiral wake was only slightly higher than the magnitude in the free-stream.

With the exception of measurements at $X/c = 1.75$, the highest $\overline{u_x^2}/U_o^2$ values were measured at the time-averaged vortex centre, appearing as a dominant peak in Figures A.7-A.11. As both streamwise distance and free-stream turbulence intensity increased, this peak became broader. The magnitude of the peak is given in Figure A.12 as a function of streamwise distance for all five cases. Higher magnitudes of $\overline{u_x^2}/U_o^2$ were measured with increasing free-stream turbulence and for all cases the peak values of $\overline{u_x^2}/U_o^2$ decreased with streamwise distance.

The streamwise behaviour of the peak values of $\overline{u_x^2}/U_o^2$ shown in Figure A.12 can possibly be explained by considering the effects of vortex wandering in combination with the decay of both the radial gradient of the streamwise velocity and of the turbulence within the vortex core. As shown in Section 6.2, the amplitude of vortex wandering increased with X/c and also with increasing free-stream turbulence. At large wandering amplitudes, the probe spends more time measuring outside the vortex core, where the radial gradient of U_x is expected to be small. Hence, as the amplitude increases, the peak $\overline{u_x^2}/U_o^2$ values can be expected to decrease. The rate of decrease of peak $\overline{u_x^2}/U_o^2$ could also be affected by

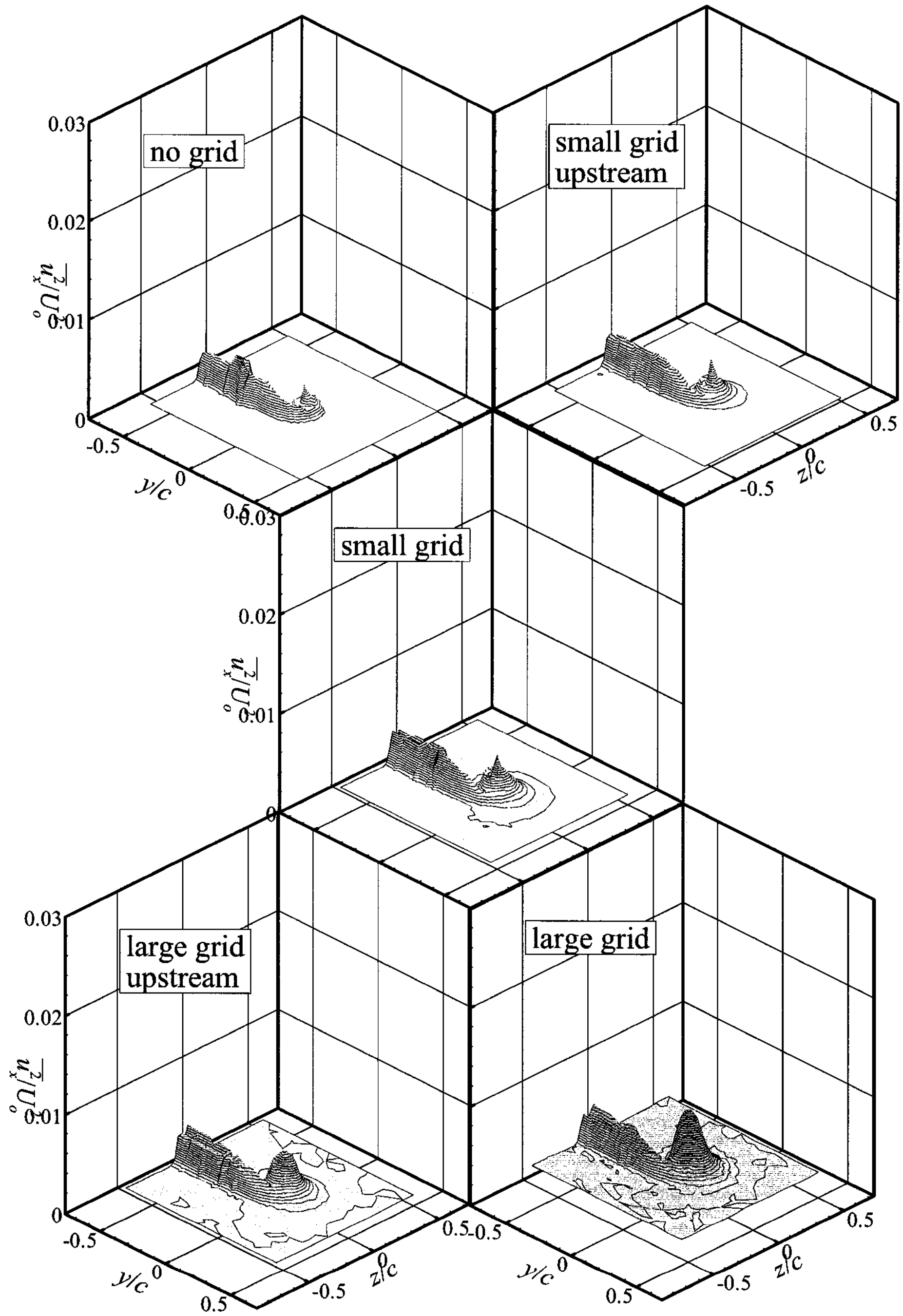

Figure A.7: Contours of $\overline{u_x^2}/U_o^2$ at $X/c = 1.75$ for each measurement case. Contours are spaced 0.0002 apart.

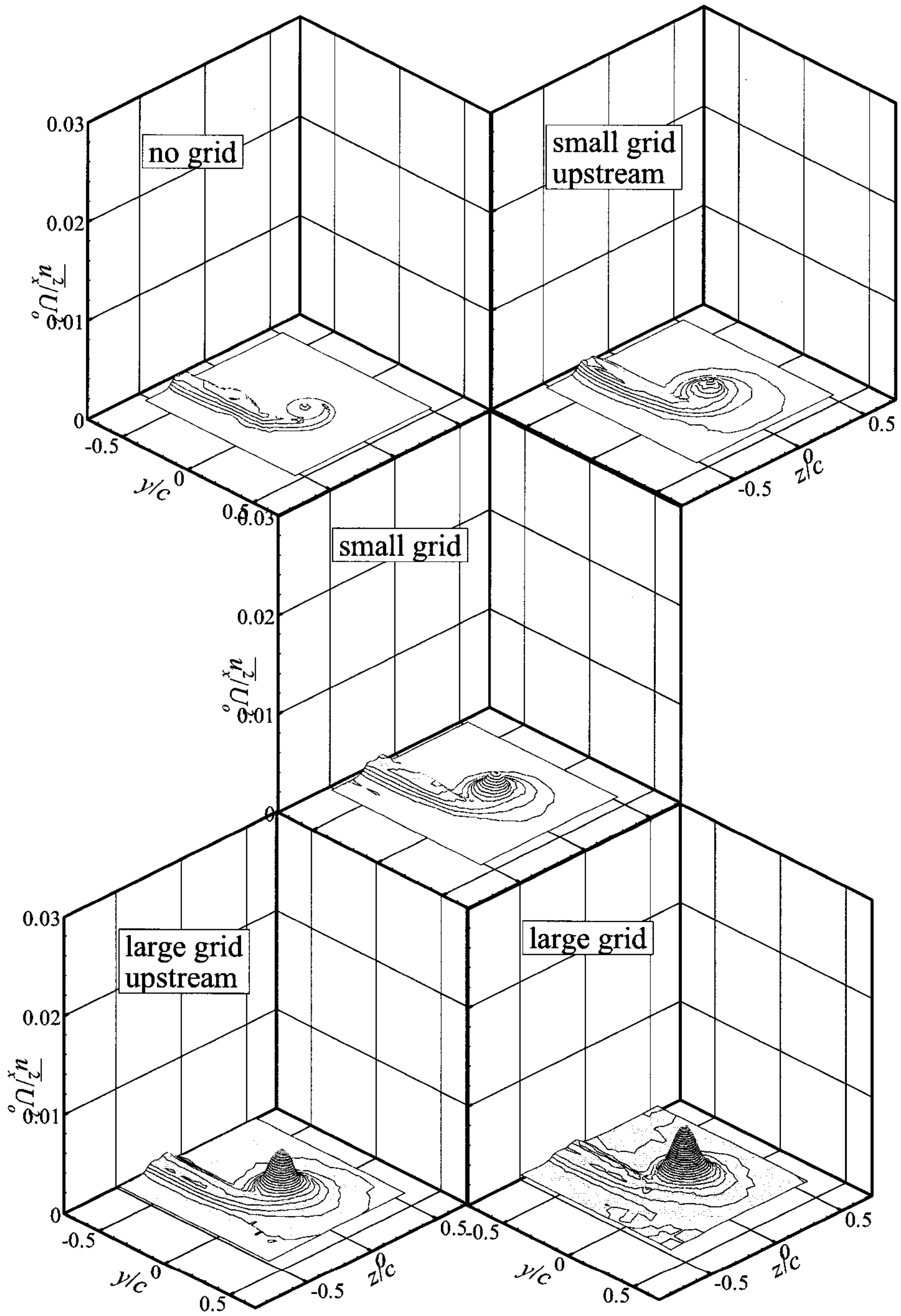

Figure A.8: Contours of $\overline{u_x^2}/U_o^2$ at $X/c = 3.75$ for each measurement case. Contours are spaced 0.0002 apart.

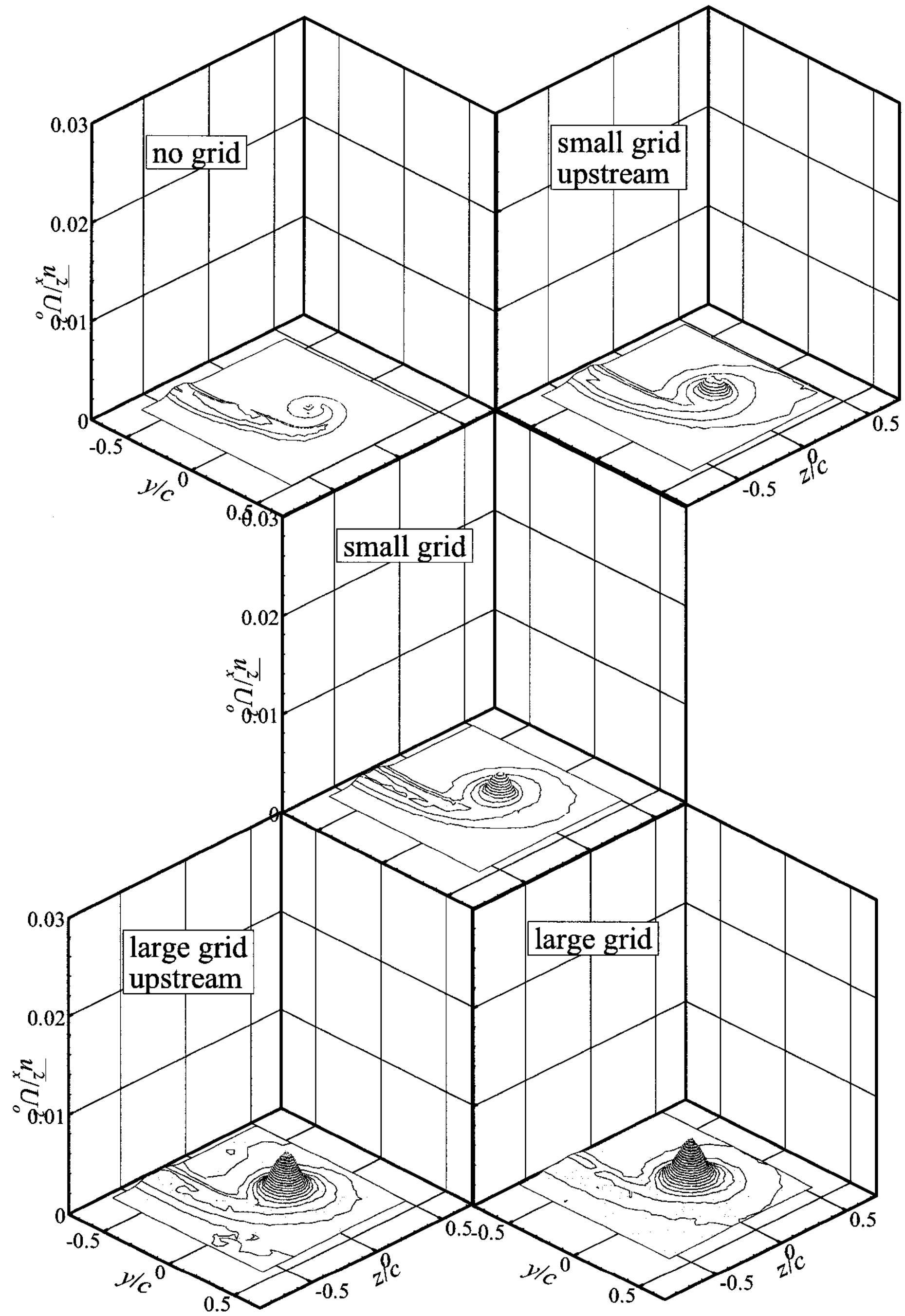

Figure A.9: Contours of $\overline{u_x^2}/U_o^2$ at $X/c = 5.75$ for each measurement case. Contours are spaced 0.0002 apart.

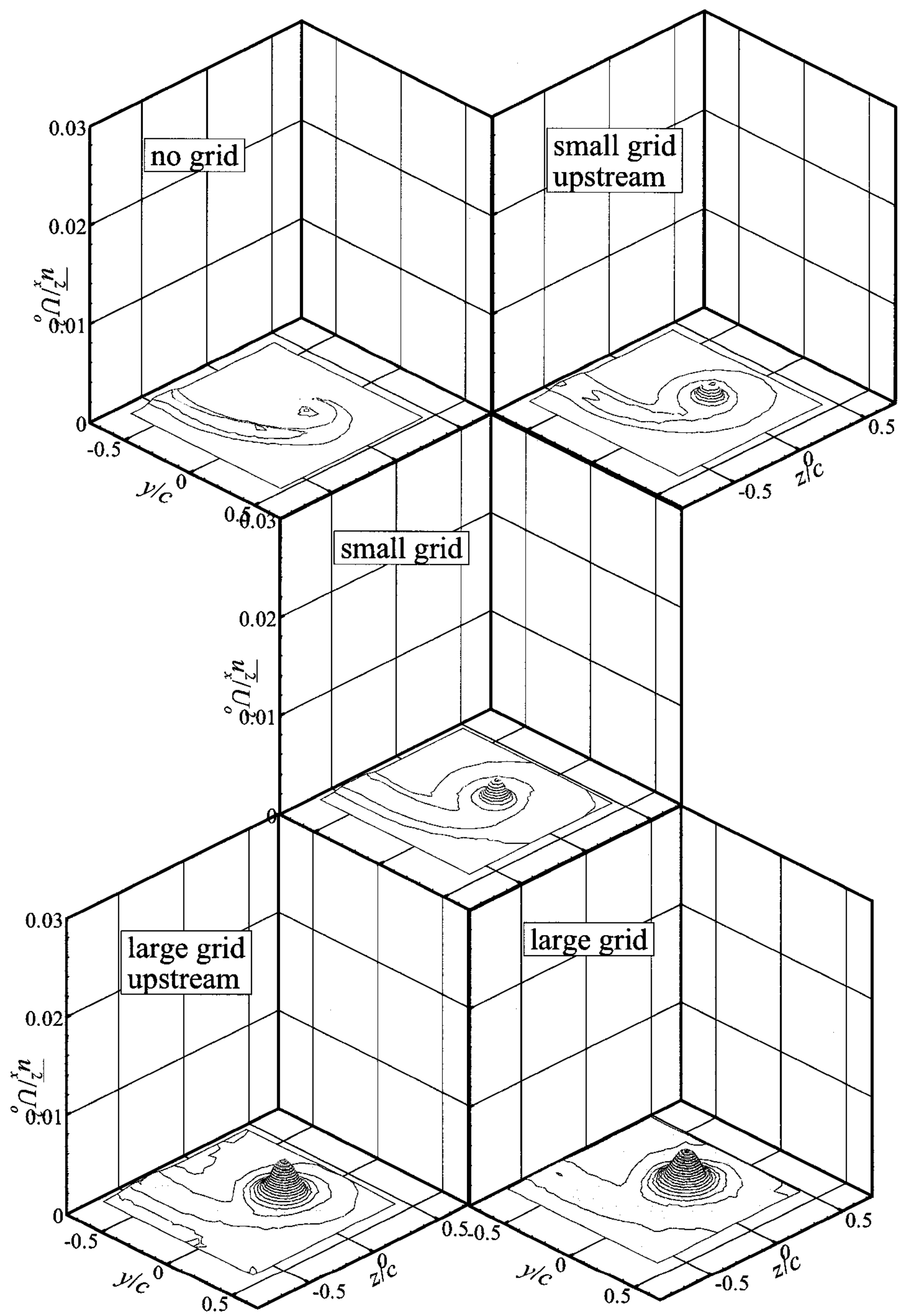

Figure A.10: Contours of $\overline{u_x^2}/U_o^2$ at $X/c = 7.75$ for each measurement case. Contours are spaced 0.0002 apart.

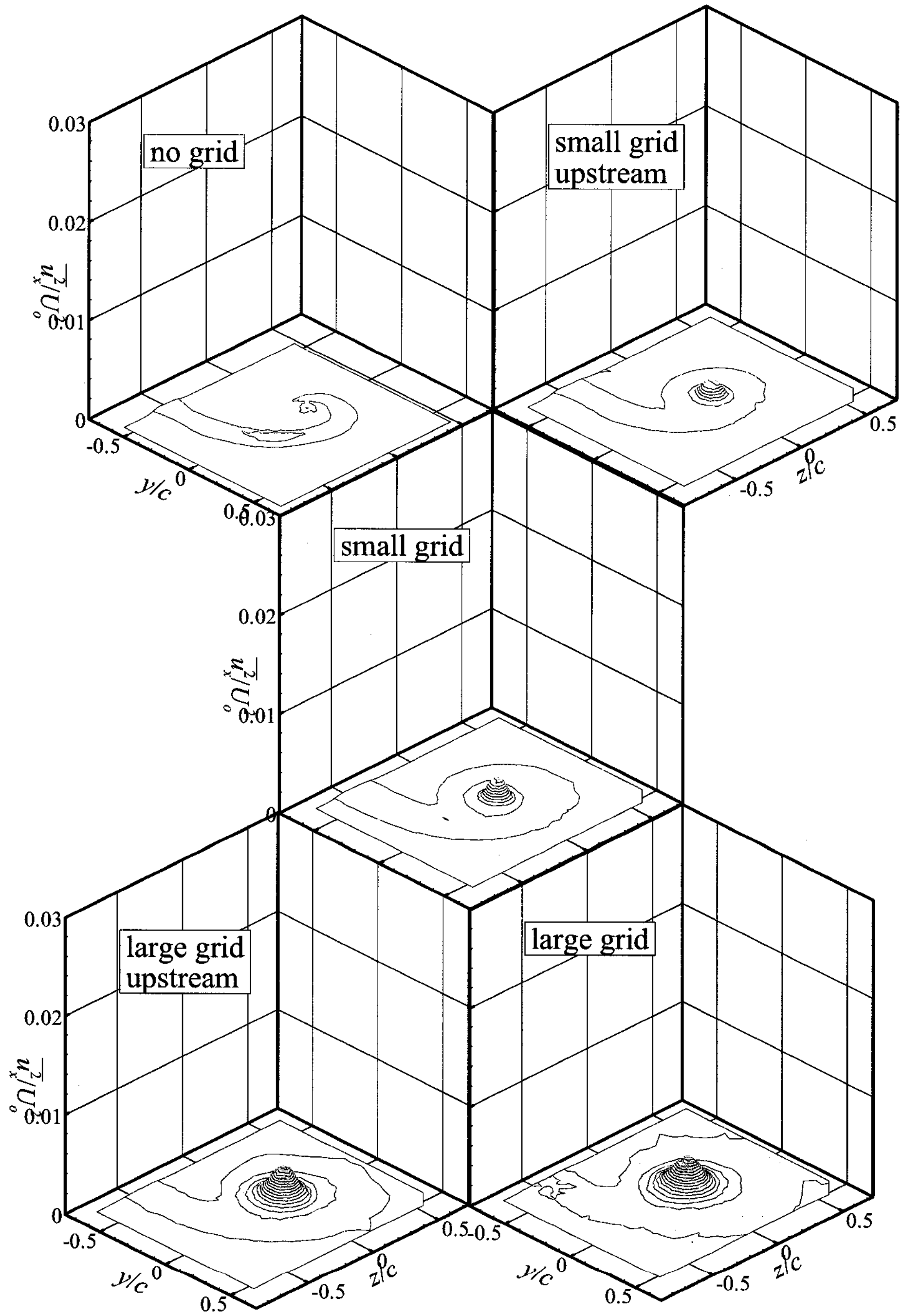

Figure A.11: Contours of $\overline{u_x^2}/U_o^2$ at $X/c = 9.75$ for each measurement case. Contours are spaced 0.0002 apart.

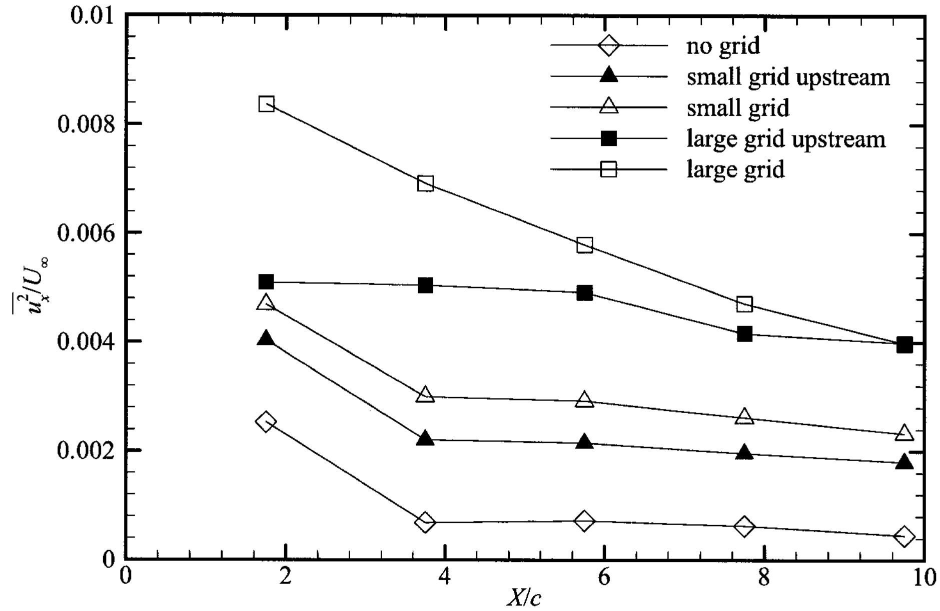

Figure A.12: Maximum $\overline{u_x^2}/U_o^2$ measured for each of the measurement cases.

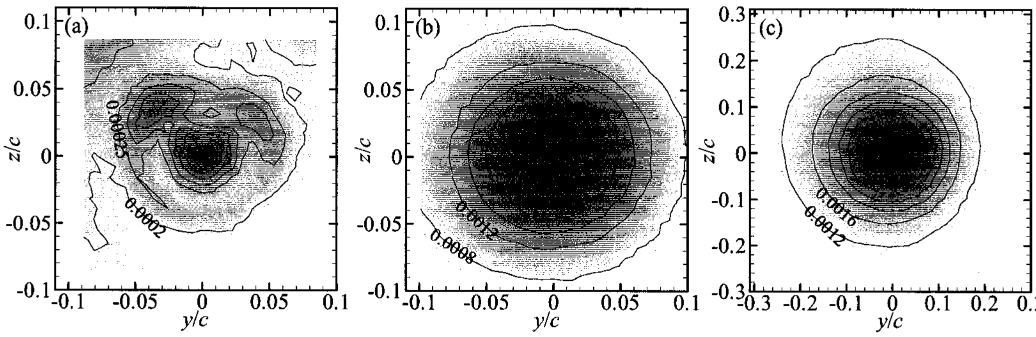

Figure A.13: Contours of $\overline{u_x^2}/U_o^2$ measured near the time-averaged vortex axis for the (a) no-grid, (b) small-grid and (c) large-grid cases.

a streamwise decrease in the radial gradient of U_x as the axial velocity deficit in the vortex core decreases. Finally, the trends of Figure A.12 could also contain some actual reduction of the local turbulence stress, however quantifying this effect is impossible because of the strong effect of vortex wandering.

The arrangement of the measured $\overline{u_x^2}/U_o^2$ values near the time-averaged vortex centre is more closely examined in Figure A.13, which shows isocontours of $\overline{u_x^2}/U_o^2$ measured in the high resolution, core-centred measurements for the no-grid, small-grid and large-grid cases at $X/c = 9.75$. Axi-symmetry of the $\overline{u_x^2}/U_o^2$ isocontours was observed for the two grid cases, however $\overline{u_x^2}/U_o^2$ measurements for the no-grid case revealed multiple peaks. The largest peak was at the time-averaged vortex centre with two evident secondary peaks, which were located asymmetrically at the same radial distance. Although the exact source of the peaks is not known, it is possible that they are caused by an increase in measurement error due to the large flow angles at this location since the peaks are approximately coincident with $\overline{U}_{\theta\,\max}$.

A.3 Time-averaged Reynolds normal stresses in the transverse directions

The measured transverse normal stresses $\overline{u_y^2}$ and $\overline{u_z^2}$, normalized by U_o^2, are shown as three-dimensional isocontours in Figures A.14-A.18 and Figures A.19-A.23, respectively, for $X/c = 1.75$, 3.75, 5.75, 7.75 and 9.75 at $\mathrm{Re}_c = 2.4 \times 10^5$ and $\alpha = 5°$. Similarities can be observed when comparing the corresponding figures of these stresses as well those of the turbulent kinetic energy and the streamwise normal stress distributions shown in Figures A.1-A.5 and Figures A.7-A.11. In particular, the spiral wake is evident as a thin region of $\overline{u_y^2}/U_o^2$ and $\overline{u_z^2}/U_o^2$ values slightly higher than those in the free-stream and the highest values of $\overline{u_y^2}/U_o^2$ and $\overline{u_z^2}/U_o^2$ were measured at the time-averaged vortex centre. The streamwise development of $\overline{u_y^2}/U_o^2$ and $\overline{u_z^2}/U_o^2$ is also similar to that of $\overline{u_x^2}/U_o^2$. With increasing free-stream turbulence and streamwise distance, the spiral wake thickens and there is decreasing difference between the magnitude of transverse normal stresses in the wake and in the free stream. At $X/c = 9.75$ in the large-grid case, the spiral wake is only scarcely evident.

As streamwise distance and free-stream turbulence intensity increase, the peaks of $\overline{u_y^2}/U_o^2$ and $\overline{u_z^2}/U_o^2$ evident at the time-averaged vortex centre in Figures A.14-A.18 and Figures A.19-A.23 broaden. However, the isocontours of $\overline{u_y^2}/U_o^2$ and $\overline{u_z^2}/U_o^2$ are not axi-symmetric but have ovoid shapes near the time-averaged vortex centre with the long axis of the oval aligned in the direction of the stress. Further away from the time-averaged vortex centre, tails are evident in the isocontours, causing them to appear more S-shaped.

At the time averaged centre of the vortex, the peak values of $\overline{u_y^2}/U_o^2$ and $\overline{u_z^2}/U_o^2$ were much greater in magnitude for the turbulent cases than for the no grid case. The peak

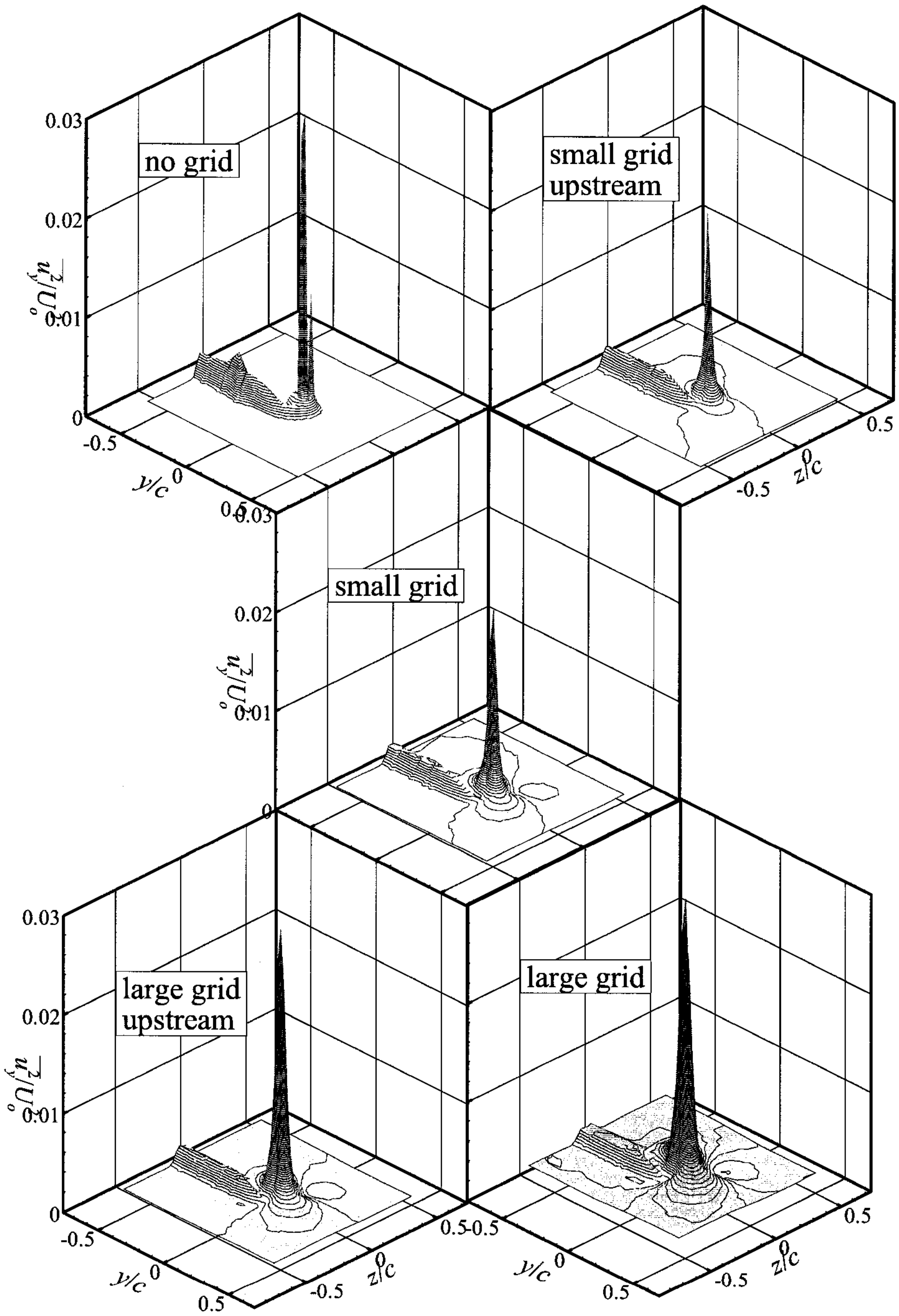

Figure A.14: Contours of $\overline{u_y^2}/U_o^2$ at $X/c = 1.75$ for each measurement case. Contours are spaced 0.0002 apart.

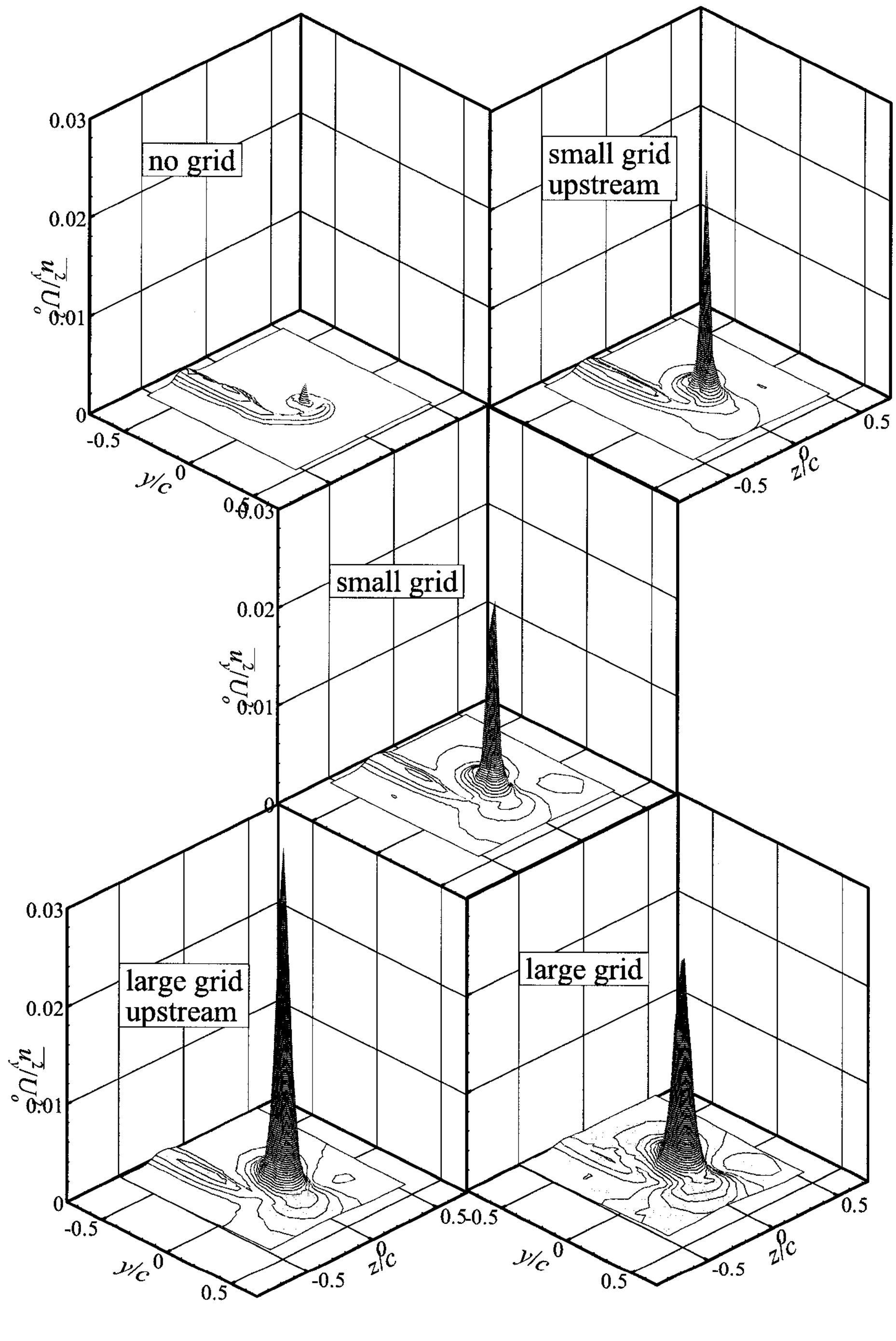

Figure A.15: Contours of $\overline{u_y^2}/U_o^2$ at $X/c = 3.75$ for each measurement case. Contours are spaced 0.0002 apart.

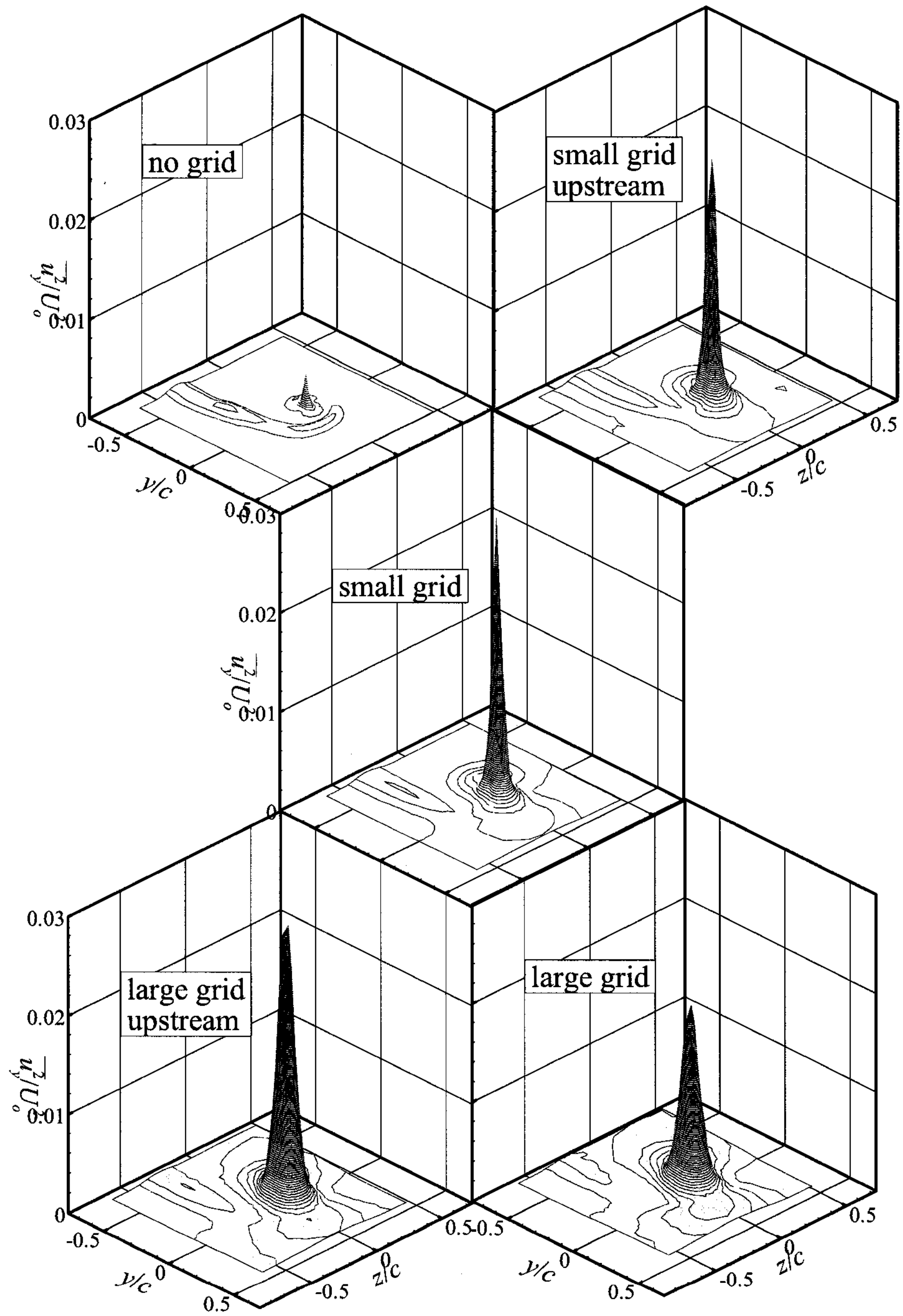

Figure A.16: Contours of $\overline{u_y^2}/U_o^2$ at $X/c = 5.75$ for each measurement case. Contours are spaced 0.0002 apart.

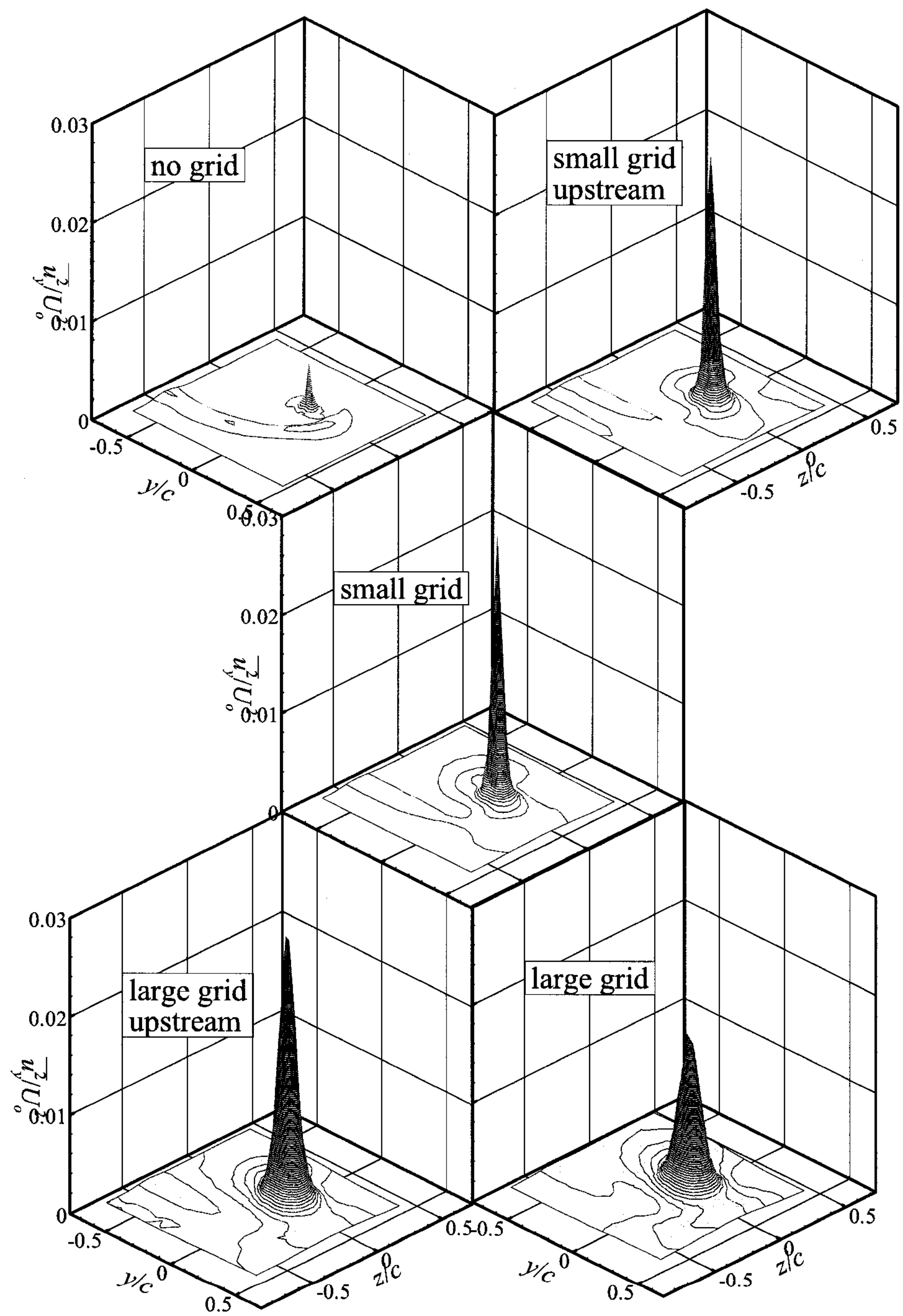

Figure A.17: Contours of $\overline{u_y^2}/U_o^2$ at $X/c = 7.75$ for each measurement case. Contours are spaced 0.0002 apart.

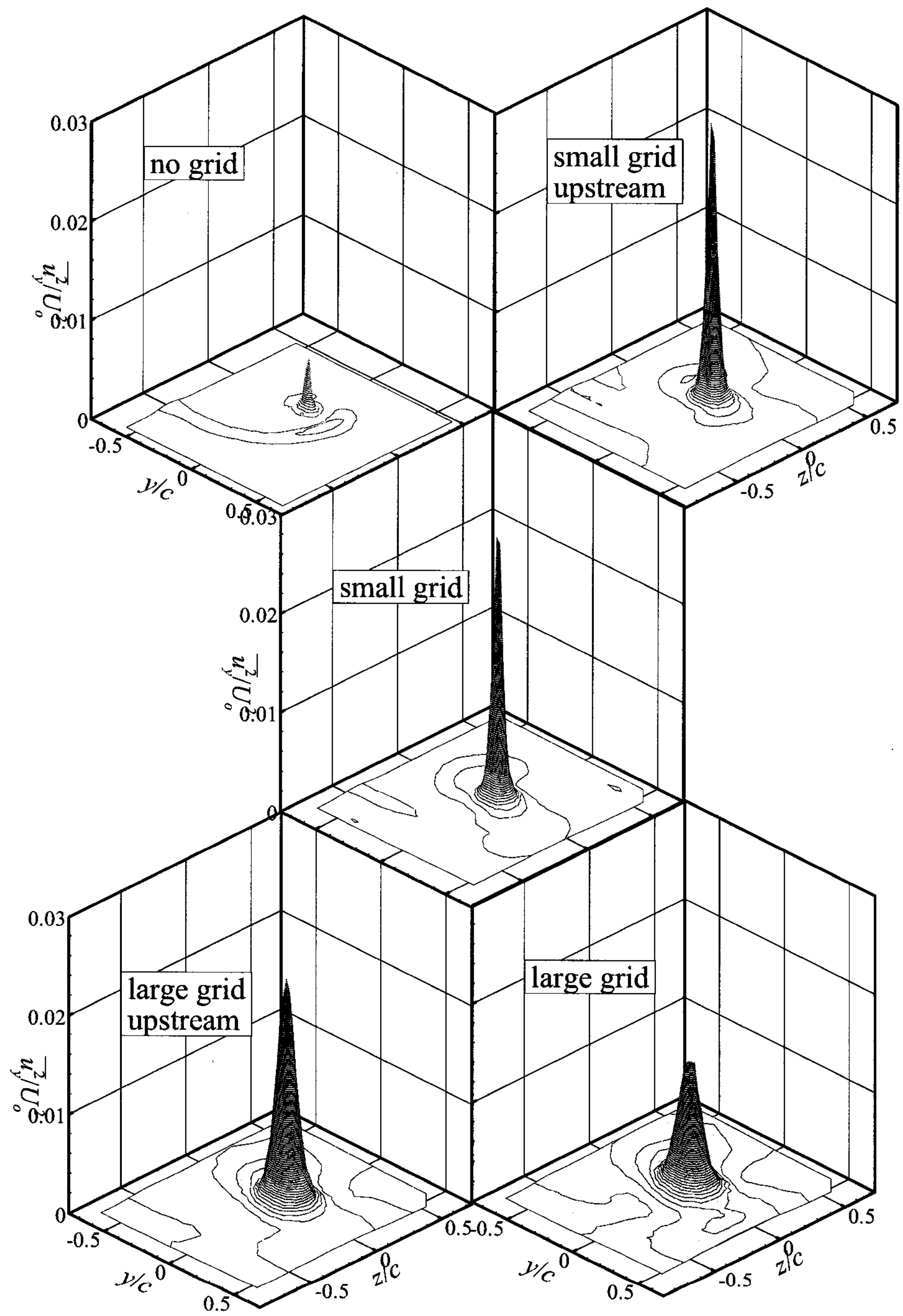

Figure A.18: Contours of $\overline{u_y^2}/U_o^2$ at $X/c = 9.75$ for each measurement case. Contours are spaced 0.0002 apart.

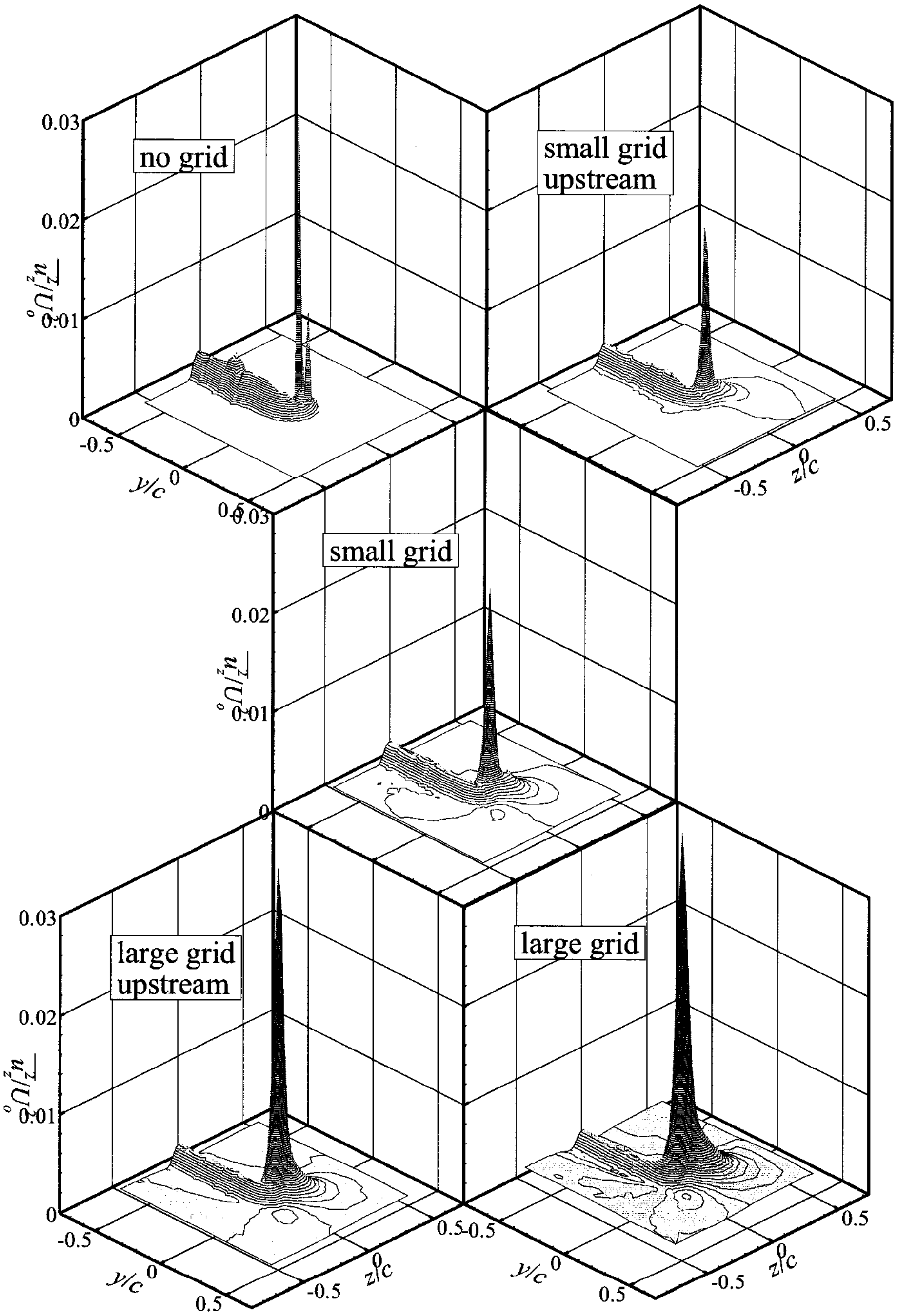

Figure A.19: Contours of $\overline{u_z^2}/U_o^2$ at $X/c = 1.75$ for each measurement case. Contours are spaced 0.0002 apart.

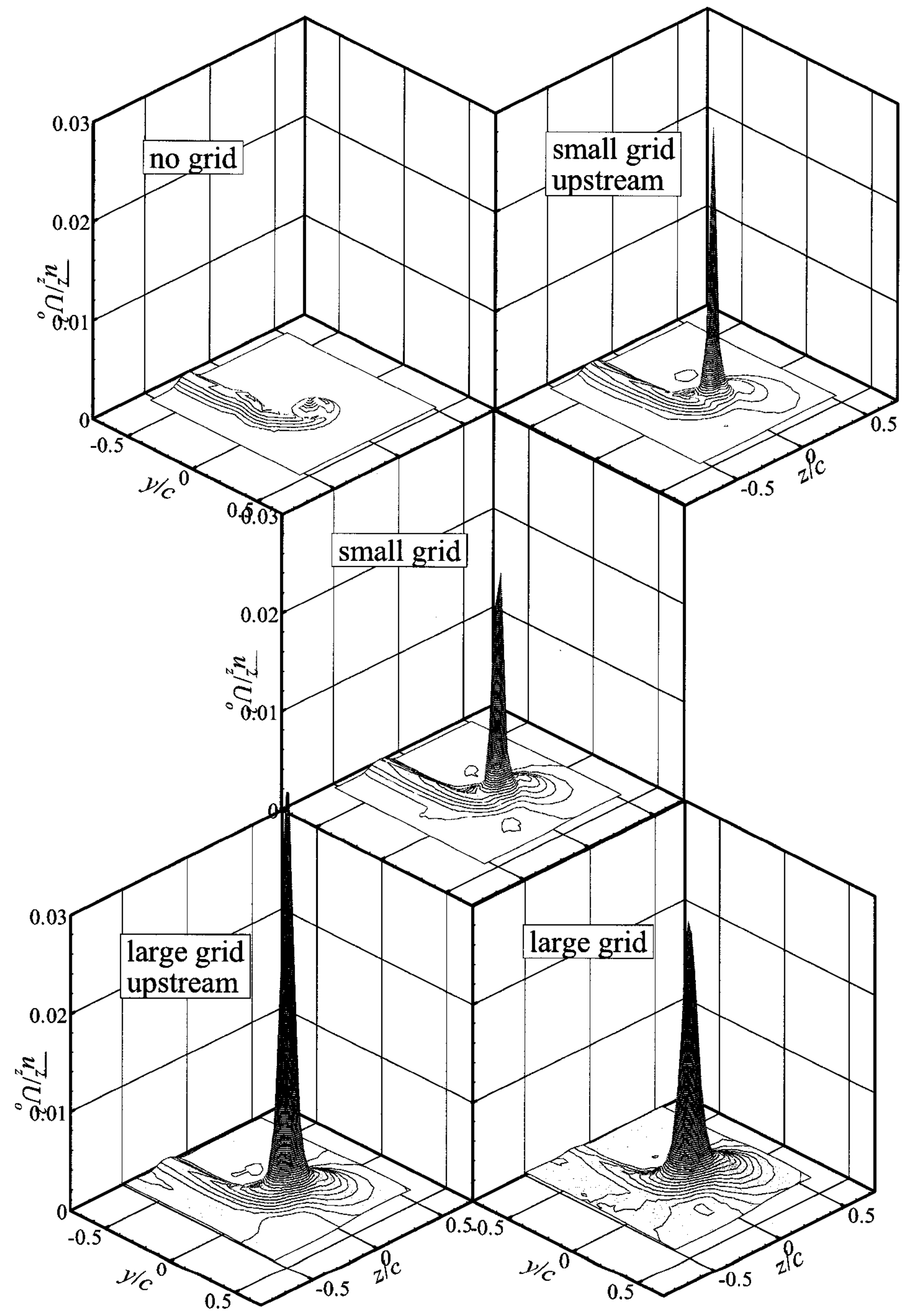

Figure A.20: Contours of $\overline{u_z^2}/U_o^2$ at $X/c = 3.75$ for each measurement case. Contours are spaced 0.0002 apart.

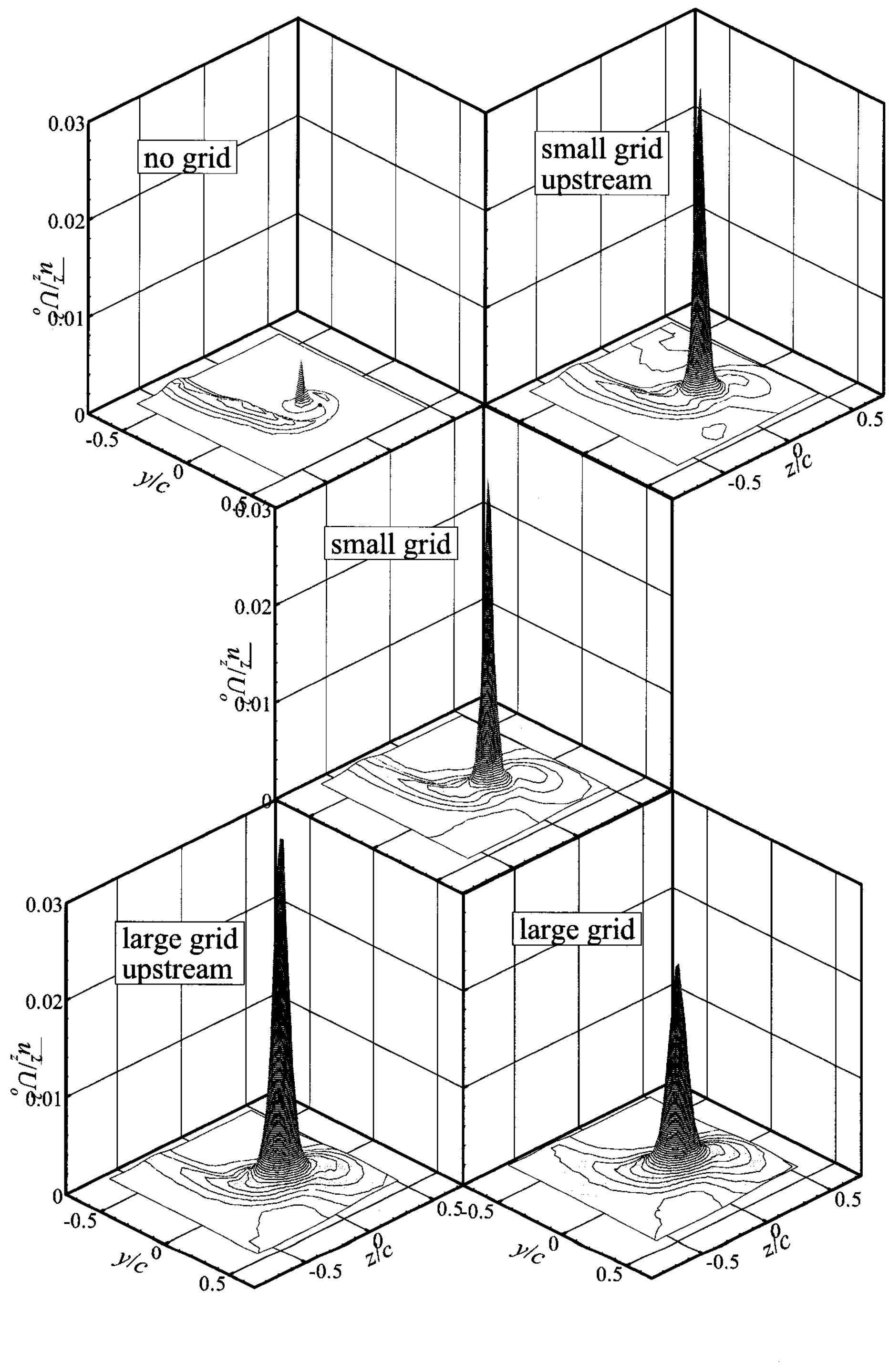

Figure A.21: Contours of $\overline{u_z^2}/U_o^2$ at $X/c = 5.75$ for each measurement case. Contours are spaced 0.0002 apart.

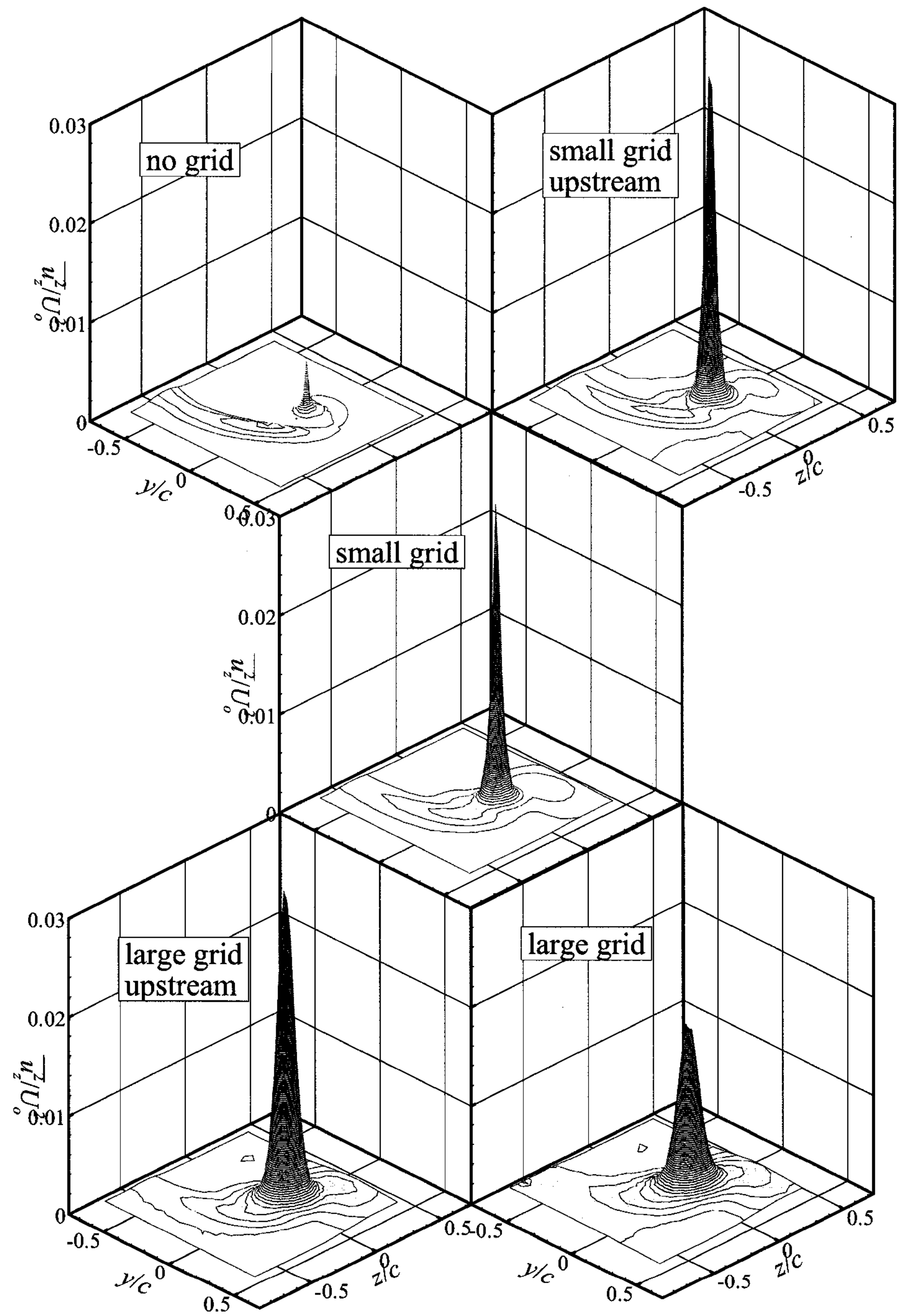

Figure A.22: Contours of $\overline{u_z^2}/U_o^2$ at $X/c = 7.75$ for each measurement case. Contours are spaced 0.0002 apart.

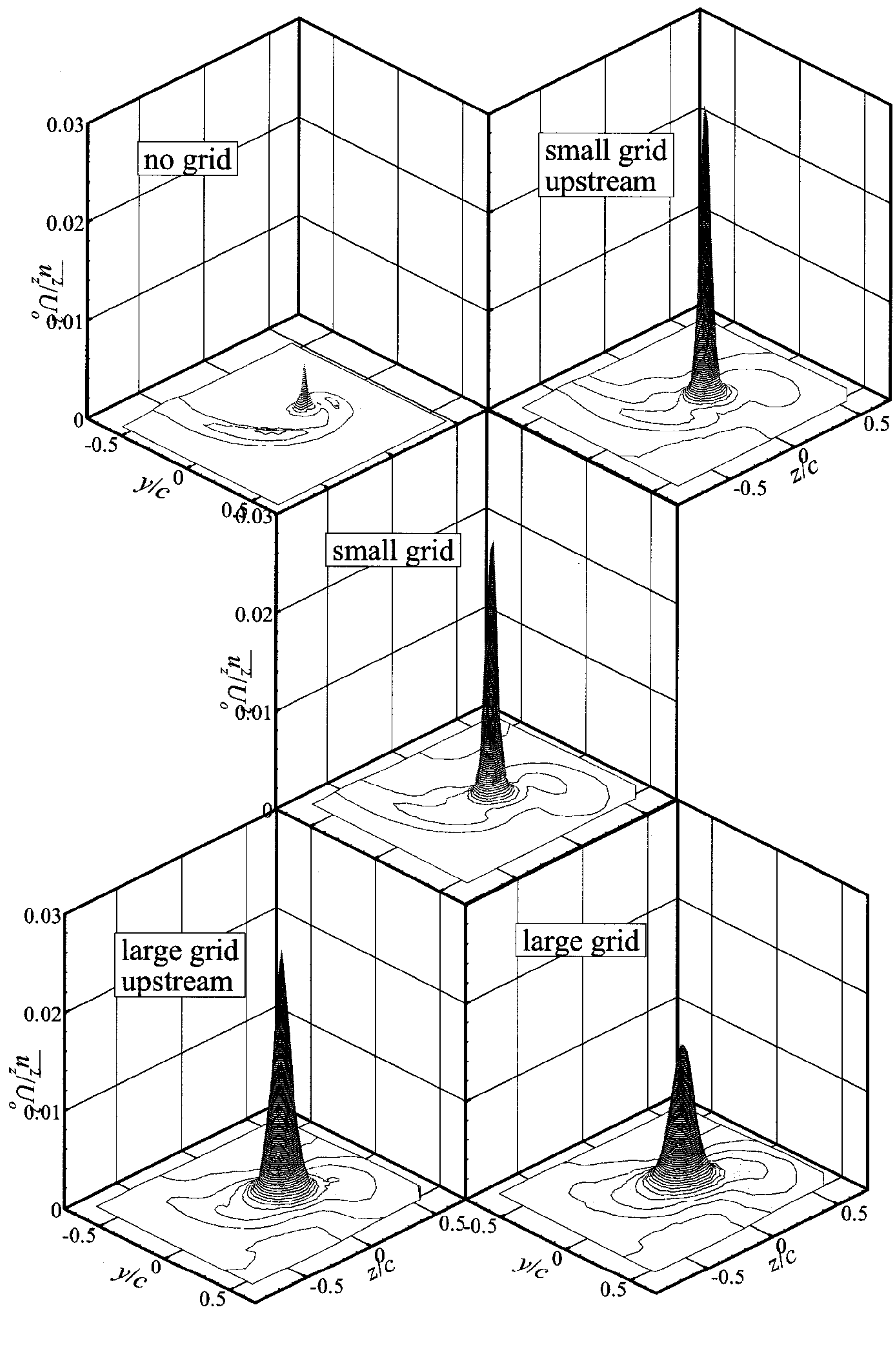

Figure A.23: Contours of $\overline{u_z^2}/U_o^2$ at $X/c = 9.75$ for each measurement case. Contours are spaced 0.0002 apart.

magnitude changed non-monotonically in the same manner that was observed for k/U_o^2 in Figure A.6. Figures A.24 and A.25 illustrate the changing peak magnitude of $\overline{u_y^2}/U_o^2$ and $\overline{u_z^2}/U_o^2$ respectively for each of the cases. The peak $\overline{u_y^2}/U_o^2$ and $\overline{u_z^2}/U_o^2$ values measured for the no grid case were initially comparable to the turbulent cases, but rapidly decreased by an order of magnitude between $X/c = 1.75$ and $X/c = 3.75$, then increased gradually downstream. Peak $\overline{u_y^2}/U_o^2$ and $\overline{u_z^2}/U_o^2$ values for the small grid upstream and small grid cases do not show any initial decrease in $\overline{u_y^2}/U_o^2$ and $\overline{u_z^2}/U_o^2$, but instead gradually increased with streamwise distance. Peak $\overline{u_y^2}/U_o^2$ and $\overline{u_z^2}/U_o^2$ values initially increased between $X/c = 1.75$ and $X/c = 3.75$, then decreased downstream. Although the initial increase in peak $\overline{u_y^2}/U_o^2$ and $\overline{u_z^2}/U_o^2$ values was not evident for the large-grid case, the magnitude decreased with streamwise distance at the same rate as for the large-grid-downstream case.

When compared to the magnitude of the peak $\overline{u_x^2}/U_o^2$ stresses plotted in Figure A.12, the peaks of $\overline{u_y^2}/U_o^2$ and $\overline{u_z^2}/U_o^2$ have significantly larger magnitudes, indicating that the similarity between the evolutions of k/U_o^2, $\overline{u_y^2}/U_o^2$ and $\overline{u_z^2}/U_o^2$ is due to the greater contribution to k from the transverse normal stresses. When comparing Figure A.24 to Figure A.25, it is evident that the measured peak values of $\overline{u_z^2}/U_o^2$ were slightly larger than those of $\overline{u_y^2}/U_o^2$. Noting that the trends in peak k can be almost entirely explained by vortex wandering, the similarity in the trends between the peak values of k/U_o^2, $\overline{u_y^2}/U_o^2$ and $\overline{u_z^2}/U_o^2$ with X/c is also consistent with wandering. Since the greatest contribution to k due to vortex wandering is due to radial gradients of U_θ, which are larger than the radial gradients of U_x. It therefore appears logical to expect that, in a Cartesian coordinate system, the wandering would result in the greatest effect on the the U_y and U_z time signals. Slight

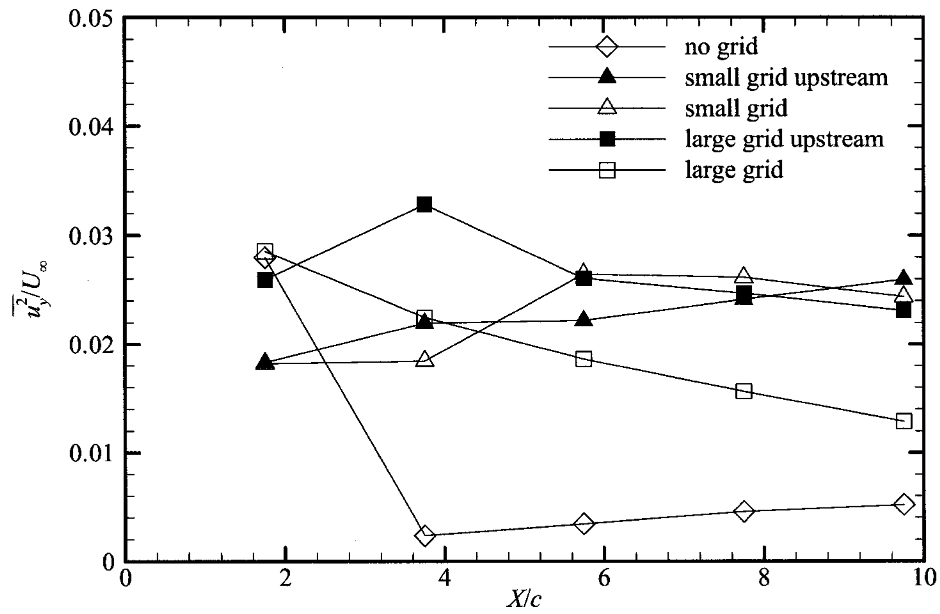

Figure A.24: Maximum $\overline{u_y^2}/U_o^2$ measured for each of the measurement cases.

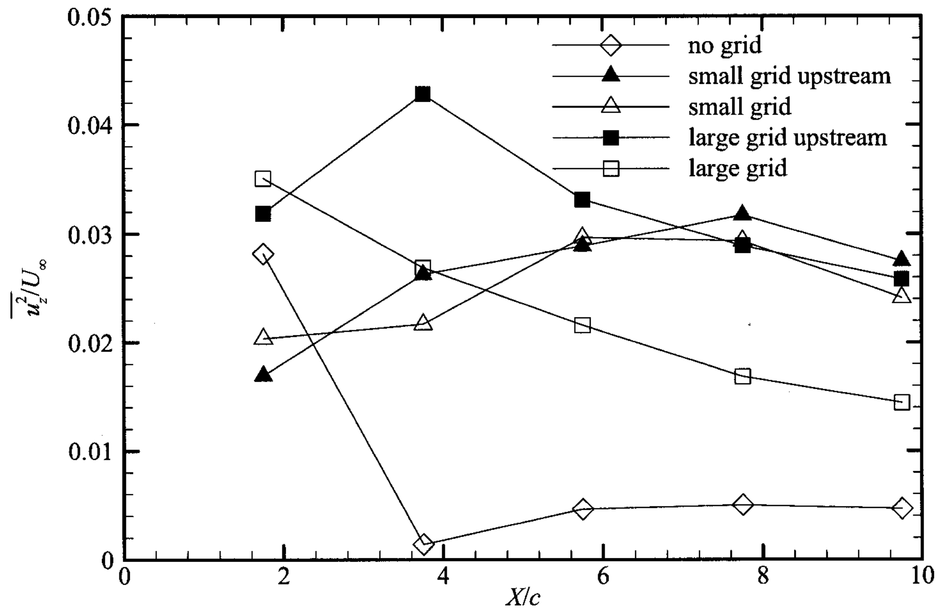

Figure A.25: Maximum $\overline{u_z^2}/U_o^2$ measured for each of the measurement cases.

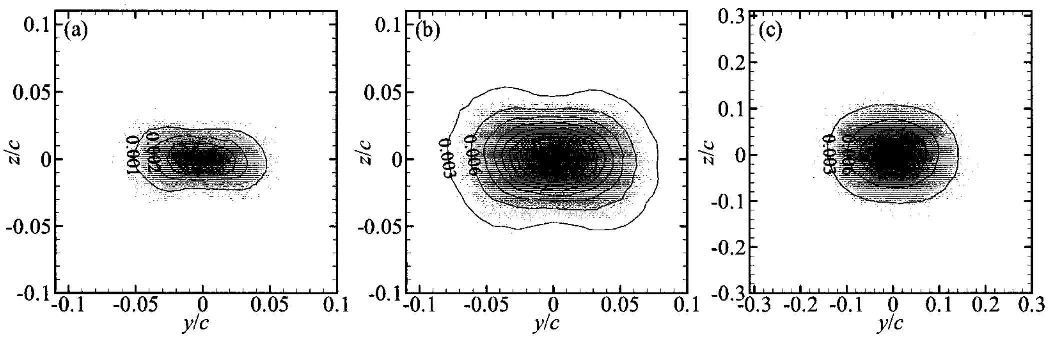

Figure A.26: Contours of $\overline{u_y^2}/U_o^2$ measured near the time-averaged vortex centre at $X/c = 9.75$ for the (a) no-grid, (b) small-grid and (c) large-grid cases.

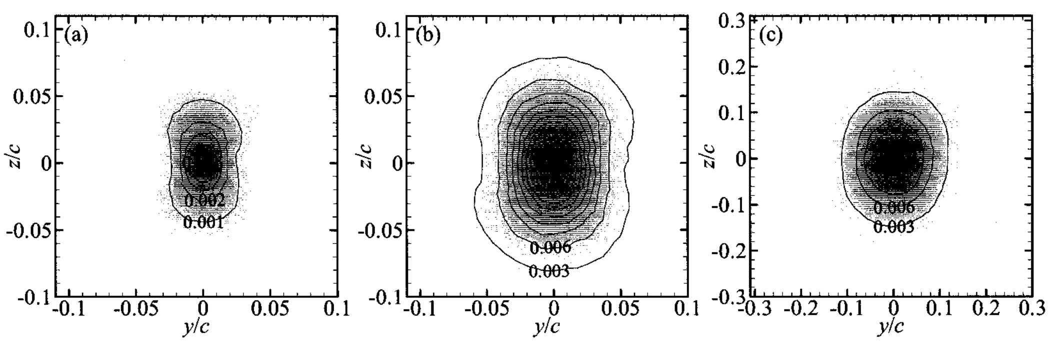

Figure A.27: Contours of $\overline{u_z^2}/U_o^2$ measured near the time-averaged vortex centre at $X/c = 9.75$ for the (a) no-grid, (b) small-grid and (c) large-grid cases.

anisotropy was also observed in the vortex wandering direction, which would cause a slight difference between the peak values of $\overline{u_y^2}/U_o^2$ and $\overline{u_z^2}/U_o^2$.

The peak transverse normal Reynolds stresses are more closely examined in Figure A.26 for $\overline{u_y^2}/U_o^2$ and Figure A.27 for $\overline{u_z^2}/U_o^2$. These figures show isocontours of $\overline{u_y^2}/U_o^2$ and $\overline{u_z^2}/U_o^2$ measured during the core-centred measurements for the no grid, small grid and large grid cases at $X/c = 9.75$. In these figures, the oval shape of the isocontours is clearly visible. Similar isocontours were presented by Devenport et al. (1996), who attributed these patterns to vortex wandering.

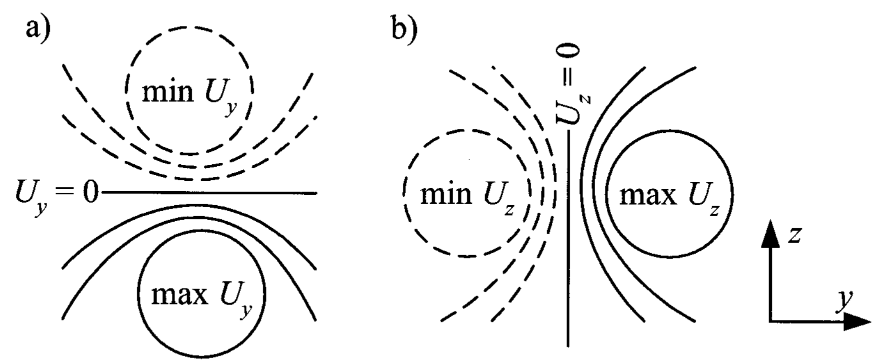

Figure A.28: Sketch of isocontours of (a) U_y and (b) U_z within an idealized vortex. Negative contours have been indicated by dashed lines.

As shown in Section 6.2, the vortex wandering causes the vortex position to be randomly distributed in the yz plane. The probability distribution of vortex position in this plane was found to be well approximated by a bi-normal probability distribution centred at $(y, z) = (0, 0)$. It is this property that results in the pattern of contours shown in Figures A.26 and A.27 when combined with the distribution of U_y and U_z in the vortex, as shown in Figure A.28. The smallest velocity gradients are near the maximum and minimum U_y and U_z values, where the velocity peaks. Hence, as the vortex wanders in the y and z directions, the smallest contribution of wandering to $\overline{u_y^2}/U_o^2$ and $\overline{u_z^2}/U_o^2$ will be near the locations of maximum and minimum U_y and U_z, which are along the z and y axes, respectively. The result is an oblong distribution of $\overline{u_y^2}/U_o^2$ and $\overline{u_z^2}/U_o^2$ with increased wandering resulting in a more diffuse appearance of the isocontours.

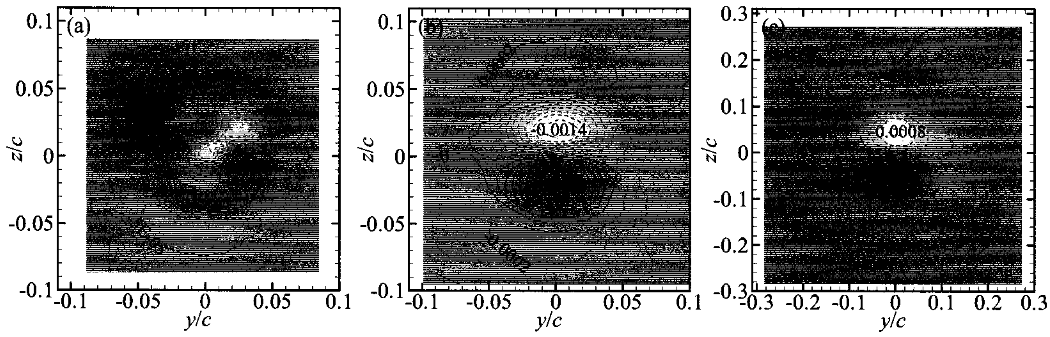

Figure A.29: Contours of $\overline{u_x u_y}/U_o^2$ measured near the time-averaged vortex centre at $X/c = 9.75$ for the (a) no-grid, (b) small-grid and (c) large-grid cases.

A.4 Time-averaged Reynolds shear stresses

The previous sections presented the measured Reynolds normal stresses and identified two regions of interest, the spiral wake and the region near the time-averaged vortex axis. Due to the spiralling nature of the wake, Reynolds stresses calculated using a Cartesian coordinate system do not have much physical relevance within the spiral wake and therefore are not presented here.

The Reynolds shear stresses, $\overline{u_x u_y}/U_o^2$, $\overline{u_x u_z}/U_o^2$ and $\overline{u_y u_z}/U_o^2$ measured near the vortex axis during the high-resolution core-centred measurements at $X/c = 9.75$ are presented as isocontours in Figure A.29a-c respectively for the no-grid, small-grid and large-grid cases at $\mathrm{Re}_c = 2.4 \times 10^5$ and $\alpha = 5°$.

Isocontours of $\overline{u_x u_y}/U_o^2$ measured for the small-grid case and large-grid case, shown in Figure A.29, have distinctly similar patterns with two kidney shaped positive and negative regions with the positive region occurring for $z < 0$ and the negative region occurring for $z > 0$. Larger peak values of $\overline{u_x u_y}/U_o^2$ were measured for the small-grid case when compared

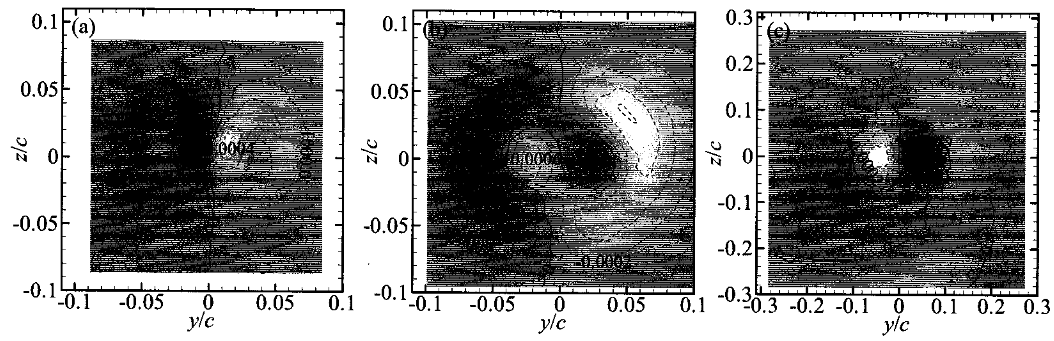

Figure A.30: Contours of $\overline{u_x u_z}/U_o^2$ measured near the time-averaged vortex centre at $X/c = 9.75$ for the (a) no-grid, (b) small-grid and (c) large-grid cases.

to the large-grid case. The smallest values of $\overline{u_x u_y}/U_o^2$ were measured for the no-grid case and no distinct pattern can be observed in the isocontours.

The isocontours of $\overline{u_x u_z}/U_o^2$, shown in Figure A.30, show slightly different patterns for each case. The no-grid case shows what appears to be a ring pattern of positive $\overline{u_x u_z}/U_o^2$ in the region $y < 0$ and negative $\overline{u_x u_z}/U_o^2$ in the region $y > 0$, with the peak values occurring very close to the time-average vortex centre. The small-grid case shows two anti-symmetric large kidney shaped areas of positive and negative stress in the $y < 0$ and $y > 0$ regions, respectively. Within the curve of the kidney shape lie two regions with opposite signs of $\overline{u_x u_z}/U_o^2$ near the time-averaged vortex centre. These smaller regions are also evident for the large-grid case with equivalent peak values, however, the larger kidney shapes are not evident.

Cloverleaf patterns of $\overline{u_y u_z}/U_o^2$ are evident for all cases in Figure A.31. These patterns have regions of negative $\overline{u_y u_z}/U_o^2$ in quadrants where $yz < 0$ and regions of positive $\overline{u_y u_z}/U_o^2$ in quadrants where $yz > 0$. Nearly identical patterns were measured by Devenport et al. (1996) and Heyes et al. (2004), who determine that the source of the patterns is vortex

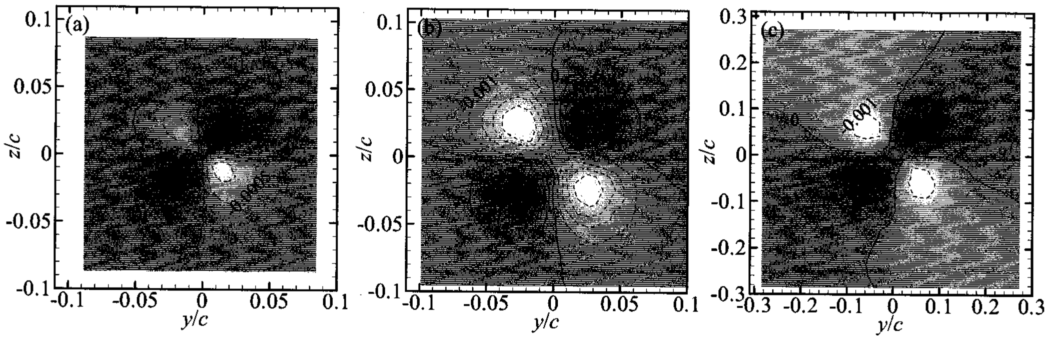

Figure A.31: Contours of $\overline{u_y u_z}/U_o^2$ measured near the time-averaged vortex centre at $X/c = 9.75$ for the (a) no-grid, (b) small-grid and (c) large-grid cases.

wandering. The magnitudes of the peak $\overline{u_y u_z}/U_o^2$ values were approximately the same for both the large-grid and the no-grid cases, however, significantly larger values were measured for the small-grid case.

The cloverleaf distribution of $\overline{u_y u_z}/U_o^2$ observed in Figure A.31 can be entirely attributed to vortex wandering. As shown in Section 6.2, vortex wandering causes the vortex position to change randomly in the yz plane. The probability distribution of vortex position in this plane was found to be approximated by a bi-normal probability distribution centred on $(y, z) = (0, 0)$. It is this property that results in the pattern of contours shown in Figure A.31 when combined with the distribution of U_y and U_z in the vortex, as shown in Figure A.28. Assuming that the vortex is in its position of greatest probability, namely at $(y, z) = (0, 0)$, we can examine the influence of movement of the vortex in different directions. Considering first the quadrant in which $y < 0$ and $z > 0$, we see that, near $r_{\theta\,\max}$, movement of the vortex in the positive y direction will cause an increase in U_y and a decrease in U_z, thus producing a negative correlation of U_y and U_z. Movement of the vortex in the negative y direction will result in increasing U_z and decreasing U_y, thus producing negative correlation. Vortex movement in the negative z direction results in decreasing U_y and increasing U_z, while the opposite occurs for movement of the vortex in the negative z direction. Therefore, in the quadrant where $y < 0$ and $z > 0$, all vortex movement will result in negative $\overline{u_y u_z}$ values near $r_{\theta\,\max}$. Repeating this exercise for the other quadrants, one would find a positive correlation of U_y and U_z in quadrants where $yz > 0$ and negative correlation of U_y and U_z in quadrants where $yz < 0$. The combination of correlations in all quadrants produces the cloverleaf pattern observed in Figure A.31. As the wandering amplitude increases, this pattern would appear less distinct.

Appendix B

Wandering correction of Devenport et al. (1996)

Devenport et al. (1996) corrected single-point measurements for the effects of vortex wandering by using an iterative technique to recover the velocity profile in the wandering frame from time averaged measurements. First, they fitted measurements of the streamwise and circumferential velocity components along the $y = 0$ axis with families of curves in the form of a series based on the Lamb-Oseen vortex, given as

$$U_{\theta m}\left(0, z\right) = \sum_{i=1}^{n} \frac{D_i}{z} \left[1 - \exp\left(\frac{-z^2}{c_i^2}\right)\right] \ . \qquad \text{(B.1)}$$

In these series fits, D_i and c_i are coefficients determined through a least-squares curve fit of the corresponding time-averaged velocity profile. Then, they assumed that the probability distribution of vortex position was binormal with parameters σ_y and σ_z equal to the rms wandering amplitudes in the y and z directions and a correlation coefficient e between the two variables, namely

$$P_v(y,z) = \frac{1}{2\pi\sigma_y\sigma_z\left(1-e^2\right)^{1/2}} \exp\left[\frac{-1}{2\left(1-e^2\right)}\left(\frac{z^2}{\sigma_z^2}+\frac{y^2}{\sigma_y^2}-\frac{2eyz}{\sigma_y\sigma_z}\right)\right] . \tag{B.2}$$

Note that c_i represents a radial scale and, to avoid complex results, one must enforce

$$c_i > \left[2\sigma_z^2\left(1-e^2\right)\right]^{1/2} , \tag{B.3}$$

which presents a constraint in the series fit of Equations B.1. Using initial guess values for σ_y and σ_z, the corrected profiles for these initial values were determined as

$$U_{\theta c}(r) = \sum_{i=1}^{n} \frac{B_i}{z}\left[1-\exp\left(\frac{-r^2}{a_i^2}\right)\right] , \tag{B.4}$$

where

$$a_i^2 = \frac{1}{2}c_i^2 - \sigma_y^2 - \sigma_z^2 + \frac{1}{2}\left[\left(2\sigma_y^2+2\sigma_z^2-c_i^2\right)^2 - 16\sigma_y^2\sigma_z^2\left(1-e^2\right) + 8\sigma_y^2 c_i^2\right]^{1/2} \tag{B.5}$$

and

$$B_i = D_i\left(2\sigma_y^2+a_i^2\right) / \left[\left(2\sigma_y^2+a_i^2\right)\left(2\sigma_z^2+a_i^2\right) - 4e^2\sigma_y^2\sigma_z^2\right]^{1/2} . \tag{B.6}$$

Once the corrected profiles were determined, the Reynolds stresses $\overline{u_y^2}_c$, $\overline{u_z^2}_c$ and $\overline{u_y u_z}_c$ at $y=0$ and $z=0$ caused by wandering of the vortex velocity profile $U_{\theta c}$ of amplitude σ_y and σ_z and were calculated as, for example,

$$\overline{u_y u_z}_c(0,0) = \int_{-\infty}^{\infty}\int_{-\infty}^{\infty} P_v(y,z)\, U_{yc}(0-y,0-z)\, U_{zc}(0-y,0-z)\, \mathrm{d}y\mathrm{d}z - U_{yc}(0,0)\, U_{zc}(0,0) \tag{B.7}$$

where U_{yc} and U_{zc} are the corrected Cartesian velocity components determined from $U_{\theta c}$; similar expressions were used to calculate $\overline{u_y^2}_c$ and $\overline{u_z^2}_c$. The Reynolds stresses calculated using Equation B.7 were compared to the measured Reynolds stresses at $(y,z)=(0,0)$ and new values of σ_y, σ_z from

$$\sigma^2_{y\text{new}} = \sigma^2_{y\text{old}}\overline{u^2_z}_{\text{meas}}/\overline{u^2_z}_c \quad \text{and} \quad \sigma^2_{y\text{new}} = \sigma^2_{z\text{old}}\overline{u^2_y}_{\text{meas}}/\overline{u^2_y}_c$$

with a new e calculated by requiring that the principal axes of the stresses be the same as those of wandering. This process was repeated until the differences between $\overline{u^2_y}_c$, $\overline{u^2_z}_c$, $\overline{u_y u_z}_c$ and $\overline{u^2_y}$, $\overline{u^2_z}$, $\overline{u_y u_z}$, respectively, decreased to an acceptable level, (i.e., $\left|\sigma_{y\text{new}} - \sigma_{y\text{old}}\right| / \sigma_{y\text{old}} < 0.1\%$ and similarly for the other parameters). This iterative procedure resulted in corrected velocity profile of $U_{\theta c}(r)$, wandering amplitudes σ_y, σ_z and correlation e.